Delineating the sulfur isotope signature of a VMS district by LA-ICP-QQQ-MS

Guillaume Barré[1], Crystal LaFlamme[1]
[1]Département de géologie et de génie géologique, Université Laval, Québec, Canada

Abstract. The demands for in situ sulfur isotopes analysis has increased in recent years. Yet, no rapid method for collecting high-resolution data with little sample preparation time is available. In this study, we developed a new analytical technique using LA-ICP-QQQ-MS, to rapidly acquire in situ $\delta^{34}S$ measurements on thin sections. This new method was tested on VMS samples from which the isotope signatures were previously characterized by bulk analyses. In situ lines of $\delta^{34}S$ analysis were performed on both pyrite and pyrrhotite from different types of VMS deposits (sub-seafloor replacement VMS, seafloor VMS and exhalites) with different bulk isotopic signatures. Overall, the in-situ measurements for each sample are consistent with the bulk signature. At the thin section scale, different analyses on the same grain return similar values that are individually slightly different from the bulk signature. However, the average signature from the different grains on a single sample is consistent with the bulk signature. It highlights the benefits of in situ analysis and validates the accuracy of this new in situ technique. This study opens new analytical opportunities for rapid in situ sulfur isotopes analysis in petrographically-characterized thin sections on different geological settings.

1 Introduction

Many metals are chalcophile and are often complexed with sulfur in the Earth's crust. Therefore, the understanding of sulfur reservoirs and the pathways of sulfur through the hydrosphere-geosphere, remain critical in ore deposit research. As sulfur can form many species and across a number of oxidation states, its pathways at the Earth's surface have been studied using its stable isotope signature $\delta^{34}S$ (e.g., Kump, 2012). Recently, the isotopic fractionation of sulfur has lent insight into its source reservoirs for a number of magmatic and/or hydrothermal deposit types, elucidating critical components for deposit formation (e.g., Seal, 2006; Hutchinson et al., 2020). For instance, in volcanogenic massive sulfide (VMS) systems, which form at, or near, the Earth's surface through the interaction of hydrothermal fluids with ocean water in often microbial-rich host rocks, sulfur isotopes have elucidated that thermochemically reduced seawater sulfate represents a significant sulfur reservoir (e.g., LaFlamme et al. 2021).

These deposit-scale sulfur isotope variations can be harnessed for an improved understanding of the spatial and temporal controls on sulfide precipitation and source reservoirs of sulfur and even metal endowment (see LaFlamme et al. 2018). However, interpreting growing $\delta^{34}S$ datasets necessitates in situ measurements, in order to analyse distinct micro-textures. Until presently, in situ $\delta^{34}S$ measurements have been commonly completed in 1-inch epoxy mounts using a secondary ion mass spectrometer (e.g., Caruso et al. 2018). However, the demand for in situ sulfur isotope analyses is growing and, therefore, rapid methods of high-resolution data collection with little sample preparation time must be developed.

Whereas other isotopic techniques requiring large, rapidly acquired datasets have moved to LA-ICPMS (e.g., U-Pb geochronology), sulfur isotope measurements have been hindered by poor ^{32}S and ^{34}S mass resolution on interfering oxides, hydroxides and argon of the plasma. New analytical developments, the LA-triple quadrupole (QQQ)-ICPMS, show promise in being able to precisely measure $\delta^{34}S$. Whereas the SIMS and LA-MC-ICP-MS instruments utilise a multi-collector to narrow the window of measurement to the very specific selected mass, the triple quadrupole places two quadrupoles (Q1 and Q3) in tandem, between which the ions of interest are reacted with a gas to change their masses and thus remove potential isobaric overlaps (known as MS/MS mode).

To demonstrate the benefit of rapidly collected $\delta^{34}S$ measurements completed in situ in petrographically-characterized thin sections by LA-QQQ-ICPMS, we present a case study in which we discriminate the sulfur isotope signature of massive sulfide lenses and exhalites in the Noranda and Matagami VMS districts of the Abitibi subprovince, Québec. Massive Cu-, Zn- and Fe-sulfides precipitated in seafloor hydrothermal systems are a result of complex water-rock interactions between magmas, hydrothermal fluids and circulating seawater as these processes influence heat and chemical fluxes and ultimately the precipitation of sulfides. When preserved in the ancient rock record these systems form VMS districts composed of three types of mineralized rock: stockwork, massive sulfide and exhalite (Huston et al. 2010). We monitor these processes by using the sulfur isotope signature and test the potential to deliver new vectoring methods that track the optimal conditions for the precipitation of massive sulfides in order to guide exploration in VMS districts.

2 Geology

The Abitibi Greenstone Belt is known to host one of the greatest Archean VMS endowments (e.g., Mercier-Langevin et al., 2011). The belt was formed between ca. 2790 to 2640 Ma and consists of a succession of volcanic and sedimentary rocks intruded by plutonic suites. All units were affected by low- to moderate-grade metamorphic overprint (Monecke et al., 2017 and references therein). Two VMS districts of the belt were sampled: the Noranda

and the Matagami districts. Three different types of deposits were sampled with different proportions of seawater sulfate incorporation and therefore different isotopic signatures are expected (Figure 1). These include: 1) The McLeod Deep mine (Matagami district) corresponds to a sub-seafloor replacement VMS where mostly magmatic isotopic signature is expected. Three different levels of the deposits were sampled: the semi massive sulfides zone, the massive sulfides lens and the stringer zone. The latter is mainly composed of large pyrite crystals with inclusions of sphalerite and chalcopyrite. The two other zones present similar sulfides assemblages of pyrite, sphalerite, chalcopyrite and pyrrhotite. Only the proportion of the different sulfides varied between the two zones. 2) Two seafloor VMS occurences in the Noranda district: Amulet and Moosehead. They are composed of pyrite, sphalerite and chalcopyrite with rare galena. Moosehead presents more sphalerite than Amulet and is associated with exhalite levels. Amulet shows alternating sphalerite-rich and chalcopyrite-rich layers always mixed with pyrite. 3) Noranda district exhalites include the 9191, 1244, 9187 and 9126. They mainly consist of laminated chert horizons with layers of pyrite ± chalcopyrite, sphalerite, pyrrhotite. They are often associated with VMS lenses and are formed from hydrothermal vents at or below the seafloor, with possible sedimentary influence (e.g., Huston et al., 2010).

3 Methodology

Analyses of pyrite and pyrrhotite were completed on 3 thin sections from the McLeod Deep VMS, 4 from the Noranda district exhalites and 1 from the Moosehead showing. They were first characterized petrographically by reflected light microscopy. In situ sulfur isotope measurements were completed on an Applied Spectra RESOlution-SE 193 nm ArF excimer laser ablation system with a large volume S155 sample cell coupled to an Agilent 8900 ICP-QQQ-MS. Four thin sections per analytical session were loaded into the cell together with reference materials in epoxy mounts. Straight or curved lines of a minimum length of 100 µm were acquired on single grains of pyrite and pyrrhotite, with a beam diameter of 38 µm. Mix of He ± Ar is used as carrier gas. In order to remove mass interferences that may be present during the analysis, oxygen was used in the reaction cell to react with isotopes S^{32} and S^{34} and increase their masses to 48 and 50, respectively. Thus, the interfering masses, which do not react with the oxygen, will be removed on the second quadrupole.

Primary matrix matched reference materials were used to calibrate instrumental mass fractionation and monitor drift throughout the session. Reference materials include Sierra pyrite ($\delta^{34}S$ = 2.17‰ ± 0.18; LaFlamme et al. 2016), and Pierre pyrrhotite ($\delta^{34}S$ = 4.73‰ ± 0.19; in-house). Secondary reference materials are used for quality control and include Iberia pyrite ($\delta^{34}S$ = 8.92‰ ± 1.11; in-house) and Montpelier pyrrhotite ($\delta^{34}S$ = 3.30‰ ± 0.19; in-house). All in-house reference materials have undergone a protocol for characterizing their chemical composition by CAMECA SX-100 electron probe micro-analyzer and isotopic signature by three sulfur extractions (by chromium-reduced sulfides solution; Canfield et al., 1986) measured by SF_6-fluorination-isotope ratio mass spectrometry at the Institut de Physique du Globe de Paris. Isotopic homogeneity was also verified by in situ measurements across multiple grains using the SIMS-1280 at University of Western Australia.

Data reduction was performed in Iolite v.4 (Paton et al., 2011) to select integration times and to identify, subtract the background and generate the $^{34}S/^{32}S$ ratios. Reference material normalization was completed by sample-standard bracketing by using the average of 2 standards before and after a series of 3 to 4 samples. Note that, standard values that differ by more than one standard deviation from the actual value are discarded and not used in data reduction processes. For unknown samples, outliers values are rejected when chemical equilibrium is assumed and their isotopic signatures differ by more than two standard deviations from the average of all similar analyses on the same sample. Uncertainty on each analysis varied from ± 1.22‰ to ± 2.17‰ and is calculated as the propagated error on the signature of the unknown determined from all the standards (primary and secondary).

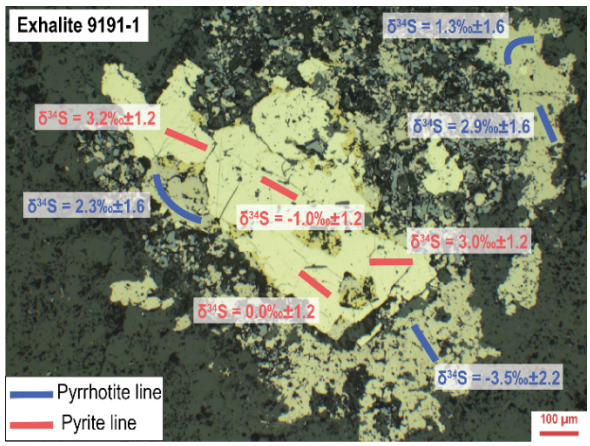

Figure 1. Reflected light microphotograph and location of analytical lines of pyrite and pyrrhotite and their respective $\delta^{34}S$ signature.

4 Results

A minimum of 4 lines of analyses were acquired on different grains of pyrite and pyrrhotite (when present) from each thin section (Figure 1). Note that uncertainties given in this section corresponds to the range of variation of the absolute values for a single sample and not the measurement error of an individual analysis. Pyrite and pyrrhotite from three samples (McLeod Deep 1, 2 and 3 on Figure 2) from the sub-seafloor replacement VMS (McLeod Deep mine, Matagami district) were analysed. All pyrite grains show similar $\delta^{34}S$ = -2.0‰ ± 1.2, when

pyrrhotite presents more variability with $\delta^{34}S$ = -0.3‰ ± 2.3. Only one exhalite from the Noranda district exhibited both pyrite and pyrrhotite (exhalite 9191), with isotopic signatures at $\delta^{34}S$ = 1.3‰ ± 2.1 and $\delta^{34}S$ = 2.6‰ ± 1.2, respectively. Pyrites from exhalites 9126 and 9187 show similar isotopic signatures at $\delta^{34}S$ = 3.3‰ ± 2.1 and $\delta^{34}S$ = 3.2‰ ± 1.4, respectively. Pyrites from exhalite 1244 and Moosehead showing (MO), also show similar values at $\delta^{34}S$ = 2.0‰ ± 1.0 and $\delta^{34}S$ = 1.7‰ ± 1.2, respectively (Figure 2). Overall, the obtained isotopic signatures are consistent within a single grain with high reproducibility between ± 0.1‰ and ± 2.2‰ (median at ± 0.7‰). The difference between two grains can be up to ± 5.1‰ in a single thin section (Figure 3).

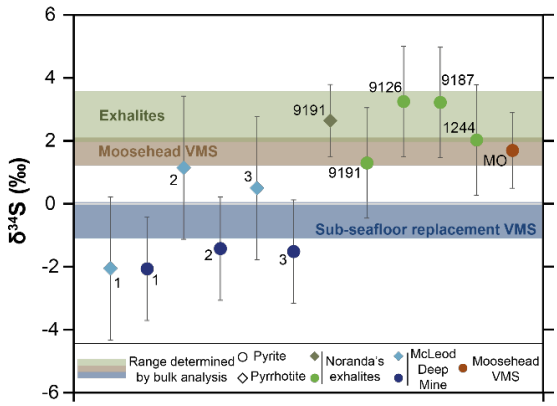

Figure 2. $\delta^{34}S$ values determined on pyrite and pyrrhotite from 8 thin sections from VMS and exhalite. Shaded areas show the range of $\delta^{34}S$ values obtained by bulk on the three different types of VMS. MO = Moosehead showing.

5 Discussion and conclusions

5.1 Suitable application of S isotopes by LA-ICPMS

The results obtained by LA-ICP-QQQ-MS were compared to the bulk isotopic signatures performed on the same samples (Barré et al., 2022). The pooling of all the pyrite and pyrrhotite data from a single thin section allows to better constrain the isotopic signature of the whole grain and to reduce the uncertainty of the values. The average of all lines of each thin section shows isotopic signatures broadly similar to bulk values. The maximum difference between the average of a single thin section and its associated bulk value is ± 1.1‰ (median at ± 0.3‰; Figure 2).

Exhalites 9126 and 1244 and the Moosehead showing have very similar isotopic signatures within a single grain with a maximum difference of ±0.7‰, while the difference between two grains of the same thin section can go up to 3.7‰. Nevertheless, for each sample the average of the two grains gives an isotopic signature similar to that of the bulk analysis (Figure 3).

Although different isotopic signatures between two pyrites can be observed in the same sample, the high reproducibility of the values within a single grain and the fact that the average of all the samples is consistent with the bulk signature, leads us to interpret isotopic variations as natural variation between grains, rather than associated to analytical error. Variations within larger grains can therefore likely be attributed to heterogeneous isotopic signatures within the same grain. Such variations cannot be observed with bulk techniques, so the reproducibility between bulk signatures and in situ averages value indicates high accuracy of the in-situ technique. The concordance between in situ and bulk isotopic signatures on a single sample show that LA-ICP-QQQ-MS is a suitable technique to determine sulfur isotopes at the thin section scale.

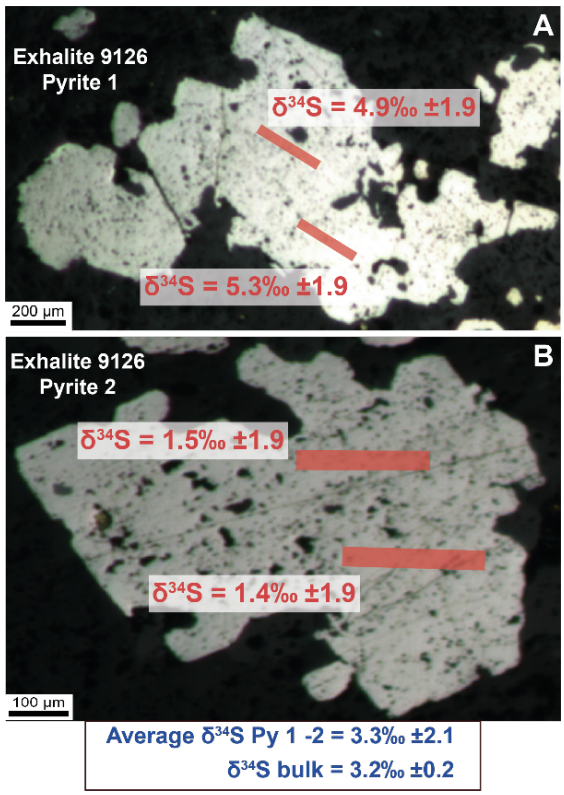

Figure 3. Reflected light microphotograph of two different pyrite grains from the same exhalite sample with the location of the lines of analysis carried out with their respective $\delta^{34}S$ signature. Note that the average of the $\delta^{34}S$ signatures of the two grains gives a value similar to the bulk value.

5.2 Delineating VMS district mineralisation using $\delta^{34}S$

Seawater sulfate influence changes depending on the type of VMS occurrences. Sub-seafloor replacement VMS will not record this influence, as sulfates precipitate before reaching the ore deposit area. Seafloor VMS will record a significant influence of seawater sulfate through the process of thermochemical sulfate reduction of seawater sulfate. In exhalite, the seawater influence can be important when it is close to a VMS deposit (Barré et al., 2022). Sulfur isotopes can be used as a vectoring tool to track this influence, discriminate

between these different VMS occurrences and determine the distance to a VMS deposit.

In this study, the analysis resolution of LA-ICP-QQQ-MS makes it possible to differentiate the isotopic signature of a sub-seafloor VMS deposit (McLeod Deep with $\delta^{34}S$ = -0.9‰ ± 2.1), from a seafloor VMS showing (Moosehead with $\delta^{34}S$ = 1.7‰ ± 1.2), and exhalite occurrences (9191, 9126, 9187 and 1244 with an average of $\delta^{34}S$ = 2.5‰ ± 1.6; Figure 4). Even though, so far, the error on a single measurement is relatively large (up to 2‰), when the data are pooled, the uncertainty decreases and leads to similar accuracy between bulk and LA-ICP-QQQ-MS. The resolution of this new technique is therefore sufficient to differentiate the types of VMS and exhalites within the same district.

Furthermore, we demonstrate here that this new technique can also differentiate between different generations of sulfides within a single thin section, which cannot be done with bulk techniques. The observation of such variations in situ is essential to better understand the variations within the deposit and thus better understand its formation. To date, only SIMS can perform such high-resolution sulfur isotope analysis. But sample preparation is time consuming, and it cannot be done on thin section. Sulfur isotopes analysis by LA-ICP-QQQ-MS in thin section is an important achievement that opens a new simple, rapid and high-resolution in situ sulfur isotopes technique. It will make it possible to increase the number of analyses that can be carried out on a single deposit and makes it possible to observe heterogeneity at the scale of the thin section or even at the grain scale.

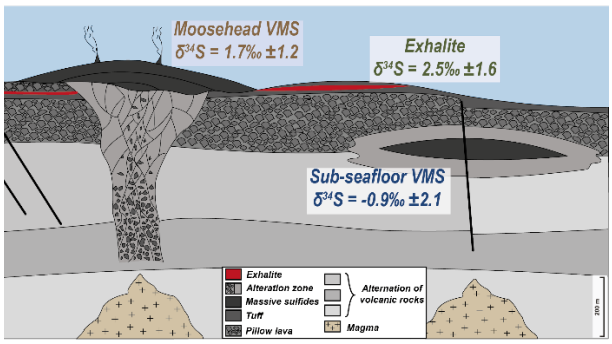

Figure 4. Sketch representing seafloor and replacement sub-seafloor VMS and exhalites with their respective $\delta^{34}S$ signature determined in bulk by SF_6 fluorination technique.

Acknowledgements

C.L. acknowledges support from the Canada Research Chair and John Evans Leaders Fund from the Canada Foundation for Innovation. The authors want to thank Pierre Cartigny from the Institut de Physique du Globe de Paris and Laure Martin from the University of Western Australia for their help on the isotopic characterization of the new sulfide reference materials by SF_6 fluorination and SIMS techniques, respectively. Marc Choquette from the Laboratoire de Microanalyses of Université Laval is also warmly thanked for the chemical characterization of these reference materials.

References

Barré, G, LaFlamme, C, Beaudoin, G, Goutier, J, Cartigny, P (2022) The application of multiple sulfur isotopes to determine the architecture of Archean VMS deposits. GAC-MAC, Abstract volume, v. 45.

Canfield, D.E, Raiswell, R, Westrich, JT, Reaves, CM, Berner, RA (1986) The use of chromium reduction in the analysis of reduced inorganic sulfur in sediments and shales. Chem Geol 54(1-2): 149-155.

Caruso S, Fiorentini ML, Hollis SP, LaFlamme C, Baugartner RJ, et al. (2018) The fluid evolution of the Nimbus Ag-Zn-(Au) deposit: an interplay between mantle plume and microbial activity. Precamb Res 317: 211-229. https://doi.org/10.1016/j.precamres.2018.08.012

Farquhar, J, Kim, ST, Masterson, A (2007) Implications from sulfur isotopes of the Nakhla meteorite for the origin of sulfate on Mars. EPSL 264(1-2): 1-8.

Huston DL, Pehrsson S, Eglington BM, Zaw K (2010) The Geology and Metallogeny of Volcanic-Hosted Massive Sulfide Deposits: Variations through Geologic Time and with Tectonic Setting. Econ Geol 105:571–591

Hutchison, W, Finch, AA, Boyce, AJ (2020) The sulfur isotope evolution of magmatic-hydrothermal fluids: Insights into ore-forming processes. Geochim Cosmo Acta 288: 176-198. https://doi.org/10.1016/j.gca.2020.07.042

Kump LR (2012) Sulfur isotopes and the stepwise oxygenation of the biosphere. Elements. DOI 10.2113/gselements.8.6.410

LaFlamme C, Barré G, Fiorentini ML, Beaudoin G, Occhipinti S, Bell J (2021) A significant seawater sulfate reservoir at 2.0 Ga determined from multiple sulfur isotope analyses of the Paleoproterozoic Degrussa Cu-Au volcanogenic massive sulfide deposit. Geochim Cosmochim Acta 295:178-193. https://doi.org/10.1016/j.gca.2020.12.018

LaFlamme C, Hollis SP, Jamieson JW, Fiorentini ML (2018) Three-dimensional spatially constrained sulfur isotopes highlight processes controlling sulfur cycling in the near surface of the Iheya North hydrothermal system, Okinawa Trough. Geochem Geophys Geosystems 19:2798-2812. https://doi.org/10.1029/2018GC007499

LaFlamme C, Martin L, Jeon H, et al. (2016) In situ multiple sulfur isotope analysis by SIMS of pyrite, chalcopyrite, pyrrhotite, and pentlandite to refine magmatic ore genetic models. Chem Geol 444.9:1-15. https://doi.org/10.1016/j.chemgeo.2016.09.032

Monecke, T, Mercier-Langevin, P, Dubé, B, Frieman, BM (2017) Geology of the Abitibi greenstone belt.

Mercier-Langevin, P, Goutier, J, Ross, PS, McNicoll, V, Monecke, T, Dion, C, Dubé, B, Thurston, P, Bécu, V, Gibson, H, Hannington, M, Galley, A (2011) The Blake River Group of the Abitibi greenstone belt and its unique VMS and gold-rich VMS endowment. Geol Surv Can 6869: 1-61.

Paton, C, Hellstrom, J, Paul, B, Woodhead, J, Hergt, J (2011) Iolite: Freeware for the visualisation and processing of mass spectrometric data. JAAS 26(12): 2508-2518.

Seal, RR (2006) Sulfur isotope geochemistry of sulfide minerals. Rev Mineral Geochem 61(1): 633-677.

Application of Next Generation Technology in Undercover Exploration

Nigel W. Brand [1,2], David J. Crook [3]
[1] Portable Spectral Services, West Perth, Australia
[2] Centre for Exploration and Targeting, University of Western Australia
[3] Mount Ridley Mines Limited, West Perth, Australia

Abstract. As mineral exploration increasingly pushes into concealed (covered) terrains, explorers must maximise the geochemical and mineralogical information gained to understand the geological setting, terrain prospectively and mineral potential at various scales. Routine, low-cost geochemical techniques enable explorers to look for anomalies within the cloud of data however mineralogical techniques that, at best provide data on the dominant mineral phases (e.g. x-ray diffraction, "XRD"), are expensive, low volume (e.g. scanning electron microscope "SEM") or qualitative (e.g. short-wave infrared "SWIR"). We present the findings of an ongoing regional evaluation study over concealed Proterozoic lithologies known to host magmatic nickel sulphides with potential to host other base-metal, gold and rare earth elements ("REE") systems within the Fraser Range, Western Australia. The data has been acquired by Micro-XRF mapping technology which can accurately quantify the chemical compositions, and through post-processing, identify and quantify mineralogy of the same geological sample. High-quality, quantitative analyses were undertaken of "end of hole" air core drill samples representing the freshest nature of the rock being drilled. The resulting datasets have identified new mineralogical features and detected chemical differences at a microscale. The Bruker M4^{PLUS} Tornado "Micro-XRF" was utilised in this study, providing rapid and non-destructive acquisition of data.

1. Introduction

Yet to be discovered mineral deposits are becoming more likely to occur in concealed terrains and the ability to see through cover to detect and understand the nature of the underlying bedrock ore environment has become a fundamental aspect of modern mineral exploration and ore deposit science (Winterburn et al 2020), with an increasing appetite for collecting and integration of mineralogical and chemical data.

Over the past two decades commercial laboratories have offered high volume, low-cost, routine, quantified multi-element geochemical analyses that are accurate and precise over ten (10) orders of magnitude, from 100 percent to parts per billion. This has given rise to an increasing demand for mineralogical information, however, a commercial high volume, low-cost, routine mineralogical identification technique does not currently exist. SEM techniques provide mineralogical data at the sub-percent range yet do not provide a routine solution due to high cost and very low production volumes; XRD at best covers analyses within three (3) orders of concentration magnitude (100% to ~1%); whilst techniques such as SWIR are high volume and low cost, however, are qualitative at best.

Advances in Micro-XRF technology, such as capillary optics, has enabled mapping at high spatial resolution, down to 20um, without sacrificing intensity or sensitivity, providing a non-destructive, quantitative method for geochemical analysis and mineralogy of samples whilst providing the spatial distribution of major, minor and abundant trace components at the mapped resolution (Fritz et al 2016; Hoehnel 2018). During mapping the entire X-ray spectrum for each pixel in the grid is collected. Geochemically, elements ranging from carbon (C) to uranium (U) are simultaneously measured with quantification limits ranging from percentages to parts per million.

Automated mineralogy is undertaken using BRUKER's Advanced Mineral Identification and Characterisation Software (AMICS) through spectral matching of an extensive real-world and synthetic mineral library. Through automation, high volume throughput can be achieved which enables the routine commercial application of this technology.

The applicability of this technology for a practical solution when exploring a concealed geological terrain is being tested under a research project sponsored by Mount Ridley Mines Limited. To date, the project has analysed over 600 drill samples collected within an area of 1,200km^2 concealed Proterozoic terrain. This forms an exploration workflow that identifies rock types to produce a geological map with overlays of potential ore-environment minerals utilising both mineralogical and chemical vectors.

The project area lies within the Biranup and Nornalup geological provinces of the Albany–Fraser Orogen which forms part of the West Australian Craton and is located along the south-eastern margin of the Archean Yilgarn Craton (Spaggiari et al 2011). The Albany–Fraser Orogen is hosted by predominantly Paleoproterozoic to Mesoproterozoic granites formed through a complex series of events.

2. Methodology

Over 600 end-of-hole drill samples have been scanned during this study. Initially, selected samples were scanned "as received" at a high resolution (25-30µm) to develop a working mineral reference library using the AMICS software. With the mineral reference library established, samples are rerun in a validation process at a lower resolution

(100-200µm) to test accuracy and precision for high volume throughput.

Once validation is completed, routine samples are cleaned and mounted “as received” in batches of ~ 24 samples with no additional preparation (Figure 1). These mounts are loaded and scanned using a BRUKER M4^{PLUS} TORNADO. Quantified geochemical analysis is undertaken using the M4 software and quantified mineralogical analysis is undertaken using AMICS. Any “unknown” minerals encountered at this stage are further assessed and when identification is verified, these will be added into the mineral reference library.

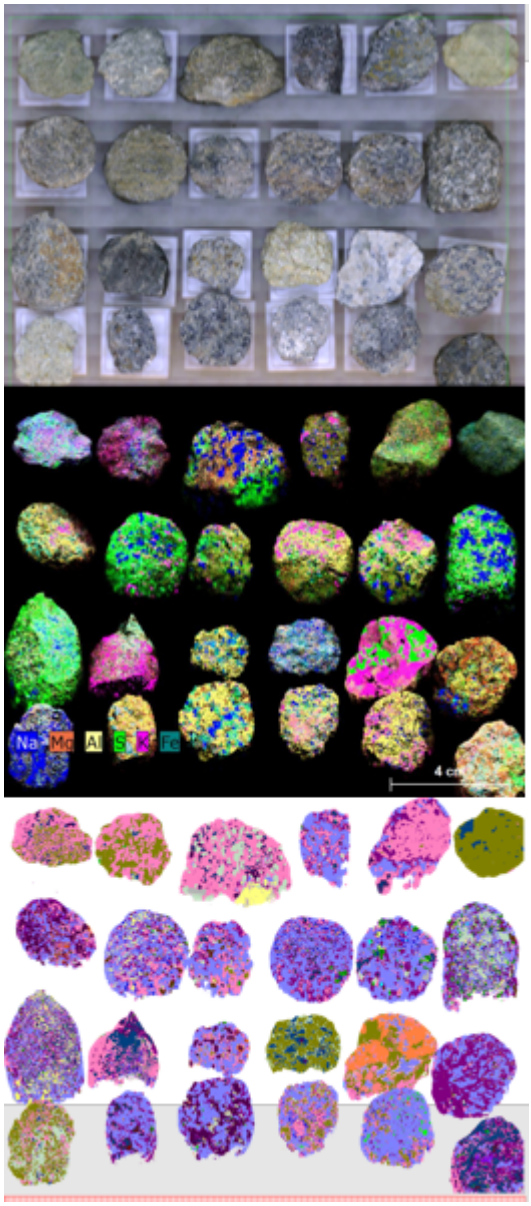

Figure 1: End of hole samples (top), chemistry (centre), mineralogy (bottom).

3. Results

Results from the study to date has identified thirty-one (31) minerals. Common rock forming minerals and minerals associated with regional metamorphism are abundant. Primary economic minerals as well as alteration minerals associated with ore environments are present in lower concentrations, typically less than 0.5% of the rock volume. Identification of ore environment minerals however is crucial when vectoring towards concealed ore deposits (Figure 2).

Given the nature of the cover sequence and weathering effects in the study area, the potential to generate false anomalies is recognised when interpreting geochemical data only. Identification of secondary mineral phases associated with a geochemical anomaly and then correlation of these minerals with the underlying basement or potential ore environment is a means of validating or discounting geochemical anomalies.

For each sample, mineralogical maps are generated showing the spatial distribution of the mineralogy, sample texture, mineral grain size, mineral associated etc (Figure 3).

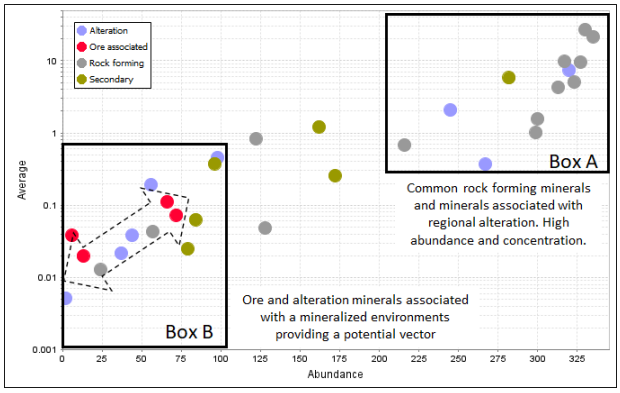

Figure 2: Abundance (number of times a mineral is identified in the data set) vs Average (average concentration of a mineral phase in the data set). “Box A” represents common rock forming minerals and minerals associated with regional alteration. “Box B” represents ore and alteration minerals associated with a mineralized environments providing potential vectors.

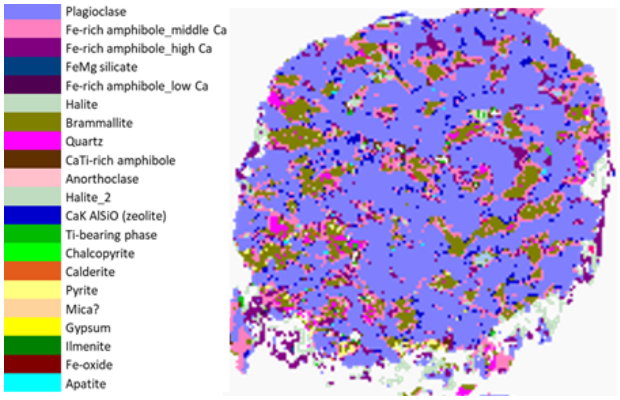

Figure 3: Mineralogical map of an “end of hole” sample, MRAC0112.

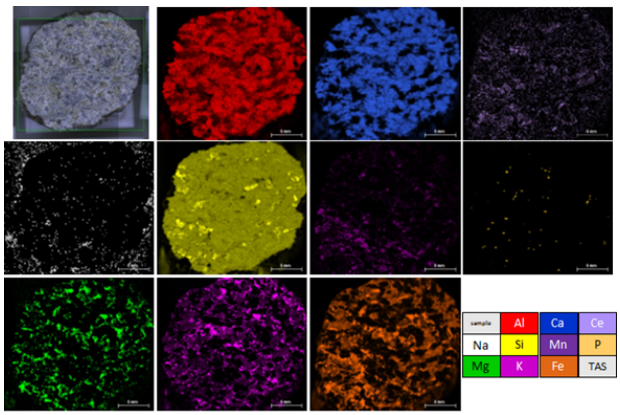

Figure 4: Individual element distribution maps show the relative element concentration within the sample MRAC0112.

Individual element distribution maps visually show the relative element concentration within the sample (Figure 4). Numerical data is used by the AMICS to ascertain the sample's constituent minerals. Common rock-forming minerals can be placed into standard IUGC petrographic diagrams to identify the underlying bedrock, which is then verified with standard geochemical plots using micro-XRF whole-of-sample geochemistry data (Figure 5).

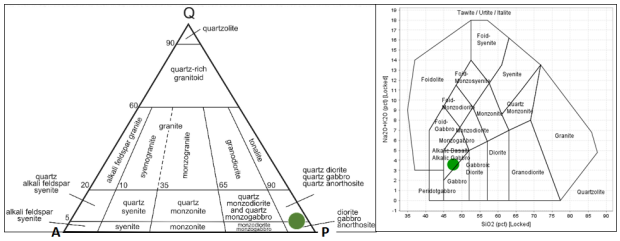

Figure 5: MRAC0112 mineral data *plotted in IUGC diagram (left) and chemical data plotted in Middlemost' 1994 TAS diagram (right).

From the end-of-hole drill sample data, the spatial distribution of individual mineral abundances can be shown (Figure 6). Common rock-forming and metamorphic minerals are used to map the underlying geology. Primary ore minerals and mineral alteration patterns associated with ore systems provide information on the terrain prospectivity, mineral potential and may act as a vector towards an ore deposit.

4. Conclusions

This paper demonstrates the application of next generation technology in undercover exploration and highlights the importance of detecting routine, high-volume low-cost quality "trace" mineralogy to identify a suite of "indicator" minerals with the potential to vector towards and detect economic mineral systems.

This pilot study forms part of a much larger regional program undertaken by Mount Ridley Mines Limited to understanding the basement geology, and mineral prospectively using a non-destructive micro-XRF technique to quantify mineralogy and chemistry and provide textural and petrography information that is "fit for purpose" for mineral exploration.

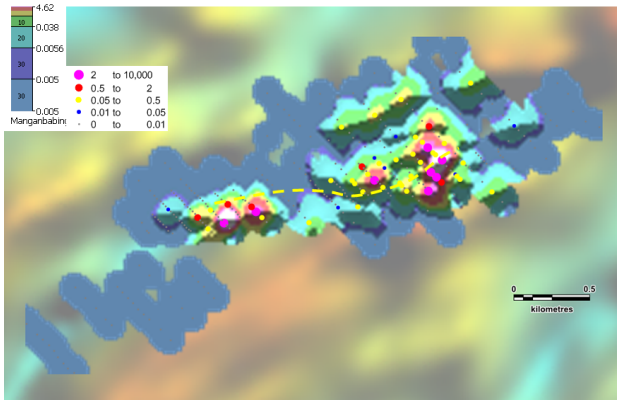

Figure 6: The spatial distribution of manganbabingtonite [$Ca_2(Mn,Fe)FeSi_5O_{14}(OH)$] a mineral associated with garnet-pyroxene-magnetite skarn.

Acknowledgments

Mt Ridley Mines Limited are thanked for their continuing support in method development and application of non-destructive technology in the mineral exploration.

References

Fritz, J., Tagle, T., Ashworth, L., Schmitt, R.-T., Hofmann, A., Luais, B., Harris, P.D.,Hoehnel, D., Ozdemir, S., Mohr-Westheide, T., Koeberl, C. (2016): Nondestructive spectroscopic and petrochemical investigations of paleoarchean SLs from the ICDP drill core BARB5, Barberton Mountain Land, South Africa. Meteorit. Planet. Sci. 51, 2441e2458.

Hoehnel, D., Reimold, W. U., Altenberger, U., Hofmann, A., Mohr-Westheide, T., Özdemir, S., & Koeberl, C. (2018): Petrographic and Micro-XRF analysis of multiple archean impact-derived spherule layers in drill core CT3 from the northern Barberton Greenstone Belt (South Africa). Journal of African Earth Sciences, 138, 264-288.

Middlemost, E.A.K. (1994): Naming materials in the magma/igneous rock system; Earth-Science Reviews, v. 37, pp. 215-224.

Spaggiari, CV, Kirkland, CL, Pawley, MJ, Smithies, RH, Wingate, MTD, Doyle, MG, Blenkinsop, TG, Clark, C, Oorschot, CW, Fox, LJ and Savage, J. (2011): The geology of the east Albany–Fraser Orogen — a field guide: Geological Survey of Western Australia, Record 2011/23, 97p.

Winterburn, P.A.; Noble, R.R. and Lawie, D. (2020): Advances in exploration geochemistry, 2007 to 2017 and beyond. Geochemistry: Exploration, Environment, Analysis, 20, 157-166.

Cassiterite: the zircon of mineral systems

Patrick A. Carr[1], Dawid Szymanowski[2], Lorenzo Tavazzani[2], Benita Pulitz[3], Torsten Vennemann[3], Cyril Chelle-Michou[2], Quentin Charbonnier[2], Zbigniew Galazka[4], Julien Mercadier[1]

[1]GeoRessources, Université de Lorraine, CNRS
[2]Institute of Geochemistry and Petrology, ETH Zürich, Switzerland
[3] Institute of Earth Sciences, University of Lausanne, Switzerland
[4]Leibniz-Institut für Kristallzüchtung, Germany

Abstract. New analytical developments and workflows are presented to determine the U–Pb age and εHf_i and $\delta^{18}O$ isotopic compositions of cassiterite (SnO_2), an ubiquitous mineral in magmatic-hydrothermal deposits. We present a multi-stage column chromatography scheme for the separation and purification of U, Pb and Hf for the determination of the U–Pb age and εHf_i from the same cassiterite solution by ID-TIMS and MC-ICP-MS, respectively. Additionally, new natural and synthetic cassiterite reference materials are presented for normalisation and validation of $\delta^{18}O$ data by ion microprobe analysis. The objective is to propose combined bulk and in-situ U–Pb age, εHf_i and $\delta^{18}O$ characterization of cassiterite in magmatic-hydrothermal mineralisation systems to constrain the temporal and genetic conditions leading to the formation of economic mineral deposits containing this mineral.

1 Introduction

Zircon ($ZrSiO_4$) is used widely by the geoscience community to determine the age (using the U–Pb decay systems) and provenance (with εHf_i and $\delta^{18}O$ isotopic compositions, for example) of the melt or fluid from which it precipitates. However, the use of zircon geochemistry for constraining these parameters in metal rich magmatic-hydrothermal systems is severely hampered by its notable absence in many mineralised environments (e.g., hydrothermal veins, greisen, breccias, skarns, pegmatites, and rare metal granites), and when present by its poor preservation due to metamictisation or secondary alteration (Figure 1). In contrast, cassiterite (SnO_2) is known to precipitate in both magmatic and hydrothermal environments associated with numerous economically important elements (Sn, W, Li, Nb, Ta, F, U, Cu, and Au) and can resist the subsequent hydrothermal alteration synonymous with these complex geological environments. Cassiterite has similar geochemical characteristics as zircon such that the age of crystallisation and the provenance of the forming melts and fluids can also potentially be determined by U-Pb geochronology, and εHf_i and $\delta^{18}O$ compositions, respectively.

To date, however, analytical protocols for the determination of U–Pb, Lu–Hf and oxygen isotopic composition of cassiterite are less advanced to that of zircon. We present new analytical developments and propose a logical workflow to determine U–Pb, Lu–Hf and oxygen isotopic composition by bulk and in-situ methods in cassiterite. The widespread availability of these techniques, and their application to mineral deposits worldwide can install cassiterite as 'the zircon of mineral systems' as initially proposed by Blevin and Norman in 2010.

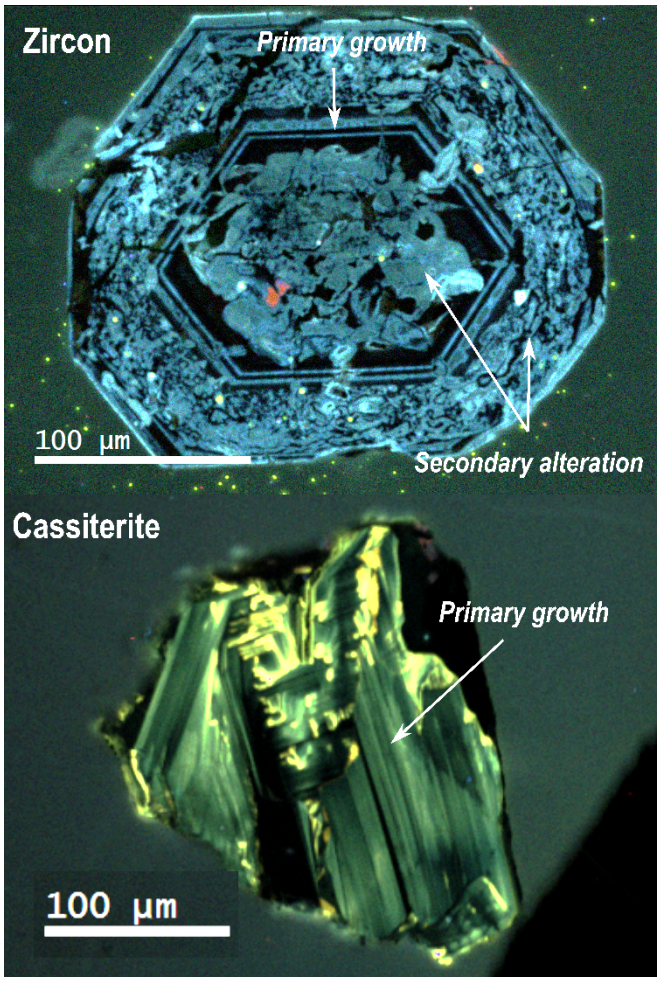

Figure 1. Cathodoluminescence images of a highly altered zircon (top) and primary cassiterite (bottom) from the magmatic-hydrothermal rare-metal prospect of St Mélany, Massif Central, France. In this context, zircon is often absent, or metamict and/or highly altered, such as its isotopic composition cannot be used to determine the age or provenance of mineralising melts and fluids. Cassiterite is commonly pristine and can be used in place of zircon for age and compositional information.

2 Analytical developments

Cassiterite can exhibit large variations in chemistry within a deposit, and within grains at the micron-scale, that highlights the need for geochemical imaging prior to isotopic analyses. The chemical heterogeneity within cassiterite also lends itself to in-

situ techniques (such as LA-[MC]-ICP-MS for U–Pb and εHf_i or SIMS for $\delta^{18}O$) to observe the range in compositions that can be found within a single crystal or an entire deposit. However, these in-situ techniques are less precise compared to bulk methods (such as ID-TIMS for U–Pb, MC-ICP-MS for εHf_i, and fluorination for $\delta^{18}O$) and require matrix-matched reference materials to correct for the artificial isotopic fractionation created during analysis. Preferably, both in-situ and bulk methods can be employed depending on the studies requirements (i.e., high analytical precision vs. high spatial precision), the degree of heterogeneity of the cassiterite to analyse or analytical tools available to researchers.

2.1 Combined U–Pb ages and εHf_i compositions

Cassiterite can contain several hundred ppm of both U and Hf such that it is suitable for isotopic analysis of these elements by both in-situ and bulk techniques. However, cassiterite often contains common Pb, such that U–Pb ages are typically determined from Discordia relationships from multiple analyses (n>20). U–Pb geochronology of cassiterite by ID-TIMS and LA-ICP-MS has been reported elsewhere (e.g., Carr et al. 2020, 2022, Tapster and Bright 2020). Current age uncertainty for U–Pb cassiterite ages is >0.1% for ID-TIMS data (Tapster and Bright 2020) and 1.9% for LA-ICP-MS (Carr et al. 2022).

A single study has presented εHf_i compositions of cassiterite by LA-MC-ICP-MS and MC-ICP-MS (Yang et al. 2023). Lu/Hf within cassiterite are generally low (<0.001) and calculation of εHf_i involves very minor corrections for in-situ decay of Lu. Solution based MC-ICP-MS can produce Hf isotopic measurement uncertainties of ± 0.2 ε, whilst LA-MC-ICP-MS is ± 2 ε (Yang et al. 2023).

Here we used a scheme based on 3-column separation and purification of U, Pb and Hf from a Sn-rich matrix and analysis at the ETH facilities, Zürich. Cassiterite dissolution is achieved with HBr decomposition in Teflon microcapsules assembled inside a Parr pressure vessel at 210ºC for at least 5 days. Separation and purification of U, Pb and Hf aliquots from initial cassiterite solutions involved passes through TRU-Spec, AG1X-8 resins and TODGA resins. This method yields low Pb blanks that are insignificant relative to the Pb derived from the sample. For most cassiterite samples, between 200 and 1000 µg of concentrate is sufficient for a high precision U–Pb and εHf_i analysis by ID-TIMS and MC-ICP-MS, respectively.

2.2 $\delta^{18}O$ compositions

Previous studies have identified large variations in $\delta^{18}O$ within cassiterite (e.g., up to 10‰ variation; Sun and Eadington 1987) indicating large changes in fluid composition and/or variable degrees of fluid mixing and/or changes in the precipitation temperature of cassiterite. More recent *in-situ* SIMS studies have identified intra-grain variations up to 2‰ at the micron scale (Carr et al. 2017). When combined with $\delta^{18}O$ in co-precipitation quartz, temperature estimates can be made assuming isotopic fractionation factors determined independently by other methods (e.g., Li et al. 2021).

These factors indicate that $\delta^{18}O$ of cassiterite is generally more appropriately determined by in-situ methods, such as SIMS. Although SIMS do not compromise precision in oxygen-rich minerals such as cassiterite, it does require matrix-matched reference materials to account for matrix-effects causing the fractionation of oxygen isotopes (Carr et al. 2017). Currently only one reference cassiterite is available to the community (Li et al. 2021). Here we present two new reference materials that can be used for normalisation and validation of $\delta^{18}O$, and quantification of laboratory and inter-laboratory reproducibility.

Refence $\delta^{18}O$ values for cassiterite were determined by CO2-laser fluorination line connected to a Finnigan MAT 253 at the Université de Lausanne, Switzerland. Approximately 2 mg of cassiterite concentrate was required for each analysis. In-situ $\delta^{18}O$ compositions were determined on a CAMECA 1280 ion microprobe at the CRPG, Nancy, France (Bouden et al. 2021).

Natural cassiterite from the eastern Kareila, Russia (sample SPG) yields preliminary $\delta^{18}O$ reference values of 2.51 ± 0.02 (SD; n=2). In-situ analyses (n=20) of multiple grains of SPG yields a session reproducibility (2SD) of 0.58‰.

Synthetic cassiterite formed through physical vapour transport and subsequently annealed at 1400ºC (sample IKZ-a; Galazka et al. 2013) yield preliminary laser fluorination $\delta^{18}O$ of 4.63 ± 0.05 (SD; n=3). Multiple analyses (n= 70) from traverses of multiple fragments of this cassiterite yields a session reproducibility of 0.47‰.

3 Analytical workflows for cassiterite isotope geochemistry

The proposed analytical workflow is shown in Figure 2. The heterogeneous composition common in cassiterite requires chemical imaging (SEM, cathodoluminescence and trace element mapping by LA-ICP-MS) prior to any quantification or isotope ratio analyses. These images can guide placement of $\delta^{18}O$ analyses and select zones rich in U and Hf that are favourable for *in-situ* analyses by SIMS and LA-(MC)-ICP-MS, respectively. Grains identified to have high U and Hf, and low common Pb and Lu/Hf by LA-ICP-MS can be plucked from epoxy mounts and selected for solution analyses involving sample dissolution, separation, and purification of U, Pb and Hf and analysis by ID-TIMS (U and Pb) and MC-ICP-MS (Hf) as in customary for zircon (e.g., Herriott et al. 2019).

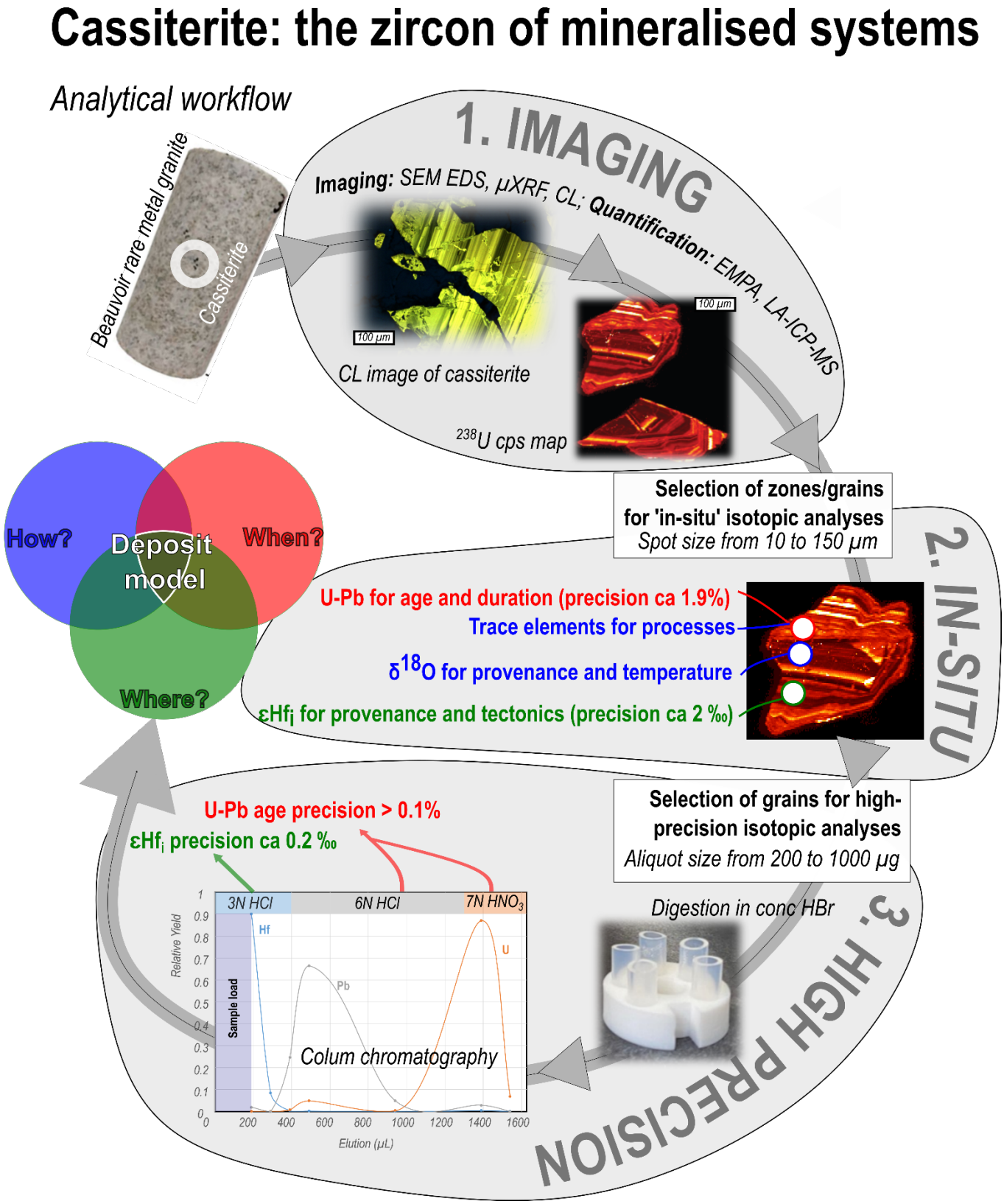

Figure 2. Analytical workflow for U–Pb, εHf_i and $\delta^{18}O$ isotopic analysis of cassiterite in three sequential steps including (1) chemical imaging, (2) *in-situ* isotopic ratio and trace element quantification and (3) high precision (bulk) isotopic ratio ID-TIMS. The combination of these data can provide unique temporal and genetic constraints on the formation of magmatic-hydrothermal deposits containing cassiterite.

4 Conclusions

The U–Pb age, εHf_i and $\delta^{18}O$ composition of cassiterite can provide direct constraints on the timing and source of fluids and melts responsible for its formation. We present a summary of recent analytical developments in high spatial resolution (i.e., LA-MC-ICP-MS and SIMS), and high measurement precision (i.e., ID-TIMS and MC-ICP-MS) analyses of cassiterite. The most appropriate methodology can be chosen based on the scientific problem to be defined and the characteristics of cassiterite (if alteration or primary zoning present). Isotopic compositions from cassiterite can be crucial in mineralised systems where zircon is absent and determining the age and source of mineralising melts and fluids is difficult. When zircon is present, this cassiterite geochemistry can also provide complementary interpretations such as cooling rates of magmatic-hydrothermal systems and fluid-rock or fluid-fluid mixing processes.

Acknowledgements

P.C. was funded by Institut Carnot ICEEL and the French National Agency through the national programme “Investissements d’avenir” of the Labex Ressources 21 (Reference ANR-10-LABX-21-RESSOURCES21). J. Cauzid and A. Lecomte are thanked for assistance with imaging techniques. L. Neymark provided the SPG cassiterite for oxygen isotope analysis. N. Bouden helped with $\delta^{18}O$ compositions by SIMS. Trace element images in Figure 2 were performed at Trinity College, Dublin with the help of D. Chew.

References

Blevin PL, Norman MD (2010) "Cassiterite: The zircon of mineral systems—A scoping study." Australian Earth Science Convention 2010, AESC2010. Poster GS2010/0483. 2010.

Bouden N, Villeneuve J, Marrocchi Y, Deloule E, Füri E, Gurenko A, Piani L, Thomassot E, Peres P, Fernandes F (2021) Triple oxygen isotope measurements by multi-collector secondary ion mass spectrometry. Frontiers in Earth Science, 8, 601169.

Carr PA, Norman MD, Bennett VC (2017) Assessment of crystallographic orientation effects on secondary ion mass spectrometry (SIMS) analysis of cassiterite. Chemical Geology, 467, 122-133.

Carr, PA, Zink S, Bennett VC, Norman MD, Amelin Y, Blevin PL (2020) A new method for U-Pb geochronology of cassiterite by ID-TIMS applied to the Mole Granite polymetallic system, eastern Australia. Chemical Geology, 539, 119539.

Carr PA, Moreira E, Neymark L, Norman MD, Mercadier J (2022) A LA-ICP-MS Comparison of Reference Materials Used in Cassiterite U-Pb Geochronology. Geostandards and Geoanalytical Research.

Galazka Z, Uecker R, Klimm D, Irmscher K, Pietsch M, Schewski R, Albrecht M, Kwasniewski A, Ganschow S, Schulz D, Guguschev C, Bertram R, Bickermann M, Fornari R (2014) Growth, characterization, and properties of bulk SnO2 single crystals. physica status solidi (a), 211(1), 66-73.

Li Y, He S, Zhang RQ, Bi XW, Feng, LJ, Tang GQ, Wang WZ, Huang F, Li XH (2021) Cassiterite oxygen isotopes in magmatic-hydrothermal systems: in situ microanalysis, fractionation factor, and applications. Mineralium Deposita, 1-19.

Sun SS, Eadington PJ (1987) Oxygen isotope evidence for the mixing of magmatic and meteoric waters during tin mineralization in the Mole Granite, New South Wales, Australia. Economic Geology, 82(1), 43-52.

Tapster S, Bright JW (2020) High-precision ID-TIMS cassiterite U–Pb systematics using a low-contamination hydrothermal decomposition: implications for LA-ICP-MS and ore deposit geochronology. Geochronology, 2(2), 425-441.

Herriott, TM, Crowley JL, Schmitz MD, Wartes MA, Gillis RJ - 2019) Exploring the law of detrital zircon: LA-ICP-MS and CA-TIMS geochronology of Jurassic forearc strata, Cook Inlet, Alaska, USA. Geology, 47 (11): 1044–1048.

Yang M, Yang YH, Romer RL, Wu ST, Wu T, Wang H (2023) In situ Hf isotope analysis of cassiterite by LA-MC-ICP-MS: Protocol and applications. Journal of Analytical Atomic Spectrometry.

Zircon and whole-rock geochemical fertility tools applied to porphyry copper deposits: case studies of Chachimbiro Volcanic Complex and Cerro Tolondro prospect, Ecuador.

Francesca Del Río[1], Massimo Chiaradia[1], Hugo Carrasco[1], Alexey Ulyanov[2], Angelo Aguilar[3], Sergio Cubelli[3], Carolina Rodríguez[3], and Carlos Urrutia[3].
[1]Section of Earth Sciences, University of Geneva, Rue des Maraîchers 13, 1205-Geneva, Switzerland.
[2]Institute of Mineralogy and Geochemistry, University of Lausanne, 1022 Chavannes-prés-Renens, 1015 Lausanne, Switzerland.
[3] CODELCO, Casa Matriz, Huérfanos 1270, Santiago, Chile.

Abstract. Bulk rock and mineral geochemical signatures commonly used in the exploration for porphyry copper deposits (PCDs) have been applied to the apparently barren Chachimbiro Volcanic Complex (CVC), and to the potentially mineralized Cerro Tolondro (CT) prospect, northern Ecuador, to understand the relationship between volcanic eruptions and the formation of PCDs.
Whole-rock geochemistry of both CVC and CT shows depleted LREE, and MREE differentiation trend, and lack an Eu negative anomaly with differentiation. CVC also portrays a MREE and HREE depletion, and an increase of Sr/Y values through time and chemical evolution.
Based on geochemical fertility indicators (e.g., Eu/Eu* versus (Ce/Nd)/Y and Dy/Yb) from trace elements measured in zircons, CVC and CT fall in the same field as mineralized PDCs, furthermore Cerro Tolondro might show a more complex magmatic evolution than Chachimbiro Volcanic Complex.

1 Introduction

The use of geochemistry for the exploration of porphyry copper deposits (PCDs) has migrated to more innovative techniques during the past decades. These techniques are designed to use bulk rock, mineral (e.g., zircon and apatite) geochemistry, and isotopic composition to quantify parameters that are considered crucial in the formation of PCDs, such as oxidation state, water content, and degree of fractionation of magmas associated with PCDs (Richards, 2015).

However, recent work by Chiaradia and Caricchi (2022) has shown that the use of geochemical tracers applied to zircon geochemistry is more complex, and that also barren volcanic centers that are associated with large eruptions (e.g., Fish Canyon Tuff, and Kneeling Nun Tuff) may present a comparable geochemical trend, as those from mineralized porphyry rocks.

For a better understanding of the meaning of zircon and apatites geochemistry in mineralized and non-mineralized volcanic systems, we are studying two nearby volcanic centers in northern Ecuador, one corresponding to the presumably barren CVC, and a target area for the potential occurrence of mineralized porphyry copper deposits, CT (Figure 1).

The Chachimbiro Volcanic Complex (CVC) is a compound volcano located in the Western Cordillera of northern Ecuador, with three Pleistocene eruptive events (405.7 ± 2.0 ka to 22'730 ± 120 ybp), and a fourth Holocene (5'760 ± 30 ybp) lateral blast explosion (Bellver Baca et al., 2020).

Cerro Tolondro (CT) corresponds to a prospect localized also in the Western Cordillera of Ecuador, few km to the north of CVC (Fig. 1). A preliminary study of geological features of the area of CT was carried out by "Exploraciones Mineras Andinas Ecuador S.A." which delineated a basement consisting of andesites and volcanoclastic sequence varying form tuff to volcanic breccias, intruded by dacitic porphyries and hydrothermal breccias (EM, 2021).

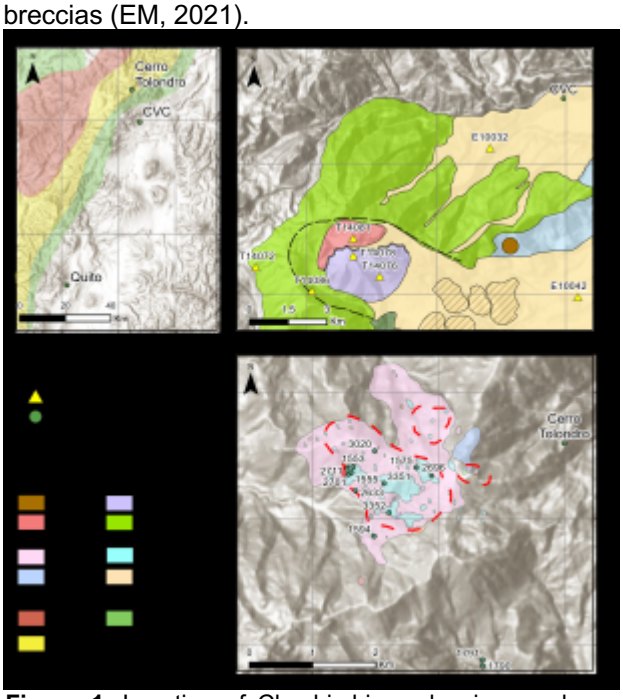

Figure 1. Location of Chachimbiro volcanic complex, and Cerro Tolondro, in northern Ecuador. Geology adapted from Bellver Baca et al. (2020), and EM (2021).

2 Methodology

Bulk rock analyses of representative Cerro Tolondro rocks were carried out at ALS Minerals Spain, whereas geochemical compositions of an extensive dataset of rocks from the Chachimbiro

Volcanic Complex are available from Bellver Baca et al. (2020).

We extracted zircon grains from samples of both volcanic centers, using conventional mineral separation techniques.

Representative zircon grains were handpicked under a binocular microscope, mounted in epoxy discs, and then polished to approximately half grain thickness. Cathodoluminescence (CL) images of both mineral phases were taken using the CamScan MV2300 instrument at Institute of Earth Sciences of the University of Lausanne, and the JEOL JSM7001F at the Faculty of Earth Sciences of the University of Geneva.

LA-ICP-MS analyses of zircons were conducted using a sector-field spectrometer Element XR in interfaced to an ASI (Australian Scientific Instruments) RESOlution 193 ArF excimer ablation system at the University of Lausanne, Switzerland, for U–Pb dating, REE and trace elements measurements.

3 Whole-rock geochemistry

Bulk rock analyses from the rock samples from the CVC have SiO_2 values between 59 – 69 wt. %, and vary from andesite to rhyodacites from the first eruptive episode (CH1) to the last one (CH4). Cerro Tolondro display a wider SiO_2 content range (52-70 wt.%), due to the hydrothermal alteration that is affecting the prospective area, Winchester and Floyd (1997) classification rock chart was used in order to examine immobile elements such as Zr/Ti_2O (Figure 2. A), the samples can be classified as andesites and dacites.

Chondrite-normalized REE patterns of CVC rocks display decreasing LREE and MREE values from the first eruptive episode to the last one, a drastic depletion of the HREE, and lack a negative Eu anomaly. Cerro Tolondro shows also a spoon-shaped pattern of the REE, but lacks the strong HREE depletion typical of the last CVC stage (CH4) and displays a small Eu negative anomaly (Figure 2. B and C).

Sr/Y values of CVC increase from CH1 to CH4, to values >50. Cerro Tolondro Sr/Y values remain mostly below 50. These low values of Sr/Y at CT are probably the result of the pervasive alteration affecting the rocks of this prospect; in fact, when plotted against the alteration index (A.I.), the lowest Sr/Y values coincide with the most altered samples (Figure 2. D).

4 U–Pb dating of zircons from Cerro Tolondro

$^{238}U/^{206}Pb$ ages of zircon spots from 4 samples of the Cerro Tolondro area are shown in Figure 3 and the mean ages of the zircon populations of each sample are reported. The fine-grained dacitic porphyry (FDP) unit yields an age of 11.48 ± 0.13 Ma (MSWD = 1.8), and the Andesite unit, 11.40 ± 0.32 Ma (MSWD = 0.84). The medium dacitic porphyry (MDP) corresponds to the youngest unit, with an age of 7.11 ± 0.14 Ma (MSWD = 1.1).

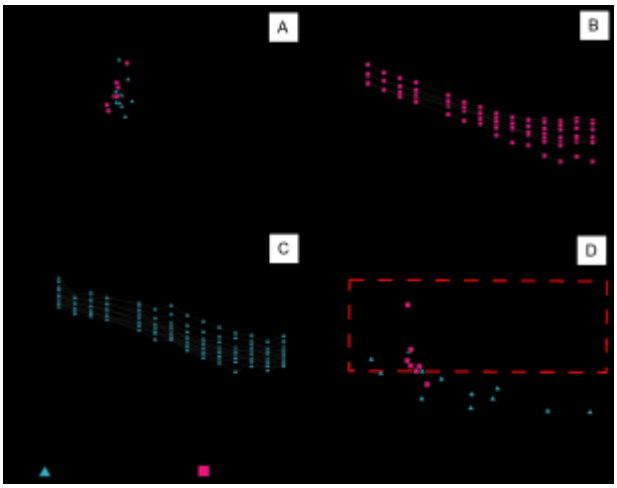

Figure 2. Whole rock chemistry. A. Winchester and Floyd (1997) classification rock chart, B. REE pattern for CVC, C. REE pattern for CT, and D. Sr/Y ratio vs Alteration Index (A.I.), where red field represents fertile signature, varying in between 50 < Sr/Y < 150.

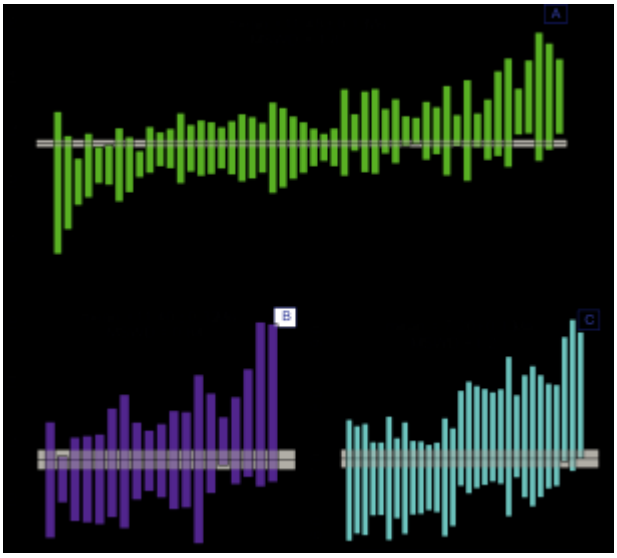

Figure 3. Weighted mean $^{238}U/^{206}Pb$ ages for Cerro Tolondro's units. A. Fine dacitic porphyry (FDP). B. Andesite. C. Intrusive porphyry. D. Medium dacitic porphyry (MDP).

5 Zircon geochemistry

The studied zircon grains present a prismatic morphology, varying from euhedral to sub-euhedral. Internal texture in most zircons exhibits oscillatory and sector zoning.

Chondrite-normalized REE patterns of zircons from CVC and Cerro Tolondro display a classic crustal zircons trend, with a depletion of LREE, a strong positive Ce anomaly, and enrichment of HREE (Figure 4. A and B).

Th/U can be used a fractionation index of the magma from which zircons have crystallized, with

zircons having higher Th/U values being those that have crystallized from less differentiated magma. Figure 4. C shows that CVC zircons are characterized by an increase of Yb/Dy with differentiation (increasing Th/U) passing from the oldest CH1 to the youngest CH4 unit (green arrow). This can be interpreted as the result of co-crystallization of zircons with amphibole and titanite, which are both minerals incorporating preferentially MREE (Dy) over HREE (Yb). For Cerro Tolondro, zircons display a similar fractionation trend, portraying an overall amphibole ± titanite fractionation, but have overall higher Th/U values. Additionally, Yb/Dy in CT extends to higher values with respect to CVC, possibly due to more extensive titanite fractionation.

We have used the classification diagrams of Lu et al. (2016) to discriminate between zircons from fertile and infertile magmatic rocks. In all these plots both CVC and CT fall in the fertile zircon fields associated with mineralized PCDs (e.g., Figure 4. D and E). The geochemical features of zircons plotting in the fertile fields in these plots are considered to indicate zircon crystallization from oxidized and hydrous magmas fractionating abundant amphibole (Lu et al., 2016).

To better understand the role that the oxidation state plays on the fertility of magmas, we applied the zircon oxybarometer proposed by Loucks et al. 2020). Figure 4 reports the range of the oxidation states of zircons from CVC and CT expressed as ΔFMQ values. The figure shows that all CVC stages and the older (ca 11-11-5 Myr old) rocks of CT have consistent ΔFMQ values around 0 or slightly above. Only the youngest (~7 Myr old) medium-grained dacitic porphyry has ΔFMQ slightly higher (~+0.5). All zircons from CVC and CT units have significantly lower ΔFMQ values than those of world-class PCDs (e.g., Chuquicamata, and El Salvador).

These comparisons highlight that whereas discrimination plots based on trace elements suggest that Cerro Tolondro and Chachimbiro volcanic complex plot in the fertile PCD field, the ΔFMQ values based on the oxybarometer of Loucks et al. (2020) display a significant difference between CVC and CT on one hand and world-class PCDs on the other.

6 Conclusion

Whole-rock geochemistry from CVC shows increasing Sr/Y values and decreasing HREE through time and with magmatic differentiation from CH1 to CH4, displaying Sr/Y values typical of fertile magmas. Cerro Tolondro lacks the heavy HREE depletion of CVC, and its Sr/Y values cannot be reliably used due to the pervasive alteration affecting the district.

Zircon mineral chemistry suggests that zircons of CVC crystallized from a magma that increasingly fractionated abundant amphibole ± titanite through time. Cerro Tolondro zircons also appear to follow an amphibole ± titanite fractionation trend although they have overall higher Th/U values and the trend is much less defined. This might suggest a more complex magmatic evolution at CT than at CVC.

Zircon trace elements of both volcanic complexes fall in the fertile fields of PCDs in various commonly used trace element plots, suggesting that the magmatic evolution of the two systems could be consistent with that of mineralized PCDs. However, the ΔFMQ values of CVC and CT are significantly lower than those of world-class deposits, suggesting that the oxidation state of magmas (expressed in the form of the equation of Loucks et al., 2020) should be assessed as an additional proxy for magma fertility in porphyry copper deposits.

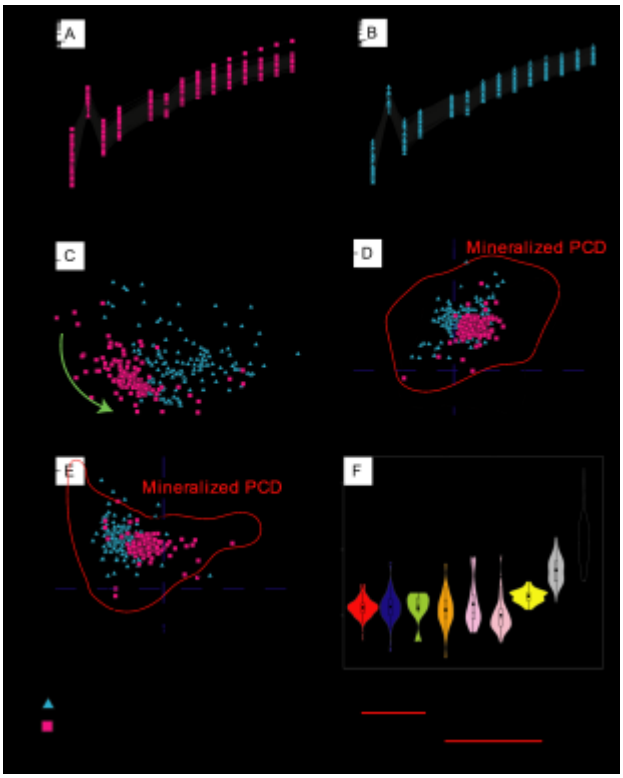

Figure 4. Zircon chemistry for CVC and CT. A. REE pattern for CVC, B. REE pattern for CT, C. Th/U vs Yb/Dy. D. Eu/Eu* compared with (Ce/Nd)/Y, E. Eu/Eu* anomaly values compared to Dy/Yb, and F. Δ FMQ variation regarding CVC and CT units, related to mineralized PCD.

Acknowledgements

We acknowledge Codelco S.A. for funding this research, carried out in the laboratories at the University of Geneva, and at the University of Lausanne. We are also grateful to Alexey Ulyanov, Agathe Martignier, Florence Begue, and Alexandra Demers-Roberge, for there help during the lab sessions.

References

Bellver-Baca M.T., Chiaradia, M., Beate, B., Beguelin, P., Deriaz, B., Mendez-Chazarra, N. & Villagómez, D. (2020). Geochemical evolution of the Quaternary Chachimbiro Volcanic Complex (frontal volcanic arc of Ecuador), Lithos, v. 356–357, 21 p.

Chiaradia, M. & Caricchi, L. (2022). Supergiant porphyry copper deposits are failed large eruptions. Communications earth & environment, v. 3, 107 p.

Exploraciones Mineras Andinas Ecuador S.A. (EM), (2021). Resultados del programa de levantamiento geoquímico y reconocimiento geológico, Proyecto Cerro Tolondro II.

Louck, R., Fiorentini, M., Henríquez, G. (2020). New magmatic oxybarometer using trace elements in zircon. Journal of Petrology, 1-30 p.

Lu, Y-J., Loucks, R., Fiorentni, M., McCuaig, C., Evans, N., Yang, Z-M, Hou, Z-Q., Kirkland, C., Parravilla, L., Kobussen, A. (2016). Zircon compositions as a pathfinder for porphyry Cu ± Mo ± Au mineral deposits. Society of Economic Geologists Special Publication, No. 19, chapter 13, 329-347 p.

Richards, J. (2015). The oxidation state, and sulfur and Cu contents of arc magmas: implications for metallogeny. Lithos, v. 233, 27-45 p.

Winchester JA, Floyd PA (1977) Geochemical discrimination of different magma series and their differentiation products using immobile elements. Chemical geology, 20, 325-343 p.

Identification and characterization of indicator minerals using µ-XRF

Léa Géring[1,2], Antoine Nadeau[1], Georges Beaudoin[1,2], Carl Guilmette[1]
[1] *Département de géologie et de génie géologique, Faculté des sciences et de génie, Université Laval*
[2] *Centre de recherche sur la géologie et l'ingénierie des ressources minérales (E4m)*

Abstract. This project aims at developing an automated method for identifying, counting, and characterizing indicator minerals (IM) of heavy mineral concentrates (HMC) based on µ-XRF data. Polycaprolactone grain mount provides homogeneous composition of non-detectable elements, and it allows grain top leveling. We develop a data processing workflow using µ-XRF raw counts maps as input. A binary image (grain/mount) is obtained using the sum of element counts and the counts in the spectral range that yield bremsstrahlung tube radiations. The next processing step use PyImageJ to recognize grain border and determine a region of interest (ROIs) at each grain centre. ROIs data is used in a decision tree that aims at identifying the mineralogy. The first layer of the decision tree classifies into a mineral group such as silicates, sulfides, phosphates, or oxides, based on count thresholds for Si, S, P. The following layers use thresholds for other element counts or count ratios. Once the mineralogy of each grain is determined, composition measurement can be performed using the appropriate calibrated method. Since µ-XRF is semi-quantitative, calibration curves need to be created to adjust the chemical method for each mineral. Calibration is achieved using Electron Probe Micro-Analyzer (EPMA) measurements on standard grains.

1 Introduction

Indicator minerals are an exploration method that enables targeting eroded deposits by sampling and analysing overburden sediments to find minerals derived from the mineralisation, its associated alteration or host rocks. This method led, for instance, to the discovery of the diamantiferous kimberlite of Lac de Gras (Canada), by Cr-pyrope counting in HMC of tills (Fipke et al 1995), and to the discovery of the Casa-Berardi gold deposit (Canada), by counting till gold grains and analysing their shape (Sauerbrei et al 1987).

IMs from the HMC are typically selected manually and analysed by a mineralogist with a binocular lense. This step is commonly called "picking". Since picking relies on visual interpretation, precision and reproducibility are highly dependent on the mineralogist expertise. The use of an automated method using µ-XRF would not only increase reproducibility for grains mineralogy identification and counting, but could also provide chemical compositions as well as grain shape information. Grain mineralogy that can be quickly derived from uXRF data, using intensity maps (counts/pixel), by implementing count thresholds or count ratios in a decision tree. This mineralogical analysis is part of a workflow (Figure 1). The objective of the automated method is to provide rapid HMC analysis as well as to improve QA/QC by making analysis reproductible.

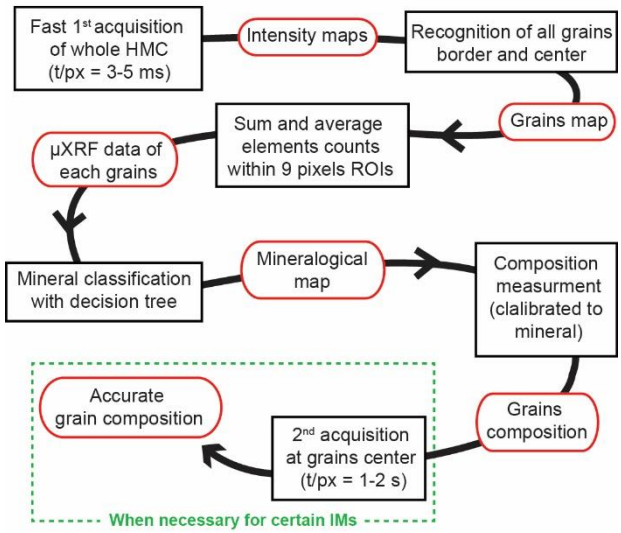

Figure 1. Proposed workflow for indicator minerals identification and composition measurement.

2 Method

2.1 Grain mount

The grain mounting method should enable optimization of data quality and to yield a low background signal. Carbon tape and polycaprolactone are suitable since they contain C, H and O, too light to be measured with x-ray fluorescence techniques.

Carbon tape is the simplest mount, allowing to directly deposit the grains on the adhesive surface. However, polycaprolactone resin enables grains top leveling, that prevents smaller grains to be hidden by bigger grains, a problem that is accentuated by the fact the source of X-ray is not orthogonal to the stage. Levelling is important because of the narrow focal depth of the beam. Intensity maps are more reliable and show less grain deformation if the z-focal plane encompasses all grain vertices. A polycaprolactone mount is thus preferred to carbon tape.

Polycaprolactone has a low temperature melting point (60°C), making it easy to manipulate. Polycaprolactone balls were placed in petri boxes and in an oven at 100°C for an hour. The top surface is levelled before it cools and solidify. After reheating the surface, it becomes ductile for about 15 minutes.

The selected grains are deposited on the surface and levelled with a press orthogonal to the surface.

2.2 Data acquisition

Micro-X-Ray Fluorescence (µ-XRF) is a spatially resolved, non-destructive technique that provides elemental analysis based on XRF spectra. Measurements were performed using a TORNADO M4 (Bruker Nano GmbH, Germany). The primary radiation is generated by applying a high voltage of 50 kV within a tube to a Rhodium anode. The Rh characteristic X-rays are focussed to a spot of 20 µm in diameter, at the chosen focal depth, by polycapillary lenses. The XRF signal emitted by the sample is collected by two detectors with a maximum rate of 130 x 10^3 counts per second (130 kcps) each. Acquisition is performed in lines, with the stage moving under the fixed primary beam. Data is acquired continuously, at a step size of 20 µm. The data for a single pixel is defined by averaging (or integrating) the signal over the time (measuring time) for the beam to cross the width of one pixel, (i.e., step width). Measuring time (t/px) must be optimized to allow the detection of light elements such as Mg, Al and Si while still offering a fast analysis. For example, 5 ms pixel time gives a fast result, but Al and Mg are not always detected over the background signal. A 30 ms pixel time gives accurate detection of lighter elements, but the complete analysis for a 1 cm^2 surface takes up to 6 hours. Different acquisition times are tested in this range to find the best compromise between timesaving and data quality. Counts are given in the number of counts per second per eV (cps/eV) to normalise counts to the energy resolution of the detector. This automated correction allows comparison of data acquired with different step widths.

2.3 Data processing

Each element intensity map can be exported from the Bruker Composite file (.bcf), as text files. These contain, for each pixel, the sum of counts in narrow energy ranges of the spectra that exhibit the characteristic peak for the element.

The software also gives the possibility to export total counts in a selected energy range. Counts within the energy range between 8.5 keV and 11.5 keV were exported. This energy range corresponds to a spectral range that exhibit bremsstrahlung radiation diffusion, referred to as the "brem. region" in the text and figures. This corresponds to primary x-ray, produced in the tube, not by Rh fluorescence, but by breaking and changing the trajectory of the electron under the effect of positive charge of Rh protons. Loss of energy of the braked electrons is converted into an x-ray. As observed for polycaprolactone (Figure 2), matter composed of light chemical elements shows generally high tube radiation diffusion because the latter are not absorbed. Total of counts in the brem. region is thus used to dissociate grains from the polycaprolactone resin.

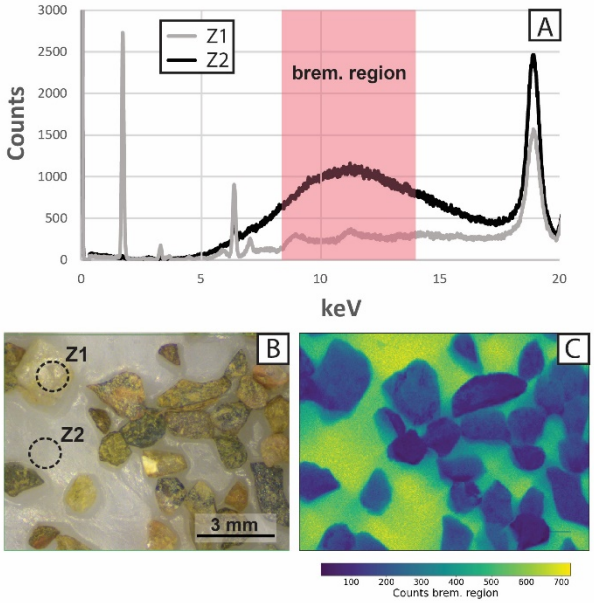

Figure 2. (A) Plot of total counts spectrum of two zones of 900 pixels, Zone 1 and 2, as referred on the optical image (B), taken by the TORNADO M4 camera. (C) Intensity map based on total counts within the brem. region, also shown in the diagram.

The primary dataset consists of intensity maps, stacked together to make a multilayered image. Each layer contains raw counts for an element, and an additional layer contains brem. region total counts. Processing of such a dataset instead of the whole spectra significantly decreases the processing time.

First, the multilayered image is converted into a *HyImage* to be treated with *hylite* (Thiele et al., 2021) an open-source python package. This package was designed to process hyperspectral data, but it works with any multi-channel image. *Hylite's* decision tree function is employed twice in the present workflow (Figure 1), (1) for the first step, to create a grain vs. mount binary image and, (2) for the mineralogical classification.

The grain/mount binary image is produced using a decision tree based on thresholds on the sum of element counts and on total counts in the brem. region. The decision tree output is further processed to define grain contours, count grains, and define a ROI at each grain centre. This step is performed with PyImageJ (Rueden et al 2022). PyImageJ implements a smoothing technique, median filtering to smooth noise while preserving sharpe edges. Next, a filter to remove holes, and, finally, the watershed function slices grains that are touching. PyImageJ also returns the coordinates of each grain 'centre from which are derived ROIs of 9 pixels. Centre coordinates are rounded to get a single pixel coordinate and derive the coordinates of the 8 other pixels in the square centred on the first pixel. The sum or the average of the element counts within the 9 pixels ROIs are the data input for the mineralogical

and compositional analysis. The mineralogical classification is realized using a second decision tree performed with *hylte*. Element counts used in the decision tree are in Figure 3.

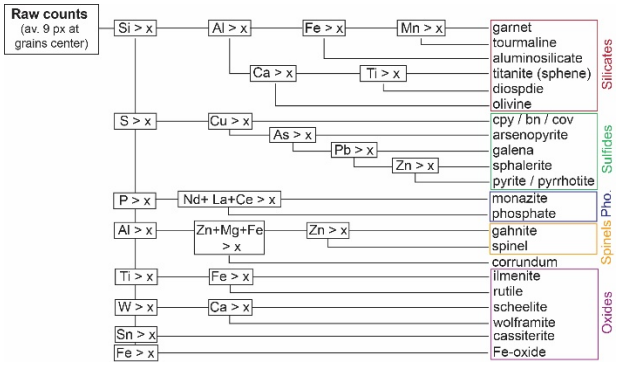

Figure 3. Decision tree for mineral classification step based on µ-XRF raw counts. Layers consist of thresholds.

The decision tree attributes, at first, a mineral group between silicates, sulfides, and phosphates by implementing thresholds for Si, S and P. If none of the thresholds are crossed, the decision tree attributes the pixel to the oxide group. Subsequent thresholds (and eventually counts rartios) are implemented to further classify within each mineral group.

2.4 Composition measurement calibration

Bruker M4 software allows the creation of composition measurement methods. Even if the absolute peak intensity for a given element is theoretically proportional to its concentration in the sample (Beckhoff et al 2006), the matrix effect of the sample is of great importance. Mineral lattice thus greatly influences the absolute peak intensity; however, this matrix effect is expected to be constant for a given mineral. To increase the precision of the µ-XRF's quantification, the software allows to input calibration parameters to correct this matrix effect. EPMA coupled with Wavelength-Dispersive X-Ray Spectroscopy (WDS) quantification is used as a reference for composition. Analysis of multiple grains with EPMA followed by µ-XRF of the same samples allows to create calibration line. Slope and offset of these linear trendlines are registered in Bruker M4 software as calibration parameters of a quantification method for the corresponding mineral group (e.g., garnet, spinel etc.).

3 Preliminary results

3.1 Grain count

Polycaprolactone mounts were tested with coarse and angular silicate grains of about 1 mm (Figure 4). Grain identification could not be done using the grayscale optical image (Figure 4A) because some grains are lighter than the polycaprolactone resin. However, in the case of HMC, grayscale image usefulness for grain identification is going to be tested. Pixels were classified as grain with the decision tree function if they fill two conditions: (1) the elements' sum is superior to 1.5% of the difference between the minimum and the maximum of the elements' sum of the dataset and (2) the brem. region counts are inferior to 35% of the difference between the maximum and the minimum brem. region counts in the dataset. Shape of grains of the produced binary image show some difference if compared to the optical image due to the fact the beam is not orthogonal to the stage, in contrast to the optical camera. Nevertheless, a good match is obtained.

The output of the decision tree is converted in a binary image (Figure 4B) that is then treated with PyImageJ functions as shown in Figure 4. The "watershed" filter did not work perfectly, for instance a grain in the middle was sliced in two particles (Figure 4D). The computed grain number is 33, whereas, the number of grains in the dataset Figure 4 is 32. Two grains were not detected and three were over-detected, i.e., two grains are detected when only one is present. The error percentage of under- and over- estimation is 6.25% and 9.37% respectively.

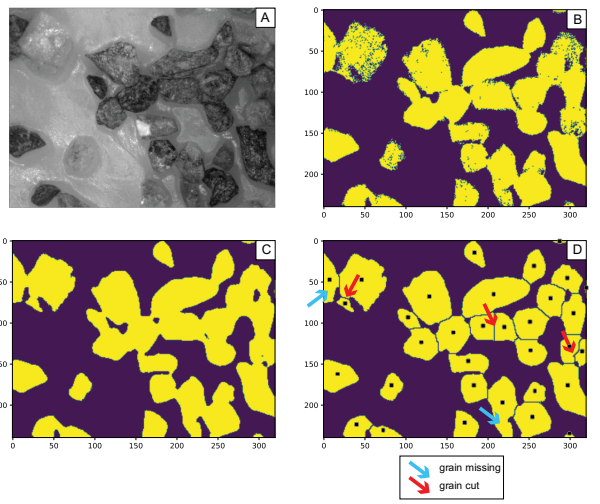

Figure 4. (A) Optical image in shades of gray. Different steps outputs after image processing: (B) binary image from first decision tree for grain and mount dissociation, (C) smoothed image of (B), (D) image with 'Fill Holes and 'Watershed' correction, black squares are nine pixels ROIs centred on grains centers.

Nine-pixel ROIs were defined based on the particle center output from PyImagej (Figure 4C). The average count for each element was calculated within each ROIs. These averages constitute the input in the mineral classification decision tree.

3.2 Mineralogy

The mineralogy decision tree was tested on multilayered images of µ-XRF data of common indicator minerals mounted on carbon tape. Tested thresholds were fixed numbers, chosen depending on counts variability of a given dataset. For

instance, the threshold for the silicate group for data acquired with measuring time of 30 ms per pixel is “Si > 5 cps”.

Figure 5 shows that minerals with simple stoichiometry such as ilmenite are easily classified, whereas for 4 olivine and 6 garnet grains are more challenging to classify. Border pixels were classified as grain based on the all elements count sum, but not as silicate, because the count for Si was too low because of “dilution” of the Si signal by matrix. Some pixels (red) are silicate because the count for Si was sufficient, but not for Al, so that the pixels were not classified into the garnet family. As a result, some pixels that belong to garnets grains were misclassified as diopside (Figure 5).

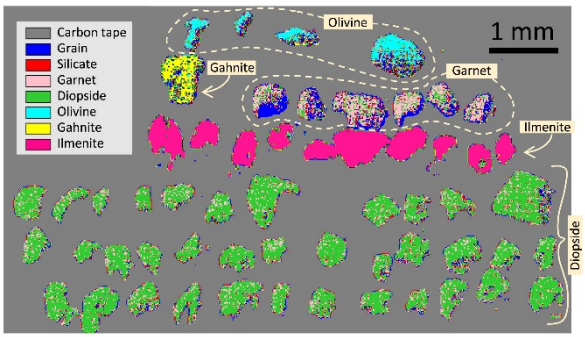

Figure 5. Decision tree output for mineral classification. Data are µ-XRF element intensity maps acquired at 50 keV, a measuring time of 30ms and a step size of 20 µm.

4. Conclusion

Grains identification based on grayscale image was not efficient in the example dataset because it contains grains that were too close in grayscale to the mount. Mineralogical and compositional analysis are based on ROI that must be at grain centre with respect to µ-XRF data, so if the ROI is based on optical image, it might be shifted and take grain border's XRF data. Grayscale optical image is however more loyal to real grain shape compared to XRF maps; thus, it is probably the most relevant dataset when it comes to automated grain shape measurements.

Classification pixel per pixel is not effective because some light elements are sometimes not detected and pixels at grain borders are not representative of grain composition. ROIs based mineral classification would have a better reliability since the classification would be based on counts integrated from several pixels. For example, 9-pixel ROIs integrate counts from the 9 spectrums that can be either summed (for thresholds) or averaged (for count ratios). The size of the ROIs can be modified according to the grain size of the analysed HMC.

Mineral classification with a simple decision tree can be considered on HMC samples because it contains minerals with a density over 3.0-3.2, which highly decrease mineralogy variability. Nevertheless, grain variety can still be extensive, and the mineralogy algorithm needs to be tested on HMC-type samples, doped with a known number of indicator minerals.

Grains topography and various grain sizes influence the absolute intensity of the characteristic peaks of the X-ray spectra. However, the relative intensity of characteristic peaks remains unchanged for a given measuring time. New branches with count ratios could be implemented in the mineral classification algorithm. Count ratios method could be efficient to classify solid solution minerals and minerals with similar compositions or stoichiometry. Grains from the garnet group, that typically have highly variable compositions, could be identified based on their Al/Si ratio since those elements are the most stable in the garnet lattice.

Crystal orientation may also influence peak intensity because of Bragg diffraction; however, it is expected to be negligible in our application.

Acknowledgements

Authors would like to thank the FRQNT, MERN, Agnico Eagle Mines, and Bruker for their financial and technical support.

References

Beckhoff, B., Kanngießer Habil, B., Langhoff, N., Wedell, R., Wolff, H. (Eds.) (2006) Handbook of practical x-ray fluorescence analysis. In: Springer Science & Business Media (ed) Springer Berlin, Heidelberg, pp 309-410. https://doi.org/10.1007/978-3-540-36722-2

Fipke, C.E., Gurney, J.J. and Moore, R.O. (1995) Diamond exploration techniques emphasising indicator mineral geochemistry and Canadian examples. Geological Survey of Canada, Canada, Bulletin 423.

Rueden, C. T., Hiner, M. C., Evans, E. L., Pinkert, M. A., Lucas, A. M., Carpenter, A. E., Cimini, B. A., Eliceiri, K. W. (2022) PyImageJ: A library for integrating ImageJ and Python, Nat Methods, 19:1326–1327, https://doi.org/10.1038/s41592-022-01655-4

Sauerbrei, J.A., Pattison, E.F., Averill, S.A. (1987) Till sampling in the Casa-Berardi gold area, Quebec: A case history in orientation and discovery. Journal of Geochemical Exploration 28:297–314. https://doi.org/10.1016/0375-6742(87)90054-9

Thiele S., Lorenz S., Kirsch M., Gloaguen R. (2020): *Hylite : A hyperspectral toolbox for open pit mapping* https://doi.org/10.5194/egusphere-egu2020-13563

Compositional variations of olivine in kimberlites: A new tool for diamond exploration

Andrea Giuliani[1], David Phillips[2], D. Graham Pearson[3], Soumendu Sarkar[2], Yaakov Weiss[4], Robin Preston[5], Michael Seller[6], Zdislav Spetius[7]
[1]ETH Zurich, Switzwerland (andrea.giuliani@erdw.ethz.ch)
[2]The University of Melbourne, Australia
[3]University of Alberta, Canada
[4]The Hebrew University of Jerusalem, Israel
[5]De Beers Group, South Africa
[6]De Beers Group, Canada
[7]Novosibirsk State University, Russia

Abstract. Understanding the diamond potential of lithospheric roots traversed by kimberlites is a complex art that largely relies on geochemical and thermobarometric constraints provided by mantle-derived garnet, clinopyroxene and chromite (diamond indicator minerals). Although it is widely acknowledged that strongly melt-metasomatised lithospheric mantle keels are associated with poor diamond preservation, the mechanisms underpinning this relationship are far from clear. Here we show that the diamond grade of kimberlites worldwide is reflected by the composition of magmatic olivine. Kimberlites with low diamond grades contain iron-rich olivine, which is typical of kimberlites that entrain and assimilate substantial amounts of lithospheric mantle material metasomatised by earlier failed pulses of kimberlite (or similar) melt. Conversely, high diamond grades are exclusively associated with kimberlites featuring Mg-rich olivine composition which sampled lithospheric mantle keels only marginally modified by interaction with precursor kimberlite or related melts. This work provides a causal link between infiltration of the deep lithosphere by carbonate-rich kimberlite melts and diamond destruction, and shows that olivine chemistry is a new and inexpensive tool for diamond exploration.

1 Introduction

Diamond exploration is a multifaceted operation that relies on combinations of multiple geophysical and geochemical methods (Kjarsgaard et al., 2019). The composition of diamond indicator minerals (DIMs) in kimberlites, including mantle-derived garnet, clinopyroxene and chromite, provides important constraints on the diamond potential of the lithospheric mantle traversed and entrained by kimberlites (Gurney et al., 1993; Nowicki et al., 2007), including the thickness of the lithospheric roots (Grutter, 2009) and, therefore, of the diamond window (that is the lithospheric layer sandwiched between the graphite-diamond stability curve and the lithosphere-asthenosphere boundary). DIMs also provide indications of the extent of depletion vs metasomatic enrichment of the lithospheric mantle, as it is well established that diamonds brought to surface by kimberlites preferentially reside in compositionally depleted lithospheric mantle roots (Gurney et al., 1993; Nowicki et al., 2007). The connection between melt-metasomatism of the deep lithosphere and diamond potential of kimberlites is well-established empirically (Griffin and Ryan, 1995; Malkovets et al., 2007), but its geological context is not well understood, e.g., What is the origin and composition of these metasomatic melts? When did this metasomatic affect the lithospheric mantle? This work targets this knowledge gap and explores a new method to enhance the diamond exploration toolbox.

2 Background: olivine in kimberlites

Kimberlites are complex hybrid rocks that contain components of magmatic, hydrothermal and xenocrystic origin (Giuliani and Pearson, 2019). Olivine is the main constituent of fresh kimberlite rocks (Mitchell, 1973, 1986) and is generally zoned between xenocrystic cores derived from disaggregation of lithospheric mantle wall rocks, and magmatic rims (Giuliani, 2018). The olivine cores do not simply represent typical mantle peridotites, but may also be sourced locally from other lithologies (e.g., megacrysts; sheared peridotites) that have experienced metasomatism by precursor kimberlite melts. In fact, it is well established that the eruption of kimberlite magmas is preceded by 'priming' of lithospheric mantle conduits by earlier failed pulses of kimberlite melt (Giuliani et al., 2014, 2016).

Recent work has shown that the average Mg# [atomic proportions of Mg/(Mg+Fe)] of xenocrystic olivine cores is directly correlated to the average Mg# of olivine rims in kimberlites on a global (Giuliani et al., 2020) and regional scale (Dalton et al., 2020; Sarkar et al., 2021; Tovey et al., 2021). This correlation, combined with extensive petrographic and experimental evidence of assimilation of entrained lithospheric mantle material by kimberlites (Mitchell, 2008; Kamenetsky et al., 2009; Russell et al., 2012; Soltys et al., 2016), suggests that the composition of kimberlite melts at surface is directly related to the composition of lithospheric mantle wall rocks which interacts with kimberlite melts *en route* to surface (Giuliani et al., 2020). It further establishes that the more intensive the metasomatism, the more Fe-rich is the composition of magmatic olivine. Therefore, olivine chemistry provides a direct link between kimberlite melt composition and lithospheric mantle wall rocks, including the extent of

kimberlite-related metasomatism of the lithospheric mantle traversed by pulses of kimberlite magma that reach the surface.

3 Working hypothesis: A connection between kimberlite composition and diamond grade

Recent experimental work by Fedortchouk et al. (2022) has confirmed existing evidence (e.g., Robinson et al., 1989) that interaction of diamonds with carbonate-rich melts akin to kimberlites at lithospheric mantle depths leads to diamond resorption. Here, we test whether a correlation exists between olivine compositions and diamond grades in kimberlites worldwide, with the poviso that the composition of olivine in kimberlites constrains the extent of kimberlite-related metasomatism of the (diamond-bearing) lithospheric mantle roots. If this hypothesis is correct, we expect to observe lower diamond grades in kimberlites that sample lithospheric mantle wall rocks that have been extensively metasomatised by precursor kimberlite melts and, therefore, contain olivine with low (average) Mg# values.

4 Results

Building up on the compilation of Giuliani et al. (2020), we have assembled a revised database that includes new electron microprobe analyses of olivine in 12 kimberlites from Russia, Canada, Brazil and South Africa, and additional results from other localities published since the previous compilation. This new dataset confirms that the average Mg# of olivine cores in kimberlites (and also diamondiferous cratonic lamproites; see Sarkar et al., 2022) is directly correlated with the average Mg# of olivine rims. Of the 100 localities for which olivine data are now available, 74 have associated diamond grades (e.g., run of mines; exploration data). Comparison of average Mg# of either olivine cores or rims (which are linearly correlated) with diamond grades indicates that high diamond grades (>50-100 cpht or carats per hundred tonne) are exclusively. associated with high-Mg# olivine, i.e. >90 for olivine cores, ≥89 for olivine rims. Conversely, the diamond grades of kimberlites featuring low-Mg# olivine are always low (<20 cpht). It should be noted that low diamond grade can also occur in kimberlites with high-Mg# olivine.

5 Implications

The correlation between average olivine Mg# (cores or rims) and diamond grades confirms our working hypothesis that kimberlite-related metasomatism is detrimental to diamond preservation. This finding provides a sound explanation for the empirical observation, based largely on garnet xenocryst compositions (Gurney et al., 1993; Griffin and Ryan, 1995; Malkovets et al., 2007; Agashev et al., 2018), that melt-metasomatism of the lithospheric mantle leads to diamond destruction.

This study highlights that the major element composition of olivine in kimberlites represents a new inexpensive tool for diamond exploration. This tool does not replace other geochemical approaches such as analyses of garnet, but can be used to rapidly assess the likelihood of high diamond grades in a kimberlite based on the extent of kimberlite metasomatism of the lithospheric mantle roots. An important caveat is that olivine compositions are relatively invariant in kimberlite pipes and clusters of kimberlites, whereas diamond grades vary on every scale. Hence, olivine compositions provide constraints on the likelihood of diamond preservation in the lithospheric mantle, but do not allow prediction of the influence of other local-scale processes which impact diamond grade such as pre-existing diamond contents in the wall rocks, sampling efficiency by kimberlite melts, sorting of entrained mantle cargo during kimberlite ascent and emplacement, dilution by country rocks, etc. Nonetheless, used in combination with other geological constraints such as the depth of the lithosphere retrieved from mantle xenolith and xenocryst studies, the composition of olivine can provide an important tool for assessing the diamond potential of a kimberlite pipe or cluster before undertaking more detailed investigations.

References

Agashev AM, Nakai Si, Serov IV, Tolstov AV, Garanin KV, Kovalchuk OE (2018) Geochemistry and origin of the Mirny field kimberlites, Siberia. Mineralogy and Petrology 112(2):597-608 doi:10.1007/s00710-018-0617-4

Dalton H, Giuliani A, O'Brien H, Phillips D, Hergt J (2020) The role of lithospheric heterogeneity on the composition of kimberlite magmas from a single field: The case of Kaavi-Kuopio, Finland. Lithos 354-355:105333 doi:https://doi.org/10.1016/j.lithos.2019.105333

Fedortchouk Y, Chinn IL, Perritt SH, Zhang Z, Stern RA, Li Z (2022) Diamond-destructive mantle metasomatism: Evidence from the internal and external textures of diamonds and their nitrogen defects. Lithos 414-415:106616 doi:https://doi.org/10.1016/j.lithos.2022.106616

Giuliani A (2018) Insights into kimberlite petrogenesis and mantle metasomatism from a review of the compositional zoning of olivine in kimberlites worldwide. Lithos 312-313:322-342 doi:https://doi.org/10.1016/j.lithos.2018.04.029

Giuliani A, Pearson DG (2019) Kimberlites: From Deep Earth to Diamond Mines. Elements 15(6):377-380 doi:10.2138/gselements.15.6.377

Giuliani A, Pearson DG, Soltys A, Dalton H, Phillips D, Foley SF, Lim E, Goemann K, Griffin WL, Mitchell RH (2020) Kimberlite genesis from a common carbonate-rich primary melt modified by lithospheric mantle assimilation. Science Advances 6(17):eaaz0424 doi:10.1126/sciadv.aaz0424

Giuliani A, Phillips D, Kamenetsky VS, Goemann K (2016) Constraints on kimberlite ascent mechanisms revealed by phlogopite compositions in kimberlites and mantle xenoliths. Lithos 240–243:189-201 doi:http://dx.doi.org/10.1016/j.lithos.2015.11.013

Giuliani A, Phillips D, Kamenetsky VS, Kendrick MA, Wyatt BA, Goemann K, Hutchinson G (2014) Petrogenesis of Mantle Polymict Breccias: Insights into Mantle Processes

Coeval with Kimberlite Magmatism. Journal of Petrology 55(4):831-858
Griffin WL, Ryan CG (1995) Trace elements in indicator minerals: area selection and target evaluation in diamond exploration. Journal of Geochemical Exploration 53(1–3):311-337 doi:http://dx.doi.org/10.1016/0375-6742(94)00015-4
Grütter HS (2009) Pyroxene xenocryst geotherms: Techniques and application. Lithos 112, Supplement 2:1167-1178 doi:http://dx.doi.org/10.1016/j.lithos.2009.03.023
Gurney JJ, Helmstaedt H, Moore RO (1993) A review of the use and application of mantle mineral geochemistry in diamond exploration. Pure and Applied Chemistry 65(12):2423-2442 doi:doi:10.1351/pac199365122423
Kamenetsky VS, Kamenetsky MB, Sobolev AV, Golovin AV, Sharygin VV, Pokhilenko NP, Sobolev NV (2009) Can pyroxenes be liquidus minerals in the kimberlite magma? Lithos 112S:213-222
Kjarsgaard BA, Januszczak N, Stiefenhofer J (2019) Diamond Exploration and Resource Evaluation of Kimberlites. Elements 15(6):411-416 doi: 10.2138/gselements.15.6.411
Malkovets VG, Griffin WL, O'Reilly SY, Wood BJ (2007) Diamond, subcalcic garnet, and mantle metasomatism: Kimberlite sampling patterns define the link. Geology 35(4):339-342 doi:10.1130/g23092a.1
Mitchell RH (1973) Composition of olivine, silica activity and oxygen fugacity in kimberlite. Lithos 6(1):65-81 doi:http://dx.doi.org/10.1016/0024-4937(73)90080-7
Mitchell RH (1986) Kimberlites: Mineralogy, Geochemistry and Petrology. Plenum Publishing Company, New York
Mitchell RH (2008) Petrology of hypabyssal kimberlites: Relevance to primary magma compositions. Journal of Volcanology and Geothermal Research 174(1-3):1-8
Nowicki TE, Moore RO, Gurney JJ, Baumgartner MC (2007) Diamonds and Associated Heavy Minerals in Kimberlite: A Review of Key Concepts and Applications. In: Maria AM, David TW (eds) Developments in Sedimentology, vol Volume 58. Elsevier, pp 1235-1267
Robinson DN, Scott JA, Van Niekerk A, Anderson VG (1989) The sequence of event reflected in the diamonds of some southern African kimberlites. In: Ross J, Jaques AL, Ferguson J, Green DH, O'Reilly SY, Danchin RV, Janse AJA (eds) Kimberlites and Related Rocks 4th International Kimberlite Conference, vol 2. Geological Society of Australia, Perth, pp 990-1000
Russell JK, Porritt LA, Lavallee Y, Dingwell DB (2012) Kimberlite ascent by assimilation-fuelled buoyancy. Nature 481(7381):352-356
Sarkar S, Giuliani A, Ghosh S, Phillips D (2021) Petrogenesis of coeval lamproites and kimberlites from the Wajrakarur field, Southern India: New insights from olivine compositions. Lithos 406-407:106524 doi:https://doi.org/10.1016/j.lithos.2021.106524
Sarkar S, Giuliani A, Phillips D, Howarth GH, Ghosh S, Dalton H (2022) Sublithospheric melt input in cratonic lamproites. Geology 50(11):1296-1300 doi:10.1130/G50384.1
Soltys A, Giuliani A, Phillips D, Kamenetsky VS, Maas R, Woodhead J, Rodemann T (2016) In-situ assimilation of mantle minerals by kimberlitic magmas — Direct evidence from a garnet wehrlite xenolith entrained in the Bultfontein kimberlite (Kimberley, South Africa). Lithos 256–257:182-196 doi:http://dx.doi.org/10.1016/j.lithos.2016.04.011
Tovey M, Giuliani A, Phillips D, Pearson DG, Sarkar C, Nowicki T, Carlson J (2021) The spatial and temporal evolution of primitive melt compositions within the Lac de Gras kimberlite field, Canada: Source evolution vs lithospheric mantle assimilation. Lithos 392-393:106142 doi:https://doi.org/10.1016/j.lithos.2021.106142

In-situ Rb-Sr dating of mica: method refinement and application to mineral resources

Andrea Giuliani[1], Marcel Guillong[1], Senan Oesch[1], Roland Mass[2], Geoff H. Howarth[3], Marco L. Fiorentini[4]
[1]ETH Zürich, Switzerland (andrea.giuliani@erdw.ehtz.ch)
[2]The University of Melbourne, Australia
[3]University of Cape Town, South Africa
[4]University of Western Australia

Abstract. In-situ Rb-Sr dating of mica by laser ablation ICP-MS/MS has recently emerged as a new tool to date a range of geological processes including mineralisation events. The majority of age results presented to date are based on Rb/Sr calibration using the widely available MicaMG pressed-powder pellet. However, several studies have reported low accuracy associated with mica Rb-Sr ages using this method or large variations in calculated Rb/Sr for the same mica attributed to the different ablation properties of MicaMG and natural mica. In this work, we first report the results of a systematic comparison between isotope-dilution and in-situ Rb/Sr ages of micas in diamondiferous kimberlites from South Africa and Sierra Leone. We confirm that employment of MicaMG as calibration material may provide inaccurate results and present a new approach to obtain accurate ages, which relies on Rb/Sr calibration using the synthetic glass NIST610 SRM and an in-house mica standard. This updated procedure is then employed to constrain the ages of other diamond deposits and address the formation of Au mineralisation in the Eastern Goldfields (Australia).

1 Introduction

In-situ Rb-Sr dating of mica by laser ablation ICP-MS/MS (or QQQ) is increasingly employed to date a range of geological processes including magmatic intrusions, metamorphic and thermal events, crustal deformation and hydrothermal mineralisation. This analytical method overcomes the isobaric interference of ^{87}Rb on ^{87}Sr, which previously hampered analysis of Sr isotopes in Rb-rich phases such as mica, by reaction of Sr^+ ions with a gas reagent (SF_6 or N_2O) in a collision cell. Rb^+ ions are not affected by this reaction and, while the isotopes of Sr are quantified as reacted species (e.g., SrO^+), ^{87}Rb is determined by measuring the abundance of unreacted and interference-free ^{85}Rb.

The majority of age results presented to date are based on Rb/Sr calibration using the widely available MicaMG pressed-powder pellet (Hogmalm et al., 2017; Gorojovsky and Alard, 2020; Olierook et al., 2020; Zametzer et al., 2022; Kirkland et al., 2023). Strontium isotope ratios are routinely calibrated using the synthetic glass NIST610 SRM. However, various studies have reported low accuracy associated with mica Rb-Sr ages using this method (e.g., Li et al., 2020; Redaa et al., 2021, 2023; Subarkah et al., 2022) or large variations in calculated Rb/Sr for the same mica attributed to the different ablation properties of MicaMG and natural mica (Redaa et al., 2021). In this work we reassess the validity of this analytical approach by comparison of age data obtained for the same materials by in-situ and isotope-dilution methods. We then develop a new robust strategy to obtain accurate in-situ mica Rb/Sr ages and show its application to the formation of ore deposits.

2 Samples and methods

Micas tested in this study are predominantly sourced from kimberlites, including Bultfontein (South Africa; 88.3 ± 0.2 Ma; 2se; Fitzpayne et al., 2020), Wimbledon (South Africa; 114.4 ± 0.8 Ma; Sarkar et al., 2023), Koidu (Sierra Leone; ~145 Ma; De Beers unpublished data) and Tonguma (Sierra Leone; no previous age constraints available but assumed to be similar to Koidu) (**Figure 1**). The Bultfontein and Wimbledon localities have been selected to test the accuracy and reproducibility of in-situ mica Rb-Sr analyses, whereas obtaining new age data for multiple samples from Koidu and Tonguma represents the main target of this study. Additional samples from Au-mineralised carbonate-rich veins in the Smokebush dolerite (Eastern Goldfields, Western Australia) are also included to test the application of this method to the formation of Archean hydrothermal ore deposits.

Independent age constraints based on mica Rb-Sr dating by isotope dilution are available for Bultfontein (Fitzpayne et al., 2020) and Wimbledon (Sarkar et al., 2023). For Koidu and Tonguma, three samples were selected for isotope dilution analysis by multi-collector (MC) ICP-MS at the University of Melbourne. We also independently tested the Rb-Sr isotope composition of MicaMG by measuring an aliquot of the same powder used to manufacture the pellets we employ for calibration of mica Rb/Sr in situ analysis by isotope dilution (results reported in Redaa et al., 2023). In-situ Rb-Sr dating of mica in grain mounts and thin sections was undertaken by laser ablation ICP MS/MS using an Agilent 8800 housed at ETH Zurich.

3 Results and discussion

The Rb-Sr isotope compositions of mica fractions (bulk, leachate, residue) were used to construct Rb-Sr isochrons using IsoplotR. The only analysed sample from Tonguma yielded a 4-point isochron corresponding to an age of 138.2 ± 0.5 Ma (2se) (Fitzpayne et al., 2023). The two Koidu samples that

were analysed yielded 3-point isochron ages within uncertainties overlapping one another (145.7 ± 0.5 Ma, and 144.9 ± 0.5 Ma) (Fitzpayne et al., 2023). These ages are indistinguishable from previous age determinations for Koidu (145 Ma; De Beers unpublished).

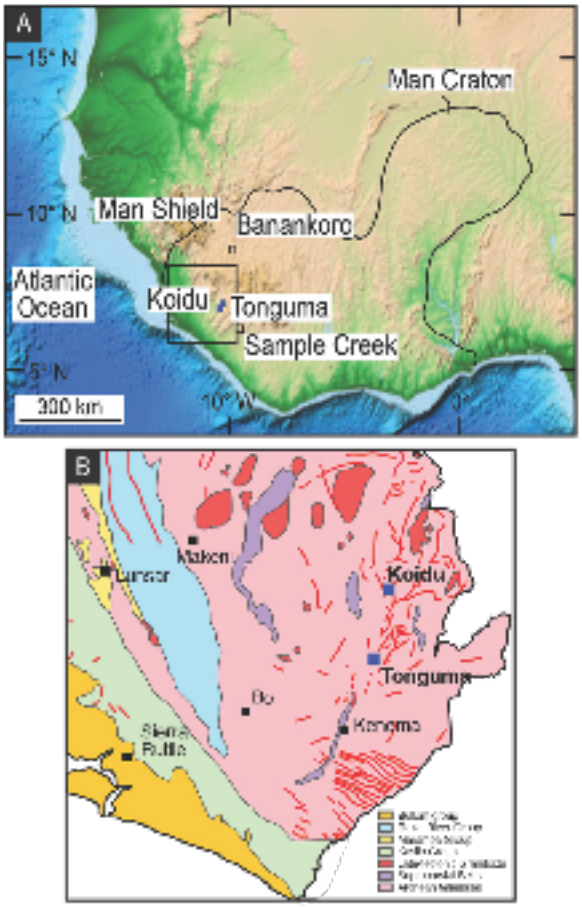

Figure 1. A) Tomographic map of West Africa showing the areal extent of the Man Craton and the positions of main kimberlite clusters; and B) inset showing a simplified map of south-eastern Sierra Leone including the positions of Tonguma and Koidu.

These ages and those previously obtained by isotope dilution for micas in South-African Cretaceous kimberlites were then compared with those obtained by laser ablation ICP-MS/MS using two different procedures. The first one is identical to the widely applied strategy of calibrating $^{87}Sr/^{86}Sr$ using the synthetic glass NIST610 SRM and $^{87}Rb/^{86}Sr$ using MicaMG. This procedure generates age results which generally do not overlap those obtained by isotope dilution with relative differences as high as 10% (**Figure 2**). We concur with Redaa et al. (2021) that this difference between solution-based and in-situ mica Rb-Sr ages probably stems from the different ablation properties of the pressed nano-powder pellet MicaMG. Poor reproducibility of Rb/Sr in MicaMG compared to NIST610 also confirms the heterogeneous behaviour of MicaMG during laser ablation.

We have therefore devised a new procedure where NIST610 is initially employed to estimate both $^{87}Sr/^{86}Sr$ and $^{87}Rb/^{86}Sr$, thus producing very stable splines for drift correction and initial calibration of Rb-Sr isotopes in mica. An in-house mica standard (from Wimbledon) is then utilised to re-calibrate $^{87}Rb/^{86}Sr$ in the mica unknowns. This procedure generates age data which match 'isotope-dilution' ages for the same micas (**Figure 1**).

For Tonguma and Koidu, pooling of laser ablation analyses of micas in multiple samples returns ages of 137.1 ± 2.0 Ma (n = 133; 5 samples) and 145.1 ± 2.4 Ma (n = 92; 4 samples), which are also indistinguishable from the solution-based age data. These data and a similarly narrow spread in mica Rb-Sr age data by individual samples for different units of each locality suggest that different intrusive units at Koidu and Tonguma were emplaced over a short time interval, which currently cannot be resolved.

Analyses of mica in carbonate-rich veins from Smokebush are currently underway and the results will be presented at the meeting.

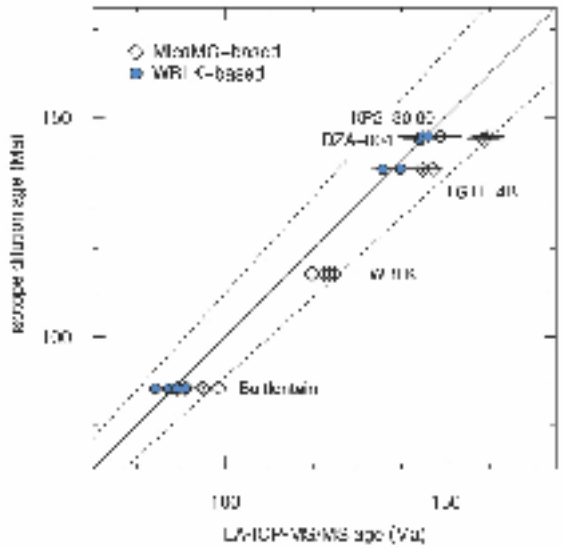

Figure 2. Comparison of mica Rb-Sr ages from LA-ICP-MS/MS vs isotope dilution. Note the difference between LA-ICP-MS/MS ages calculated using MicaMG or Wimbledon (WBLK) to calibrate Rb/Sr in the mica unknowns, where only the latter approach provides accurate results.

4 Conclusions

In-situ Rb-Sr dating of mica by LA-ICP-MS/MS can provide excellent age constraints and is much quicker and less expensive compared to conventional isotope-dilution methods. Although this method does not achieve the same level of precision of isotope dilution analyses, it allows to preserve textural context and can be combined with analysis of trace element concentrations thus enabling combination of petrological, geochemical and isotopic information. However, additional effort is required to improve the current limitations of in-situ mica Rb-Sr dating. This work shows that

employment of MicaMG as primary calibration standard is not recommended and developments of suitable mica reference materials showing large spread in Rb/Sr such as our Wimbledon mica is required.

References

Fitzpayne A, Giuliani A, Hergt J, Woodhead JD, Maas R (2020) Isotopic analyses of clinopyroxenes demonstrate the effects of kimberlite melt metasomatism upon the lithospheric mantle. Lithos 370-371:105595 doi:https://doi.org/10.1016/j.lithos.2020.105595

Fitzpayne A, Giuliani A, Howarth GH, Peters BJ, Fehr MA, Maas R (2023) Major-, trace-element and Sr-Nd-Hf isotope geochemistry of diamondiferous dykes from Tonguma and Koidu, Sierra Leone: Highly micaceous kimberlites formed by assimilation of metasomatised lithospheric mantle rocks. Chemical Geology 630:121475 doi:https://doi.org/10.1016/j.chemgeo.2023.121475

Gorojovsky L, Alard O (2020) Optimisation of laser and mass spectrometer parameters for the in situ analysis of Rb/Sr ratios by LA-ICP-MS/MS. Journal of Analytical Atomic Spectrometry doi:10.1039/D0JA00308E

Hogmalm KJ, Zack T, Karlsson AKO, Sjöqvist ASL, Garbe-Schönberg D (2017) In situ Rb–Sr and K–Ca dating by LA-ICP-MS/MS: an evaluation of N2O and SF6 as reaction gases. Journal of Analytical Atomic Spectrometry 32(2):305-313 doi:10.1039/C6JA00362A

Kirkland CL, Olierook HKH, Danišík M, Liebmann J, Hollis J, Ribeiro BV, Rankenburg K (2023) Dating mylonitic overprinting of ancient rocks. Communications Earth & Environment 4(1):47 doi:10.1038/s43247-023-00709-5

Li S-S, Santosh M, Farkaš J, Redaa A, Ganguly S, Kim SW, Zhang C, Gilbert S, Zack T (2020) Coupled U-Pb and Rb-Sr laser ablation geochronology trace Archean to Proterozoic crustal evolution in the Dharwar Craton, India. Precambrian Research 343:105709 doi:https://doi.org/10.1016/j.precamres.2020.105709

Olierook HKH, Rankenburg K, Ulrich S, Kirkland CL, Evans NJ, Brown S, McInnes BIA, Prent A, Gillespie J, McDonald B, Darragh M (2020) Resolving multiple geological events using in situ Rb–Sr geochronology: implications for metallogenesis at Tropicana, Western Australia. Geochronology 2(2):283-303 doi:10.5194/gchron-2-283-2020

Redaa A, Farkaš J, Gilbert S, Collins AS, Löhr S, Vasegh D, Forster M, Blades M, Zack T, Giuliani A, Maas R, Baldermann A, Dietzel M, Garbe-Schönberg D (2023) Testing Nano-Powder and Fused-Glass Mineral Reference Materials for In Situ Rb-Sr Dating of Glauconite, Phlogopite, Biotite and Feldspar via LA-ICP-MS/MS. Geostandards and Geoanalytical Research 47(1):23-48 doi:https://doi.org/10.1111/ggr.12467

Redaa A, Farkaš J, Gilbert S, Collins AS, Wade B, Löhr S, Zack T, Garbe-Schönberg D (2021) Assessment of elemental fractionation and matrix effects during in situ Rb–Sr dating of phlogopite by LA-ICP-MS/MS: implications for the accuracy and precision of mineral ages. Journal of Analytical Atomic Spectrometry 36(2):322-344 doi:10.1039/D0JA00299B

Sarkar S, Giuliani A, Dalton H, Phillips D, Ghosh S, Misev S, Maas R (2023) Derivation of lamproites and kimberlites from a common evolving source in the convective mantle: The case for southern African “transitional kimberlites”. Journal of Petrology:accepted pending minor revisions

Subarkah D, Nixon AL, Jimenez M, Collins AS, Blades ML, Farkaš J, Gilbert SE, Holford S, Jarrett A (2022) Constraining the geothermal parameters of in situ Rb–Sr dating on Proterozoic shales and their subsequent applications. Geochronology 4(2):577-600 doi:10.5194/gchron-4-577-2022

Zametzer A, Kirkland CL, Barham M, Hartnady MIH, Bath AB, Rankenburg K (2022) Episodic alteration within a gold-bearing Archean shear zone revealed by in situ biotite Rb–Sr dating. Precambrian Research 382:106872 doi:https://doi.org/10.1016/j.precamres.2022.106872

Standardized and Automated 3D Mineralogy of Ores

Jose R. A. Godinho[1]
[1] *Helmholtz-Zentrum Dresden-Rossendorf, Helmholtz Institute Freiberg for Resource Technology. j.godinho@hzdr.de*

Abstract. Quantitative mineralogy of geological materials has been limited to 2D imaging methods that use chemical information from cross-sections of a material to automatically classify it's mineral phases. A more comprehensive mineralogical analysis of the real microstructures inside a material can be done in 3D using X-ray Computed Tomography (CT). Nevertheless, a widespread use of the technique has been limited by the lack of standardized methods to classify and to quantify minerals from 3D images that do not contain chemical information. This is mostly due to 3D image artefacts that hinder the ability to process the data in a standardized way, which is hindered further by the variety of scanners and software available at different laboratories. Here, results from the first standardized workflow for automated 3D mineralogy using CT are presented. The results from different types of ores (Au, Cu, Fe, Cr and REE) are compared with other standard methods 2D-based automated mineralogy and XRD. The advantages and disadvantages of using 3D characterization are discussed as well as the advantages of using the proposed workflow relative to traditional 3D image analysis.

1 Introduction

Image artefacts and partial volume in voxels at interphases are inevitable in 3D images resulting from CT. This makes image processing based on the grey-scale of the whole 3D image time consuming and the results can be strongly influenced user input bias due to the lack of automation and standardization of the different image processing steps. These are strong reasons to prevent the adoption of CT and 3D imaging for routine ore characterization. For this to become a reality, two steps are required, 1) to reduce and account for the imaging artefacts with minimum subjective image processing, and 2) to standardize and automate the quantification workflow, similar to available 2D automated mineralogy methods.

The first standardized workflow, **M**ounted **S**ingle **Pa**rticle **C**haracterization for **M**ineralogical **An**alysis (MSPaCMAn) to implement these steps was recently proposed (Godinho et al. 2021; Godinho et al. 2023). Here, the workflow is applied to reference samples and different ore types, to quantify their mineralogical composition in a semi-automated way.

2 Methods

The MSPaCMAn workflow consists of the following sequence of steps (Fig.1): 1) sample preparation as a particle dispersion where a spacer is used to minimize the particles to touch. This step simplifies the image processing, which enables automation. 2) Particle segmentation is done using deep learning model that has been pre-trained in dozens of samples and can distinguish the particles from the background without user input (Gotkowski et al. 2023). 3) Phase classification is done using a decision tree with criteria based on the grey-scale and geometrical properties of each particle. This allows to reduce the complexity of the microstructures in the whole image into less complex subvolumes that are sample specific. 4) Phase quantification is calculated at the particle-level using the grey-values of all voxels in the particle, which allows taking in consideration the partial volume at interphases. This improves the detection limit of grains, improves accuracy and decreases user input bias.

3 Results

The MSPaCMAn workflow has been validated in several reference samples containing particles of known composition. For example, in Figure 2 several minerals typically present in sulphide concentrates are analysed in the same sample. With the exception of the denser arsenopyrite, the other phases have similar x-ray attenuation coefficients. Consequently, it would be difficult to distinguish those phases, especially if they appear associated as it is often the case in ores. Nevertheless using single particle histograms it is possible to distinguish the phase based on the distinctive grey-values at the maximum of the peaks. As shown in figure 1 magnetite and pyrite can be classified correctly even if they are associated in complex microstructures.

Figure 3 shows a sample containing quartz and biotite. Biotite has a characteristic thin shape, thus its characteristic grey-scale is shifted towards lower values that those expected based solely on the attenuation coefficient. Consequently, the two phases cannot be distinguished base only on the grey-scale. Nevertheless, the since the grey-values of the peaks from the single particle histograms are a function of the geometrical properties of the biotite particles, this function can be used as a classification criteria.

The method is currently being test in real ore with different degrees of complexity, e.g., chromite ore, sulphide-cupper ores, REE rich carbonates, iron ores, and gold-rich quartz-pyrite. Quantitative validation of the results is done using XRD, 2D-based automated mineralogy and chemical essays.

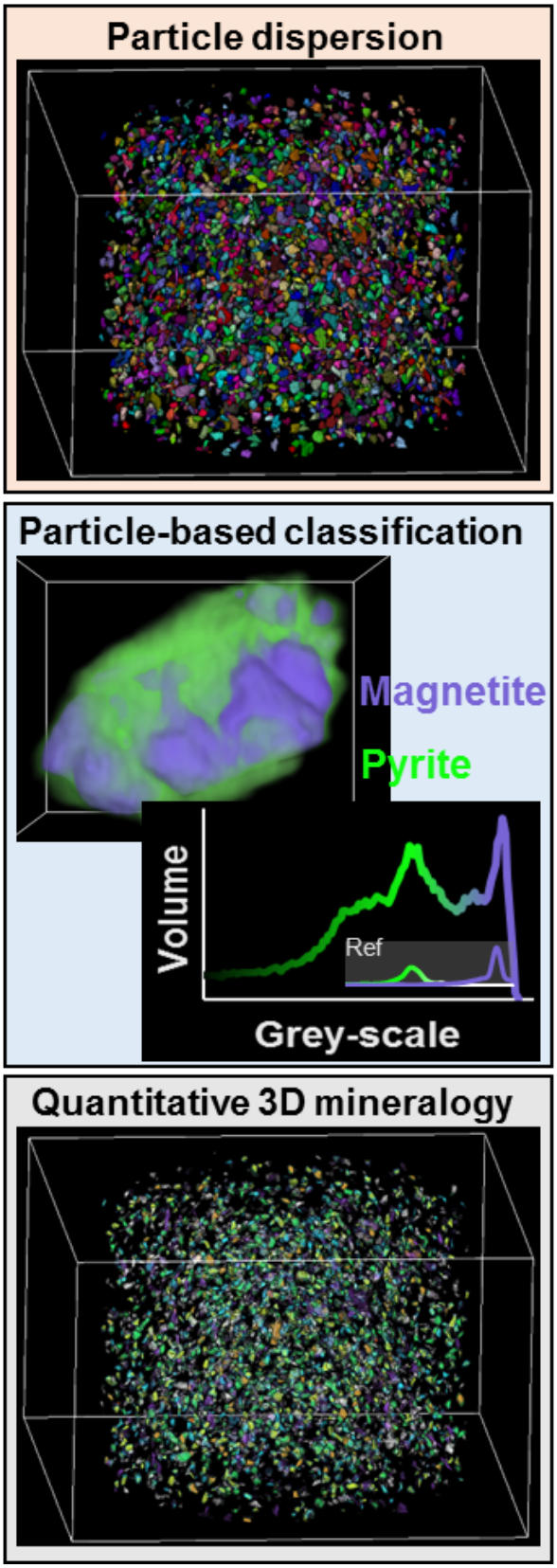

Figure 1. Representation of the key steps of MSPaCMAn: Sample preparation, particle-based histogram analysis, automatic classification and quantification of all particles.

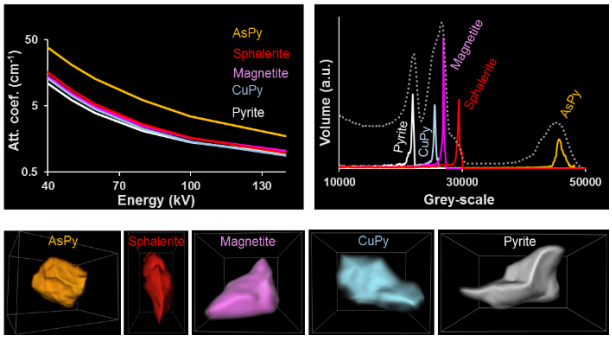

Figure 2. Analysis of the theoretical x-ray attenuation coefficient and particle histograms from a reference sample containing arsenopyrite (AsPy, orange), sphalerite (red), magnetite (pink), chalcopyrite (CuPy, blue) and pyrite (white). The histogram of the entire 3D image (dashed line) is compared with the histogram of individual particles, one per phase.

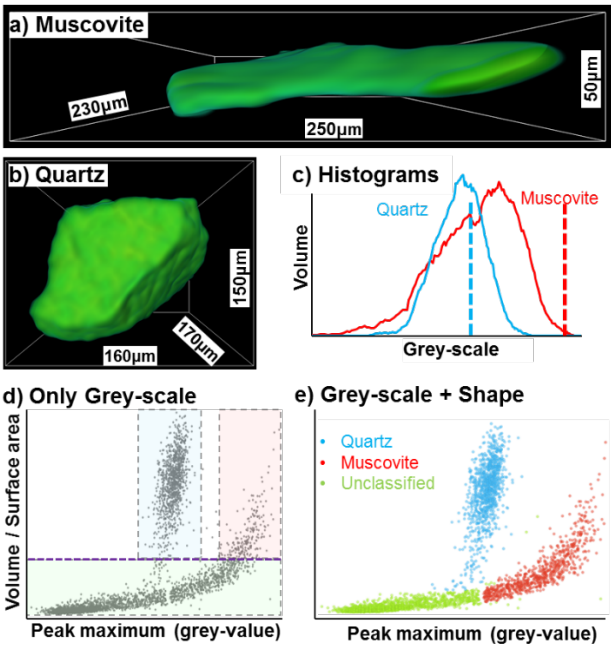

Figure 3. Comparison between particles with different composition and shape. **a)** muscovite particle, and **b)** quartz particle. **c)** histograms of the particles (a) and (b). The dashed lines correspond to the theoretical peak position of the pure phases. **d)** Representation of the variation of the volume to surface area ratio as a function of the maximum peak grey-value for a mixture of particles containing muscovite and quartz, similar to (a) and (b). Blue and red boxes identify the areas within which the particles could be identified as quartz or muscovite based only on the grey-scale; and the purple line marks the expected detection limit. **e)** Same data as (d) but the particles are individually analysed and the classification uses both the peak grey-value and the V/SA of each individual particle.

4 Conclusion

Similar to 2D-based automated quantitative mineralogy methods, the presented workflow includes sample preparation and criteria-based classification. Although in 3D these criteria are based on particle histograms instead of chemical spectra. This poses some limitations to distinguish

mineral phases especially for complex microstructures. Nevertheless, for large grains and for sparsely distributed phases (cases subject to 2D stereological bias), the method shows advantages relative to 2D methods. Additionally, when compared to traditional 3D image processing, the method lowers the size detection limit of grains and increases the contrast resolution.

Altogether, the MSPaCMAn workflow opens the door for standardized 3D characterization with particle-level resolution. The possibility to automate the workflow gives hope to reducing the costs and time for 3D characterization, thus making it more desirable to the raw materials industry. The third dimension can unleash new possibilities in minerals processing and particle technology.

References

Godinho, J.R.A.; Grilo, B.L.D.; Hellmuth, F.; Siddique, A. *Minerals* **2021**, *11*, 947. https://doi.org/10.3390/min11090947

Godinho, J.R.A.; Hassanzadeh, A.; Heinig, T. *Nat Resour Res* **2023,** *32*, 479–499. https://doi.org/10.1007/s11053-023-10169-5

Gotkowski, K.; Gupta, S.; Godinho, J.R.A.; Tochtrop, C.G.S.; Maier-Hein, K.H.; Isensee, F. *arXiv preprint* **2023**. arXiv:2301.13319

How trace elements are incorporated into pyrite, a view from mm- to nano-scale

Daniel D. Gregory[1], Anthony Chappaz[2], Sandra D. Taylor[3], Daniel E. Perea[4], Libor Kovarik[3], and John B. Cliff[4]
[1]Department of Earth Sciences, University of Toronto, Toronto, ON, M5S3B1, Canada
[2]STARLAB, Earth and Atmospheric Sciences, Central Michigan University, MI 48858 USA
[3]Physical and Computational Sciences Directorate, Pacific Northwest National Laboratory, Richland, WA 99354, USA
[4]Earth and Biological Sciences Directorate, Pacific Northwest National Laboratory, Richland, WA 99354, USA

Abstract. Pyrite trace element chemistry is important for understanding evolution of ore fluids in mineralizing systems. Much of the understanding of how metals are held in pyrite is based on micro-scale techniques such as LA-ICPMS and electron microprobe. This requires assumptions to be made when interpreting the results regarding whether elements are held as micro-inclusions versus as substitutions into the pyrite lattice. In this contribution, we use micro- to nano-scale analyses including LA-ICPMS, NanoSIMS, and atom probe tomography (APT) to investigate trace element deportment in pyrite from sites characterized by high trace element concentrations (Black Butte SEDEX deposit) and one characterized by medium to low trace element concentrations (Leicester pyrite member, New York). We further use synchrotron based XANES to investigate the redox state of As and how that relates to trace element enrichment. We find that trace elements are highly heterogeneous at all scales investigated and that interpretation of how trace elements are incorporated into pyrite using even micro-scale techniques must be pursued with caution.

1 Introduction

Pyrite is a common mineral in many different ore deposits and can incorporate several different elements into its structure. As such, pyrite trace element chemistry has received significant interest as a potential vector to mineralization as fluid composition is likely a significant factor in the end trace element chemistry of the pyrite (Belousov et al., 2016). However, several other factors may affect the trace element content of the pyrite including other mineral phases precipitating at the same time as the pyrite, fluid temperature, boiling, wall rock interactions and presence of other elements in the pyrite that may influence incorporation of other trace elements. This latter factor is the subject of this study, specifically the effect that As, and As redox state, has on trace element incorporation into pyrite.

It has been known for some time that As may affect the incorporation of some trace elements into the pyrite lattice and that its redox state can affect which elements are preferentially incorporated. When As^- substitutes for S it has been shown that elements similar to Fe are preferentially incorporated (e.g. Ni and Co) (Reich and Becker, 2006). Alternatively, from a charge balance perspective, if As(+III) substitutes for Fe(+II), then, for every 2 As atoms, there needs to be one cation gap in the pyrite structure to accommodate more large cations like Au(+I) or Pb(+II), leading to their relatively high concentration in the pyrite (Deditius et al., 2008). As can also be incorporated as amorphous Fe-S-As nano-inclusions (Deditius et al., 2009) which would not necessarily increase the incorporation of other elements. However, while it has been shown that these processes may increase the incorporation of various trace elements, and thus affect the partition coefficient of the trace elements into pyrite, it has not been shown that this is the dominant control of pyrite trace element incorporation. In this contribution we use a variety of different techniques applied to samples from two sites (high and medium trace element concentration) to determine the spatial variability of trace elements in pyrite, from the micrometer to nanometer scale, while considering the variation in redox state, to determine whether As content and/or redox state are the dominant controls on trace element concentration in pyrite.

2 Methods

We used a combination of in situ techniques to identify associations of different trace elements with As. These started in larger scale to guide higher chemical sensitivity and spatial resolution composition mapping techniques from identified textures to gain data at progressively finer scales. The first step involved using LA-ICPMS conducted at the University of Tasmania. This utilized a 193 nm ArF excimer ATL Atlex ILR laser coupled to an Agilent 7700 ICP-MS. 35 µm spot sizes were used and point spots were ablated in a pure He atmosphere at 5 Hz. The ablated material was then mixed with Ar to improve efficiency of the aerosol transport. LA-ICPMS maps were also constructed. These analyses utilizing a similar methodology with the spot analyses with the exception that line scans were employed and smaller spot size were used (13 µm); see Gregory et al., (2016) for more details.

Next, representative textures were analyzed with nanoscale secondary ion mass spectrometry (NanoSIMS) composition mapping using a Cameca NanoSIMS 50L housed at the Environmental Molecular Sciences Laboratory (EMSL) at the Pacific Northwest National Laboratory (PNNL) This provided 50 µm x 50 µm maps of the trace and major element abundances of selected textures of the pyrite. Two steps were used to produce the maps. The first maps were produced for negative ions ($^{12}C_2^-$, $^{12}C^{14}N^-$, $^{28}Si^-$, $^{34}S^-$, $^{75}As^-$, $^{78}Se^-$, and $^{80}Se^-$), then the

same area was mapped for positive ions ($^{58}Ni^{+}$, $^{63}Cu^{+}$, $^{66}Zn^{+}$, $^{68}Zn^{+}$, and $^{133}Cs^{+}$). A 2 pA primary beam with a probe diameter of 120-400 nm was used. This provided microscale spatial correlations of different elements with As.

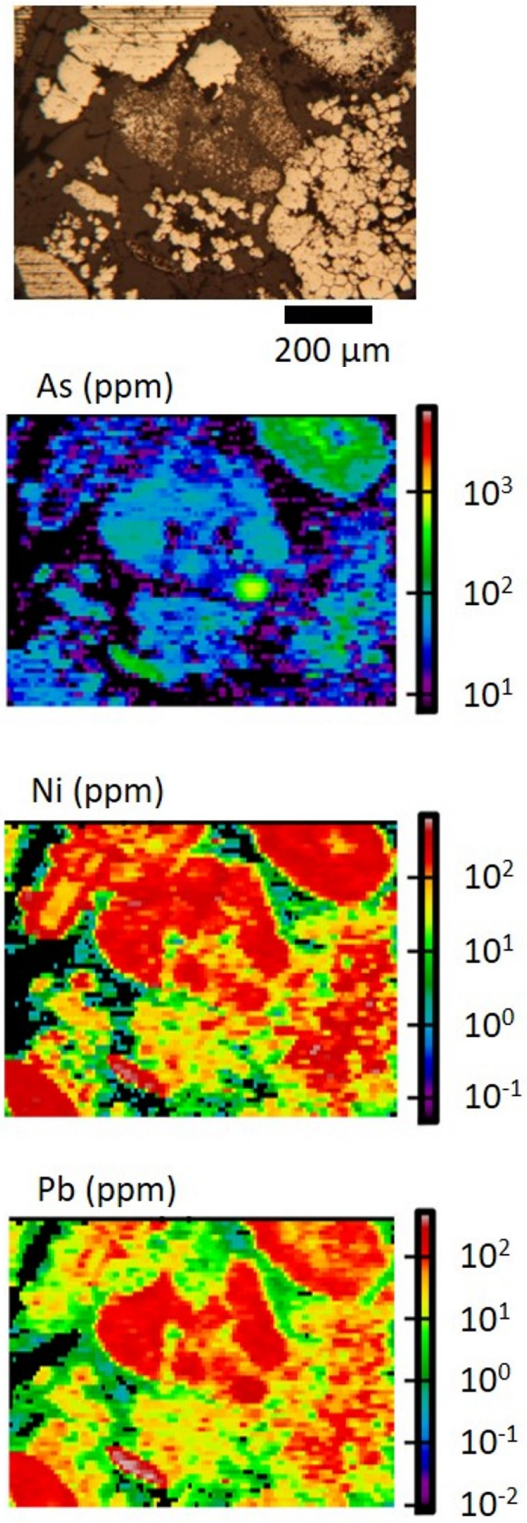

Figure 1. LA-ICPMS trace element maps of one sample from the Leicester pyrite member (low to medium trace element content. Note the variable correlation of the enrichment of the As, Ni, and Pb.

Regions of interest for Atom probe tomography (APT) analysis, were identified using the NanoSIMS data. Micro-sized regions of interest were prepared for APT analyses using a Thermo Fischer Scientific Helios Nanolab 600i focused ion beam (FIB) scanning electron microscope (SEM) which physically lifted it out and shaped the regions of interest into specimens needles. APT analysis was conducted on a CAMECA Local Electrode Atom Probe (LEAP) 4000X-HR in laser-assisted mode utilizing a 355 nm UV laser with an energy per pulse range between 35 and 65 pJ. A laser pulse repetition range of 100-250 kHz was used. A detection rate of 0.002 ions per pulse was maintained by varying the voltage applied to the specimen.

Synchrotron based spectroscopic techniques were applied to determine As speciation for a selection of four samples at the Advanced Photon Source (Argonne National Laboratory). Micro-focused XANES spectra were collected at sector 20. For each sample, 2-3 ROIs were targeted with a beam size of 50 μm^2. As a first step, we produced As elemental maps of 500 μm^2 for each ROIs using µ-XRF. Subsequently, we collected µ-XANES spectra for As at the following K-edge energy: 11,867 eV. At least three spectra per spot were be merged to improve signal to-noise ratio. Spectra were interpreted using four As standards. We processed and analyzed all the data using the Demeter software package.

3 Samples

A high trace element pyrite sample from the Black Butte SEDEX deposit, Montana and a medium to low trace element content pyrite sample from the Leicester Pyrite Member, New York state were chosen to investigate the effects of both the trace element content of the fluids from which the pyrite formed on its end trace element content and how the metals are held within it. The Leicester Pyrite Member is thought to have formed in Devonian-aged sedimentary rocks and later concentrated through re-sedimentation. It provides an example of a low temperature, relatively low trace element formation environment. The sample from the Black Butte SEDEX deposit formed at elevated temperatures (~200-350 °C) and in a relatively high trace element environment.

4 Results

In the laser ablation maps there was clear variation in trace element content in the different textures and parts of the pyrite within the samples (Figure 1). Of particular interest is the variable correlation between the As and other elements. In some regions, there is clear correlation between areas of As and areas of enrichment of Ni and Pb, as well as other trace elements. This is further supported in the NanoSIMS maps that, at a finer scale, show a similar variable enrichment of Se and Ni with no obvious visual

correlation with As (Figure 2). However, other samples show distinct correlation between As and other trace elements. The same observations are made at the nano-scale using atom probe tomography where there is a general association between trace metal enrichments and the presence of As in regions of the pyrite samples. However, this is not always the case as there are also regions where there are element enrichments independent of As.

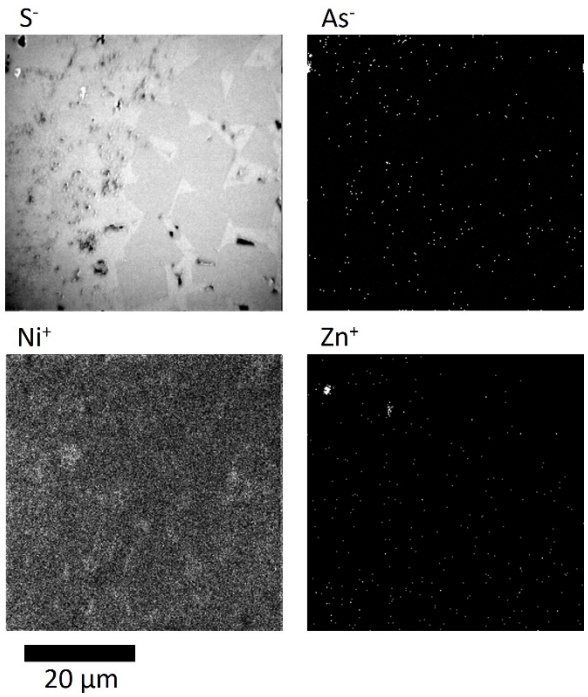

Figure 2. NanoSIMS trace element maps from the Leicester Pyrite Member, note the Zn and Ni enrichments that do not correlate with As enrichments. Modified after Gregory et al., (2019).

The speciation of As is highly variable intra and inter samples. The average As oxidation state ranges from 0.8 to 2.6 for 10 ROIs across four samples (Figure 3).

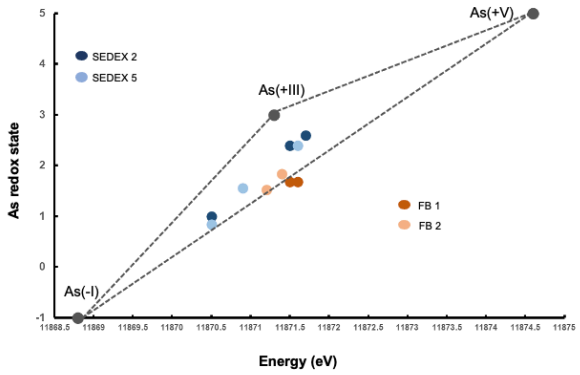

Figure 3. As average oxidation state for 10 ROIs

5 Discussion and Conclusions

The analyses conducted in this study show high variability in pyrite trace element content and As concentration. This suggests that in some cases As may facilitate the enrichment of trace elements in pyrite, such as Cu and Ni, as has been hypothesized. However, at the micro- to nano-scale, this is frequently not the case. Thus, interpretations of the manner and causes for enrichment of trace elements in pyrite must be done with caution as these enrichments can vary significantly across very small distances.

We argue that, general inferences of composition of the formative fluids can sometimes be made by investigating the concentrations of trace elements in pyrite. However, due to the high levels of heterogeneity observed at all scales investigated, attempts to tie specific elements with the uptake of other elements should be done with caution and that a direct calculation of fluid concentration from pyrite concentration is likely to be unachievable.

Acknowledgements

NanoSIMS and APT analyses were performed under a project award (#49860) from the Environmental Molecular Sciences Laboratory, a DOE Office of Science User Facility sponsored by the Biological and Environmental Research program under Contract No. DE-AC05-76RL01830. We also acknowledge the NSERC Discovery Grant to Daniel Gregory.

References

Belousov, I., Large, R., Meffre, S., Danyushevsky, L., Steadman, J., and Beardsmore, T. (2016) Pyrite compositions from VHMS and orogenic Au deposits in the Yilgarn Craton, Western Australia: Implications for gold and copper exploration. Ore Geology Reviews.

Deditius, A. P., Utsunomiya, S., Ewing, R. C., and Kesler, S. E. (2009) Nanoscale “liquid” inclusions of As-Fe-S in arsenian pyrite. American Mineralogist 94: 391-394.

Deditius, A. P., Utsunomiya, S., Renock, D., Ewing, R. C., Ramana, C. V., Becker, U., and Kesler, S. E. (2008) A proposed new type of arsenian pyrite: Composition, nanostructure and geological significance. Geochimica et Cosmochimica Acta 72: 2919-2933.

Gregory, D. D., Large, R. R., Bath, A. B., Steadman, J. A., Wu, S., Danyushevsky, L., Bull, S. W., Holden, P., and Ireland, T. R. (2016) Trace Element Content of Pyrite from the Kapai Slate, St. Ives Gold District, Western Australia. Economic Geology 111: 1297-1320.

Gregory, D., Mukherjee, I., Olson, S. L., Large, R. R., Danyushevsky, L. V., Stepanov, A. S., Avila, J. N., Cliff, J., Ireland, T. R., and Raiswell, R. (2019) The formation mechanisms of sedimentary pyrite nodules determined by trace element and sulfur isotope microanalysis. Geochimica et Cosmochimica Acta 259: 53-68.

Reich, M., and Becker, U. (2006) First-principles calculations of the thermodynamic mixing properties of arsenic incorporation into pyrite and marcasite. Chemical Geology 225: 278-290

Mineralization age of the Kar'ernoe ore occurrence, Polar Urals revealed by the U-Th/He dating of pyrite

Ekaterina Ivanova[1,2], Olga Yakubovich[1,2], Maria Anosova[3], Eugeniya Tuykova[4,5] and Ivan Sobolev[4]
[1]Institute of Earth Sciences, Saint-Petersburg University, Saint-Petersburg, Russia
[2]Institute of Precambrian Geology and Geochronology (IPGG), Russian Academy of Sciences (RAS), Saint-Petersburg, Russia
[3]Vernadsky Institute of Geochemistry and Analytical chemistry (GEOKHI), Russian Academy of Sciences, Moscow, Russia
[4]Institute of Geology of Ore Deposits, Petrography, Mineralogy and Geochemistry (IGEM), Russian Academy of Sciences, Moscow, Russia
[5]Geoinformation Research Centre (NGIC) Russian Academy of Sciences, Moscow, Russia

Abstract. The Kar'ernoe gold ore occurrence is located within the volcanogenic rocks of the Toupugol-Khanmeishor district on the eastern slope of the Polar Urals. The age of mineralization of the volcanogenic rocks was determined by the U-Th/He dating of pyrite. Two events of ore formation are established. The first stage (424±6 Ma (2σ); n=4) is coeval with sedimentation of the volcanogenic rocks. The later stage (400±6 Ma (2σ); n=3) reflects the newly formation/recrystallization of pyrite due to the emplacement of the diorites of the Sob complex. Thus, the Kar'ernoe gold ore occurrence might represent the initial sulfide stages of ore formation in the Toupugol-Khanmeishor ore district.

Introduction

The Toupugol-Khanmeishor ore district is a relatively understudied region in the Polar Urals, which is believed to have a potential for discovering gold deposits (Vikentyev et al. 2017). Regional provenance studies require reconstruction of the ore-magmatic systems of the Paleozoic island-arc system of the Polar Urals. Accurate geochronological data is essential to the developing of such models. Herein we applied a novel approach of U-Th/He dating of pyrite in order to estimate the age of mineralization of the Upper Silurian-Lower Devonian island-arc volcanogenic rocks of the Kar'ernoe ore occurrence and to establish its relation to the known magmatic and tectonic activity in the area.

1 Fundamentals of the U-Th/He dating of pyrite

The U-Th/He system is known to be widely used in the field of low temperature thermochronology (Farley et al. 2002; Flowers et al. 2022). Recent advances in understanding of the He behavior in native metals, pyrite and Fe oxyhydroxide phases made He dating technique suitable for geochronological studies (Shukolyukov et al. 2012; Farley et al. 2018; Yakubovich et al. 2019).

Radiogenic ^{4}He is produced by the alpha-decay of ^{235}U, ^{238}U, ^{232}Th isotopes. Uranium can be present in pyrite in the form of micron-size mineral inclusions (uraninite, apatite, monazite, rutile) and/or as a relatively homogeneous impurity (Baranov 1966). Concentration of U in pyrite in average varies from 0.2 to 11 μg/g (Melekestseva et al. 2014; Yakubovich et al. 2020). Long alpha-stopping distances (11–34 μm) prevent He accumulation within micron-size inclusions of U- and Th-bearing phases, which implies that U-Th/He age corresponds to the age of pyrite formation. High thermal retentivity of radiogenic He in pyrite is confirmed by step-heating experiments (Yakubovich et al. 2019) and by the results of pyrite dating from the slightly metamorphized VMS type Uzelga deposit, South Urals (Yakubovich et al. 2020).

2 Object of study

2.1 Geological setting

The Toupugol-Khanmeishor gold ore region is located in the northern part of the Voikar zone, which belong to the Polar-Ural island-arc system (Fig.1). The northwestern part of the Voikar zone is mainly composed of Late Ordovician oceanic formations of the ophiolite association and borders along the Main Ural Fault with the Paleozoic-Late Proterozoic formations of the West Ural megazone. The southeastern part of the zone is dominated by Late Ordovician-Middle Devonian island-arc rocks of the Malouralsk volcanoplutonic belt, overlain by a thick Mesozoic-Cenozoic sedimentary cover of the West Siberian Plate (Volchkov et al. 2008).

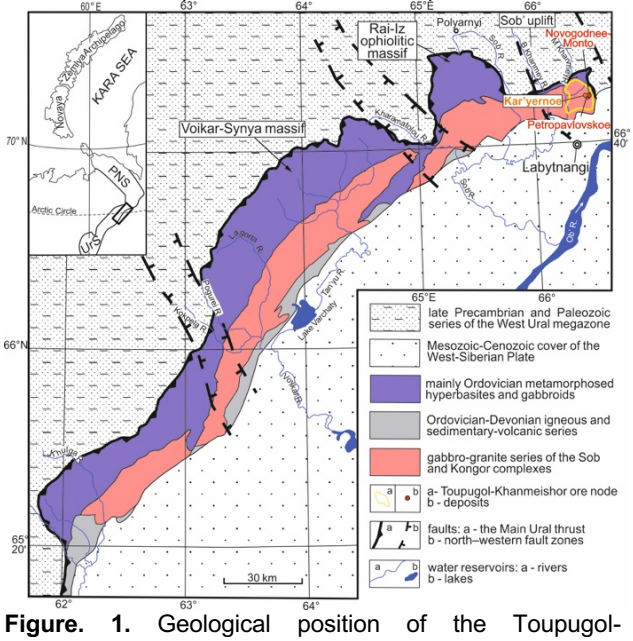

Figure. 1. Geological position of the Toupugol-Khanmeishor ore district in the structures of the Polar Urals using data from (Yazeva et al. 1984; Sobolev et al. 2017)

Two gold ore deposits are known in that area: gold-iron-skarn Novogodnee-Monto (7 t Au), and gold-porphyry Petropavlovskoe (26 t Au) deposits (Vikentyev et al. 2017).

The Kar'ernoe ore occurrence is located in a flank of the Novogodnensky ore field in 2 km southwest of the Novogodnee-Monto gold deposit. Estimated resources of the Kar'ernoe ore occurrence is 5 tons of Au (P_2 category; Volchkov et al. 2008). Mineralization is host by Upper Silurian-Lower Devonian volcanic-sedimentary (flyschoids, polymictic breccias with fragments of volcanic, intrusive and carbonate rocks) and volcanic rocks of the Tupugolskaya formation. Early-Middle Devonian diorite porphyrites and quartz diorites of the Sob complex, as well as Early Carboniferous dykes of dolerites, lamprophyres, and monzodiorite-porphyries of the Musyur complex cut these volcanic-sedimentary rocks (Volchkov et al. 2008). Intense shearing, cataclasis, brecciation, limited by the Tupugolsky and Eviegansky faults, are developed within the deposit. Interlayers of fine clastic carbonate rocks host layered sulfide and pyrite mineralization.

2.2 Sample description

A sample 14/32 of medium-fine clastic crystal-clastic ore, with abundant dissemination and layered dissemination of pyrite, was collected from the Kar'ernoe ore district (Fig. 2,3; 66°48'12"N, 66°26'05"E). The wavy-layered texture forms a successive alternation of tuffs and tuffites. The tuffaceous layers are grouped into gradation series with a gradual decrease in the dimension of the pyroclastic material up the section. The ore mineral is mainly distributed in the form of scattered small cubic sections (0.005×0.005 mm) and their intergrowths; larger crystals (up to 0.4×0.4 mm) are less common. Pyrite forms lenticular segregations, reaching a size of 0.04×0.4 mm, and clusters of 0.12×0.2 mm. Veinlets of quartz-carbonate (up to 1.8 mm) and carbonate compositions (up to 0.08 mm) cut the rocks.

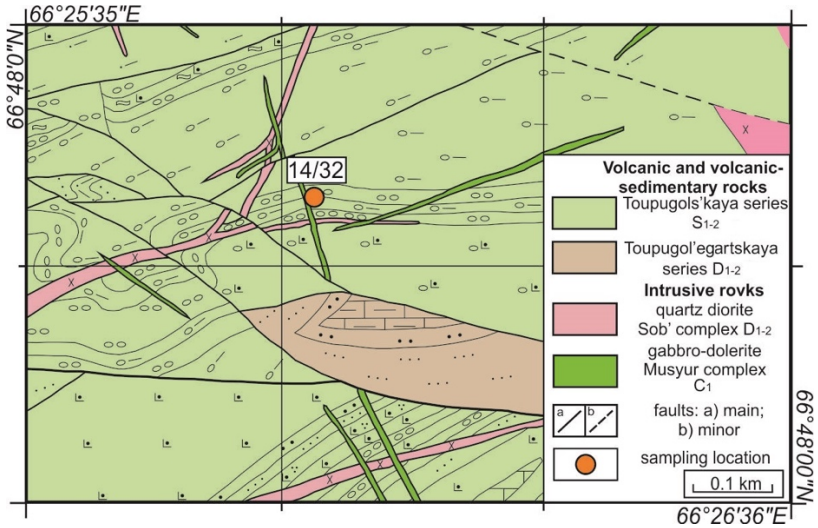

Figure 2. Geological scheme of the Kar'ernoe ore occurrence and sampling location, using data of Pryamonosov (2004).

3 Methodology

Pyrite grains were isolated from the rock sample 14/32 (Fig.2) by the separation in heavy liquids technique at the IGEM RAS (Moscow). Individual grains with sizes > 200 μm without visible inclusions (stereo microscope with an × 5 magnification) were selected for U-Th/He dating and electron microscopy study. Microanalyses of pyrite was done from the polished sections using a Hitachi S-3400N scanning electron microscope equipped with an AzTec Energy 350 X-ray spectral analysis detector at the Geomodel Resource Center of St. Petersburg State University (St. Petersburg).

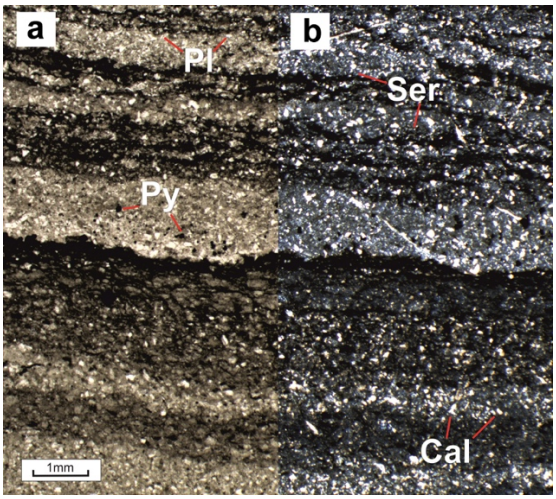

Figure. 3. Petrographic features of tuffites of the Kar'ernoe ore occurrence in thin section of sample 14/32: a) under plane polarized light; b) under crossed nicol. Cal-calcite; Pl-plagioclase; Py-pyrite; Ser-sericite.

3.1 Helium measurements

For each measurement 4–5 pyrite grains were combined in a joint sample with mass of 1.5–2.5 mg and placed in a quartz ampoule. Prior the He measurement the ampoule was sealed under forevacuum conditions (10^{-3} Torr). The gas content of radiogenic He was measured on a highly sensitive mass spectrometer MSU-G-01-M at the IPPG RAS (St. Petersburg) following the procedure described in Yakubovich et al., 2021.

3.2 Uranium and Th measurements

Mass fractions of U and Th were obtained by the isotopic dilution method. Degassed quartz ampoule was spiked with ^{230}Th-^{235}U tracer and dissolved in a mixture of acids (aqua regia (0.4 ml), HF conc (0.5 ml) and $HClO_4$ (0.05 ml)) in closed teflon vials at a temperature of 180°C within 24 hours. The $^{235}U/^{238}U$ and $^{230}Th/^{232}Th$ isotopic ratios were measured using the ELEMENT XR ICP MS at the GEOKHI RAS (Moscow). The accuracy of the analytical procedure was monitored by the parallel measurements of the Durango apatite, which is an international U-Th/He standard. Empty quartz ampoules were used in order to determine the He, U and Th blank of the measurements.

3.3 U-Th/He age calculation

U-Th/He ages were calculated using the IsoplotR software (Vermeesch 2018). Given the relatively large size of the analyzed grains alpha-recoil corrections were not applied.

4. Results

4.1 Electron microscopy

Pyrite grains from the sample 14/32 has a zonal distribution of arsenic impurities, which can reach mass fraction of up to 3 wt. % (Fig. 5). Most common mineral inclusion are galena and chalcopyrite. Less often pyrrhotite, sphalerite, and arsenopyrite were observed. Among U- and Th- bearing phases small (less than 10 μm) precipitates of titanite, rutile, rarely apatite, were established.

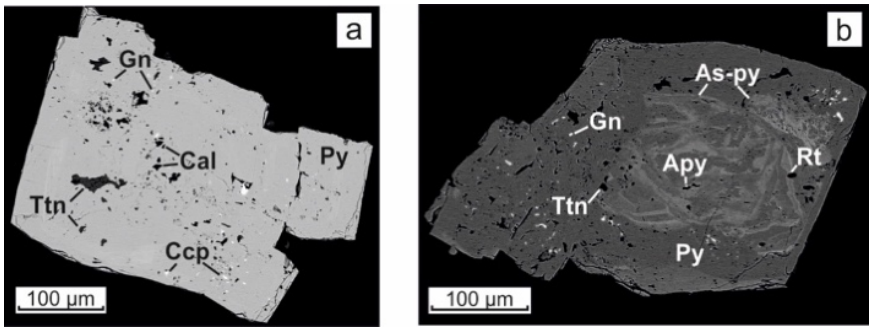

Figure 5. BSE images of pyrite from the Kar'ernoe ore occurrence: a) mineral inclusions in a pyrite crystal; b) zonal distribution of arsenic in pyrite. Apy – arsenopyrite; As-Py – arsenic pyrite; Cal – calcite; Ccp – chalcopyrite; Gn – galena; Py – pyrite; Rt – rutile; Ttn – titanite.

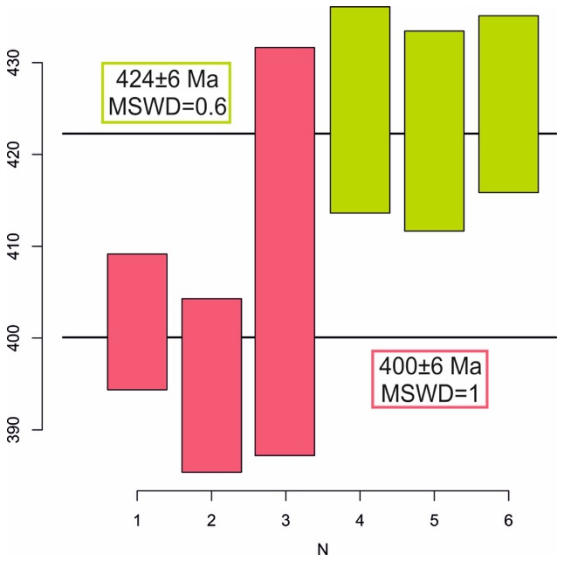

Figure 6. Weighted mean plot for pyrite from the Kar'ernoe ore occurrence, constructed in the IsoplotR software ver 5.2.

4.2 Dating results

In total six subsamples of pyrite from the sample 14/32 were dated. The He concentration is in a range of 9.40–3.27 10^{-8} cm^3/g, which is significantly higher than the concentration of trapped He (Yakubovich et al. 2019). The U mass fraction varies from 0.54 to 1.68 μg/g (Th/U ratio = 0.45-0.48). Four pyrite subsamples have shown age values that overlap within 95% level of confidence (Fig. 6) with weighted mean age of 424±6 Ma (2σ). Three subsamples overlap within 95% level of confidence and have weighted mean age of 400±6 Ma (2σ).

5. Discussion

The U-Th/He age of pyrite from the volcanogenic rocks of the Kar'ernoe ore occurrence, calculated for six subsamples, corresponds to the Late Silurian. U-Th/He ages show relatively large dispersion which might reflect several mineralization events. The age of 424±6 Ma (2σ) is coeval with the sedimentation age of the Toupugolskaya formation which is established as late wenlock – ludlow (biostratigraphy; Zyleva et al. 2014). Younger age of

400±6 Ma (2σ) might reflect pyrite formation/recrystallization due to the emplacement of plagiogranites of the late phase of the Sob complex (403±4 Ma; zircon U-Pb; Sobolev et al. 2018). Rocks of the Sob complex are developed within first tens of meters from the sampling location (Fig. 2). The interpretation of data is complicated by the fact that several grains were used to determine the age of subsample. The clusterisation of the U-Th/He ages requires us to propose higher U content in the one of the generations which allows to hide U-Th/He signal of the another one. Additional measurements of the single grains of pyrite are required in order to confirm that suggestion.

U-Th/He age of the pyrite from the Kar'ernoe ore occurrence (400–424 Ma) is remarkable older than U-Th/He age of pyrite from the Novogodnee Monto deposit (382±8 Ma; Yakubovich et al., 2021). Thus, despite its belonging to the the Novogodnensky ore field, Kar'ernoe ore occurrence represents initial stages of sulfide mineralization within the Toupugol-Khanmeishor gold ore region.

6. Conclusion

U-Th/He dating results of six subsamples of pyrite from the Kar'ernoe ore occurrence (400–424 Ma) indicates mineralization were formed at the initial stages of ore formation in the Toupugol-Khanmeishor ore cluster.

Funding

This research was supported by the RSF (project 22-77-10088).

References

Baranov, E.N. and Vertepov, G.I. (1966) Concentration of Uranium in Sulphides as an Indicator of Possible Uranium Deposit; At. Energy, v. 20, p. 170–171.

Farley, K.A. (2002) (U-Th)/He Dating: Techniques, Calibrations and Applications. Rev. Mineral. Geochem, v. 47, p. 819–843.

Farley, K.A. (2018) Helium diffusion parameters of hematite from a single-diffusion-domain crystal; Geochimica at Cosmochimica Acta, v. 231, p. 117–129.

Flowers, R.M.; Zeitler, P.K.; Danišík, M.; Reiners, P.W.; Gautheron, C.; Ketcham, R.A.; Metcalf J.R.; Stockli D.F.; Enkelmann E.; Brown R.W. (2022) (U-Th)/He Chronology: Part 1. Data, Uncertainty, and Reporting; GSA Bulletin, p. 1–33.

Volchkov, A.; Girfanov, M.; Kryazhev, S.; Andreev, A.; Cheremsin, A.; Mansurov, R. (2008) The Position of Gold Mineralization of the Toupugol-Khanmeyshor Ore Area in Ore-Containing Complexes, Their Mineral and Geochemical Characteristics and Comparison with the Reference Objects of the Novogodnee-Monto Mineralized Area; unpublished report, Moscow, Russia.

Zyleva L.I., Konovalov, A.L, Kazak, A.P., et al. (2014) Gosudarstvennaya geologicheskaya karta Rossiiskoi Federatsii. Masshtab 1:1000000 (3-e pokol.). Ser. Zap.-Sibirskaya. List Q-42, Salekhard; Ob. Zap. (State Geologica Map of the Russian Federation on a Scale 1 : 1000000 (3rd Generation). West Siberian Series. Sheet Q-42, Salekhard, Explanatory Note), SPb.: Kart. fabr. VSEGEI.

Melekestseva, I.Y.; Tret'yakov, G.A.; Nimis, P. et al. (2014) Barite-rich massive sulfides from the Semenov-1 hydrothermal field (Mid-Atlantic Ridge, 13°30.87′ N): evidence for phase separation and magmatic input; Marine Geology, v. 349, p. 37–54.

Shukolyukov, Y.A.; Yakubovich, O.V.; Mochalov, A.G.; Kotov, A.B.; Sal'nikova, E.B.; Yakovleva, S.Z.; Korneev, S.I.; Gorokhovskii, B.M. (2012) New Geochronometer for the Direct Isotopic Dating of Native Platinum Minerals (^{190}Pt-^{4}He Method); Petrology, v. 20, p. 491–505.

Sobolev, I.D.; Soboleva, A.A.; Udoratina, O.V.; Kaneva T.A.; Kulikova K.V.; Vikentiev I.V.; Khubanov V.B.; Buyantuev M.D.; Hourigan J.K. (2017) First Results of U-Pb (LA-ICP-MS) Dating of Detrital Zircons from Paleozoic Island Arc Clastic Rocks of Polar Urals; Bull. Moscow Soc. Nat. Geol. Ser., v. 92, p. 3–26.

Sobolev, I.D.; Vikentyev, I.V.; Soboleva, A.; Travin, A.V. (2018) Results of U/Pb SIMS Dating of Zircons and 39Ar/40Ar Age of Plagioclase from Rocks of the Sob Complex (Petropavlovsk Gold Deposit, Polar Urals); in Proc. Conf. Methods and Geological Results of Studying Isotopic Geochronometric Systems of Minerals and Rocks, IGEM RAS: Moscow, Russia, p. 398–401.

Yakubovich, O.V., Vikentyev, I.V., Bryanskiy, N.V., Zarubina, O.V., Gorokhovskii, B.M. (2019) Dating pyrite by radiogenic helium: new approach to determine the age of hydrothermal processes; Life with Ore Deposits on Earth – 15th SGA Biennial Meeting 2019 Proceedings, Glasgow, v. 1, p. 194–197.

Yakubovich, O.V.; Vikentyev, I.V.; Zarubina, O.V.; Bryanskiy, N.V.; Gorokhovskii, B.M. (2019) U–Th–He Dating of Pyrite from the Uzelga Copper-Zinc Massive Sulfide Deposit (South Urals, Russia): First Application of a New Geochronometer; Dokl. Earth Sci, v. 485, p. 368–371.

Yakubovich, O.; Podolskaya, M.; Vikentyev, I.; Fokina, E.; Kotov, A. (2020) U-Th-He Geochronology of Pyrite from the Uzelga VMS Deposit (South Urals) – New Perspectives for Direct Dating of the Ore-Forming Processes; Minerals, v. 10, 629.

Yakubovich O., Vikentyev I., Ivanova E., Podolskaya M., Sobolev I., Tyukova E., Kotov A. (2021) U-Th-He Geochronology of Pyrite from Alteration of the Au-Fe-Skarn Novogodnee-Monto Deposit (Polar Urals, Russia) — The Next Step in the Development of a New Approach for Direct Dating of Ore-Forming Processes. Geosciences, v. 11, 408.

Yazeva, R.G. and Bochkarev, V.V. (1984) Voikar Volcanoplutonic Belt, Polar Urals; Uralian Sci. Center, USSR Acad. Sci., Sverdlovsk, Ukraine.

Vermeesch P. (2018) Isoplot R: A free and open toolbox for geochronology; Geoscience Frontiers, v. 9 (5), p. 1479–1493.

Vikentyev, I.V.; Mansurov, R.K.; Ivanova, Y.N.; Tyukova, E.E.; Sobolev, I.D.; Abramova, V.D.; Vykhristenko, R.I.; Trofimov, A.P.; Khubanov, V.B.; Groznova, E.O.; et al. (2017) Porphyry-Style Petropavlovskoe Gold Deposit, the Polar Urals: Geological Position, Mineralogy, and Formation Conditions; Geol. Ore Depos, v. 59, p. 482–520.

Hyperspectral mineral mapping on exploration core from the Au-rich from LaRonde Penna VMS deposit, Quebec, Canada in the shortwave infrared

Friederike Körting [1], Julio Hernandez [1], Pesal Koirala [1], Miranda Lehman [2], Thomas Monecke [2], David Lindblom [3], Oskar Jonsson [3] , Constantin Hildebrand [1]
[1]Norsk Elektro Optikk AS, Hyspex, www.hyspex.com
[2]Center to Advance the Science of Exploration to Reclamation in Mining, Department of Geology and Geological Engineering, Colorado School of Mines, https://caserm.mines.edu/
[3]Prediktera AB, www.prediktera.com

Abstract. Utilizing HySpex cameras covering the spectral range between 930 and 2500 nm, full core boxes from the LaRonde Penna deposit can be scanned within seconds. Using the newly developed Prediktera's Breeze GEO software, real-time mineral mapping is achieved. This includes an expert-system-based analysis using the publicly available USGS Material Identification and Classification Algorithm for mineral identification, a feature modelling via minimum wavelength mapping , and a comparison-based approach via the spectral angle mapper. Drill cores from the LaRonde Penna deposit are being scanned and interpreted. The deposit is located within the Archean Abitibi greenstone belt of Ontario and Quebec, Canada, which is home to numerous volcanogenic massive sulphide (VMS) deposits. LaRonde Penna contains an endowment of 71 Mt of ore grading on average 3.9 g/t Au and economic grades of Zn, Cu and Pd. Scanning cores hyperspectrally for this well-studied deposit opens up a unique opportunity for research and development. The HySpex system's mineral mapping capabilities are presented in close cooperation with renowned academic and industrial partners through the Center to Advance the Science of Exploration to Reclamation in Mining led by the Colorado School of Mines and Virginia Tech.

1 Introduction

Society's mineral demand is driven by the ongoing green energy transition and is expected to increase substantially in the next decades. This requires the identification of new mineral resources, which typically involves drilling of the subsurface. The amount of drilling performed per project depends on geological characteristics of the deposit under investigation such as the shape and sizes of the mineralized zones and associated alteration halos. Drill core is typically logged visually, which involves documentation of key parameters such as lithology, mineral assemblages, and the location and orientation of structures. The visual logging is often supplemented by sub-sampling for geochemical or mineralogical analysis. Sample analysis is destructive, expensive and time-consuming. Hyperspectral imagery (HSI) offers a fast, replicable, non-destructive method for logging drill core mineralogically(Bedini 2017; Krupnik and Khan 2019; Rajan Girija and Mayappan 2019).

2 The developed hardware and software solution

HSI imagery is used to identify areas of significance and visualize mineral-spectral changes downhole. To the best of our knowledge, all commercial solutions operate as offline, post-acquisition data analysis services using data processing and modelling algorithms customized for a specific exploration site. This limits the usability and access to the data beyond the initial requirements of the end user. An upgrade of the models or reprocessing of the data is often only possible at an additional cost. For research activities, this presents a limit as samples from a variety of sites or different campaigns are often necessary and need to be analysed flexibly. Identifying this need, the hyperspectral hardware developer HySpex and the software provider Prediktera developed a high-resolution, hyperspectral core imager to allow self-determination of data analysis for research projects. The system incorporates Prediktera's Breeze GEO software to offer seamless data acquisition, flexible modelling capabilities, user adjustment and real-time mineral analysis capabilities. The main aim of this development is to make the user fully independent to carry out their own data analysis.

The integrated solution for hyperspectral drill core imaging is being developed in close cooperation with academic and industrial partners through the Center to Advance the Science of Exploration to Reclamation in Mining (CASERM). CASERM is a collaborative research centre for geoscience data use in the mining industry lead by Colorado School of Mines and Virginia Tech. CASERM members actively research approaches to bridge the different scales in geoscientific research and aim to provide tangible research answers for the industry to provide "Mineralogy Across Scales".

As an example of the capabilities of the instrumentation, methods and analysis tools, an exploration drill hole from the LaRonde Penna volcanogenic massive sulphide (VMS) deposit was scanned and analysed. This drill hole displays the important alteration mineral assemblages surrounding the ore zone. LaRonde Penna is the largest gold-rich VMS deposits in the world and is

located within the southern portion of the Archean Abitibi greenstone belt of Ontario and Quebec, Canada.

3 Datasets

Endmember minerals of interest for this deposit were defined by a SEM-based thin section analysis at the Colorado School of Mines via the TESCAN Integrated Mineral Analyzer (TIMA) software. The core contains significant portions of plagioclase, amphibole, andalusite/kyanite, biotite, calcite, chlorite, clinozoisite, epidote, garnet, margarite, muscovite, quartz, staurolite, tourmaline as well as different sulphide mineralss (pyrite, sphalerite and chalcopyrite). Not the entirety of these minerals can be mapped in the SWIR spectral range. Figure 1 shows the plot of the spectrally active minerals for this study, the VNIR-SWIR reference spectra were obtained from the USGS spectral library version 7 (Kokaly et al. 2017).

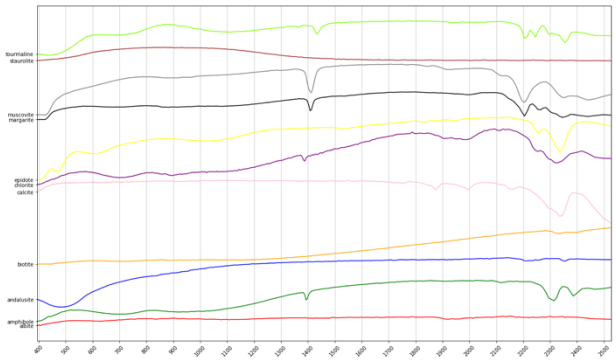

Figure 1. VNIR and SWIR spectra relevant to the LaRonde-Penna deposit from USGS spectral library version 7. X-axis shows the wavelength range from 400 – 2500 nm. The minerals plotted from top to bottom are tourmaline (light green), staurolite (maroon), muscovite (grey), margarite (black), epidote (yellow), chlorite (purple), calcite (pink), biotite (orange), andalusite (blue), amphibole (dark green) and albite (red).

Forty-nine core boxes from the LaRonde Penna deposits were scanned hyperspectrally, using the HySpex SWIR384 camera (specification see table 1) from diamond drill hole 3125-162A at a depth of 1135.6 to 1265.0 meters. Core depth logging was achieved within breeze GEO by manually logging the start and end depth of each box and adjusting the depth for eventual core loss. An example of the false-colour SWIR-RGB of core box #28 is given in Figure 2.

Table 1. HySpex SWIR384 main specifications.

SWIR 384	
Spectral range	930-2500 nm
Spatial pixels	384
Spectral channels	288
Spectral sampling	5.45 nm
FOV	16°
Linear field of view (FOV) for 1 m lens	294 mm
Pixel size on scene across/along	0.77/ 0.77 mm
Bit resolution	16 bit
Noise floor	150 e-
Dynamic range	7500
Peak SNR (at full resolution)	> 1100
Max speed (at full resolution)	400 fps
Camera interface	CameraLink

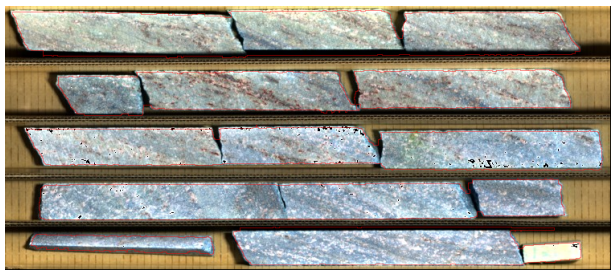

Figure 2. False-colour RGB image of a representative core box (R: 1225 nm, G: 1660 nm, B: 2150 nm).

4 Mineral and spectral anomaly classification in the SWIR

Near-real time classification of the core is achieved using the USGS Material Identification and Classification Algorithm (MICA; Kokaly 2011) and a feature modelling approach referred to as minimum wavelength modelling (MWL; van Ruitenbeek and van der Meer 2014; van der Meer et al. 2018; Hecker et al. 2019).

The prediction of USGS MICA and MWL takes about 6 min in Breeze GEO for the 49 core boxes measured (130 m of core). The SWIR file size for each core box is ~300 MB, with a total file size of ca. 13.5 GB. USGS MICA mapping is carried out via a publicly available MICA Command File (mcf) named “mica_cmds_2micron_usgshyspex_vswir3177_v4a_mtnpass” containing 91 materials described in the expert system. The pixel count is carried out for different, user-defined mapped minerals. MWL was performed between 2100 and 2450 nm. Different mineral feature products are explored that are commonly used and found in commercial HSI analyses tool and a staple for HSI mineral exploration (e.g., white mica chemistry, MgOH, Al/clay, $Fe^{2+}OH$). Simple spectral indices are explored on this dataset as well. The USGS MICA classification is shown in Figure 3.

The MWL modelling of the deepest feature in the chosen wavelength range (2100-2450 nm) highlights spectral changes in the core but is less straightforward to interpret than per-pixel mineral

maps. Figure 4 shows a representative core box in which a change from blue colours (2205 nm) to yellow (2330 nm) to green (2248 nm) occurs from top to bottom.

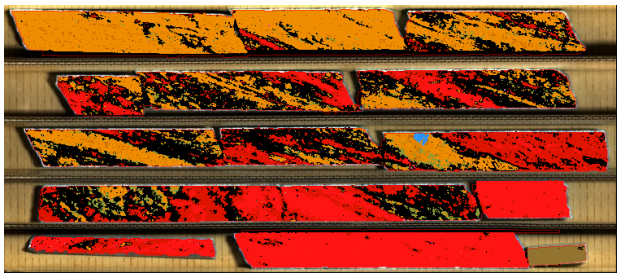

Figure 3. USGS MICA classification of a representative core box. Red colours indicate presence of epidote/chlorite, orange colours indicate presence of white micas. Green colours indicate serpentine mineral mixtures and blue colours indicate kaolinite-clay mixtures.

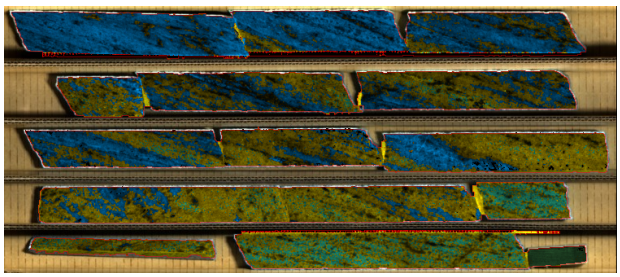

Figure 4. MWL mapping of a representative core box. Colour coding shows the wavelength position of the deepest mapped feature. Blue colours (2205 nm) to yellow (2330 nm) to green (2248 nm) is visible throughout the box indicating a gradual change with depth. Colour brightness indicates the depth of the feature, where brighter colours show deeper features.

5 Results

General trends in the white mica occurrence plot are visible in the USGS MICA analysis. The average white mica pixel counts were plotted for all 49 core boxes in Table 2. This average represents the pixel area classified as white mica in each box rather than the absolute percentages. It highlights the changes in white mica occurrence depth and shows changes that can be investigated further. Main rock-forming minerals cannot be classified (e.g., feldspars and quartz) in the SWIR. Bulk geochemistry or mineralogical analyses of the core via validation measurements have not been available for the example core but XRF-based geochemistry can be imported into breeze GEO to support the HSI-based mineralogy in user-defined segments. Mineral abundance determined in Breeze GEO will be further validated for the LaRonde Penna drill core in cooperation with CASERM.

Table 2. White mica pixel count [%] for a total of 49 core boxes from LaRonde-Penna. The USGS MICA analysis was used.

Box	Depth [m]	USGS all white mica [%]	USGS all white mica
1	1135.6	22.78	
2	1137.8	8.46	
3	1140.4	13.64	
4	1142.9	1.93	
5	1145.2	0.91	
6	1147.5	11.17	
7	1154.3	58.10	
8	1157.3	49.70	
9	1159.4	19.00	
10	1161.8	1.74	
11	1164.5	3.63	
12	1167.1	0.10	
13	1169.5	1.40	
14	1172.0	10.80	
15	1174.4	1.10	
16	1177.1	2.21	
17	1179.5	3.19	
18	1182.2	0.01	
19	1184.4	0.01	
20	1187.8	15.54	
21	1190.8	49.59	
22	1193.8	89.95	
23	1196.4	90.33	
24	1199.2	92.76	
25	1201.8	90.36	
26	1204.2	90.30	
27	1207.6	69.58	
28	1209.5	23.75	
29	1212.0	0.68	
30	1214.6	14.26	
31	1217.0	44.70	
32	1219.7	71.46	
33	1222.5	79.22	
34	1226.0	87.70	
35	1229.1	89.30	
36	1231.9	92.28	
37	1234.6	90.27	
38	1237.0	89.39	
39	1239.8	83.88	
40	1242.3	70.90	
41	1245.0	69.38	
42	1247.8	44.29	
43	1250.6	13.52	
44	1253.2	4.63	
45	1256.0	45.15	
46	1258.7	44.78	
47	1260.7	46.99	
48	1262.6	33.60	
49	1265.0	18.79	

In the USGS MICA analysis, epidote and chlorite are mapped frequently along the core, color-coded as red (Figure 5). The distinct absorption features for these minerals are as follows (the deepest features are marked with an asterisk): Epidote has distinct absorptions at 2255 nm and 2335* nm, chlorite has absorption features around 2245 nm, 2328* nm and 2386 nm. Muscovite exhibits

absorption features around 2205* nm and 2345 nm (Krupnik and Khan 2019).

The plot of chlorite (clinochlore and thuringite) against epidote shows the similarity of both spectra in the SWIR wavelength range (2100 nm and onwards; Figure 5). This complicates a clear distinction between these phases. The classification of chlorite in areas also indicate the potential presence of epidote and vice-versa and the two mineral groups cannot be distinguished well from each other.

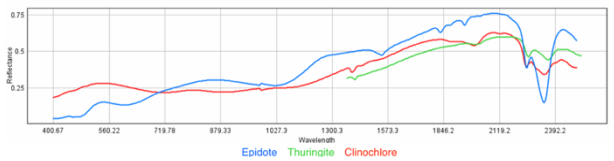

Figure 5. Spectral plot of chlorite vs. epidote. Spectra plotted within Breeze GEO. The color-coding of the spectra is different to the colours used in the USGS MICA classification. Minerals include epidote (blue), thuringite (green) and clinochlore (red).

6 Conclusions

The results presented in this paper show promising advancements in the development of both hardware and software for core scanning that enables the user to take matters into their own hands with minimum time spent on setting up hyperspectral imaging data acquisition and analysis routines. The visualization of the workflow with a plug-and-play approach allows for an automated approach to core segmentation, analysis and adjustments in each. The HySpex laboratory acquisition setup provided sufficiently high turnover rates of 300 meters a day in the controlled environment of the Core Scanning Lab facility at Colorado School of Mines but future hardware developments will focus on a more modular design, wider belt enabling to scan two boxes simultaneously and a wider field of view of the VNIR-SWIR cameras. A casing will protect the cameras from stray light, dust and other influencing factors and allow a more versatile hardware setup adaptable to different types of facilities and environments. The Breeze GEO software allows for a new level of interactivity with the data and enables a user-led setup of workflows including standard and expert-based classification routines. Near-real-time correction and classification and the possibility of adjustment of workflows following on-site interpretation of the data enable the user to adjust data analysis and interpretation based on new information from research.

Acknowledgements

This study was achieved in close collaboration with the Center to Advance the Science of Exploration to Reclamation in Mining, which is an industry-university collaborative research centre between Colorado School of Mines and Virginia Tech under NSF award numbers 1822108 and 1822146. Drill core from the LaRonde Penna deposit was made available by Agnico Eagle. We thank Patrick Mercier-Langevin from the Geological Survey of Canada for in-depth discussions on the geology of the LaRonde Penna deposit and the implications of this study. Raymond Kokaly and Todd Hoefen from the USGS as well as Katharina Pfaff from Colorado School of Mines are acknowledged for providing insights into hyperspectral data interpretation. The USGS PRISM MICA algorithms were implemented into Breeze GEO. This would not have been possible without obtaining the code and detailed documentation.

References

Bedini E (2017) The use of hyperspectral remote sensing for mineral exploration: A review, JHRS 7:189–211

Hecker C, van Ruitenbeek FJA, van der Werff HMA, Bakker WH, Hewson RD, van der Meer FD., (2019) Spectral absorption feature analysis for finding ore: A Tutorial on using the method in geological remote sensing, IEEE Geosci Remote Sens Mag 7:51–71

Kokaly R F (2011), PRISM: Processing Routines in IDL for Spectroscopic Measurements (Installation Manual and User's Guide, Version 1.0)

Kokaly RF, Clark RN, Swayze GA, Livo KE, Hoefen TM, Pearson NC., Wise RA, Benzel WM, Lowers HA, Driscoll RL, Klein AJ (2017) USGS Spectral Library Version 7"

Krupnik, D, and Khan, S, (2019) Close-range, ground-based hyperspectral imaging for mining applications at various scales: Review and case studies. Earth Science Review 198: 102952

Rajan Girija R, Mayappan S (2019) Mapping of mineral resources and lithological units: a review of remote sensing techniques. Int J Image Data Fusion **10:**79–106

Van der Meer F, Kopačková V, Koucká L, van der Werff HMA, van Ruitenbeek FJA, Bakker WH (2018) Wavelength feature mapping as a proxy to mineral chemistry for investigating geologic systems: An example from the Rodalquilar epithermal system. Int J Appl Earth Obs Geoinf 64:237–248

van Ruitenbeek FJA, Bakker WH, van der Werff HMA, Zegers TE, Oosthoek JHP, Omer ZA, Marsh SH, van der Meer FD (2014) Mapping the wavelength position of deepest absorption features to explore mineral diversity in hyperspectral images. Planet Space Sci 101**:**108–117

Characterisation of apatite-bearing magnetite ore in drillcores using µ-XRF

Carolina Månbro[1], Joanna Kolodziejczyk[2], Patrick Krolop[2], Eva Öberg[2], Mehdi Parian[1],
[1]Mineral and Metallurgical Engineering, Luleå University of Technology, Luleå, Sweden
[2]Process and Product Development, LKAB, Malmberget and Kiruna, Sweden

Abstract. The convention of using bulk chemical assays by XRF in determination of the grade of a deposit provides a somewhat erratic result since the element/s of interest often occur in more than just the target mineral/s. By analysing the chemical composition of individual mineral crystals in exploration drillcores a clearer picture of the deposit can be attained since it visualizes the distribution of elements in minerals. Furthermore, by investigating individual minerals the possibility of finding additional mineral/s of interest increases and the extraction process can be adapted to process all minerals of interest to get the best possible recovery.

1 Introduction

Northern Sweden is the type locality for iron oxide-apatite (IOA) deposits, commonly referred to as "Kiruna type" based on the special character of the ores (Geijer 1931, Martinsson et al. 2016).

To date, the apatite from these ores have been regarded waste since the demand for apatite/ phosphor has been too low for an economically viable extraction. However, the increased demand for mineral fertilisers in combination with the low cadmium content of the apatite in Swedish IOA (Håkansson et al. 2023) have caused extraction of phosphor from apatite to be more eligible. Furthermore, the apatite in Swedish iron oxide deposits hosts rare earth elements (REE) classified as critical raw materials (CRM) needed for the green transition (Blengini et al. 2020). Thus, apatite concentrate from Swedish iron oxide deposits can offer an intra-European production of materials that are now mainly imported from outside of the EU, making the supply chain less vulnerable to global events and politics.

Analysing samples using traditional X-ray fluorescence (XRF) for chemical assays is a good method if a bulk composition is sought. However, the recent decades have seen a rapid development of laboratory scale micro-X-ray fluorescence (µ-XRF). Thus, analyses that were previously only possible in synchrotron facilities are now possible to perform in benchtop µ-XRF instruments, making the technology more accessible (Flude et al. 2017). Elemental and mineralogical analysis by µ-XRF is a more detailed analytical method compared to XRF and provides spatial distribution of elements in the sample. The elemental information can further be converted to mineral maps using an automated mineralogy software. Also, the µ-XRF is capable of analysing powders as well as surface of whole rock samples, and so, these analyses can be performed in a non-destructive manner. Consequently, a modern µ-XRF can combine detailed analyses with good accessibility thus establishing an alternative workflow capable of reporting chemical assays as well as element – mineral affiliation/s and textural information.

Another feature in the µ-XRF is the large range of resolution in which the analyses can be performed. On the larger scale, resolutions on 100's of µm can be used, whereas on a smaller scale a resolution down to 10 µm is possible. Thus, in opting for a coarser resolution the analytical time can be very quick (minutes for dm-scale samples), whereas a fine resolution analysis is as time consuming as a scanning electron microscopy (SEM)-based analysis.

2 Methods

Drill core fragments representing various mineral associations from IOA occurrences in Northern Sweden were examined. The drillcores were cut and one half powdered for XRF analysis at LKAB chemical laboratory Malmberget. The remaining powdered samples and the other half of the drill-cores were sent to Luleå University of Technology (LTU) for further analyses.

The drillcore samples were analysed by a Bruker M4 Tornado µ-XRF instrument under medium vacuum (2 mbar), using a Rh-tube, 50 kV voltage, and 600 µA current. Samples with Fe content of 30 % or more were analysed at 300 µA current to avoid flooding the detectors. Analytical time per pixel was 10 ms, and the size of the area scanned 160x30 mm. Three different resolutions were applied, 500 µm, 200 µm, and 50 µm, in order to evaluate the impact of resolution on precision.

The powdered samples were ground to <10 µm using an X-ray diffraction (XRD) McCrone mill and fitted in Ø 26 mm XRD sample holders. These samples were analysed in the µ-XRF following the same procedure as for the drillcores but with an analysed area of 16x10 mm. The powdered samples were additionally analysed using a Malvern Panalytical Empyrean for X-ray diffraction analysis.

The data collected from the µ-XRF scans were analysed in both the M4 software for elemental distribution and association, and in Bruker's advanced mineral analysis and characterisation software (AMICS) for mineralogy, mineral distribution, and mineral association. Quantitative XRD analyses (Rietveld refinement) were

performed in the HighScore Plus software using the PDF-4 mineral database.

3 Results

The data collected from µ-XRF analysis of drillcores, and powdered samples were used for comparison with the results from XRF chemical assays. The µ-XRF drillcore analyses were also used to generate elemental maps and to produce mineral maps in AMICS.

3.1 Chemical composition

Data from the XRF chemical assays were compared to powder and drillcore samples analysed in µ-XRF.

Comparing the results from the chemical assays by XRF to that of the µ-XRF scanned powdered samples shows a good correlation with high R^2-values (Figure 1).

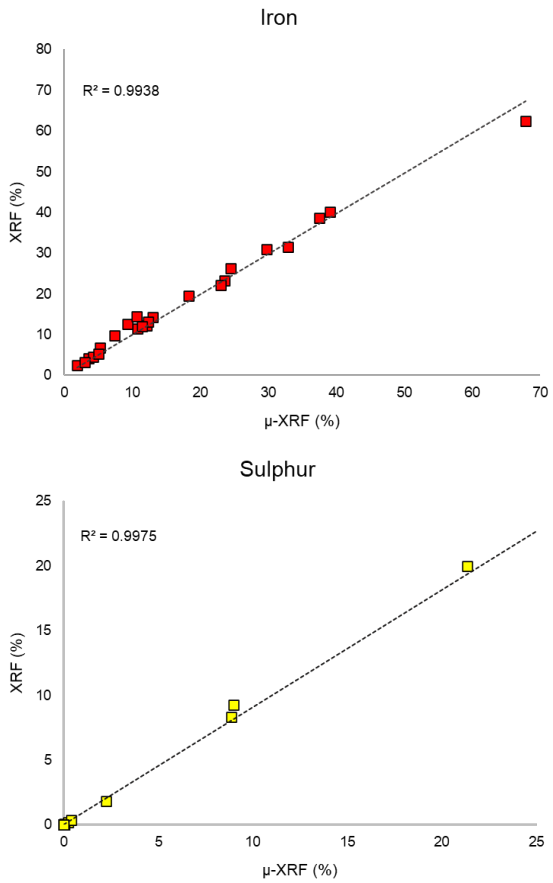

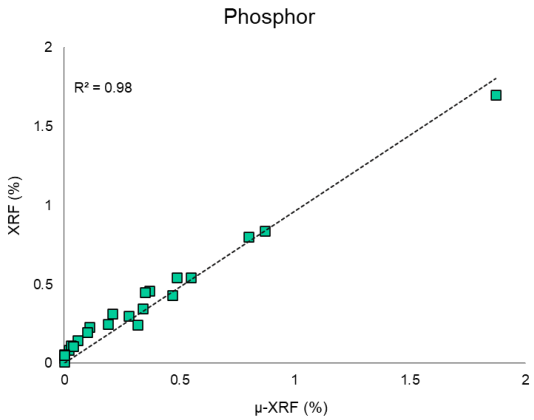

Figure 1. Comparison of XRF assays and µ-XRF data for Fe, S, and P in powdered samples.

However, when the assays are plotted against the results from drillcore analysis a correlation is still present, although it is lower than for the powdered samples based on sample inhomogeneity across different scales (Figure 2). The correlation between the beforementioned was not resolution dependent and chemical variation in the results from the three different resolutions used was negligible.

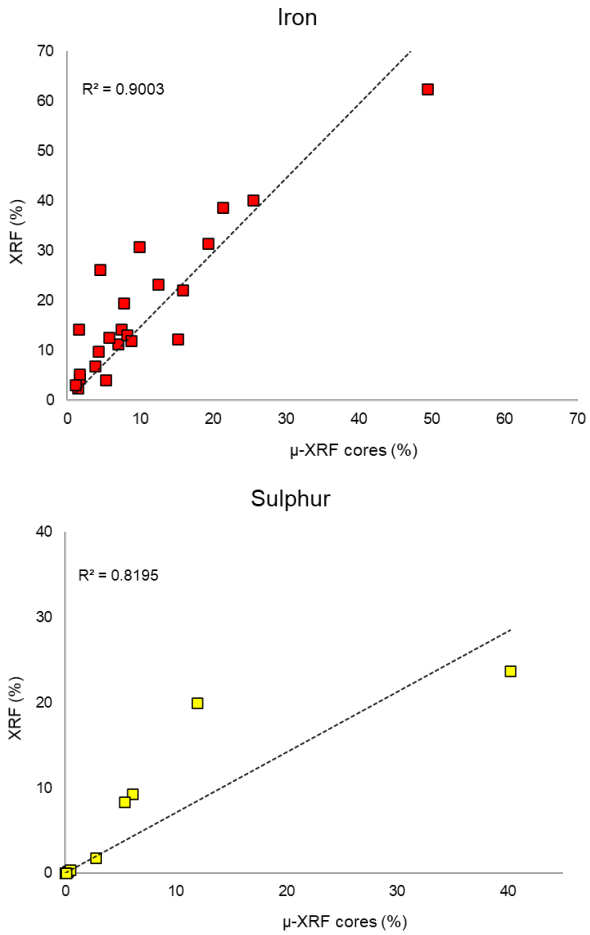

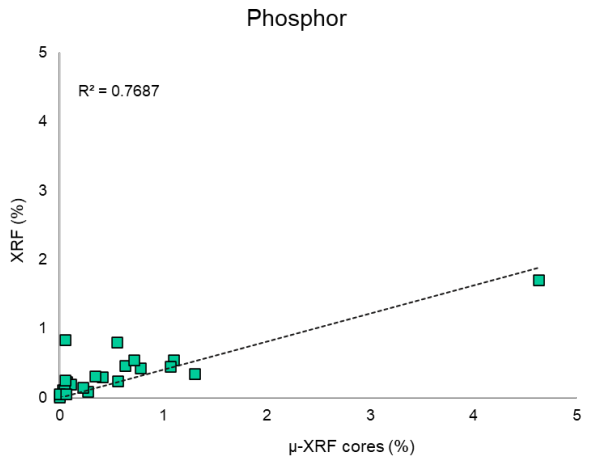

Figure 2. Comparison of XRF assays and µ-XRF data for Fe, S, and P in drillcore samples.

3.2 Elemental distribution

Elemental maps were produced for all drillcores. From these, two representable samples were selected for this work.

Figures 3 and 4 show the element distribution of Fe, P, and S in sample M19 and M09, respectively. From these it is clear that both samples contain minerals with a high Fe-content, mainly Fe-oxide/s, and that P occurs in discrete crystals. Sulphur, however, shows different distribution patterns in the two samples with S in sample M19 mainly occurring in discrete areas, e.g., the cross-cutting vein, whereas S in sample M09 is disseminated throughout the sample but also show a higher concentration in association with P. Thus, the S-bearing minerals differ between areas within the same deposit.

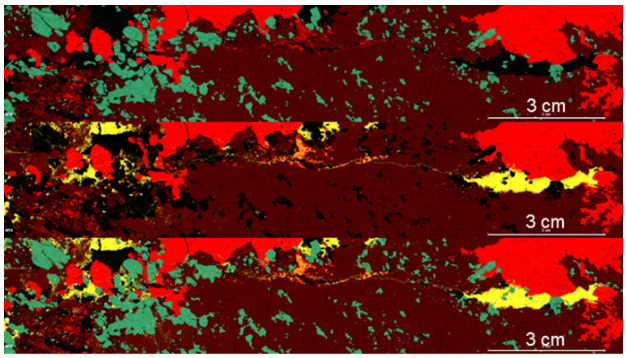

Figure 3. Elemental maps from drillcore sample M19 with Fe in red, P in green, and S in yellow. Top show Fe and P, middle Fe and S, and bottom Fe, P, and S.

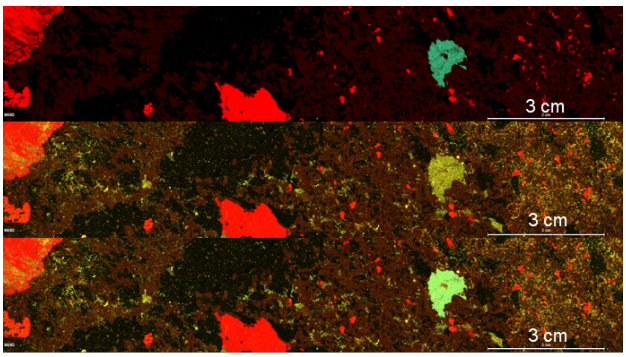

Figure 4. Elemental maps from drillcore sample M09 with Fe in red, P in green, and S in yellow. Top show Fe and P, middle Fe and S, and bottom Fe, P, and S.

3.3 Modal mineralogy

Mineral maps and modal abundance were acquired using AMICS. This is a Bruker specific software with a built-in mineralogical database.

X-ray images and mineral maps from AMICS as well as mosaic images acquired from the M4 software are shown in Figure 5 and 6. The minerals in the false colour mineral maps have been grouped to yield a more distinct transition between minerals and to enhance visibility of the modal distribution.

4 Discussion

Recent work has demonstrated the application of µ-XRF analysis on geological samples to be an efficient approach (e.g., Flude et al., 2017; Menzies et al., 2022; Parian et al. 2022; Månbro and Parian 2023).

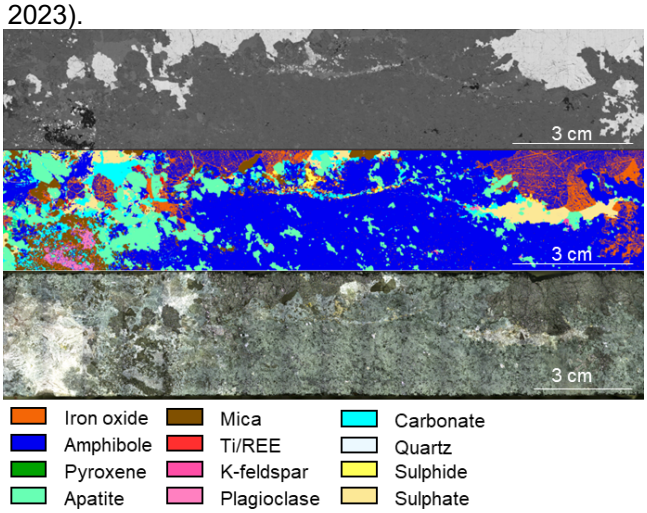

Figure 5. X-ray intensity image (top), mineral map (middle), and mosaic scan from µ-XRF (bottom) of sample M19.

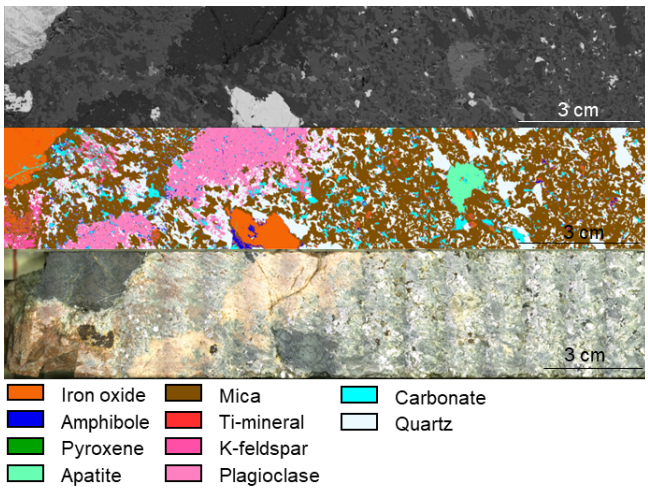

Figure 6. X-ray intensity image (top), mineral map (middle), and mosaic scan from µ-XRF (bottom) of sample M09.

Chemical assays normally require samples to be ground to a fine fraction on which XRF is performed. This approach gives a bulk rock composition and is destructive by nature. Chemical assay acquired by µ-XRF is here shown to perform as well on powdered samples as traditional XRF. The chemical information from scanning of the rock surface is dependent on a few additional parameters, e.g., texture and mineral distribution in the sample. However, the results from drillcore scanning show that even highly variable, textured samples like the ones used in this work provide good correlation with the XRF data, and therefore a representative chemical composition of the bulk rock composition.

Mineral identification and quantification are typically done on epoxy samples with fractions < 1 mm using SEM and an automated mineralogy software, e.g., QEMSCAN, although mineral identification by SEM is also possible on cm-scale, non-powdered samples. From the powdered sample analysis, liberation can also be determined.

When utilising a µ-XRF characterisation software like AMICS, dm-scale, whole rock samples can be analysed, and crushing is not needed. However, it is also possible to analyse the mineralogy of coarse powders. Thus, µ-XRF analyses can be performed in a non-destructive way. Since the sample size that can be analysed in the µ-XRF is larger than for the SEM, it could potentially provide more representative data, i.e., the µ-XRF can produce high quality data from larger, whole rock samples. Quantification of the mineralogy in a sample can also be extracted from the AMICS software, as can the degree of liberation.

However, the X-ray beam in the µ-XRF is of higher intensity than an electron beam in a SEM. This means that beam penetration in a sample is deeper in µ-XRF compared to SEM analyses. This penetration depth leads to signals from below the surface of the sample to be detected and might therefore cause a contamination of the signal from the underlying minerals. This impedes converting elemental spectra to mineralogy since the generated spectra may not match or mismatch existing known mineral standard spectra. This is especially common in samples where the ore includes elements with high atomic numbers, e.g., iron oxides, and the gangue mineralogy is lighter, e.g., feldspars. Furthermore, distinguishing iron oxide minerals, e.g., magnetite and hematite are not tangible by µ-XRF but has also been shown difficult with SEM-based software (Krolop et al. 2019).

One way to work around this is to cross-reference Fe oxides and the gangue mineralogy with an additional mineralogical analytical method, e.g., XRD, optical microscopy, or core logging, from which the parameters in AMICS can be changed to better suit the individual sample or deposit.

However, in some circumstances the beam penetration has proven beneficial when analysing for bulk chemistry since the area scan obtains a slight depth (Månbro and Parian 2023). The identification of heavy elements at depth in the sample can be valuable in REE and precious/heavy metal exploration. These elements are often present at low values in the rock (ppm to ppb), and therefore detection of signals from below the sample surface can provide information that otherwise could have been overlooked.

5 Conclusions

Characterisation of geological samples is an important part of several disciplines, but perhaps most so for the mining industry. At present, the typical workflow in analysing samples includes routine chemical analysis of exploration and mining drillcores, core logging, and selected XRD and SEM analyses as well additional optical microscopy. In processing plant, complementary information about mineral liberation after the comminution and separation stages are collected.

The work presented here shows that utilising the µ-XRF for characterisation of samples ranging from whole rock to fine powders is comparable to traditional methods that typically uses smaller sample sizes, are more time consuming, and that are destructive. When analysing high-grade samples however, some challenges are presented in correctly classifying the minerals at the sample surface due to the beam penetration. This however can be averted if the characterisation workflow includes an additional mineral identification method, e.g., XRD or core logging, from which a baseline mineralogy can be determined and the identification in the characterisation software improved to get a better fit data set.

An important factor in achieving a good recovery is to know which minerals are carrying the element/s of interest. In this aspect the µ-XRF analysis has some advantages compared to the traditional methods e.g., being able to analyse larger sample sizes compared to SEM analysis. Therefore, a workflow including µ-XRF analysis already in the

exploration stage could increase the sample throughput, provide a more holistic view of the deposit and consequently more correct predictions of processing quality and performance since identification of the minerals carrying the element/s of interest can be determined and these therefore possibly targeted more efficiently.

Acknowledgements

The authors would like to thank Dr. Andrew Menzies for his support during analytical work.

References

Blengini G A, Latunussa C EL, Eynard U, Matos CT de, Wittmer D, Georgitzikis K, Pavel C, Carrara S, Mancini L, Unguru M, Blagoeva D, Mathieux F, Pennington D (2020). European Commission, Study on the review of the list of Critical Raw Materials - Final Report, Critical Raw Materials Factsheets. https://doi.org/10.2873/11619

Geijer (1931) The iron ores of the Kiruna type. Sverige Geologiska Undersökning, C624, pp. 1-32

Flude S, Haschke M, Storey M (2017). Application of benchtop micro-XRF to geological materials. Mineral. Mag. 81, 923–948. https://doi.org/10.1180/minmag.2016.080.150

Håkansson U, Jonsén P, Jonsén R, Holmström Å, Larsson K, Jolsterå R, Vikström L (2023) Circular Production of Phosphorous and Rare Earth Elements. Conference in Minerals Engineering, Luleå, Sweden 7-8 Feb 2023, 111-116.

Krolop P, Jantschke A, Gilbricht S, Niiranen K, Seifert T (2019) Mineralogical imaging for characterization of the Per Geijer Apatite iron ores in the Kiruna District, Northern Sweden: A comparative study of mineral liberation analysis and raman imaging. Minerals, 9(9), 544.

Menzies A H, Tagle R, Reinhardt F, Hirschle C, Schellkopf L J, Kelly N, (2022). High-speed Micro-XRF Analysis of Rock Samples and Drill Cores. Microsc. Microanal. 28, 650–651. https://doi.org/10.1017/s1431927622003117

Martinsson O, Billström K, Broman C, Weihed P and Wanhainen C (2016) Metallogeny of the northern Norrbotten ore province, northern Fennoscandian Shield with emphasis on IOCG and apatite-iron ore deposits. Ore Geology Reviews, 78, 447-492.

Månbro C, Parian M (2023) Chemical and Mineralogical Characterisation of Iron Ore Drillcore Using µ-XRF. Conference in Minerals Engineering, Luleå, Sweden 7-8 Feb 2023, 157-171.

Continuous X-Ray Fluorescence Core Scanning: Application Examples and Methodology Developments

Miranda Lehman [1], Thomas Monecke [1], Erik Tharalson [1], Angus Tod [2], Annelie Lundström [3], Alexander Seyfarth [4], Susann Stolze [1], Katharina Pfaff [1]
[1]Department of Geology and Geological Engineering, Colorado School of Mines, 1516 Illinois St. Golden, Colorado, USA
[2]Minalyze Australia, U6 175 Campbell Street, 9104 Belmont, Western Australia
[3]Minalyze Sweden, Industrivägen 4, 433 61 Sävedalen, Sweden
[4]SGS North America, 5576 West River Oaks Rd Janesville, Wisconsin, USA

Abstract. Exploration drilling forms an integral part of mineral exploration programs. A great deal of time and money is spent on the logging of the drill core, the collection of data, and the preparation of samples for laboratory-based analysis. Workflows generally involve a high amount of human intervention. The Minalyzer continuous X-ray fluorescence core scanner can produce high-resolution photographs, 3D LiDAR point clouds, and depth associated major and minor element geochemical results of drill core in a non-destructive, timely manner. In addition to geochemical results, these outputs are used to accurately depth register drill core, perform RQD analysis, and calculate bulk densities. By implementing the core scanner into mineral exploration workflows, the processing and understanding of drill core can be sped up, and performed in a non-destructive manner with high accuracy and precision.

1 Introduction

The criticality of mineral and material resources is one of the greatest challenges for modern society and a major bottleneck as the world works toward the green energy transition. Ambitious net-zero carbon emission targets can only be achieved through a substantial increase in mineral resource discovery, development, and production. These factors will result in increased exploration drilling as drill core represents the only direct source of information constraining the subsurface geology.

Large exploration programs commonly face a range of workflow issues when working with drill core. This includes problems arising from the fact that core logging is subjective and inconsistencies between different core logging geologists complicate 3D modelling of the subsurface. In addition, laboratory-based geochemical analyses of core samples are slow and assay data are often obtained weeks to months following sample submission, preventing their use in decision making during ongoing drilling campaigns.

Many current workflow challenges can be overcome using modern core scanning technology such as the Minalyzer continuous X-ray fluorescence (XRF) core scanner (Fig. 1). This instrument, described in detail by Sjöqvist et al. (2015), is a patented, non-destructive analytical tool that offers a unique reorganization of drilling and logging program workflow. The continuous XRF core scanner is equipped with a high-resolution line scan camera for RGB photography, a 3D LiDAR scanner to create 3D point clouds, and a silicon drift detector (SDD) to produce quality geochemical results within an elemental range of Na to U. Analytical turn-around times are short when post-processing strategies are optimized.

The images, point clouds, and geochemical data that the Minalyzer continuous XRF core scanner produces can be used for a variety of calculations within the proprietary Minalogger software (ML2). These include rock quality designation (RQD) analysis, X-ray specific gravity, volume bulk density calculations, and down hole geochemical trends. All of these are accurately depth registered and calculated at a user defined interval (10 cm, 1 m, etc.). Scanning drill core using this instrument as the first step of a core logging workflow has the potential to replace the need for the initial time-consuming steps such as photography and RQD analysis. Continuous downhole geochemical results can be used to guide ongoing drilling programs and to create strategic assay sampling methods that cut down the number of samples that need to be sent out for laboratory-based analysis reducing cost.

The Minalyzer continuous XRF core scanner is currently being used in a variety of industrial settings as a reliable exploration tool and in academic settings, such as Colorado School of Mines to conduct research on drill core. Core scan data are uploaded to a cloud-based viewing and interpretation platform, minalogger.com, that allows permanent archiving and can be used to export data into industry-standard software packages such as Leapfrog Geo or ioGAS™.

2 Methodology

2.1 Sample preparation and core scanning

Preparing core to be scanned in the Minalyzer continuous XRF core scanner requires minimal effort. Full, uncut core is ideal for scanning with this instrument, but cut core can also be easily scanned. Core pieces should be arranged to be as level and flat as possible. Core must be cleaned if visually dirty. Each core box is loaded and placed into the same position on the instrument stage. Once a core box is loaded and correctly positioned, the instrument begins its pre-scan phase during which photographs, and a LiDAR scan are taken. The instrument uses the 3D point cloud to create the

scan path the X-ray detector can take along the core while also maintaining a

Figure 1. The Minalyzer continuous X-ray fluorescence (XRF) core scanner at Colorado School of Mines.

consistent distance from the core surface. The user has the ability to edit the scan paths if needed.

At the beginning and end of each day OREAS Certified Reference Materials (CRM) are scanned using the same scan settings used for the project. These CRMs are used day to day to check for detector drift and play an important role in post-processing as described below.

2.2 Scan settings

The Minalyzer continuous XRF core scanner can capture an elemental range of Na to U depending on the scanning settings (voltage, current, and scanning speed), the environment, and the X-ray tube anode. Typically, to capture all light and heavy elements of interest, two scans are performed on each core box. This includes one run at settings optimized for heavy elements and a second scan setting with a He purge optimal to capture light elements. If two or more scan settings are desired, the Minalyzer CS will conduct these scans using the same scan path created during the pre-scan phase.

The user also defines the scanning speed at which the detector nominally moves along the surface of the core. This speed ranges between 0.1 mm/sec up to 40 mm/sec, with 10 mm/sec offering the best trade off of detection limits and speed. During scanning, the detector maintains a consistent distance from the surface of the core, which is based on the 3D model. The collected X-ray spectra are binned and saved every 10 mm into a single multi-multi channel analyser (MMCA) file for each core box at each scan setting.

2.3 Depth registration

After scanning, the core must be depth registered in the Minalogger software (ML2). This is an important step of the post-processing routine that must be executed with consistency and accuracy. ML2 uses the 3D point cloud to display an image and height map for each core box while it is being depth registered. Depth logging can be done in feet or meters and the material in each box can be logged as competent core, weathered core, or rubble. When depth registering using the “core” function it is important to mark all the fractures along the core for later RQD calculations. A core loss function can be used to define areas of missing core. Depth blocks or true depth markers can also be added to mark the locations and corresponding depths of known depth measurements down hole. These functions all have an accuracy of several millimetres. Depth registration creates an accurate depth log outlining material type, fracture locations, and core recovery.

2.4 Rock quality designation

After the core is logged, the RQD function in Minalogger.com allows the user to define each fracture logged in the core during depth registration as a true break or a manmade break. Any core logged as rubble receives a 0% designation. These designations can be analysed at any interval defined by the user. Results are binned into the defined intervals corresponding to depth and output in a summary file.

2.5 Image stitching

RGB images are collected in four overlapping strips during the pre-scan phase and brought into the ML2 software to create a stitching and cropping template.

This template can be applied to all boxes in a given drill hole. Additional templates can be produced and applied to individually selected boxes as needed.

2.6 Multi-channel analyser (MCA) file generation

After depth registration is finalized, each 10 mm bin of collected spectral data in the MMCA file is assigned a depth based on its location on the drill core. After an interval is defined, such as 10 cm or 1 meter, spectra within the interval are collated to create an MCA file for each interval for the entire length of the drill hole. A summary_MCA file is generated during this step that contains the from and to depths of each interval along with other important metadata.

2.7 Spectral analysis

Collected spectra are de-convoluted and quantified based off of fundamental parameters. For each drill hole and scan setting a Multiple Least Squared (MLSQ) calibration file is produced from the CRM scanned during the project. The generated interval MCA files for an entire drill hole are then batch quantified against the corresponding MLSQ file. This initial step creates data that is calibrated using CRM, but it is not matrix matched which can cause deviations in the average accuracy of the data. The de-convolution software outputs a summary_XRF file for each drill hole that contains the processed elemental geochemistry.

Finally, the batched data is combined with depth data to create a preliminary depth-registered geochemistry data set. During post-processing, calibration factors derived from lab assay comparisons can be applied to the preliminary data to produce a matrix-matched calibrated dataset.

2.8 X-ray specific gravity

To calculate the X-ray specific gravity (X-SG™) a subset of varying samples is chosen from the scanned drill hole. Submerged specific gravity is calculated for each chosen sample in the set and then used as a calibration set.

By comparing the quantified Compton values and submerged specific gravity calculation values, a calibration factor is created for the sample set. The resulting calibration factor is applied to the entire drill hole to obtain accurate X-SG™.

2.9 Volume bulk density

The volume bulk density of drill core is calculated using the standard density formula. The volume for this calculation is derived from the point cloud produced for each core tray during the pre-scan phase and each box is weighed to determine the mass. The complete description of these calculations is outlined in Arthursson et al. (2021).

3 Methodology developments

Ongoing methodology improvements focus on the implementation of a digital pulse processor that will allow the count rate of the detector to be significantly increased. Implementation of the digital pulse processor will allow for lower detection limits while still maintaining a typical scan speed such as 10 mm/s. Alternatively, the scan speed could be increased to enhance the throughput of the core.

A long-wave ultra-violet (UV) light source is also being added as an additional imaging option during the pre-scanning phase. A long-wave UV light source can illuminate certain minerals of interest such as carbonate phases and is most widely used to identify oil bearing core during oil and natural gas exploration.

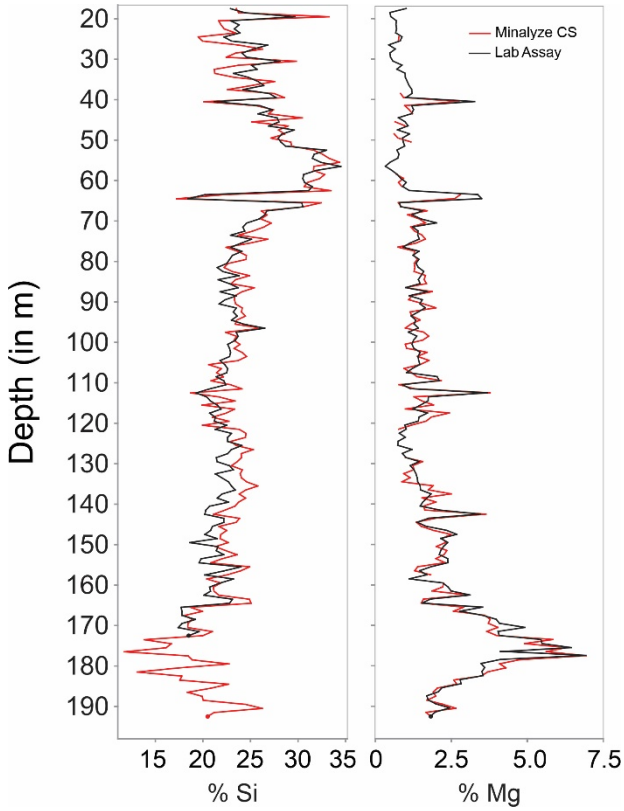

Figure 2. Comparison of XRF results for Si and Mg values collected using the Minalyzer CS (red) and lab assay results (black).

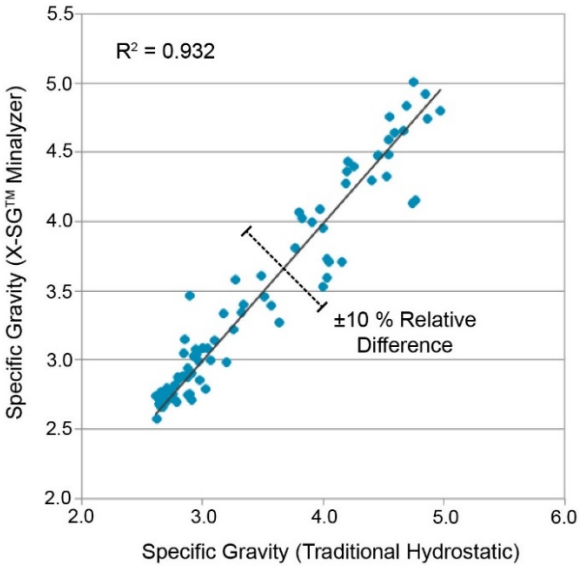

Figure 3. X-SG™ values versus traditional calculated hydrostatic values for the same drill hole showing a linear 1:1 ratio and the ±10 % relative difference.

4 Discussion and conclusions

The Minalyzer continuous XRF core scanner offers a variety of solutions for academic and industrial analysis. To test the accuracy of continuous XRF results, the core scanner data can be compared to laboratory-based assays obtained from the same core. Although it is not expected for these datasets to match perfectly due to differences in the instrumental methods used, sample volume analysed, and possible sample heterogeneities, it is expected that they correlate to one another. Figure 2 displays Minalyzer and laboratory-based assay datasets for Si and Mg values plotted down hole from a project in Mount Isa Inlier, Australia. A visual correlation can be seen in Figure 2, with associated R^2 values of 0.9819 for Si and 0.9785 for Mg.

RQD and fracture frequency calculated in Minalogger.com based on depth registration from an epithermal deposit in the western United States was compared to the RQD performed by a geologist at the mine site. The Minalogger analysis was performed using the same parameters used at the mine site. As expected, the results were very similar, and upon further inspection the Minalogger.com results were more accurate. Results from Minalogger.com had a higher accuracy because the calculations are based off the depth registration allowing measurements and fracture counts to be exact compared to using the traditional method of employing a tape measure.

Previous work has established that the volume bulk density calculation method using the 3D point clouds produced by the Minalyzer yields highly reliable data (Arthursson et al. 2021).

In general, calculating the specific gravity of drill core is important for resource estimation, but is a labour-intensive process that involves hydrostatic weight measurements for a large number of samples. A drill hole was scanned using the Minalyzer continuous XRF core scanner that already had an associated specific gravity dataset to compare results from each method. From the Minalyzer dataset, a variety of core segments were chosen to represent visually different rock types within the drill hole, and the hydrostatic weight was calculated. These values were used to create a calibration factor. The resulting calibrated X-SG™ values were plotted against the values calculated using the traditional method. Figure 3 shows that R^2 = 0.93 with relative difference between the datasets of ± 10 %.

The Minalyzer continuous XRF core scanner is a proven analytical tool that was introduced to the market in 2014 and is currently being implemented at multiple active mine sites. Though this is a robust system, method and hardware developments such as adding a UV light source for UV imaging and a digital pulse processor to increase detection limits are only going to increase the relevance and usefulness of this core scanner and cast a wider net of applications. The presented methods and calculations have a large upside because the values needed for the calculations are almost all collected during scanning or can be easily implemented into the workflow. Being able to digitise depth registered drill core with all of the associated datasets within days of drilling creates usable and accurate databases that can be accessed anywhere in the world.

Acknowledgements

This work was supported, in part, by the National Science Foundation and conducted within the Center to Advance the Science of Exploration to Reclamation in Mining (CASERM) which is a joint industry-university collaborative research centre between the Colorado School of Mines and the Virginia Tech under award numbers 1822146 and 1822108.

References

Arthursson M, Tod A, Dellar E, Lundström A (2021) Digitalizing the mining industry – 3D scanning of core trays to produce volumetric bulk densities. Third Australasian Exploration Geoscience Conference, Brisbane, 2021, Extended Abstracts, 5 p.

Sjöqvist ASL, Arthursson M, Lundström A, Calderón Estrada E, Inerfeldt A, Lorenz H (2015) An innovative optical and chemical drill core scanner. Sci Drill 19:13–16

XRD clustering and quantitative analysis as a fingerprinting technique to study ore deposits

Sheida Makvandi[1], Jean Cauzid[2], Alexandre Tarantola[2], Vasilios Melfos[3], Panagiotis Voudouris[4]
[1]Application Competence Centre, Malvern Panalytical, Almelo, the Netherlands
[2]GeoRessources - Université de Lorraine-CNRS, Vandoeuvre-lès-Nancy CEDEX – France
[3]School of Geology, Aristotle University, Thessaloniki, Greece
[4]Faculty of Geology and Geoenvironment, National and Kapodistrian University of Athens, Athens, Greece

Abstract. This study highlights the importance and efficiency of XRD clustering and quantitative analysis (using the Rietveld method) in metallogenic studies as a principal mineralogical assessment tool for the optimization of both field sampling and sample selection for further geochemical investigations. In this regard, 24 samples representative of various Oligocene epithermal and telescoped porphyry-epithermal deposits from Greece, their associated alteration zones and igneous host rocks were measured by XRD. The XRD scans were also investigated by PCA and cluster analysis in HighScore Plus software to distinguish their mineralogical similarity and differences; identify the representative scans of each cluster for phase identification and quantification. As a result, samples with mineral assemblages typical of epithermal and/or porphyry deposits cluster together or plot each other's vicinity, whilst those typical of advanced alteration zones also form (a) separate cluster(s). However, some felsic and mafic igneous host-rock samples are classified in the same clusters, which indicates the alteration of their original mineralogy over multiple phases of alteration and mineralization in their respective geological settings. The abundance of alteration minerals in these rocks reported in the XRD results supports this hypothesis. The XRD results were compared and showed very good agreement with trace element and bulk chemical data and VNIR-SWIR results.

1 Introduction

Identification and quantification of mineral assemblages in geological samples are primary steps after field sampling, which can serve two purposes: providing guidance for the optimization of the sampling strategy, and reducing the number of samples for further investigations using other mineralogical and geochemical techniques such as laser ablation inductively coupled plasma mass spectrometry (LA-ICP-MS), Laser Induced Breakdown Spectroscopy (LIBS) and/or scanning electron microscopy-energy dispersive X-ray spectroscopy (SEM-EDS). These methods despite their precision and efficiency are expensive and relatively slow, and the interpretation of the results requires petrographic data.

Whilst optical microscopy is conventionally accepted as a principal tool for mineralogical assessments, the precision of petrographic studies largely relies on the operator's knowledge and expertise. This is where hiring a complementary but more sophisticated technique, such as X-Ray Diffraction (XRD), seems essential. Over a million crystal structures are available in references libraries for mineral identification in XRD patterns. These structure data can also be used to create a calculated profile that through the Rietveld method (Rietveld 1969) can quantify the abundance of all minerals present in a sample. A distinct benefit of quantitative XRD (QXRD) is that the data can be further analyzed separately or in combination with data from other techniques with multivariate statistical methods to reveal hidden information in the dataset and provides insights for ore deposits or provenance discrimination studies. Thus, this study aims to highlight the value of XRD clustering and quantitative analysis as a rapid and cost-effective method in the study of porphyry and epithermal deposits.

2 Geological contexts

The Hellenides are part of the Alpine chain, resulting from the collision between the African and the Eurasian continents, which spread from the Alps to SE Asia. In Greece, the orogen consists of three continental blocks (Adria, Pelagonia and Rhodopia) accreted during the Hellenic subduction (Dewey et al. 1973, Ring et al. 2010), which evolved in two stages: a compressional event starting Late Jurassic and culminating Mid-Cretaceous, followed by an ongoing extension resulting from the slab rollback (Jolivet and Brun 2010, Jolivet et al. 2013). Therefore, large volumes of arc and post-collisional magmas intruded the thinned crust from Rhodope (Oligocene to Early Miocene) to the Cyclades (Middle Miocene to Pliocene). Many of these magmatic systems host porphyry-epithermal systems (Voudouris et al. 2019). This study focuses on the Rhodope province, which consists of four metamorphic core complexes -the Rhodope Massif -surrounded by a belt of slightly metamorphosed sedimentary and volcano-sedimentary rocks -the Circum-Rhodope belt.

Magmatism in the Rhodope Massif and the Circum-Rhodope belt ranges from calc-alkaline through high-K calc-alkaline to shoshonitic, and it is characterized by voluminous lavas and pyroclastics of andesitic to rhyolitic composition and their subvolcanic/plutonic equivalents. Outcropping alteration zones around porphyry bodies cover the entire series: potassic, sodic-calcic, propylitic, sericitic, argillic, advanced argillic, K-feldspar (adularia) and silicic.

3 Sampling and analytical methods

Sampling focused on building an exhaustive collection of the host rocks, intrusive bodies, alteration types, including overprinted ones, and mineralized veins of the district. A total of 40 samples were collected, from which, the samples without mineralized veins were cut in two pieces, and one piece was pulverized and sent for whole rock analysis at the SARM-CRPG facility (Service d'Analyse des Roches et Minéraux). The second piece was analyzed using a portable Spectral Evolution SR6500 VNIR-SWIR spectrometer at the GeoRessources laboratory.

A subset of 24 samples that were representative of all host igneous rocks, mineralization and associated alteration zones were analyzed by XRD at the Application Competence Centre, Malvern Panalytical, in the Netherlands. These samples originate from the Santa Barbara-Sykorachi (StB; 4 samples), Konos Hill (KH; 5 samples), Kassiteres (Ka; 3 samples), St Philippos (StP; 5 samples), Maronia (Ma; 4 samples), Pefka-Loutros (Pe; 1 sample) and Myli-Aisymi (My; 2 samples) prospects. All of them are Oligocene deposits either epithermal (StB, StP, Pe) or telescoped porphyry-epithermal (KH, Ma, My) systems (Voudouris et al. 2019). Table 1 summarizes the sample description, and cluster analysis results.

3.1 XRD measurements and Rietveld analysis

The XRD scans were collected using the Minerals Edition of Aeris compact X-Ray diffractometer from Malvern Panalytical with power settings of 40 kV–15 mA, equipped with a cobalt-anode X-ray tube, a goniometer radius of 145 mm, 0.04 rad. soller slits, 1/4° divergence slit, a 23 mm mask, low beam-knife position, step size 0.02° and acquisition time of 29 s/step. The Bragg-Brentano measurement covered a range of 5-75° 2θ allowing the detection of clay minerals and heavy minerals such as Fe oxides/hydroxides and sulfides. The use of cobalt radiation was applied to prevent the emission of Fe fluorescence. Fluorescence comes when using Cu radiation in analyzing Fe, Cu, and/or Mn-containing materials. This, therefore, improves the penetration depth of X-rays in the sample and improves counting statistics. The use of a linear PIXcel1D Medipix3 detector with an active length of 5.54° 2θ allows a scan acquisition time of a few minutes. The phase identification was done in the Malvern Panalytical's HighScore Plus software version 5.1 (Degen et al. 2014) using the ICDD PDF-4 database (Gates-Rector & Blanton 2019).

Table 1. Samples description and cluster analysis results. Number 0 indicates the samples that could not cluster with others because their district mineralogy (acting as outliers in the analysis).

Sample ID	Deposit	Lithology and alteration	Cluster number & colour
116-01	StB	Quartz vein	0 (black)
116-02		Andesite_Sericitic	0 (black)
116-03		Andesite_Chloritic-sericitic	1 (blue)
116-04		Andesite_Propylitic	2 (green)
118-05	KH	Granodiorite_Sodic-calcic	2 (green)
119-01		Clays_Serisitic	4 (brown)
119-02		Clays_Propylitic	4 (brown)
119-03		Monzodiorite_Serisitic	1 (blue)
119-04		Monzodiorite_Sotassic	5 (electric blue)
119-05	Ka	Diorite_Potassic	2 (green)
120-01		Monzodiorite_Chloritic-sericitic	4 (brown)
121-01		Rhyolite_Sericitic	4 (brown)
121-02	StP	Advanced clay alteration	0 (black)
121-04		Advanced clay alteration	3 (grey)
121-05		Advanced clay alteration	0 (black)
121-06		Advanced clay alteration	3 (grey)
121-07		Granodiorite_Propylitic	1 (blue)
122-01	Ma	Monzogabbro_Potassic	5 (electric blue)
122-02		Granite_Potassic	2 (green)
122-03		Monzogabbro_Propylitic	5 (electric blue)
123-02		Rhyolite_Sericitic	4 (brown)
123-03	Pe	Rhyolite_Chloritic-sericitic	0 (black)
124-03	My	Rhyolite_Sericitic	2 (green)
124-04		Rhyolite_Propylitic	4 (brown)

The peak position overlapping of critical minerals such as sphalerite with pyrite supports the use of Rietveld refinement as a full pattern fitting approach, in contrary to classical straight-line calibration methods that can cause a bias in the results. The Rietveld refinement requires XRD scans of a certain quality that includes a low and flat background and high diffraction intensities (most intense peak with >10,000 counts). In this study, every quality scan was collected within 7 minutes of measurement. A signal 3 times above the noise level is detectable, whilst a signal 10 times above the noise level is required for accurate phase quantification. The average signal-to-noise ratio in the collected XRD scans is 125. This means all minor and trace phases in the studied samples were detectable and quantifiable. The accuracy of XRD results was validated by comparison with the bulk chemistry, X-Ray fluorescence and VNIR-SWIR data published in previous studies (e.g., Jeong et al. 2016).

3.2 Extended cluster analysis

The phase identification was performed on specific XRD scans selected by extended cluster analysis (creation of correlation matrix, agglomerative hierarchical cluster analysis, grouping, and visualization) and Principal Component Analysis (PCA) and marked as a representative or outlier scan. Figure 2 shows a compare-view of 10 representative and outlier scans. Both PCA and cluster analysis of XRD scans were done in HighScore Plus software.

Cluster analysis aims to simplify the analysis of a large amount of data. It automatically sorts all (closely related) scans of an experiment into separate groups and marks the most representative scan of each group as well as the most outlying scans within each group (Degen et al. 2014). Samples that are clustered together show similar mineralogy. Therefore, it is only necessary to identify and quantify phases in the most representative scan of each cluster to create an

analytical routine (Degen et al 2014; Pernechele et al 2021). The other scans in the group can be inserted and automatically analysed in their corresponding routine. This is more efficient when analysing multiple samples originating from the same type of rocks/lithology or in quality control environments.

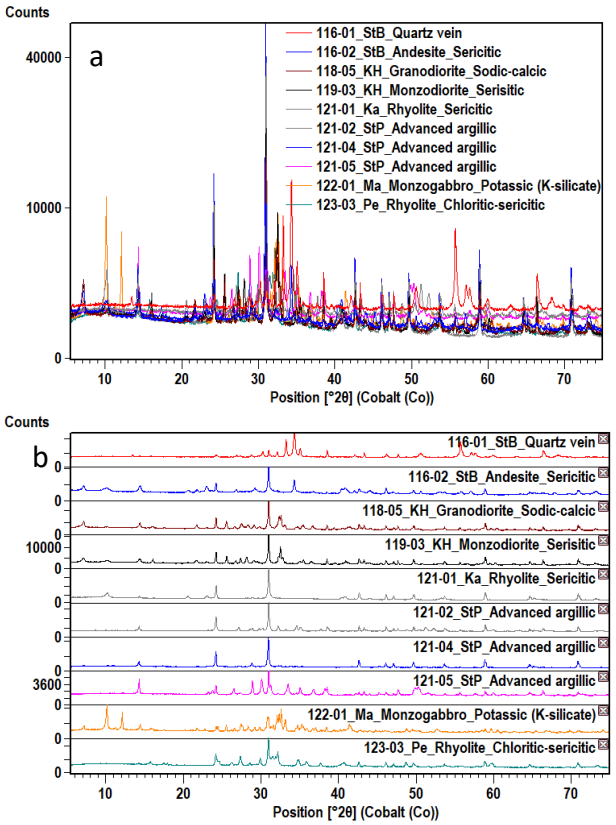

Figure 1. a) An overlay-view and **b)** a 2D-view of 10 XRD scans: 5 scans representative of 5 clusters and 5 so-called outliers (samples 116-01, 116-02, 121-02, 121-05, 123-03) that could not cluster with others because of their distinct mineralogy. A different XRD pattern simply corresponds to a different mineralogy.

4 Results and discussion

The dendrogram after cluster analysis (Figure 2) shows that 15 out of the 24 studied samples can be grouped into five clusters, whereas five samples do not belong to any of these groups given their distinct mineralogy. One of these so-called outliers is Sample 116-01 (Figure 3), which was collected from a quartz/sulfide vein at Santa Barbara-Sykorachi. The XRD analysis differentiates this sample as it consists of about 42.7 wt% calcite, 13.2 wt% chalcopyrite, 10.4 wt% sphalerite, and 2.9 wt% galena (a typical assemblage of epithermal mineralization; Voudouris et al 2019).

In addition, the XRD analysis discriminates this sample due to the occurrence of 9.0 wt% rudashevskyite (Fe-dominant member of sphalerite group) and 0.8 wt% cerussite ($PbCO_3$). In contrary, the other 3 samples from this area are from variably altered andesites (sericitic, chloritic-sericitic, and propylitic) and are mainly composed of feldspars (calcic and/or potassic) ± calcite ± clinochlore ± muscovite and quartz. Between 11.0 to 21.0 wt% illite was measured in sericitic and chloritic-sericitic andesites samples (116-02 and 116-03).

As depicted by the dendrogram in Figure 2, sample 116-01 despite its distinct mineralogical characteristics, shows some similarity to advanced argillic samples (samples 121-02 to 121-06) from St Philippos. This is consistent with their epithermal origin/association (Voudouris et al. 2019). According to the QXRD results, the advanced argillic samples are mainly composed of quartz (36.3 to 85.6 wt%), dickite (5.2 to 21.0 wt%), also variably contain pyrite (0.9 to 12.5 wt%) and a minor amount of galena (0.2 to 2.1 wt%). In contrast, the presence of 11.9 wt% anglesite ($PbSO_4$) and 2.4 wt% tennantite ($Cu_{12}As_4S_{12}$) in sample 121-02, and 42.6 wt% baryte and 1.3 wt% anglesite in sample 121-05 can also explain their dissimilarity to samples 121-04 and 121-06 (Figure 2).

In addition to samples 121-02 to 121-06, the presence of pyrite in association with clay minerals has been confirmed by the XRD-Rietveld analysis in other samples such as samples 118-05 and 119-01 to 119-04 from Konos Hill, sample119-05 from Kassiteres, and sample 123-02 from Maronia. This mineralogical association is characteristic of polymetallic epithermal deposits overprinting and/or occurring laterally from porphyry-style mineralization (Voudouris et al 2019).

Trace and major element composition of the 24 samples measured by ICP-MS and LIBS indicate that these samples averagely contain 18.4 ppm lithium. The XRD-Rietveld analysis identifies lepidolite, fluorannite, petalite, and griceite as the Li-containing minerals. The highest abundance of lepidolite is detected in rhyolite samples with sericitic alteration from Kassiteres and Myli-Aisymi (5.2 wt% in sample 121-1 and 2.7 wt% in sample 124-03) followed by monzogabbro with potassic (K-silicate) alteration from Maronia (sample 122-01) that contains 2.3 wt% lepidolite. The VNIR-SWIR results also confirmed the presence of lepidolite in samples 119-05-Ka, 122-01-Ma, 122-03-MA, 124-03-My and 124-04-My. They were tested using portable LIBS, which revealed the presence of Li.

In certain samples such as monzongabbro with potassic alteration from Maronia, fluoroannite is Li-bearing (5.3 wt% in sample 122-01, and 3.5 wt% in sample 122-03). This result emphasizes on one of the advantages of mineralogical analysis by XRD, which is indirect chemical fingerprinting (based on a stoichiometric formula of identified phases). The XRD reference databases commonly include multiple candidates for every mineral that may differ in their minor elements chemistry (e.g., Ni- or As-containing pyrite; Ni-, Cu-, Zn- or Ti-bearing magnetite). Elemental substitution or impurities can slightly affect the mineral's diffraction pattern. For instance, in the spinel structure of magnetite, the presence and increase in the Ti content results in an

increase in unit-cell parameter, oxygen fractional coordinate, and tetrahedral bond length, and a marginal decrease in the octahedral bond length (Bosi et al. 2009).

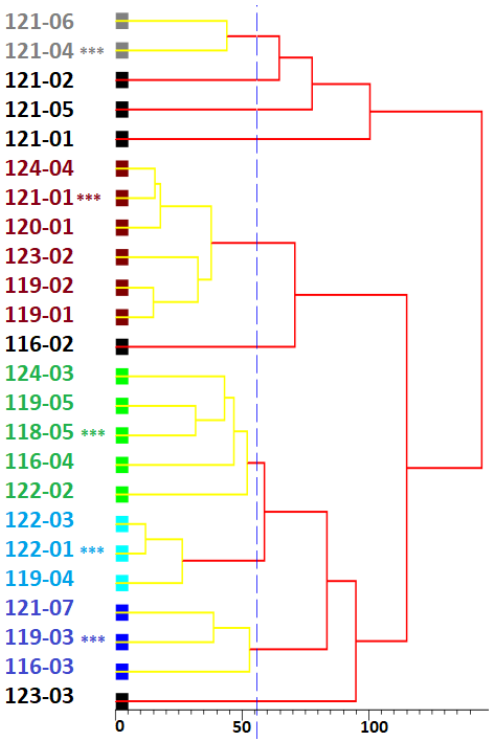

Figure 2. Dendrogram after cluster analysis based on the correlation matrix from 24 studied samples. X-axis shows the dissimilarity of the tie bars. Every colour represents a distinct cluster, except for black that specifies the outliers. The most representative scan of each cluster is indicated by ***.

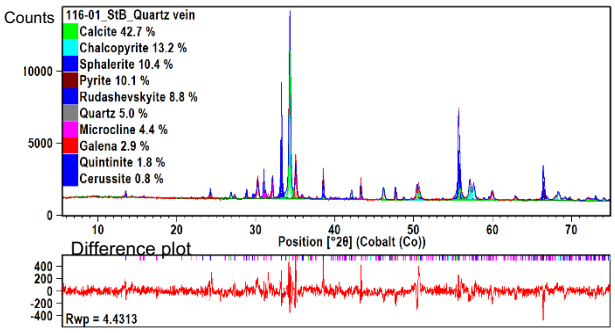

Figure 3. Rietveld analysis of XRD data of sample 116-01 in HighScore Plus. Distinct mineralogy that differentiates epithermal mineralization from alteration zones and host rocks. The difference plot shows the difference between the measured and calculated intensities/profiles. An Rwp = 4.4 indicates the reliability of the Rietveld refinement and accuracy of the phase quantification.

5 Conclusions

Quality scans collected in 7 minutes in Aeris compact XRD system show the potential of XRD as a time- and cost-effective technique for ore deposit mineralogical studies, and sample selection for further investigations with other techniques. PCA and cluster analysis of XRD patterns in HighScore Plus is an efficient approach to analyze many data as they simplify the complexity of such a dataset and reveal the hidden correlation between different observations. As a result, the XRD scans of 24 studied samples were grouped in 5 clusters and 5 outliers showing the diverse mineralogy of these samples. The Rietveld analysis of XRD patterns also indicates a different abundance of minerals in each sample. This study showed the presence of lepidolite, fluorannite, petalite, and griceite as Li-containing minerals in some of studied the lithologies (particularly in rhyolite samples with sericitic alteration). Pyrite occurrence in clay-rich assemblages was also detected as a signature of epithermal mineralization.

Acknowledgments

T. Degen, M. Sommariva, and M. Pernechele (Malvern Panalytical, the Netherlands) are thanked for their technical support on XRD measurements and data analysis. M. Fisher (GeoRessources, Université de Lorraine) is thanked for the VNIR-SWIR and geochemical data acquisition and interpretation as part of her master's degree thesis.

References

Bosi F, Hålenius U, Skogby H (2009) Crystal chemistry of the magnetite-ulvöspinel series. American Mineralogist 94, 181-189.

Degen T, Sadki M, Bron E, König U, Nénert G (2014) The High Score Suite. Powder Diffraction 29, S13–S18.

Dewey JE, Pittman WC III, Ryan WBF, Bonnin J (1973) Plate tectonics and the evolution of the Alpine system. Geol. Soc. Am. Bull., 84 (10) 3137-3180.

Gates-Rector S, Blanton T (2019) The Powder Diffraction File: A Quality Materials Characterization Database. Powder Diffraction 34, 352-360.

Jeong Y, Yu J, Koh SM, Heo CH, Lee J (2016) Spectral characteristics of minerals associated with skarn deposits: a case study of Weondong skarn deposit, South Korea. Geosciences Journal 20, 167-182.

Jolivet L, Brun J-P, (2010) Cenozoic geodynamic evolution of the Aegean region. Int. J. Earth Sci. 99, 109–138.

Jolivet L, Faccenna C, Huet B, Labrousse L, Le Pourhiet L, et al (2013) Aegean tectonics: strain localization, slab tearing and trench retreat. Tectonophysics 597, 1–33.

Pernechele M, López Á, Davoise D, Maestre M, König U, Norberg N (2021) Value of Rapid Mineralogical Monitoring of Copper Ores. Minerals 11, 1142.

Rietveld HM (1969) A profile refinement method for nuclear and magnetic structures. Journal of Applied Crystallography 2 (2), 65-71.

Ring U, Glodny J, Will T, Thomson S (2010) The Hellenic subduction system: high pressure metamorphism, exhumation, normal faulting, and large-scale extension. Ann. Rev. Earth Plan. Sci. 38, 45–76.

Voudouris P, Repstock A, Spry PG, Frenzel M, Mavrogonatos C, et al (2022) Physicochemical constraints on indium-, tin-, germanium-, gallium-, gold-, and tellurium-bearing mineralizations in the Pefka and St Philippos polymetallic vein- and breccia-type deposits, Greece. Ore Geol. Rev., 140, 104348.

Voudouris P, Mavrogonatos C, Spry PG, Baker T, Melfos V, et al (2019) Porphyry and epithermal deposits in Greece: An overview, new discoveries, and mineralogical constraints on their genesis. Ore Geol. Rev., 107, 654-691.

Integrated analysis of the Consorcio prospect in Cunas emerald mine (Colombia), tool to determine mineralization stages and related by-products

Andrés S. Martín-Ravelo[123]
[1]*Departamento de Geociencias, Universidad Nacional de Colombia, Bogotá, Colombia*
[2]*Society of Geology Applied to Mineral Deposits – Student Chapter UNAL, Bogotá, Colombia*
[3]*Caracterización Tecnológica de Minerales research group, Bogotá, Colombia*

Abstract. This work includes the main results and research proposal under development by students and researchers from the Universidad Nacional de Colombia (SGA Student Chapter and Caracterización Tecnológica de Minerales research group) linked to the "LitoCo" project, focused on determining the conditions of the mineralization stages that originated the emerald deposits located in Cunas emerald mine and the closes "Consorcio" prospect (Maripi-Boyacá, Colombia). This study is based on stratigraphy, petrography, geochemistry (XRD and XRF) and gamma-ray spectral geology, joining efforts to delimit new productive zones of emeralds through local-regional correlations, while the extraction potential of critical minerals present as stored by-products (REE elements, stone aggregates and clay minerals; for construction and industrial use) is evaluated.

1 Introduction

Colombia has been the largest emerald producer since ancient history. Nowadays, its role has passed to a second place due to arise of large producers in other parts of the world, occupying the third place in terms of emerald production, after Zambia and Brazil. Emeralds in the world are typically found in metamorphic aureoles or pegmatitic veins in countries like Zambia, Brazil, Pakistan, or Ethiopia (González-Durán et al. 2021). Colombian deposits are unique, due to mineralization occurs in sedimentary rocks by hydrothermal processes related to high diagenesis and low grade metamorphism (equal to found in sediment-hosted Pb-Zn or Mississippi Valley Type deposits) without magmatism or high-grade regional metamorphism (Giuliani et al. 2019), inside organic-rich black shales, calcareous mudstones, limestones and evaporitic siltstones of early-Cretaceous age (Valanginian to Hauterivian-Barremian), belonging to Rosablanca, Furatena and Muzo formations (González-Durán et al. 2021).

This work covers the lithostratigraphy and petrography of a deposit corresponding to Cunas emerald mine, within the Maripí District (MD), one of the Colombian emerald mining districts, all of them distributed N-NE along both flanks of the Andes eastern cordillera, between the provinces of Cundinamarca and Boyacá: Western Emerald Belt (WEB, including the municipalities-districts of Muzo-Quipama, Peñas Blancas, Coscuez and Maripí), and Eastern Emerald Belt (EEB, including the municipalities-districts Chivor, Macanal and Gachalá).

The Cunas mine has been exploited for at least 30 years since its discovery in the 1990's. Between Cunas and La Pita mine (Figure 1) there is a coarse-vein of high-quality emeralds, within the Consorcio prospect (consortium in Spanish, named for the joint exploitation of both companies). Since then, multiple studies have been conducting to determine the mineralization conditions that occurred to form these emeralds and how they vary with respect to other mines. Several additional proposals to better understand the genesis and potential of emerald deposits for not only gems but also by-products (REE's elements, stone aggregates and clay minerals) are X-ray diffraction, X-ray fluorescence and gamma spectrometry, that we are going to mention next.

The main structures in WEB are tight syncline-anticline folds oriented N30°E, parallel to SE-verging thrust faults, such as Coscuez, Peñas Blancas and Rio Minero (leader thrust fault), cut by the Rio Itoco strike fault, oriented 50°SE separating numerous mines. These are interpretated as fault propagation folds in a compressive and transpressive regime, where the detachment levels correspond to ductile beds of albitites and other evaporitic rocks of Cretaceous formations, juxtaposing these rocks and moving overpressured connate fluids (brines) between faults, escaping and triggering intense hydraulic fracturing. In each WEB deposit, there is evidence of complex deformation resulting in polyphasic duplex structure, as well as growth of chloritoid porphyroblasts and therefore a low-grade metamorphism process (Branquet et al. 1999).

According to Giuliani et al. (2019) in the hinges of the folds develops tectonic and hydrothermal breccias when fluids percolate and leach rocks during successive pulses of fault fluid flow and dilatant sites resulting from shear fracturing synchronous to thrust fault propagation, crystallizing emeralds after albitization, early sulphates reduction and carbonization. Thus, the large mines are developed recognize these structures (e.g. Peñas Blancas, Coscuez, La Pava and Puerto Arturo mines are following the Alto de la Chapa and Coscuez anticlines). At the Cunas mine and Consorcio prospect (Figure 1), mineralization occurs in WNW flank of Muzo syncline, along decimetres-thick carbonate veins and hydrothermal breccias cut bedding (Romero et al. 2021; Martín-Ravelo and Romero-Ordóñez 2022).

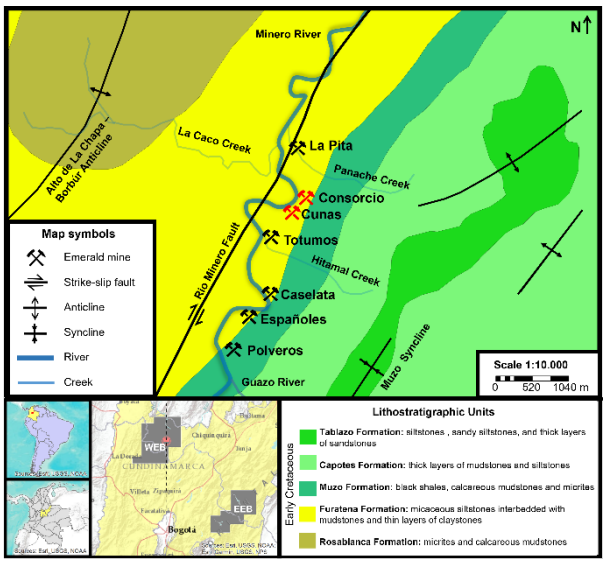

Figure 1. Maripí District (MD) geological map, showing Cunas mine and Consorcio prospect. Modified of Martín-Ravelo and Romero-Ordóñez (2022)

Mineralization stages occur simultaneously to develop the tectonic structures (González-Durán et al. 2021). Albitization occurs when brines leach the rocks and crystallizes metasomatic albite due to mobilization of solution of alkaline composition (Na^+, Ca^+, Fe^+, Mg^+) forming thrust-breccias parallel to the lamination called “cenicero” by the miners (Giuliani et al. 2019). Alkalinity then stimulates sulphate reduction in the presence of black shales organic matter, releases HCO_3^- and H_2S to form pyrite and carbonates as the solution acidifies. Carbonization receives its name due to crystallization of calcite and dolomite in veins in paragenesis with quartz + fluorite + parisite + emerald, resulting in an enrichment in light REEs and high Cr-V ratios and poor iron content as a chemical fingerprint of emerald gems. Finally, supergenic stage and compressional deformation occur, forming red tectonic breccias cemented by pyrite and ankerite. Mineralization conditions of emeralds are known at the Cunas mine (Romero-Ordóñez et al 2021) formed at low temperature ~260-340°C, pressure ~850-2400 bar, high density 1,03 g/cm^3 and elevated salinity ~39% wt., as result of the mixture of two hydrothermal fluids.

The mineralizations have been dated at different ages, both in EEB and WEB. Most accepted age for the WEB deposits corresponds to the Eocene-Oligocene (Giuliani et al. 2019) during a pulse of tectonic uplift of Andes eastern cordillera (38-32 Ma, using ^{40}Ar-^{39}Ar in muscovite) and are younger than EEB (65 Ma, using Ar method too), framing this latest age in extensive deformation during Cretaceous-Paleogene margin. However, other authors propose similar ages for EEB and WEB, with important tectonic implications. Romero-Ordóñez (1999) gives an age of 67 Ma (using Rb-Sr in cogenetic carbonates) and Altenberger et al. (2022) gives ~47 to 51 Ma (using U-Pb-Th in parisite), so the discussion remains open to define the time and processes that formed the Colombian emeralds.

3 Methods

Petrography and stratigraphy studies were conducted in field and Universidad Nacional de Colombia, which are the baseline for the analyses developed within the "LitoCo" project fully financed by the same university.

A 1:1000 scale stratigraphic section was built along the Consorcio prospect, consisting of an ascending stratigraphic tunnel in an E direction and parallel to dip of W flank of the Muzo syncline (Figure 1). It consists of 444 m of non-poorly altered siliciclastic and mixed rocks, composed of mudstones, siltstones and grey blackish claystones interbedded with beds of decimetres and meters of fine-medium grained sandstones. Some beds are calcareous, locally fossiliferous and correspond to mudstone-wackestone rocks.

120 hand samples from the Consorcio prospect and Cunas mine were collected and classified to elaborate eleven polished thin sections (PTS). Together 3 PTS from CDTEC Gemlab (Bogotá, Colombia) underwent petrography and complementary micro-Raman spectroscopy. Were used Zeiss Axio Scope-A1 microscope and Horiba Scientific LabRAM Evolution Raman spectrometer coupled Olympus BX41 microscope. Nineteen rock samples from the Consorcio stratigraphic section (Figure 2) were ground and sieved with 60 mesh, separating 100 µm fraction to perform x-ray diffraction and x-ray fluorescence (thin fraction), as well as characterization of organic matter macerals (coarse fraction) with reflected light petrography. The Briquettes were prepared based on the ASTM D 2797 standard in ore and coal petrography 223-220 lab of Universidad Nacional de Colombia.

4 Results

4.1 Stratigraphy

Eight segments were recognized along the Consorcio section (Figure 2), grouping into two formations described from base to top, and defined in WEB and other mines (Terraza 2019).

Furatena formation covers the first 7 segments, consisting in ~133 m of black siltstones and mudstones with plane-parallel lamination of quartz, mica and organic matter interbedded with dm-thick sheet of very fine to medium grained sandstones, with more or less pyrite (associated with black levels rich in organic matter), either as massive microcrystalline crystals and red-orange ferruginous patinas, or as mm-thick concordant veins (especially in segment 4). Concordant veins of calcite+pyrite appear in segments 5 and 6, being more fissile due to grow of muscovite interbedded with black claystones and orange patinas. All formation has calcite patinas, except for a sporadic layer of mudstone-wackestone present in segment 7.

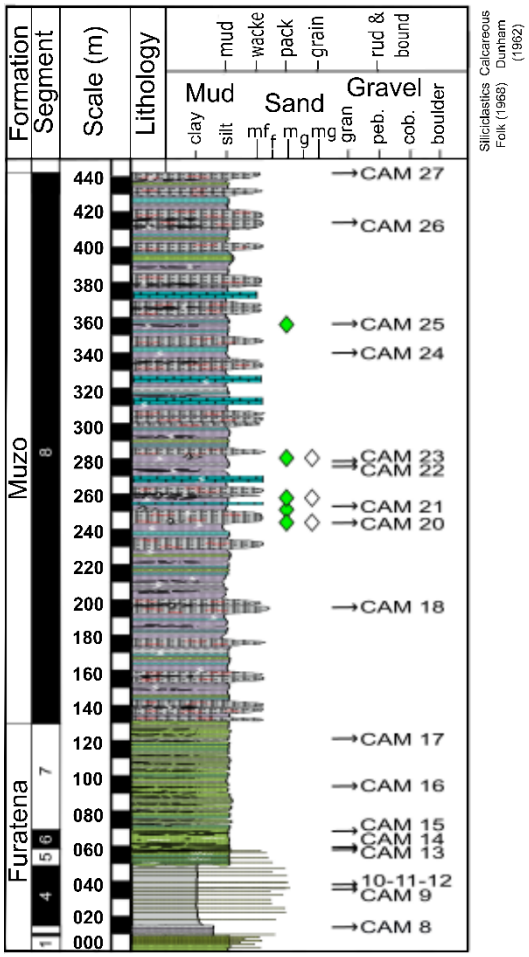

Figure 2. Stratigraphic column of Consorcio prospect, showing each of nineteen samples collected. Modified of Martín-Ravelo and Romero-Ordóñez (2022)

Muzo formation covers the upper part of segment 7 and segment 8, above to Furatena formation in net contact, marked by change from siliciclastics to more calcareous rocks without leaving the mixed character. They consist in ~311 m of organic-rich black siltstones and mudstones with plane-parallel lamination (organic levels up to 50 cm thick); interbedded with beds of very fine-fine sandstone meters thick (up to 5 m), with wavy plane-parallel surfaces cemented by carbonates and foraminifera fossils levels, which can be classified as mudstone-wackestone. Siltstones and mudstones have more fissility surfaces than lithologies of the Furatena formation, due to micas decrease. Muzo formation have millimetric veins of pyrite with ferruginous patinas concordant, also tangential- almost orthogonal (to stratification) fibrous calcite veins dm thick, in paragenesis with Cr-muscovite or fuchsite. These veins are cut by rhombohedral calcite and dolomite concordant veins, forming hydrothermal breccias with quartz, fluorite, parisite and emeralds.

Thickness of Muzo formation is greater than the reported in type section (~180 m) and the same as other mines (Jiménez 2017). All these observations (reported jointly by Martín-Ravelo and Romero-Ordóñez (2022)) for rocks from Furatena and Muzo formations allowed to interpret them as transgressive onlap deposits over inner ramp, as storm-influence lagoon, due to sedimentation regime change from siliciclastics to calcareous deposition. Contrast in thickness between the Consorcio section and type section may be due to half-graben basin geometry to explain the high angle thrust system and folds developed in WEB (Terraza 2019).

4.2 Petrography

Five stages of mineralization were recognized based on textures and cross-cut relations. From older to younger: premineral, albitization, carbonization (I), carbonization (II) and supergene.

Premineral is represented by low or unaltered rocks that show relictic textures and partial replacements, such as organic matter with clastic texture (lamination), recrystallization of foraminifera, and diagenetic cement (Figure 3a). Albitization occurs when albite replaces pre-existing minerals and introduce euhedral pyrite and muscovite. Carbonization (I) and (II) receive their names due to the development of fibrous calcite veins cut by rhombohedral carbonates veins (calcite+dolomite) (Figure 3b) in paragenesis with quarz, fluorite, parisite and emerald (Figure 3c, 3d).

Similarly, LitoCo project contemplates the evaluation of macerals combining micro-Raman spectrometry to evaluate the reflectance and thermal maturity reached by rocks during emerald mineralization and diagenesis.

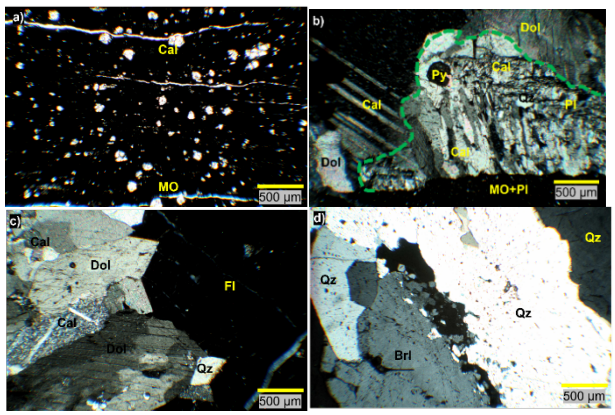

Figure 3. a Premineral stage (with foraminifera). **b** Rhombohedral carbonate veins (calcite and dolomite) cut fibrous calcite+pyrite veins. **c** Calcite + dolomite + quarz + fluorite ± parisite paragenesis in emerald veins. **d** Emerald (beryl) in paragenesis with quartz forming lamellae texture.

5 Research proposal (in development)

5.1 X-ray diffraction (XRD) and x-ray fluorescence (XRF)

Based on previous studies (González-Durán et al. 2021), we as research team of LitoCo project propose new methodologies to contribute to the exploration of emeralds and by-products, considering the proximity to other mines and taking advantage of the work near two important emerald

mines. XRD and XRF provide information of spatial variations in metasomatism because of evolution of main trapping emerald structures, even complementing diagenesis observation considering analysis as differential thermal curves (Araujo et al. 2004) and determining the paleo-conditions of host rock deposit (Mantilla et al. 2004). In addition, XRD-XRF analysis (low-cost geochemistry) provides information on the crystalline structure and composition of phosphates (monazite, xenotime, apatite), clay minerals, carbonates and feldspars present in emerald host rocks, so it can be evaluated the potential to produce fertilizers, pottery, and construction materials.

5.2 Gamma-ray spectrometry

Gamma-ray spectrometry allows the measure the radiation emitted by radioactive isotopes in host rock, seeking to quantify and allowing to determine the natural content of light REEs (e.g. Y, Sc, La, Ce, Nd, Sm, Eu, Tb) and other associated elements (V, Co, Cs and U), due to basin reduction conditions and presence of high phyllosilicates content (Condie 1991; Jiménez 2017), with a greater exploitation potential than conventional sources such as zircon, complementing the unassessed amounts of (Ce,La)-Parisite, Monazite and Ce-Bastnaesite in Colombian emerald deposits (Giuliani et al. 2019). As in the oil and gas industry, gamma ray spectrometry can be used to build logs like open hole logs, and therefore for use in regional exploration if combined with lithological logging (e.g., extant stratigraphic section) (Serra 1984).

6 Conclusions

Five mineralization stages were recognized in Cunas mine and Consorcio prospect, equally to other emerald mines (Puerto Arturo, Tequendama, La Pava, Coscuez). Therefore, there are great possibilities of developing this deposit and discover new opportunities in coming years. With a growing demand of REEs and raw materials, mining must be rethought to extract the maximum amount of materials that the mine produces and that are currently wasted, using relative new technologies.

Acknowledgements

To Universidad Nacional de Colombia, especially to PGP program with LitoCo project for support. To "Caracterización Tecnológica de Minerales" research group for gamma-spectrometry analysis and lattice lab (224-106A, Ciudad Blanca, Bogotá) for XRD-XRF analysis. Likewise, to professors Ariel Cadena, Gustavo Sarmiento, Juan Carlos Molano, Jimmy Fernández, Thomas Cramer and Fernando Romero. To the Rotlewicz brothers (Jimmy and Paul), the Rodríguez brothers (Orlando and Hugo), Carlos Rodríguez, and the countless emerald lovers (miners, businesspeople, researchers) who allowed samples, financial support and fieldtrip, laboratories, and experience.

References

Altenberger U, Rojas-Agramonte Y, Yang Y, Fernández-Lamus J, Häger T, Guenter C, Gonzalez-Pinzón A, Cahrris-Leal F, Artel J (2022) In Situ U–Th–Pb dating of parisite: Implication for the age of mineralization of Colombian emeralds. Minerals 12(10), 1232: 1-16. https://doi.org/10.3390/min12101232

Araujo JH, Francisco SN, Acchar W, Gomez UU (2004) Thermal Decomposition of Illite. Materials Research 7(2) http://doi.org/10.1590/S1516-14392004000200024

Branquet Y, Laumonier B, Cheilletz A, Giuliani G (1999) Emeralds in the eastern cordillera of Colombia: Two tectonic settings for one mineralization. Geology 27: 597-600. https://doi.org/10.1130/0091-7613(1999)027%3C0597:EITECO%3E2.3.CO;2

Condie KC (1991) Another look at rare earth elements in shales. Geochimica et Cosmochimca Acta 55(9): 2527-2531. https://doi.org/10.1016/0016-7037(91)90370-K

Giuliani G, Groat LA, Marshall D, Fallick AE, Branquet Y (2019) Emerald deposits: A review and enhanced classification. Minerals 9(2), 105: 1-63. https://doi.org/10.3390/min9020105

González-Durán AF, García-Toloza J, Bonilla GE, Cedeño-Ochoa CJ, Angarita-Sarmiento LG, Castañeda-Gómez AJ, Parra-Bastidas SD, Bocanegra-Rodríguez LC, Montaña-Cárdenas J, López-Castillo CL (2021) Geoquímica y mineralogía de la mina La Pava, Muzo-Quípama: Implicaciones en la exploración de esmeraldas en Colombia. Boletín de Geología, 43(2): 117-142. https://doi.org/10.18273/revbol.v43n2-2021007

Jiménez J (2017) Estudio químico, mineralógico y espectroscópico de las esmeraldas colombianas en los distritos mineros de Chivor, Muzo y Coscuez y su aplicación en la determinación de origen geográfico. MSc Thesis, Universidad Nacional de Colombia. Recovered from https://repositorio.unal.edu.co/handle/unal/63927

Mantilla FL, García RC, Uribe PE (2004) Caracterización y significado de la alofana y la haloysita en rocas de la formación Paja (Cretácico inferior). Borde occidental de la cordillera oriental, Colombia. Boletín de Geología, 26(43): 11-22. Recovered from https://revistas.uis.edu.co/index.php/revistaboletindegeologia/article/view/914

Martín-Ravelo AS, Romero-Ordóñez FE (2022) Petrografía de las rocas de Consorcio en la mina de esmeraldas de Cunas (Maripí, Boyacá). Relación estratigráfica con rocas del Valle Medio del Magdalena (Colombia). Boletín de Geología 44(2): 125-143. https://doi.org/10.18273/revbol.v44n2-2022006

Romero-Ordóñez FH, González-Durán AF, García-Toloza J, Rotlewicz-Cohen J, Cedeño-Ochoa CJ, Alvarado-González HR, Angarita-Sarmiento LG (2021) Mineralogy and fluid inclusions of the Cunas emerald mine, Maripí – Boyacá, Colombia. Earth Sciences Research Journal 25(2): 139-156. https://doi.org/10.15446/esrj.v25n2.90210

Romero-Ordóñez FH, Schultz-Güttler RA, Kogi K (1999) Geoquímica del Rubidio-Estroncio y edad de las esmeraldas colombianas. Geología Colombiana 25: 221-239. Recovered from https://repositorio.unal.edu.co/handle/unal/42082

Serra O (1984) 7. Natural gamma-ray spectrometry. In: Serra O (ed) Fundamentals of Well-Log Interpretation,15 vol. Amsterdam – Oxford – New York – Tokyo, pp 113-134. https://doi.org/10.1016/S0376-7361(08)70421-7

Terraza R (2019) Notas sobre el context tectonoestratigráfico de formación de las esmeraldas colombianas. Boletín Geológico 45: 37-48. https://doi.org/10.32685/0120-1425/boletingeo.45.2019.486

LA-ICP-MS trace element composition of stibnite from the Kizhnica-Hajvalia-Badovc ore field, Kosovo

Sławomir Mederski[1], Jaroslav Pršek[1], Konrad Kluza[1], Dimitrina Dimitrova[2]
[1]*AGH University of Science and Technology, Kraków, Poland*
[2]*Geological Institute, Bulgarian Academy of Sciences, Sofia, Bulgaria*

Abstract. The chemical composition and trace element concentration in stibnite from the Kizhnica-Hajvalia-Badovc (KHB) ore field (Kosovo) was studied. Trace element measurements in stibnite from 2 localities (Janjevo stibnite-quartz vein and Badovc stibnite-rhodochrosite breccia) were conducted using LA-ICP-MS technique. In addition to the typical enrichments in As, Pb, Hg, or Cu known from the literature, stibnite from the KHB ore field shows the highest known concentrations of Tl (up to 213 ppm) and Ag (up to 146 ppm). In addition, elevated concentrations of As (up to 4,100 ppm), Pb (up to 2,000 ppm), Hg (up to 316 ppm), and Cu (up to 46.9 ppm) are observed. The following three independent mechanisms of incorporation of the above-mentioned trace elements into the stibnite structure are presented: (1) $As^{3+} \leftrightarrow Sb^{3+}$; (2) $(Cu^{+} + Ag^{+}) + Pb^{2+} \leftrightarrow Sb^{3+} + \square$; and (3) $Tl^{+} + Hg^{2+} \leftrightarrow Sb^{3+} + \square$.

1 Introduction

Stibnite is the most common ore mineral of antimony and is present in a variety of deposit genetic types. Most of them are associated with hydrothermal systems - epithermal and mesothermal veins, sediment-hosted and Carlin-type Au deposits, but also hot-spring deposits (Seal et al. 2017). These deposits are often located on the periphery of orogenic Au deposits, intrusion-related Au deposits, and porphyry Cu-Mo deposits. The main production of antimony ores comes from quartz-stibnite veins and replacement Sb deposits (Fu et al. 2020; 2022).

Antimony deposits are usually mineralogically monotonous with the only economic mineral - stibnite. However, stibnite can occur in either Sb-Au, Sb-W, or Sb-As±Tl association, and thus can be characterized by various trace elements (Fu et al. 2020). Stibnite can incorporate into its structure both trivalent As^{3+}, but also, through heterovalent substitutions, divalent elements such as Pb^{2+}, or Hg^{2+}, and monovalent elements such as Cu^{+}, Ag^{+}, and Tl^{+}. The trace element data in stibnite measured by the LA-ICP-MS technique began to be published relatively recently (only after 2020), mainly from the world's largest Sb deposits located in China such as Xikuangshan, Daocaowan, Woxi, and Banxi (Fu et al. 2020; 2022; Song et al. 2022). However, some genetic types, particularly Carlin-type and sediment-hosted gold deposits (SHGD), have no data. And consequently, the nature of the behavior of the diagnostic pathfinder elements known for these environments (such as thallium, mercury, or arsenic) in the context of substitution mechanisms in stibnite, is not known.

In addition, data from numerous European deposits are lacking, with the only data coming from the Gerakario deposit in Greece (Stergiou et al. 2022). In Europe, there are several Sb-As±Tl deposits and mineral occurrences within the Mediterranean Region (Janković 1989). These can be divided into two groups - the Triassic and the Neogene. The first are associated with the intercontinental rift and volcanogenic-sedimentary sequences and are hosted mainly by carbonate rocks. On the other hand, Neogene deposits are associated with calc-alkaline volcanism along the closure zone of the ocean (Janković 1989). One of the regions of Neogene Sb mineralization is the Kizhnica-Hajvalia-Badovc (KHB) ore field in the Kosovo in Vardar Zone (Fig. 1). Hydrothermal mineralization that is responsible for the formation of stibnite-rich veins and breccias in the KHB ore field is associated with a concealed porphyry system (Mederski et al. 2022b). In this paper, we present data on trace elements in stibnite obtained by LA-ICP-MS technique and demonstrate possible substitution mechanisms in stibnite.

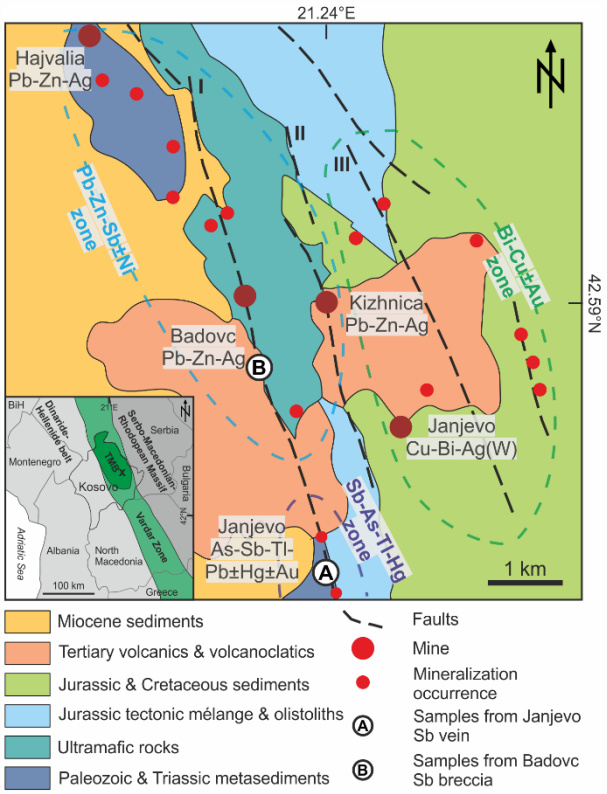

Figure 1. Simplified geological map of Kizhnica- Hajvalia-Badovc ore field with the sampling locations. Abbreviations: I = Hajvalia- Badovc Zone; II = Kizhnica Zone; III = Okosnica Zone.

2 Geology

The Kizhnica-Hajvalia-Badovc ore field is situated in the southern part of the Trepça Mineral Belt (TMB). In the KHB ore field area are present Paleozoic-Triassic metasedimentary complex (schists and marbles), Triassic-Jurassic ultramafic complex, Jurassic tectonic mélange with olistoliths, Jurassic-Cretaceous flysch series, Neogene volcanic and volcanoclastic rocks (mainly andesites), and Miocene sediments (Fig. 1). Moreover, the area is intersected by 3 major tectonic zones that controlled hydrothermal mineralization (Fig. 1).

The study area shows the presence of many styles of polymetallic hydrothermal mineralization: veins, stockwork-impregnation, carbonate-replacement, listvenite-hosted, and skarn/hornfels. Three documented Pb-Zn-Ag deposits occur within the KHB ore field (Kizhnica, Hajvalia, and Badovc) and they are associated with the Pb-Zn-Sb±Ni zone described by Mederski et al. (2021; 2022a) (Fig. 1). In addition, mineral occurrences associated with the Bi-Cu±Au system are described in the eastern part of the KHB ore field (Mederski et al. 2021), while a distal Sb-As-Tl-Hg mineralization is observed in its southern part (Mederski et al. 2022b) (Fig. 1).

3 Samples and methods

3.1 Investigated material

The studied samples containing stibnite were collected from 2 localities in the KHB ore field: Janjevo stibnite-quartz vein and Badovc stibnite-rhodochrosite breccia (Fig. 1).

Janjevo is a recently discovered location with As-Sb-Tl-Pb±Hg±Au mineralization hosted by Upper Triassic marbles (Mederski et al. 2022b). Two generations of stibnite have been distinguished here. The first generation occurs in the quartz-stibnite vein that intersects marbles. Stibnite forms prismatic needles up to about 5 cm (Fig. 2a) and occurs in association with quartz, minor dolomite, pyrite, As-Tl-Sb-Hg pyrite, sphalerite, and secondary minerals: gypsum, valentinite, and native sulfur. The second generation forms small, disseminated aggregates inside the dolomitized lenses in the As-Sb-Tl-Pb profile in the marbles. First-generation stibnite was used for the study using the LA-ICP-MS technique.

Stibnite samples from the second locality were collected from alteration zones and andesite-listvenite contacts of the Pb-Zn-Ag Badovc deposit on the hills north of Shashkofc. The dominant here are massive-banded Pb-Zn-Sb ores, as well as Pb-Zn-Sb±Ni listvenite hosted ores (Mederski et al. 2022a). The rhodochrosite-stibnite breccia ores that are the subject of this research, with stibnite crystals up to 2 cm in size (Fig. 2b-c), have also been discovered here. Stibnite occurs in simple paragenesis with rhodochrosite, sphalerite, and pyrite. In addition, some ore fragments show strong brecciation, while stibnite was found in breccias cutting across the previously mentioned massive-banded Pb-Zn-Sb ores. In addition, one sample with massive stibnite was found in association with quartz, pyrite, sphalerite and berthierite.

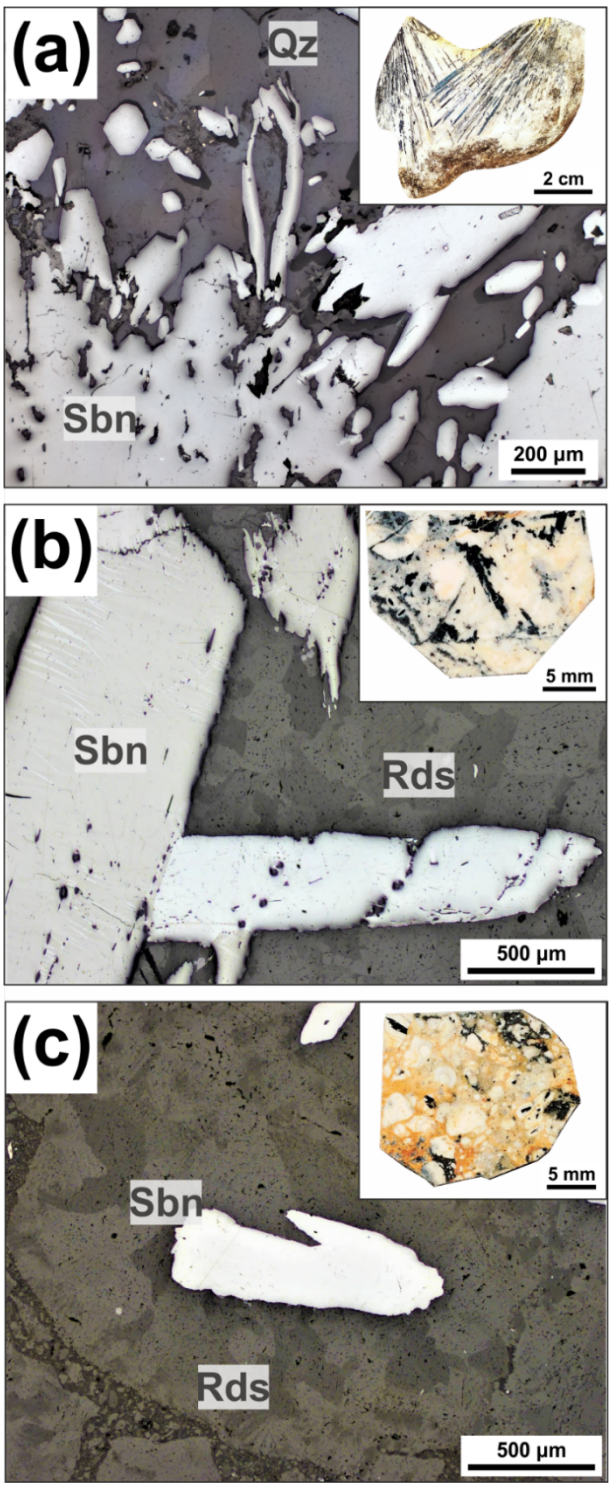

Figure 2. Hand specimen and reflected light microphotographs of selected stibnite from the KHB ore field. **(a)** Typical stibnite needles from quartz vein - Janjevo. **(b)** Idiomorphic stibnite crystal with visible polysynthetic twinning from rhodochrosite ore, Badovc. **(c)** Euhedral stibnite crystal in rhodochrosite breccia, Badovc. Qz = Quartz; Rds = Rhodochrosite; Sbn = Stibnite.

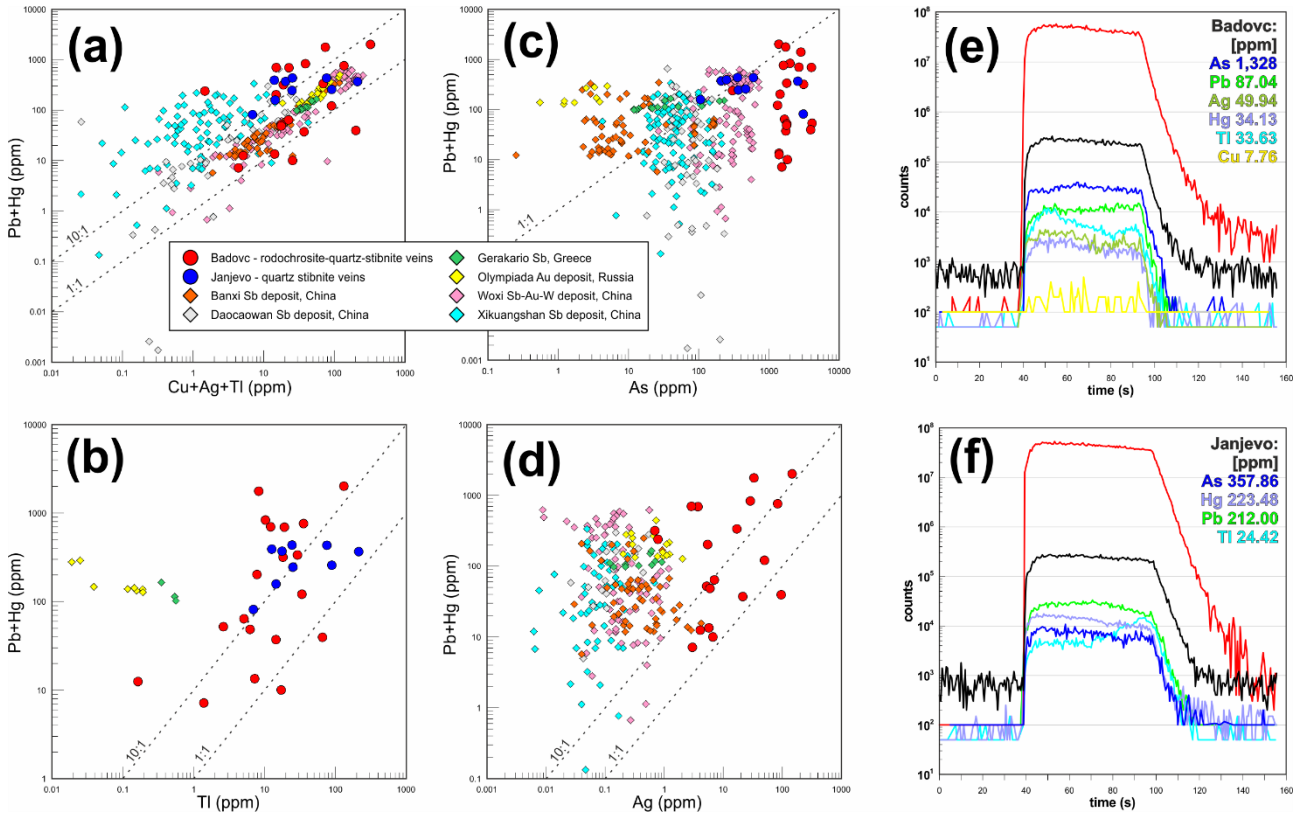

Figure 3. Compositional relationships in stibnite from the KHB ore field compared with available literature data (Fu et al. 2020; 2022; Silyanov et al. 2022; Song et al. 2022; Stergiou et al. 2022) **(a-d)**. Selected time-resolved laser ablation ICP-MS depth profiles of stibnite from Badovc **(e)** and Janjevo **(f)**.

3.2 Analytical techniques

Preliminary chemical analyses of stibnite were carried out by electron microprobe (EPMA) - JEOL Super Probe 8230 in the Laboratory of Critical Elements at Faculty of Geology, Geophysics, and Environmental Protection, AGH-UST, Kraków Poland.

Trace element concentrations in stibnite were measured by laser ablation inductively coupled plasma mass spectrometry (LA-ICP-MS) using a PerkinElmer ELAN DRC-e ICP mass spectrometer combined with a New Wave UP193-FX excimer laser ablation system at the Geological Institute, Bulgarian Academy of Sciences, Sofia, Bulgaria. The ablation was conducted in He medium. To maximize sensitivity, the ICP-MS was optimized daily concerning the oxide production rate of ThO/Th (0.5%). Operating conditions of the laser system include 6 Hz repetition rate; 20 to 35 µm spot size; and energy density on analyzed minerals and standards of 3.3-3.4 J/cm^2 (at 35 µm spot) and 2.9-3.1 J/cm^2 (at 20 and 25 µm spot). The nebulizer gas flow rate was 0.8 L/min, while auxiliary and make-up gas flows rates were 0.92 L/min. The analysis time was 100 s (background: 40 s, laser-on the sample: 60 s). The acquisition dwells time was set to 0.02 s for ^{71}Ga, ^{74}Ge, ^{107}Ag, ^{125}Te, ^{202}Hg, ^{205}Tl; to 0.03 s for ^{115}In, ^{118}Sn; to 0.04 s for ^{197}Au, and 0.01 s for all other monitored isotope masses - ^{34}S, ^{49}Ti, ^{51}V, ^{53}Cr, ^{55}Mn, ^{57}Fe, ^{59}Co, ^{60}Ni, ^{65}Cu, ^{66}Zn, ^{75}As, ^{77}Se, ^{82}Se, ^{95}Mo, ^{111}Cd, ^{121}Sb, ^{181}Ta,^{182}W, ^{208}Pb, and ^{209}Bi. Targeted spots in the polished sections were predefined to avoid obvious mineral inclusions. Repeated external standardization was conducted by analyzing NIST SRM 610 glass standard and the USGS Mass 1 sulfide standard. Data reduction was undertaken using antimony (determined by EPMA) as an internal standard and by SILLS software (Guillong et al. 2008).

4 Stibnite geochemistry

The main trace elements found in stibnite from the KHB ore field are As, Pb, Hg, Tl, Cu and Ag. Stibnite from both localities shows a similar geochemical signature, although they differ mainly in Cu and Ag content.

Arsenic is the major substituting element in the studied stibnite (Fig. 3c). Higher contents of As are observed in stibnite from Badovc (302–4,100 ppm) - the median is 1,760 ppm, while in Janjevo it is 206–3,080 ppm (median: 368 ppm).

The main divalent elements are **lead** and **mercury**. The medians for lead content are, respectively: 120 ppm for Janjevo and 144 ppm for Badovc. However, individual analyses reach up to 2,000 ppm of Pb with evident homogeneous spectra (Fig. 3e-f). On the other hand, stibnite from Janjevo shows significantly higher Hg contents (45.40–316 ppm; median 102 ppm) than in Badovc (0.53–34.13 ppm; median 6.09 ppm).

Both localities show the presence of **thallium**: in Janjevo the concentrations range 6.94–213 ppm (median 24.42 ppm), and in Badovc 0.16–132 ppm

(median 12.18 ppm) (Fig. 3b). In addition, lower **copper** concentrations are observed, with ranges of 1.08–2.79 ppm (median 1.89 ppm) in Janjevo and 0.69–46.9 ppm (median 7.76 ppm) in Badovc. In addition, stibnite from Badovc exhibits a **silver** concentration between 0.69 and 146 ppm (median 6.30 ppm) (Fig. 3d).

5 Discussion

The mechanisms of trace elements incorporation in stibnite have previously been described by Fu et al. (2020) - $2Sb^{3+} \leftrightarrow Cu^{+} + Pb^{2+} + As^{3+}$, and Song et al. (2022) - $3Sb^{3+} \leftrightarrow As^{3+} + 2Cu^{+} + Hg^{2+} + Pb^{2+}$. Analysis of trace elements in stibnite from the KHB ore field, as well as higher concentrations of some elements such as Ag and Tl, suggests the presence of several independent substitutions in stibnite. In addition, LA-ICP-MS spectra show a homogeneous distribution that suggests the presence of these metals in the stibnite structure rather than inclusions (Fig. 2e-f).

First, the arsenic in the KHB ore field does not correlate significantly with any other trace element, suggesting the presence of a simple $As^{3+} \leftrightarrow Sb^{3+}$ substitution.

Secondly, stibnite from the KHB ore field shows the highest concentrations of other monovalent cations, such as Cu^{+} reported so far, including Tl^{+} (Fig. 3b) and Ag^{+} (Fig. 3d). In addition to the character of the fluids, this is because the rhodochrosite breccia from Badovc and the quartz vein from Janjevo lack typical base-metal sulfides like galena or chalcopyrite, which could preferentially incorporate these elements (Pb, Cu, Ag, Tl).

Copper as in other localities correlates well with Pb (0.82) (Fu et al. 2020; 2022), but is also well correlated with Ag (0.82), while Ag also correlates with Pb (0.57), and no relationship is seen between Ag and Hg (-0.01). These results suggest the presence of heterovalent $(Cu^{+} + Ag^{+}) + Pb^{2+} \leftrightarrow Sb^{3+} + \square$ substitution in stibnite from Badovc. In contrast to other known localities, silver, rather than copper, is more important in this substitution in Badovc.

In addition, stibnite from the KHB ore field shows the highest enrichment in thallium reported in the literature so far (Fig. 3b). The mechanism of thallium incorporation is related to mercury, both metals can be named diagnostic pathfinder elements for Carlin-type gold deposits and are found in numerous hydrothermal sediment-hosted systems. The suggested mechanism for incorporation of Tl and Hg is $Tl^{+} + Hg^{2+} \leftrightarrow Sb^{3+} + \square$. Furthermore, observing the complex graph of Pb+Hg *vs.* Cu+Ag+Tl (Fig. 3a), it is visible that the stibnite from China's sediment-hosted Sb deposits Xikuangshan and Daocaowan does not follow the trend observed in other known deposits caused by $Cu^{+} + Pb^{2+} \leftrightarrow Sb^{3+}$ substitution. Stibnite from these locations has the highest Hg content, even above 100 ppm (Fu et al. 2020; Song et al. 2022), and clearly some not-measured monovalent element is missing - probably thallium, which is very common in such systems.

Investigations on stibnite from the KHB ore field show that at low hydrothermal temperatures stibnite (Badovc: 180-240°C, Janjevo: 230-260°C; Mederski et al. 2022a) can incorporate a wide range of trace elements such as As, Pb, Hg, Tl, Ag, and Cu.

Acknowledgements

The research was funded by the Society of Economic Geologists Canada Foundation (SEGCF) Student Research Grant 2019 and the Society of Economic Geologists Foundation (SEGF) Newmont Mining Corporation Student Grant 2020.

References

Fu S, Hu R, Bi X, Sullivan NA, Yan J (2020) Trace element composition of stibnite: Substitution mechanism and implications for the genesis of Sb deposits in southern China. Appl Geochem 118:104637

Fu S, Wang T, Yan J, Pan L, Wei L, Lan Q, Fu S (2022) Formation of the Banxi Sb deposit in Eastern Yangtze Block: Evidence from individual fluid inclusion analyses, trace element chemistry, and He-Ar-S isotopes. Ore Geol Rev 146:104949

Guillong M, Meier DL, Allan MM, Heinrich CA, Yardley BWD (2008) Appendix A6: SILLS: A MATLAB based program for the reduction of laser ablation ICPMS data of homogeneous materials and inclusions. In: Sylvester P (ed). Laser Ablation ICP–MS in the Earth Sciences: Current Practices and Outstanding Issues. Vancouver, Mineral Assoc Canada, Short Course 40:328–333

Janković S (1989) Sb-As-Tl Mineral Associations in the Mediterranean Region. Int Geol Rev 31:262–273

Mederski S, Pršek J, Dimitrova D, Hyseni B (2021). A Combined EPMA and LA-ICP-MS Investigation on Bi-Cu-Au Mineralization from the Kizhnica Ore Field (Vardar Zone, Kosovo). Minerals 11:1223

Mederski S, Pršek J, Dimitrova D (2022a) Trace elements in sphalerite from the Kizhnica-Hajvalia-Badovc ore field, Kosovo: an example of In-bearing sphalerite. In: The Critical Role of Minerals in the Carbon-Neutral Future 16th Biennial SGA Meeting: Rotorua, New Zealand, 2022. Proceedings Volume 1:239–242

Mederski S, Pršek J, Majzlan J, Kiefer S, Dimitrova D, Milovský R, Bender Koch C, Kozień D (2022b) Geochemistry and textural evolution of As-Tl-Sb-Hg-rich pyrite from a sediment-hosted As-Sb-Tl-Pb±Hg±Au mineralization in Janjevo, Kosovo. Ore Geol Rev 151:105221

Seal RR, Schulz KJ, De Young JH, Sutphin DM, Drew LJ, Carlin JF, Berger BR (2017) Antimony. In: Critical mineral resources of the United States–Economic and environmental geology and prospects for future supply. U.S. Geological Survey, pp. 1–30

Silyanov SA, Sazonov AM, Naumov EA, Lobastov BM, Zvyagina YA, Artemyev DA, Nekrasova NA, Pirajno F (2022) Mineral Paragenesis, formation stages and trace elements in sulfides of the Olympiada gold deposit (Yenisei Ridge, Russia). Ore Geol Rev 143:104750

Song X, Lai J, Xu J, Liu X, Li B, He H, Wang Y, Shi J, Wang C, Wen C (2022) Material Source and Genesis of the Daocaowan Sb Deposit in the Xikuangshan Ore Field: LA-ICP-MS Trace Elements and Sulfur Isotope Evidence from Stibnite. Minerals 12:1407

Stergiou CL, Melfos V, Voudouris P, Papadopoulou L, Spry PG, Peytcheva I, Dimitrova D, Stefanova E (2022) A Fluid Inclusion and Critical/Rare Metal Study of Epithermal Quartz-Stibnite Veins Associated with the Gerakario Porphyry Deposit, Northern Greece. Appl Sci 12:909

Rapid and on-site elemental quantitative analyses using handheld LIBS : the Beauvoir granite case study

Naila Mezoued[1], Cécile Fabre[1], Jean Cauzid[1], Michel cathelineau[1], Christophe Ballouard[1]
[1]*GeoRessources CNRS-Université de Lorraine, BP 70239, 54506 Vandoeuvre-les-Nancy, France*

Abstract. Acquiring geochemical data during mineral exploration is long and costly. Thus, using portable spectroscopic tools such as a handheld LIBS device to obtain qualitative and quantitative data on-site within seconds represents a breakthrough for the mining industry. In this context, light elements Li and Be as well as trace elements Rb and Cs were targeted to develop quantitative models using a handheld LIBS device. Hole core portions from the Beauvoir granite deposit were analyzed with limited sample preparation to reproduce field conditions. Different normalization methods (SNV, total spectrum area, and internal standard) were assessed to enhance model performances. Both univariate and multivariate approaches were evaluated. The final calibration curve for each element was chosen based on the lowest RMSE obtained. Furthermore, considering the heterogeneous character of rock samples and potential signal fluctuation due to laser or/and plasma fluctuation, the repeatability of the technique was tested using successive LIBS measurements on the same sample.

1. Introduction

One of the key steps to locate potential ore deposits is acquiring reliable geochemical data representative enough to highlight the prevalence of targeted elements across a study area. To do so, samples from outcrops or drilled cores, are prepared and analyzed to determine the whole rock elemental composition. It can take several weeks to months before results are available, which delays considerably effective decision-making and strategy optimization during prospecting.

In this framework, the use of portable spectroscopic devices such pLIBS to develop innovative geochemical methods seems more promising than ever(Senesi and al 2021). The spectral signal obtained provides qualitative both quantitative data in near real-time with minimal sample preparation(Fabre and al 2021; Wise and al 2022). Therefore, beyond field observations, geologists have now the ability to generate valuable geochemical information on the field to optimize rocks sampling, identify geochemical pathfinders, and improve decision-making during field exploration or drilling campaigns. This extended abstract focuses on how to estimate the elemental composition of unprepared core samples, in particular, lithium content using a handheld LIBS device.

2. Methodology

2.1 laser-induced breakdown spectroscopy (LIBS) technique

Similar to a laboratory setup(Miziolek 2006), a handheld LIBS device uses a high-energy laser to vaporize a fraction of the material at the surface of a sample initiating a micro-plasma plume. As the excited atoms, ions, and molecules forming the plasma return to low energy levels, photons are expelled. The emitted light is then collected and processed through detectors and broadband spectrometers. The atomic spectrum obtained records the signal intensity at specific wavelengths. The distinct position of emission lines reveals the elemental composition of a sample while measuring the concentration of these elements requires individual calibration curves.

The specific model used is the Z300 portable LIBS (SciAps) which is characterized by a 1064 nm pulsed Nd-YAG laser that delivers 5-6 mJ per pulse at a repetition rate set at 10 Hz. its spectrometers cover a large spectral band from 190 to 950 nm allowing elements detection from H to U. The analyses are performed at atmospheric pressure and ambient temperature but under constant argon flush to enhance signal intensity. No sample preparation is required except for a relatively flat surface to guarantee signal quality.

2.2 The Beauvoir granite Although the superficial part of the Beauvoir granite was exploited since the 19th for kaolin, it was only in 1985 during the first Geologie profonde de la France (GPF) drilling project that the lithium potential of the unaltered granite was discovered(Cuney and al 1992). This rare metals leucogranite characterized by high Li, Rb, Cs, Nb, Ta, P, and F content is composed mainly of quartz, albite, and Li-rich micas (lepidolite and zinnwaldite) while phosphate minerals, fluorite, topaz, and orthoclase can be found in varied proportions through the magmatic body(Rossi and al 1987). Since GPF, two drilling campaigns were conducted by Imerys. The first one explores the northern, central, and southern parts of the granite. While, the second, more extensive, started in 2021, and will continue till 2023 as part of the EMILI project. The project intend to confirm the economic potential of the deposit for lithium extraction and refine the Beauvoir granite geological model to achieve Imerys provisional plan to start production by 2028.

2.2 Samples

LIBS technique is sensitive to chemical matrix effects (El Haddad and al 2014). thus, to quantify effectively an element, it is recommended to use reference samples of the same matrice composition to calibrate the spectral signal. Hence, to represent best the homogeneous composition of the Beauvoir granite and determine lithium content in hole core portions (Figure 1), 15 granite samples from the 2018 and 2021 drilling campaigns were analyzed as references. The samples selected cover the broad range of lithium concentrations observed in the beauvoir granite, ranging from low (Li < 1000 ppm) to high (Li > 6000 ppm) values. Only unaltered or very low alteration percentage rock samples were considered. The greisen and kaolinized facies, not targeted for lithium extraction, were excluded. To extend the calibration curve to lithium-depleted samples, three more granite samples from massif central containing low grades (70-334ppm) were also included.

2.3 Data acquisition and processing The LIBS analyses were acquired according to a

Figure 1. Major Li emission lines from handheld LIBS spectrum.

vertical profile covering the total length of the core portions, with 1 point placed every

Figure 1. Major Lithium emission lines from the NIST LIBS database.

centimeter. Each point is in fact 36 zones analyzed arranged in a rectangular shape grid (2.7x2.5 mm). The signal obtained for a point corresponds to the average signal of 4 laser shots for each zone. The mean size of a LIBS micro-plasma crater is around 300 um. Thus, Acquiring a significant number of shots per sample allows us to i) reduce any shot-to-shot variability caused by the plasma fluctuation and ii) obtain representative LIBS spectra of the entire sample, especially in heterogenous compositions such as rocks.

The emission lines of the targeted elements were identified using the handheld LIBS spectral database and NIST database. Then, a processing sequence was implemented using Spectragryph 1.3 software to perform individual spectrum baseline correction and extract the peak area at specific spectral intervals. The handheld LIBS software (ProfileBuilder) can be used to generate internal calibration curves accessible on the tool(Fabre 2022). However, due to the large number of data acquired on whole core portions (> 300 points per sample), external regression models were built using statistical computing software. The R-squared (R^2) and root mean squared error (RMSE) were used to evaluate statistically each model.

3. Results and discussion

3.1 LIBS elements detection Using handheld LIBS allows us to detect both major elements (Si, Al, Na, K, and Li) forming most of the Beauvoir granite minerals as well as elements such as Rb, Cs, and Be occuring in smaller amounts. The lithium signal is mostly observed in 4 intervals at 460, 610, 670, and 812 nm (Figure 1). The triple peak at 460 nm appears to be correlated with the highest lithium concentrations.

Rb and Cs, were also investigated, considering their potential to be co-extracted from lepidolite(Zhang 2022), the main Li-bearing mineral in the Beauvoir granite. The atomic emission lines of these elements are mostly visible in the near-infrared region at 779-794 nm for Rb and 852-894 nm for Cs. Since, the average content of Be in the Beauvoir granite is above the detection limit of the LIBS tool, the Be signal could be identified at 225, 569, and 555 nm.

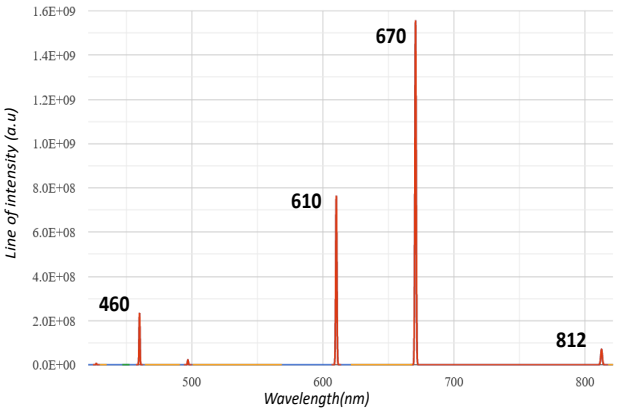

3.2 Quantitative analysis

Figure 2 displays the quantitative models for lithium developed on the Beauvoir granite samples. Multiple approaches were tested (unshown data) either using the sum of lithium signal over the selected emission lines or calculating the ratio of the total lithium signal to the signal of chosen elements on normalized and raw LIBS spectra. Overall, the lithium signal acquired by the LIBS tool correlates linearly with the geochemical data (70 to 7950 ppm) of the reference samples. The results obtained show that the statistical performances of the Li calibration curve (R2=0.95, RMSE=608 ppm) were improved by using Si, Al, Rb, and Mn as internal standards and normalizing the LIBS

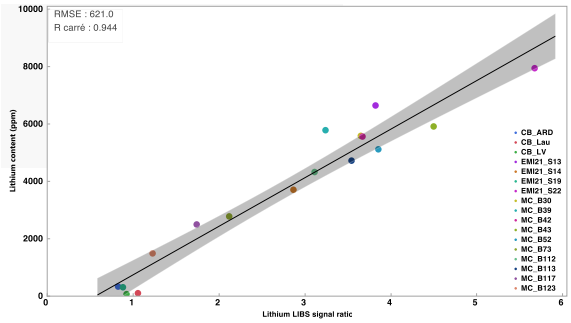

Figure 2. Lithium and Rubidium quantitative models developped using Handheld LIBS analyses.

spectra acquired by the total area of each individual spectrum. Although tested, no distinct improvement was made using multivariate models for lithium quantification.

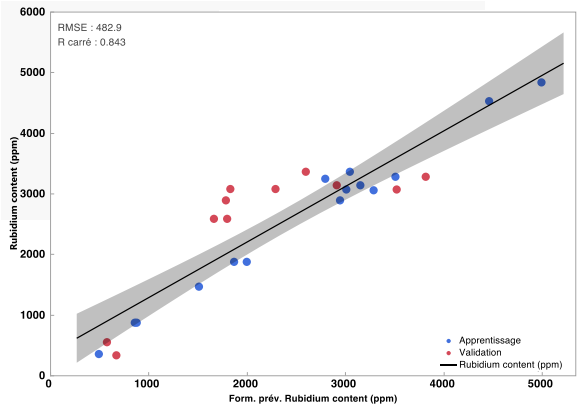

Considering the inhomogeneous character of rock samples, the shift observed on some samples could reflect physical matrix effects such as texture, hardness, or alteration proportion on the ablation process. In fact, work is still going on to determine how specific facies and grain size as well as veins occurrence can impact models prediction.

While the trace elements Rb, Cs, and Be were well detected by the LIBS device, none of the univariate models tested produced robust results, hence multivariate models were implemented to improve the overall quantification performance for these elements. The particular method used is interval PLS regression which allows building models to include multiple explanatory variables by selecting specific spectral intervals. The results illustrate the relation between the actual values of these elements in the reference samples and the predicted values of the multivariate models developed. The best model calculated for Rb includes five components and shows R^2=0.84 and RMSE=482 ppm (Figure 2). For Cs, 6 components were used to obtain R^2=0.89 and RMSE=131 ppm. Beryllium model shows a performance of R^2 =0.99 and RMSE of 4 ppm. Although, Be and Cs models should be completed by further analyses since only a limited number of the overall granite samples were included due to the lack of geochemical data.

3.3 Measures repeatability

One of the challenges of quantitative LIBS analyses is to guarantee a similar signal during separate measurements on the same sample due

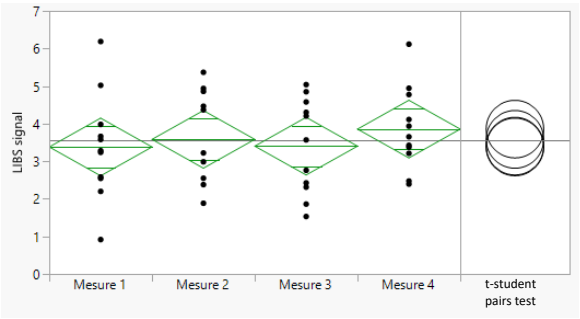

to potential fluctuation of laser or plasma parameters, especially in heterogeneous samples such as rocks. In order to compare the LIBS signal obtained on the same sample, during successive measurements with same portable tool and identical acquisition settings, 4 separate measurements performed at 2 different locations on the granite sample were acquired (Figure 3).

Next, an one way ANOVA test was computed to assess the variation of the LIBS ratio signal normalized at the total area between different measurements.The results obtained for all groups (F-value = 0.33/ p-value = 0.80) and between pairs groups revealed no statistically significant difference in the LIBS signal ratio obtained between the 4 measures on the same sample. This implies that the sampling strategy used which consists of analyzing a consequent number of points organized according to a vertical profile, helps to ensure a reliable LIBS signal during separate measurements of the same sample.

Figure 3. Analysis of variance performed on whole rock signals obtained from 4 separate LIBS measurements acquired on the same granite sample

Conclusion

This work aims to develop analytical methodologies to generate rapid quantitative geochemical data on unprepared core samples during mineral prospection. For this purpose, the handheld LIBS, which can detect both light and heavy elements, was used to build quantitative models to predict the concentration of light elements Li and Be as well as trace elements Rb and Cs. Reference samples were selected from the targeted deposit, the Beauvoir granite, in order to limit chemical matrix effects. Depleted granite samples from massif central were also analyzed to cover low-concentration values. Considering the heterogeneous character of granite samples, multiple analysis points were acquired then averaged to obtain a representative LIBS signal over 4m core portions. Both, Univariate and multivariate analyses were applied on normalized (total area spectrum, SNV, internal standard) and raw LIBS spectra to assess the most statistically robust model for each element. Finally, the evaluation of separate measurements of the same sample reveals no statistically significant difference between the mean LIBS signal ratio obtained on the same sample. Overall, LIBS demonstrate great potential to generate rapid and reliable geochemical data on unprepared granite sample to support-effective decision-making during exploration campaigns on potential ore deposits.

Acknowledgments

We would like to acknowledge Imerys and LabEx RESSOURCES 21 [ANR-10-LABX-21-01] for providing financial support to this study. M.Cathelineau and C.Ballouard for providing a number of the granite samples analyzed and the related geochemical data.

References

Cuney, M., Marignac, C., Weisbrod, A., 1992. The Beauvoir topaz-lepidolite albite granite (Massif Central, France); the disseminated magmatic Sn-Li-Ta-Nb-Be mineralization. Economic Geology 87, 1766–1794. https://doi.org/10.2113/gsecongeo.87.7.1766

El Haddad, J., Canioni, L., Bousquet, B., 2014. Good practices in LIBS analysis: Review and advices. Spectrochimica Acta Part B: Atomic Spectroscopy 101, 171–182. https://doi.org/10.1016/j.sab.2014.08.039

Fabre, C., Ourti, N.E., Ballouard, C., Mercadier, J., Cauzid, J., 2022. Handheld LIBS analysis for in situ quantification of Li and detection of the trace elements (Be, Rb and Cs). Journal of Geochemical Exploration 236, 106979. https://doi.org/10.1016/j.gexplo.2022.106979

Fabre, C., Ourti, N.E., Mercadier, J., Cardoso-Fernandes, J., Dias, F., Perrotta, M., Koerting, F., Lima, A., Kaestner, F., Koellner, N., Linnen, R., Benn, D., Martins, T., Cauzid, J., 2021. Analyses of Li-Rich Minerals Using Handheld LIBS Tool. Data 6, 68. https://doi.org/10.3390/data6060068

Miziolek, A.W., Palleschi, V., Schechter, I., 2006. Laser Induced Breakdown Spectroscopy. Cambridge University Press.

ROSSI, P., AUTRAN, A., BURNOL, L., CUNEY, M., OHNENSTETTER, D., MONIER, C., PIANTONE, P., RAIMBAULT, L., VIALLEFOND, L., 1987. Logs pétrographiques et géochimiques du granite de Beauvoir dans le sondage Echassières I. Minéralogie et géochimie comparées. Géol. Fr 111–135.

Senesi, G.S., Harmon, R.S., Hark, R.R., 2021. Field-portable and handheld laser-induced breakdown spectroscopy: Historical review, current status and future prospects. Spectrochimica Acta Part B: Atomic Spectroscopy 175, 106013. https://doi.org/10.1016/j.sab.2020.106013

Wise, M.A., Harmon, R.S., Curry, A., Jennings, M., Grimac, Z., Khashchevskaya, D., 2022. Handheld LIBS for Li Exploration: An Example from the Carolina Tin-Spodumene Belt, USA. Minerals 12, 77. https://doi.org/10.3390/min12010077

Zhang, X., Chen, Z., Rohani, S., He, M., Tan, X., Liu, W., 2022. Simultaneous extraction of lithium, rubidium, cesium and potassium from lepidolite via roasting with iron(II) sulfate followed by water leaching. Hydrometallurgy 208, 105820. https://doi.org/10.1016/j.hydromet.2022.105820

Pyrite analysis enhanced by dimensionality reduction: investigating texture, trace elements, and sulphur isotope signatures in the Kibali gold district, DRC.

Yann Mpaka Waku[1, 2, 3], Bjorn P. von der Heyden[1], Gary Hurst[2], David Lawrence[2], Etienne Mwandale[2], Sarah Glynn[4, 5]

[1] Department of Earth Sciences, Stellenbosch University, South Africa
[2] Barrick Gold Corporation, Toronto, ON, Canada
[3] Department of Geosciences, University of Kinshasa, DR Congo
[4] School of Geosciences, University of the Witwatersrand, Johannesburg, South Africa
[5] GFZ German Research Centre for Geosciences, Potsdam, Germany

Abstract. Pyrite is the most abundant sulphide mineral in the various ore zones hosted within the world-class Kibali gold district. Because of its affinity for trace elements and gold incorporation, pyrite mineral chemistry is increasingly being used as a powerful tool to assess the characteristics of ore formation. This study presents a novel dimensionality reduction-based approach for pyrite classification. This approach incorporates the strengths of both Uniform Manifold Approximation and Projection (UMAP) and Principal Component Analysis (PCA) with k-Means clustering to analyse the large trace element datasets derived from in-situ laser ablation inductively coupled plasma mass spectrometry (LA-ICP-MS) including sulphur isotope from Secondary Ion Mass Spectrometry (SIMS). The results suggest that 8 clusters may be defined from the pyrite mineral chemistry signatures. This clustering served to direct a refined classification relative to the initial textural analysis. We anticipate that our approach may be adopted by other workers who wish to disentangle complex pyrite growth and gold mineralisation histories in a variety of geological contexts.

1. Introduction

Archean greenstone belts are well-known metallogenic settings known for hosting a significant number of orogenic gold deposits (e.g. Kalgoorlie, Kurnalpi, Pilbara, Abitibi, Barberton, Kibalian, and others). Deciphering the timing and mechanisms of gold mineralisation within these belts is a non-trivial task, given that they have commonly experienced protracted and complex geological histories. Increasingly, studies are utilising pyrite trace element signatures as one of the suites of tools to better understand the conditions giving rise to ore formation. The utility of pyrite mineral chemistry is ensured by its ubiquity within orogenic gold deposits (where auriferous pyrites commonly represent a significant ore mineral), and by its propensity to incorporate a range of trace elements into its mineral structure. Laser-Ablation Inductively Coupled Plasma Mass Spectroscopy (LA-ICP-MS) is increasingly applied as the analytical tool of choice, especially when coupled to traditional microscopy investigations that detail the pyrite mineral textures. The power of LA-ICP-MS approaches is that they can quantify the concentration of multiple elements simultaneously at a spatial resolution as small as 15 µm and in either spot or mapping mode. The large and rich datasets that emanate from LA-ICP-MS studies are highly amenable to further detailed investigation using dimensionality reduction and 'big data' techniques.

The Kibali gold district, located in the Congo Craton, comprises a number of deposits with a total Au endowment of greater than 23 Moz (Allibone et al. 2020). Within these deposits, Au is hosted primarily (~90%) in auriferous pyrite (Lawrence 2011; Bird 2016; Allibone et al. 2020). Therefore, a careful investigation of pyrite would provide a significant opportunity to investigate the genesis of gold mineralisation in this district. This study aims to provide further insight into the textures, trace elements, and sulphur isotope characteristics of pyrite in the Kibali gold district using LA-ICP-MS and Secondary Ion Mass Spectrometry (SIMS) analyses. We developed a new combination of dimensionality reduction methods, comprising Uniform Manifold Approximation and Projection (UMAP) and Principal Component Analysis (PCA) with k-Means clustering to classify and analyse trace elements in pyrites. Our work thus highlights the benefits of dimensionality reduction in mineral chemistry analyses and highlights its utility towards improving pyrite trace element classification and interpretation.

2. Regional and local geology

The Kibalian Moto greenstone belt is located in the Neoarchean northeastern Congolese Congo Craton (Fig. 1a). The belt comprises volcanosedimentary rocks deposited from before 2640 Ma until ~2625 Ma (Allibone et al. 2020). The central part of the Moto greenstone belt is the most gold endowment zone, where several deposits and prospects are aligned within the ca. 60 km boundary belt structure known as the "KZ trend".

The Karagba-Chauffeur-Durba (KCD) deposit contains 85 to 90% of the current gold resources in the Kibali Gold Mine permit. The deposit (Fig. 1b) is hosted by metamorphosed volcanosedimentary rocks and is characterised by large hydrothermal alteration. The pre-ore stage ACSA-a alteration —

an acronym for "Albite, Carbonate, Silica, Alteration" with -a indicating less destructive alteration and -b denoting total destruction of the original rock texture—occurred during the tight to the isoclinal folding event, while the ore-stage exhibits a quartz-carbonate-sulphides-gold paragenesis associated with the more texturally damaging ACSA-b alteration (Lawrence 2011; Bird, 2016; Allibone et al., 2020). The mineralisation penetrates and replaces the siliclastic rocks, BIF, and chert host rocks lithologies, typically manifesting as fine disseminations or cm to mm-sized sulphide veins. Recent studies suggest the possibility of pre-metamorphic gold mineralisation in the KCD area, as gold grains in conglomerate units were found to be larger in size and to occur mainly within the gangue mineral assemblage as free gold, distal to sulphide minerals (Mpaka et al. submitted).

Apart from the KCD deposit and its peripheral deposits (Gorumbwa, Kombokolo, Rhino and Agbarabo), the Pakaka-Tete Bakangwe and Kalimva deposits were also considered in this study. The latter deposits are located respectively towards the northeast and northwest of the KCD deposit along the regional KZ trend (Fig. 1b). The geology is divided into two sequences: the hanging wall consisting of metamorphosed and altered basalt and volcaniclastic and the footwall comprising immature gritstone, sandstone, minor pebbly conglomerate, and BIF (Allibone et al. 2020). Gold mineralisation at Pakaka and Kalimva is found within a km-scale shear zone, while at Tete Bakangwe and KCD, folded footwall rocks are the main host for mineralisation (Allibone et al. 2020).

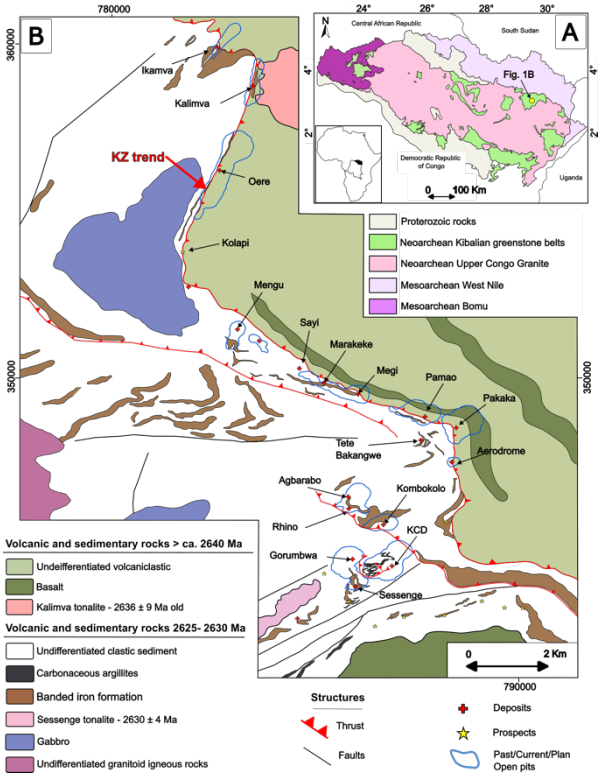

Figure 1. Summary geologic map of: (A) northeastern Congolese Congo Craton and (B) Kibali gold district. Modified after Bird (2016) and Allibone et al. (2020).

3. Methods

A total of 91 samples were collected from 26 diamond drill holes at eight deposits. 101 Polished sections were prepared, and 12 samples were selected for trace element analyses. Scanning Electron Microscopy (SEM) analyses at the Central Analytical Facility in Stellenbosch University were conducted on carbon-coated mounts using Zeiss EVO MA15VP with an OXFORD INCA Electron Dispersive Spectrometer (SEM-EDS) and Wavelength Dispersive Spectrometer (WDS). LA-ICP-MS at the Central Analytical Facility in Stellenbosch University was used for trace element analyses of pyrite, with monitored isotopes including ^{34}S, ^{47}Ti, ^{51}V, ^{52}Cr, ^{55}Mn, ^{57}Fe, ^{59}Co, ^{60}Ni, ^{63}Cu, ^{66}Zn, ^{69}Ga, ^{71}Ga, ^{72}Ge, ^{75}As, ^{77}Se, ^{95}Mo, ^{107}Ag, ^{111}Cd, ^{115}In, ^{118}Sn, ^{121}Sb, ^{128}Te, ^{133}Cs, ^{139}La, ^{157}Gd, ^{182}W, ^{197}Au, ^{202}Hg, ^{205}Tl, ^{208}Pb, and ^{209}Bi. The study also used SIMS to measure the $\delta^{34}S$ sulphur isotope composition in a different pyrite generation within six samples. The SIMS analyses were conducted using the virtual SIMS facility at the University of the Witwatersrand, which is connected via an internet-based link to the Cameca 1280-HR instrument located at the Helmholtz Zentrum Potsdam in Germany.

4. Results

4.1. Pyrite textures

Five main types of pyrite have been identified in samples from the Kibali Gold District based on occurrence, grain size, morphology, and detailed textural analysis (Fig. 2). Pyrite-0 (Fig. 2a) is microcrystalline and occurs in the Kalimva deposit. Pyrite-1 (Fig. 2b) is small and commonly found along phyllosilicate mineral foliation. Pyrite-2 (Fig. 2c) appears as euhedral to subhedral grains with a core-rim texture (core = py-2a, core with inclusions = py-2b, homogeneous rims = py-2c, and zoned rims with arsenic-rich bands = py-2cz, Fig. 2d). Pyrite-3 (Fig. 2e) occurs as massive pyrite-veinlets and often replaces pyrrhotite. Pyrite-4 (Fig. 2f) is characterised by large pyrite grains and often occurs as isolated grains in the matrix or within quartz veins.

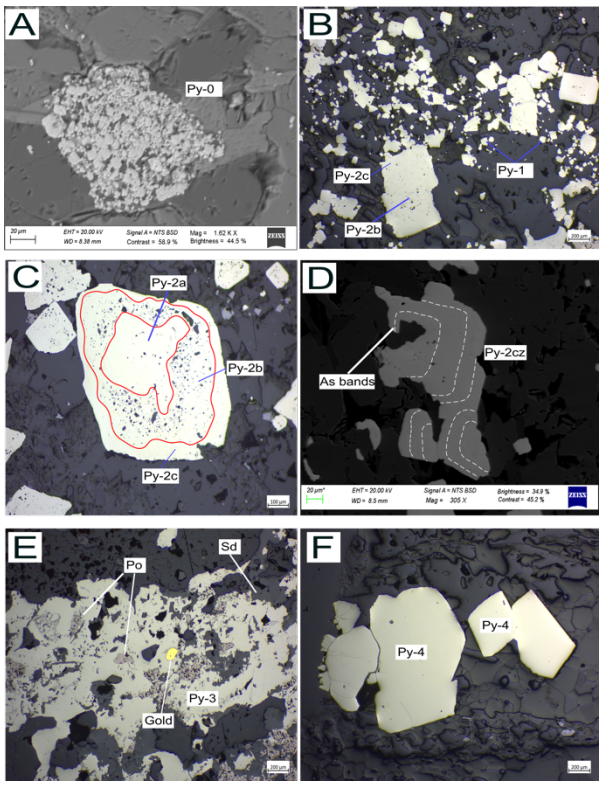

Figure 2. BSE and reflected light photomicrographs from the Kibali Gold district show different pyrite types' textural characteristics. A. Fine microcrystalline grains of pyrite (py-0). B. Disseminated fine-grained py-1 and coarse-grained py-2. C. Subhedral pyrite grain showing core-rim texture with core free-inclusion (py-2a) rimmed by rich-inclusion pyrite (py-2b) and surrounded by free-inclusion pyrite (py-2c). D. Subhedral core-rim pyrite with As-rich bands zonation (py-2cz). E. Irregular pyrite veinlet (py-3) replacing pyrrhotite and replaced by siderite. F. Coarse euhedral to subhedral poor-inclusion pyrite (py-4) grains. Abbreviations: Py: pyrite; Po: pyrrhotite; Au: gold; Sd: Siderite

4.2. Multivariate statistical analyses of trace elements

Using a dataset of 310 individual chemical measurements, distinct clusters were determined using the UMAP algorithm (Fig. 3). The data reduction process was performed using ioGAS software. The k-Means algorithm yielded 8 clusters, which is 68% different from the classification obtained visually (Fig. 3a, b). Furthermore, PCA analysis supports different groups with specific trace element vectors. The findings indicate a negative correlation between PC1 and Se, Ni, Co ± Ge, which are typically found in conjunction with py-4b and py-2c. Conversely, Pb and Sb exhibit a positive correlation with PC1. The dominant positive contributors to PC2 are W, Cr, and V, which are spatially linked with py-0, py-1, py-2a, and py-2b. On the other hand, Bi, Ag, Au, and Cu are part of a negative vector group associated with PC2, which is spatially linked with py-2cz (Fig. 3c, d).

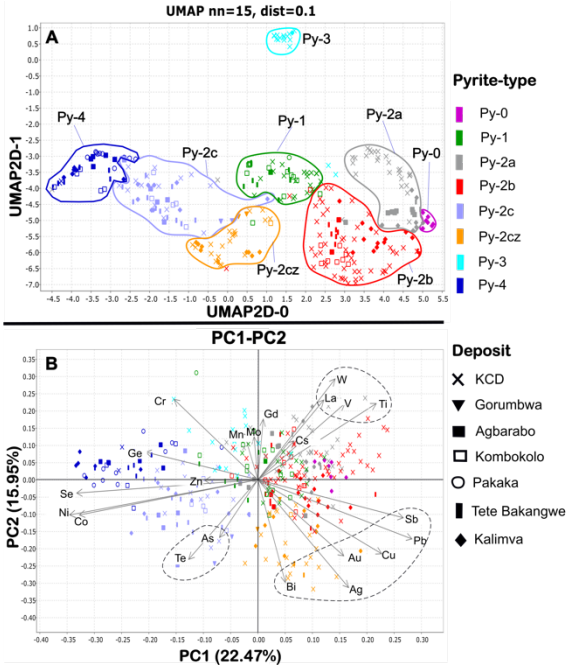

Figure 3. Selected bivariate plots of UMAP and PCA. A. 2D UMAP projection plot with sample grouping using K-means clustering (K = 8). B. PCA plot with trace elements against pyrite types.

4.3. Trace element patterns and maps

The trace element analyses indicate significant differences among the pyrite types. Py-4, py-2c, and py-3 show depleted gold content, while py-0, py-1, py-2b, and py-2cz exhibit a higher concentration of gold. Arsenic displays low concentrations in py-3 and high values in other types, with py-0 having the highest median value. Py-4 and py-2c contain significant amounts of Co and Ni, respectively, with varying distributions across the Kibali district.

LA-ICP-MS elemental mapping was performed on seven pyrite grains from various deposits in the Kibali gold district. The spatial distribution pattern of trace elements in pyrite-2 grains from KCD and Tete Bakangwe are similar. Py-2a (cores) hosted in barren quartz-carbonate altered BIF protolith have low concentrations of most elements, except for Co, Ni, Mn, Cu, Cr, Zn, and As, which are concentrated in the outer zone. Py-2b (cores with inclusions) have elevated levels of Au, As, Bi, Cr, Cu, Gd, La, Mn, Pb, Sb, Ti, V, W, and Zn, while py-2c (homogenous rims) is relatively enriched in Co, Ni, Se, and Te in the outer zone.

4.4. Sulphur isotopes of pyrite

The $\delta^{34}S$ values of pyrite were analysed at 60 spots, ranging from -0.05 to 7.65‰ with a mean of 3.34‰ (stdv=1.89). The py-0 (n=6) ranged from 0.56 to 1.85‰, while py-1 (n=3) yielded values between 2.27 and 2.61‰. Py-2 exhibited a wide range, with py-2a ranging from 2.21 to 2.75‰, py-2b (n=20) ranging from -0.05 to 5.41‰, py-2c (n=14) ranging from 1.65 to 5.78‰, and py-2cz

(n=6) ranging from 5.36 to 7.65‰. Py-3 (n=7) ranged between 3.15 and 4.64‰.

5. Preliminary discussion and conclusions

Orogenic gold deposits formed during the Precambrian era exhibit a complex evolution that involves multiple stages of metamorphism, ductile to brittle deformation, and cycling of ore fluids (Pitcairn and Goldfarb, 2022). Determining the timing of gold incorporation in sulphides can be challenging in these deposits due to the overlapping later stages of deformation. This phenomenon was observed in the Kibali gold district, where pyrite displayed a wide degree of grain size and morphology variation.

The discrimination of the different pyrite generations by applying new dimensionality reduction methods to the trace element data combined with sulphur isotope analyses has allowed us better to constrain the evolution of mineralisation in the Kibali district. Importantly, consideration of the pyrite trace element signatures in multi-parameter space has assisted in refining the pyrite classification relative to the initial textural classification. Thus, the PC graphs help show the spot analyses' multivariate nature. This allows for a data description and straightforward interpretation that is not possible using the basic statistics.

These mineral chemistry, sulphur isotope and textural insights help to develop and constrain the genetic model for the various pyrite generations in the Kibali gold district. The fine-grained and nodular texture and the elevated trace element content of the py-0 generation suggest an early sedimentary origin with S isotope composition averaging 1.39‰ (e.g., Large et al. 2009), likely by rapid formation within the pore waters in a basaltic-volcaniclastic basin. The py-1, py-2a and py-2b generations show distinctive similarities in their trace element behaviour, notably showing correlation with the elements V, La, Ti and Cr. These signatures may be related to micro to nanoscale inclusions, an insight which is supported by SEM analyses. These siderophile elements suggest that the pyrite may have formed by the interaction between a fluid and oxide minerals such as magnetite. Sulphidation reactions such as these are commonly observed in the banded iron formation units of the Kibali district. The py-3 generation has chemical signatures most strongly correlating with Mn, Zn and Mo and particularly the Mn content may suggest that this generation forms by carbonate replacement, again a phenomenon that is common in the alteration haloes of orogenic gold deposits. The most auriferous pyrites are py-2cz which show high Ag, Ag, As, Bi, Cu, Pb, Sb and Te, and which also have the highest sulphur isotope signature. This is likely to represent the ore fluid. Py-4 has high Co, Ni and Se content which may derive from interaction between fluid and more mafic lithologies. This generation is paragenetically late and postdates the mineralisation event.

To summarise, the application of dimensionality reduction methods not only facilitates improved pyrite classification based on their chemistry but also aids in interpreting their genesis. This research outcome can substantially enhance the accuracy of differentiating between pyrite types in diverse geological settings. Our investigation establishes a groundwork for potential dimensionality reduction-based research on trace element incorporation in minerals, extending beyond pyrite. This technique may advance our comprehension of mineral formation mechanisms, which is pivotal in succeeding in mineral exploration.

1 Acknowledgements

The authors would like to thank Barrick Gold Corporation for their financial support and for granting access to data. The valuable contribution of Frédéric Couffignal in assisting with the SIMS analyses is much appreciated. Mrs. Madelaine Frazenburg, Dr. Alicia Botes and Mrs. Riana Rossouw are acknowledged for their assistance during the SEM and LA-ICP-MS analyses. Furthermore, the authors express their gratitude to the Kibali geologists for their helpful assistance and constructive discussions.

2 References

Allibone, A., Vargas C., Mwandale E., Kwibisa J., Jongens R., Quick S., Komarnisky N., Fanning M., Bird P., MacKenzie D., Turnbull R., Holliday J. (2020): Orogenic Gold Deposits of the Kibali District, Neoarchean Moto Belt, Northeastern Democratic Republic of Congo, Society of Economic Geologists, SEG Special Publications, no. 23, pp. 185–201.

Bird, P.J., (2016): Evolution of the Kibali Granite-Greenstone Belt, North East Democratic Republic of the Congo, and Controls on Gold Mineralisation at the Kibali Gold Deposit. PhD, Kingston University London. 325p.

Groves, D.I., Goldfarb R.J., Robert F., Hart C.J. R. (2003): Gold Deposits in Metamorphic Belts: Overview of Current Understanding, Outstanding Problems, Future Research, and Exploration Significance Economic Geology. Vol. 98, pp. 1–29.

Large, R.R., Maslennikov, V., Robert, F., Danyushevsky, L.V., and Chang, Z., (2007): Multistage sedimentary and metamorphic origin of pyrite and gold in the giant Sukhoi Log deposit, Lena gold province, Russia: Economic Geology, v. 102, p. 1232–1267.

Lawrence, D.M. (2011): Petrographic Studies on the Kibali Gold Deposit, NE Democratic Republic of Congo: D. Lawrence 2011 Sample Suite. Unpublished Kibali internal report, Kingston University London, 21 p.

Mpaka Y.W, von der Heyden B.P, Bampata T., Luzolo F.N, Mwandale E. (submitted): Gold characteristics in the conglomeratic units of the mineralised Archean Moto Greenstone Belt, DRC.

Pitcairn I. and Goldfarb R.J. (2022): Orogenic gold: is a genetic association with magmatism realistic? Mineralium Deposita 58, 5–35.

Phytoremediation, a less costly prospect for tailings rehabilitation

Phumudzo G. Munyai[1], Humbulani R. Mundalamo[1], Jason S. Ogola[1], Luke Chimuka[2]
[1]Department of Earth Sciences, University of Venda, Private Bag X5050, Thohoyandou, 0950, South Africa
[2]Department of Environmental Analytical Chemistry, Wits University, Private Bag 3, Johannesburg, 2050, South Africa

Abstract. Gold mine waste is considered as the major source of toxic metals in the environment however these toxic metals can be removed from the mine waste, soil and water by a process called phytoremediation which involves the use of plants to remove and immobilize toxic metals. A mineralogical characterization was conducted at Klein Letaba tailings storage facility (TSF) to quantify the presence of metals. Previous studies revealed an abundance of metals such as Pb, Cr, Ni and As. However, the extent of remediating metals from the TFS has not been adequately investigated in the Giyani Greenstone Belt (GGB). The TSF mainly comprises high metal concentrations of Pb, Ni, As and Cr. Plants and tailings were seasonally collected on the TFS for chemical and mineralogical characterization. XRF and ICP-OES analysis revealed the metal concentrations and distribution. The focus of the study was to investigate the potential of metal extraction from native plant species growing on the mine TSF which could not be extracted by the mine using physical-chemical techniques.

1 Introduction

The Giyani Greenstone Belt is known for its gold mineralisation, and it has been exploited at Klein Letaba, Louis Moore, Birthday, Golden Osprey and Fumani mines (Weilers 1956). All these mines are closed but the metals within their respective TSF can cause environmental and health problems.

Mining operations produce different sorts of wastes, frequently in huge amounts. The vast majority of these wastes are discarded into surface facilities, making extensive structures that require exploration and support to guarantee their long load solidness (Karlsson et al. 2014). Metals are essential in living organisms at lower concentrations and as such when they are absent living organisms suffer from deficiency, alternatively when these metals are available in excess concentrations, they result in being toxic to both human health and the surrounding environment (Sabine 2009). Large amounts of waste have been generated and mobilized due to mining, agricultural and industrial activities.

Tailings are a by-product of the gold mining industry, and the discharge of this waste material can have a significant environmental impact. To reduce this impact, phytoremediation has been proposed as an effective and economically viable method for removing metals from gold mine tailings (Peer et al. 2005). Both metal and non-metal mining activities generate huge quantity of waste rocks, which damages the aesthetics of the area. Particularly, in case of metal mining, activities such as crushing, grinding, washing, smelting and all the other process used to extract, concentrate metals, generate a large amount of waste rocks and tailings which scars the landscape, disrupts the ecosystems, and destroys microbial communities. Waste materials that remain after the extraction of usable ores are dumped on the surrounding land, which is the sources of toxic metals, leave the land devoid of topsoil, nutrients and supportive microflora and vegetation, thus remains barren (Mukhopadhyay and Maiti 2010).

Phytoremediation efforts have largely focused on the use of plants to accelerate the degradation of organic contaminants, usually in concert with root rhizosphere microorganisms, or remove hazardous metals from the soil and water (Peer et al. 2005). Phytoremediation of contaminated sites is a relatively inexpensive and aesthetically pleasing to the public compared to alternate remediation strategies which involve excavation or chemical in-situ stabilization. This is one of the best remediation strategies for metal extraction and stabilisation of the mine tailings using native plant species (Peer et al. 2005).

The Giyani Greenstone Belt (GGB) situated in the north-eastern part of the Limpopo Province in South Africa is home to abandoned mine sites. These mine sites are a constant danger to nearby communities due to the risks associated with tailings dam, disused mine shafts, pit lakes and dilapidated mine buildings (Mhlongo et al. 2020).

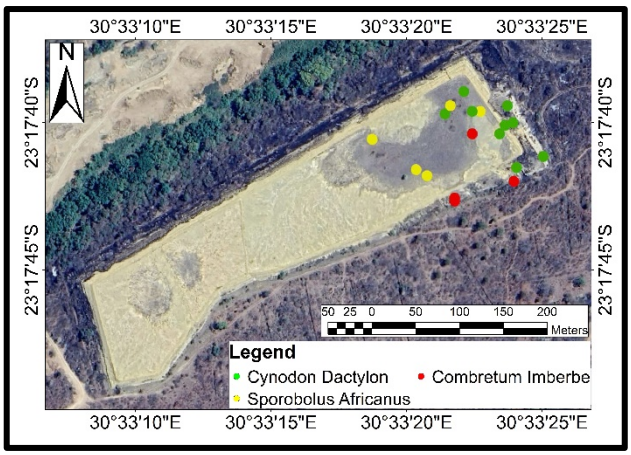

Figure 1. Sample locations of native plant species growing on the TSF for summer 2020.

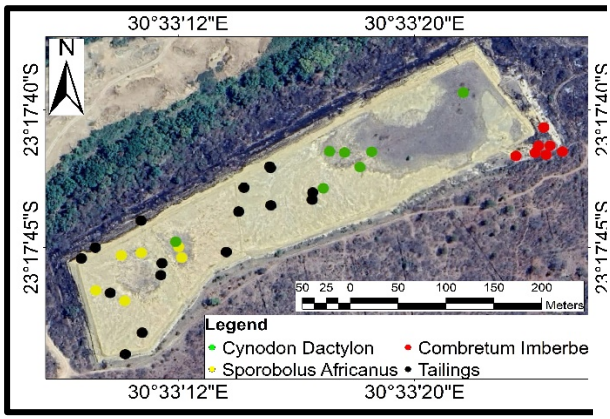

Figure 2. Sample locations of native plant species growing on the TSF for winter 2021.

A. Combretum imberbe *B. Cynodon dactylon* *C. Sporobolus africanus*

Figure 3. Dominant plant species growing on the TSF.

2 Methodology

A total of 80 plants and tailings samples were randomly and seasonally collected at Klein Letaba TFS for metals concentration analysis as part of the feasibility study. 5 ccontrol samples were collected away from the mine site but within similar geological setting. This helped during comparative study to ascertain that these metals are indeed extracted from the mine due to anthropogenic activities. The metal concentration results from the reconnaissance study were used to develop evidential uptake of the dominant plants in the study area.

Each composite sample was split into two representative aliquots for chemical and mineralogical analysis. The first aliquot was analysed using X-ray fluorescence spectrometry (XRF) at University of Venda Mining and Environmental Geology laboratory and the second aliquot was digested using microwave digestion technique at University of Venda Hydrology and Water Resources laboratory then sent out to Madzivhandila Agricultural Centre for Inductively coupled plasma optical emissions spectrometry (ICP-OES) analysis.

3 Results

3.1 Identification of native plant species

Three dominant plant species growing and thriving well were identified growing on the TSF: *Combretum imberbe, Cynodon dactylon and Sporobolus africanus*. These plant species were found to be hyperaccumulators of Pb and Ni (> 1000 mg kg^{-1}) because they were able to uptake and translocate metals from the roots to the shoot then leaves.

3.2 Geochemistry of Klein Letaba TSF

Major trace elements were identified namely, Pb, Cr, As, Ni, Cu and Co in their order of abundance indicates the distribution and dispersion of metals across the study area. A high geochemical signature across the entire area was revealed high to moderate concentrations.

3.3 Metal concentrations of plants: summer season

Pb (KLT1S14) recorded 1700 mg kg^{-1} on the and Ni (KLT1S14) recorded metal concertation of 1101.03 mg kg^{-1} on the roots for the Combretum imberbe plant, whereas Pb (KLT1S1) had concentration of 1525.8 mg kg^{-1} on the roots and 1204.3 mg kg^{-1} on the stem. These values exceed the ground tissues in concentration which are present in the soil (Baker and Brooks 1989).

Table 1. Metal concentrations of plants on different parts during summer (wet) season where red denotes high concentrations and yellow indicates intermediate concentrations.

SAMPLE ID	Pb (mg/kg)	Ni (mg/kg)	As (mg/kg)	Zn (mg/kg)	Cu (mg/kg)	Co (mg/kg)	Cr (mg/kg)	Cd (mg/kg)
KLT1S14 ROOT	1700,71	1101,03	511,25	80,41	25,12	16,12	510,1	0,01
KLT1S14 STEM	980,33	507,14	90,87	23,04	15,85	9,4	358,23	0
KLT1S14 LEAF	750	810,23	305,25	62,35	18,32	13,3	200,61	0
KLT1S22 ROOT	2307,25	1407	984,04	62,7	20,04	10,01	609,32	0,01
KLT1S22 STEM	1150	670,02	270,02	15,32	12,01	5,23	460,1	0
KLT1S22 LEAF	810	890,36	547,01	54,1	17,24	8,11	216,45	0
KLT1C1 ROOT	11,1	58	1,5	15,5	2,1	1,1	48,3	0,01
KLT1C1 STEM	9,2	23,1	0,5	8,4	0,8	0,2	35,8	0
KLT1C1 LEAF	2,9	37,1	1,1	10,2	1,6	0,9	22,5	0
KLT1C2 ROOT	12,3	52,2	2,1	23,4	16,7	2,2	36,5	0,01
KLT1C2 STEM	8,2	15,3	1,3	115	10,4	1,1	29,4	0
KLT1C2 LEAF	6,4	25,4	1,6	15,4	12,2	2,1	21,6	0,01
KLT1S1 ROOT	1525,8	754,6	741,2	95,1	25,2	13,7	740,5	0,1
KLT1S1 STEM AND LEAF	1204,3	521,4	245,6	114,23	14,03	4,65	314,8	0,01
KLT1S5 ROOT	513,2	60,1	56,7	52,2	16,1	25,6	241,8	0,1
KLT1S5 STEM AND LEAF	250,1	24,5	32,4	58,1	9,4	15,9	65,7	0,01
KLT1S15 ROOT	1370,5	1230,7	580,8	123,5	78,5	12,4	873,96	0,01
KLT1S15 STEM AND ROOT	750,4	780,6	350,7	260,9	50,6	3,5	563,58	0

Table 1 shows that uptake of metals by *Combretum imberbe, Cynodon dactylon* and *Sporobolus africanus* was following the order roots>stem>leaves. The uptake was high on the *Combretum imberbe* plant as compared to the grass species (*Cynodon dactylon* and *Sporobolus africanus*).

3.4 Metal concentrations of plants: winter season

During winter season, the order of abundance of uptake shows that the leaves have high metal concentration followed by the stem then the roots (Table 2) whereas the grass species (*Cynodon dactylon*) the concentration is high in roots followed by the shoot.

Table 2. Metal concentrations of plants on different parts during winter (dry) season

Sample ID	Name	Cr (ppm)	Cu (ppm)	Co (ppm)	Ni (ppm)	Pb (ppm)	Zn (ppm)	Mn (ppm)	Fe (ppm)
KLP1S1	Shoot	3.878	2.175	1.337	0.425	3.502	1.327	315.9	172.2
S	Root	3.589	2.180	1.262	0.040	3.573	0.370	200.50	31.99
KLP1S4	Shoot	3.522	2.250	1.212	0	3.458	0.996	128.9	59.57
S	Root	3.309	2.339	1.155	0	3.476	0.274	78.10	103.8
KLP2S1	Shoot	3.571	2.172	1.158	0.621	3.437	1.915	333.9	185.2
S	Root	3.781	2.461	1.960	1.990	3.525	2.589	259.4	209.9
KLP3S2	Shoot	3.552	2.345	1.722	0.183	3.299	1.049	99.55	166.2
C	Root	4.006	3.252	1.994	5.989	3.335	7.381	255.1	200.1
KLP3S4	Shoot	3.505	2.338	1.628	0	3.488	1.424	112.8	72.48
C	Root	2.690	2.207	1.598	0	3.702	1.242	93.84	53.24
KLP3S7	Shoot	1.965	2.250	1.683	0	3.733	1.261	153.2	149.5
C	Root	2.318	2.173	1.726	2.854	3.778	7.270	208.1	210.2
KLP4S1	Leaves	2.261	2.114	1.567	0	3.00	0	55.3	26.88
Cl	Stem	2.384	2.373	1.810	1.479	3.167	1.733	65.59	45.87
	Root	2.481	2.487	2.013	4.053	3.743	18.09	50.43	136.2
KLP4S3	Leaves	2.110	2.063	2.533	0.524	3.071	7.167	55.3	156.3
Cl	Stem	2.206	2.055	2.375	3.089	3.639	7.140	57.96	106.7
	Root	1.990	2.899	2.134	3.120	3.572	10.75	69.86	125.6
KLP4S5	Leaves	1.775	1.886	2.464	0.909	3.021	6.402	292.5	195.2
Cl	Stem	1.223	1.817	2.309	8.523	3.067	2.384	0	14.24
	Root	1.409	1.862	2.294	0	2.864	0.244	0	13.92
KLP4S7	Leaves	1.429	1.891	2.418	0.842	3.394	3.193	104.9	125.5

Table 2 shows very little up to no concentrations at all due to the fact that the plants are dormant during winter season. The leaves accumulate more concentration, bind and die then re-circulate the metals in leaves and metals in soil in the same location. Rate of metal uptake during winter season is very little and previous studies revealed that the plants tend to uptake more nutrients in wet seasons as compared to dry season. This will help to determine the best time to harvest the plants.

4 Conclusions

This study revealed that the native plant species growing and thriving well on the TSF are hyperaccumulators of Pb and Nickel during summer (wet) season, whereas during winter (dry) season the plant species are dormant and tend to take up very minimal up to no concentration of metals because they bind and die resulting in withering of the leaves on the TSF. This phenomenon is known as the re-circulation of metals in leaves and metals in soil in the same location. These hyperaccumulator plant species can accumulate metals in their above ground tissues in concentrations far exceeding those present in the soil.

3 Acknowledgements

Special thanks to DSI-NRF-CIMERA for funding this project. Prof. J.S. Ogola, Prof. L. Chimuka, Dr. H.R. Mundalamo, University of Venda, Wits University and SANBI are thanked for supervision, guidance, analysis and pot culture experiments and Klein Letaba mine tailings owners for granting permission to access the mine tailings and acquiring samples.

4 References

Baker AJM, Brooks RR (1989) Terrestrial higher plants which hyperaccumulate metallic elements - A review of their distribution, Ecology and Phytochemistry. Journal of Biorecovery 1: 81-126.

Karlsson S, Sjöberg V, Ogar A, Bäckström M et al (2014) Leachability of Cu, Zn, As, Ba, and Pb from refuse in the Zelany most tailings dam. An Interdisplinary response to mine water challenges. In: Sun and Wang (eds), pp. 121-125.

Mhlongo S E, Amponsah-Dacosta F, Kadyamatimba A et al (2020) Appraisal of strategies for dealing with the physical hazards of abandoned surface mine excavations: A case study of frankie and nyala mines in South Africa, J Minerals. https://doi.10.3390/min10020145

Mukhopadhyay S, Maiti, SK (2010) Phytoremediation of metal mine waste. Journal of Applied Ecology and Environmental Research 8(3): 207-222.

Peer WA, Freeman JL, Baxter IR, Richards EL, Murphy AS et al (2014). Phytoremediation and hyperaccumulator plants. Dissertation. University of Maryland, College Park.

Sabine M and Wendy G (2009). Human health effects of metals. Dissertation. Kansas State University.

Weilers WF, (1956) The geology of Klein Letaba gold mine in the Sutherland Range, North-Eastern Transvaal. Dissertation. Stellenbosch University 33: 445-479.

Continuous element mapping of drill cores from the Bushveld Complex, SA using LIBS and µEDXRF

Wilhelm Nikonow[1], Dieter Rammlmair[2], Jeannet A. Meima[1]
[1]Federal Institute for Geosciences and Natural Resources (BGR), Stilleweg 2, 30655 Hannover, Germany
[2]Institute of Mineralogy, Leibniz University Hannover, 30167 Hannover, Germany

Abstract. This paper discusses the complexity of mechanisms responsible for the variation in element composition in magnetitite layers within the Upper Zone of the Bushveld Complex in South Africa. It presents a methodological approach to obtain continuous data on element distributions along several drill core metres using micro energy dispersive X-ray fluorescence microscopy (µEDXRF) and laser-induced breakdown spectroscopy (LIBS). The focus is on magnetitite layer 21 at about 223 m depth of the drill core BH7772 from the Eastern Limb.
The data shows that the method of using µEDXRF and LIBS for element mapping at the micrometre scale is promising for providing continuous data on element distributions along several drill core metres. The results indicate that the variability in the composition of the magnetitite layers is even more complex than the large scale data known from the literature describe. This underlines the problem of obtaining a sufficient number of samples for representative data, while considering practical limitations of sampling and analysis in regards to time and effort. The combination of LIBS and µEDXRF can help to understand the complex processes responsible for the variation in element composition within the magnetitite layers.

1 Introduction

The Bushveld Complex in South Africa hosts the largest ultramafic-mafic intrusion in the world. Its Upper Zone contains a series of magnetitite layers, which hold vast resources of vanadium and chromium. These layers display certain trends in element composition along their occurrence within the Upper Zone. While titanium and chromium generally decrease with depth, vanadium increases with concentrations of two wt.-% V_2O_5 in the lowest layers (Scoon and Mitchell 2012; Molyneux 1974; Klemm et al. 1985). Chromium is also known to show rapid upwards depletion within magnetite layers (Cawthorn and McCarthy 1980).

Several processes have been discussed in the literature to be responsible for the variation: fractional crystallisation, magma mixing and compositional convection, partial recrystallization and assimilation as well as reactive melt infiltration (e.g. Kruger and Latypov 2020a; Veksler and Charlier 2015; Yao and Mungall 2022).

The forming processes are still in discussion. This demonstrates the complexity of the mechanisms taking place at different scales. While the general trends are known, they can change and even be inverted on a smaller scale. Considering the large variation over the drill core depth, results will differ depending on the sampling distance of each data point. The variability raises the question of what sampling distance is necessary to have representative data of the magnetitite layers. While it is practically impossible to sample at micrometre resolution over the full Upper Zone, the complexity requires high data density.

The methodological progress in the areas of element mapping using micro energy dispersive X-ray fluorescence microscopy (µEDXRF) and laser induced breakdown spectroscopy (LIBS) seems promising to provide a solution to the aforementioned problem. Scanning drill core halves in 2D over several metres on a micrometre scale can provide the information needed. This work provides a method to obtain continuous data on element distributions along several drill core metres.

2 Materials and methods

The samples for this work were donated for academic research by Impala Platinum Ltd. The core BH7772 was drilled in the Eastern Limb of the Bushveld Complex at N -24.5092° E 29.8945°, about 20 km east of the Marula Mine and 50 km northwest of Burgersfort. It covers about 1337 m of the Upper Zone with some of the underlying Main Zone. The geology is dominated mostly by gabbro-norites, norites and mottled anorthosites with some granites and ultramafic pegmatites. The Upper Zone contains more than 20 layers or seams of magnetitite. This work deals with the layer 21 at about 223 m depth; the main magnetite layer is located at 1068 m. The numbering of these layers varies in the literature, but layer 21 is easily identifiable due to its thickness of more than 10 m containing mostly magnetite, with some ilmenite, plagioclase, clino- and orthopyroxene, olivine and sulphides (Molyneux 1974; Von Gruenewaldt 1973).

About 10 m of core from layer 21 were analysed using µEDXRF, LIBS, electron microprobe analysis (EMPA) and thin section microscopy. For the LIBS analysis the GeoLIBScanner from Laser Technik Berlin (LTB) was used with a Nd:YAG laser operating at 1064 nm with a mapping step size of 75 µm. The system has a wide-band spectrograph and CCD (210 – 1000 nm) with a spectral resolution of 0.047 – 0.222 nm. A stripe of about 1 cm was measured along the core providing spectra that can be used for element distribution maps of almost all elements (Meima et al. 2022b; Meima et al. 2022a; Kuhn et al. 2016).

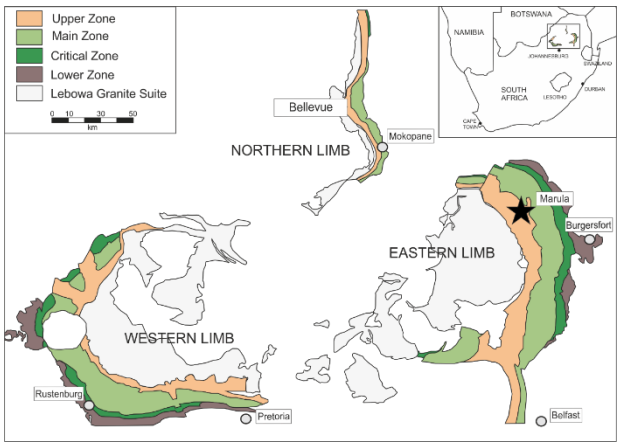

Figure 1. Overview of the Bushveld Complex adapted after Junge et al. (2015). Samples of this work are from the Eastern Limb; a star marks the drill core location, which is about 20 km east of the Marula Mine and 50 km northwest of Burgersfort.

In order to display the chemical variability within the magnetite, the procedure from Meima et al. (2022b) was adapted, where spectra are assigned a mineral name using the supervised classification algorithm spectral angle mapper (SAM) and a mineral database. The area of magnetite was cleaned off mixed pixels using unsupervised classification and thresholds for intensities of Si, Ti, S and Li. The resulting areas display the mostly pure magnetite. Within this area, median values of Cr intensities per pixel row are calculated and plotted along the drill core. Meima et al. (2022b) showed that intensity ratios with narrow spectral ranges from LIBS within one mineral matrix can be considered proportional to element concentrations measured with EMPA. Single spot EMPA data will be used to calibrate the element intensities from LIBS.

For µEDXRF analysis, the M4 Tornado Plus from Bruker was used (Nikonow et al. 2019; Kaskes et al. 2021; Barnes et al. 2016). It operates with a Rh tube at 50 kV and 600 µA providing energy dispersive spectra for areas of up to 15 x 20 cm. The samples were measured with a spatial resolution of 40 µm and a dwell time of 5 ms per spot. The X-ray spot size is focussed by a poly-capillary to about 20 µm (Nikonow and Rammlmair 2016).

The spectra are classified using SAM and a mineral database that has been created over time at BGR, based mostly on EMPA data and containing more than 8000 mineral spectra including solid solution minerals (Nikonow and Rammlmair 2017).

3 Results and discussion

The results from the LIBS and EDXRF analysis are displayed in figure 2. The LIBS data provides a contiguous overview of the Cr variation along the drill core at a spatial resolution of 75 µm (figure 2a). It shows a great variation on the 10 m scale. According to EMPA data from about 130 analyses on magnetite of this core section, the Cr_2O_3 content varies between below detection limit and 1.5 wt.-% with a median of 0.2 wt.-% Cr_2O_3 (median values per four thin section in figure 2a). There is no general trend along the profile, but rather a wave-like behaviour reaching lows at about 218 m and 213.5 m and a high at about 216.5 m with several distinct excursions in both directions. Several authors have described apparent cyclic variations within the monomineralic layers of the Bushveld Complex on a macro scale, proposing ideas on the formation of these layers (Tegner et al. 2006; Junge et al. 2014; Scoon and Mitchell 2012). However, on a micro scale, the general trends can differ or even be inverted (Yao and Mungall 2022; Kruger and Latypov 2020b) and, therefore, contradicting a model of fractional crystallisation. Consequently, the scale has to be considered in order to study and explain rhythmic cycles or reversals of general trends.

Figure 2b shows a zoom-in from 215 to 216 m, with the corresponding mineral distribution map from µEDXRF in figure 2c. The continuous spatial resolution of 75 µm from LIBS provides detailed information on the Cr distribution showing that in the upper 30 cm with mostly massive magnetite there is a small but steady trend towards higher Cr intensities. At about 215.3 m depth, the proportions of plagioclase, pyroxene and biotite increase resulting in a greater variation of Cr intensity with many smaller increases and decreases within the magnetite layers. The peak at 215.55 m can be attributed to the occurrence of small-grained clinopyroxene, plagioclase, amphibole, apatite and ilmenite within a groundmass of magnetite. There are several other steep increases of Cr intensities at 215.3 m, 215.45 m and 215.75 m, all of them seem connected to the presence of pyroxenes. However, the Cr_2O_3 concentration in clinopyroxene does not exceed 0.05 wt.-% with a median below the detection limit, according to EMPA. Other authors observed a relation of higher Cr content with the presence of plagioclase, interpreted as magma replenishment or reactive melt infiltration (Yao and Mungall 2022; Scoon and Mitchell 2012). The plagioclase in the upper part of figure 2b) has mostly no effect on the Cr intensity. Only where plagioclase occurs in combination with reaction rims of clinopyroxene, olivine, amphiboles and biotite Cr shows higher variability. Thus, the mechanisms resulting in the variability of Cr in magnetitite are not yet fully understood. However, continuous element mapping of several drill core metres at micrometre resolution in combination with mineral information from µEDXRF including neighbouring minerals can contribute to the understanding of these processes.

4 Conclusions

A drill core section of about 10 m length from the Bushveld Complex was analysed by LIBS and µEDXRF. LIBS data provide element distributions along the drill core at high spatial resolution in the micrometre range, while being able to analyse full core boxes. The combination of metre and micrometre scale with chemical and mineralogical

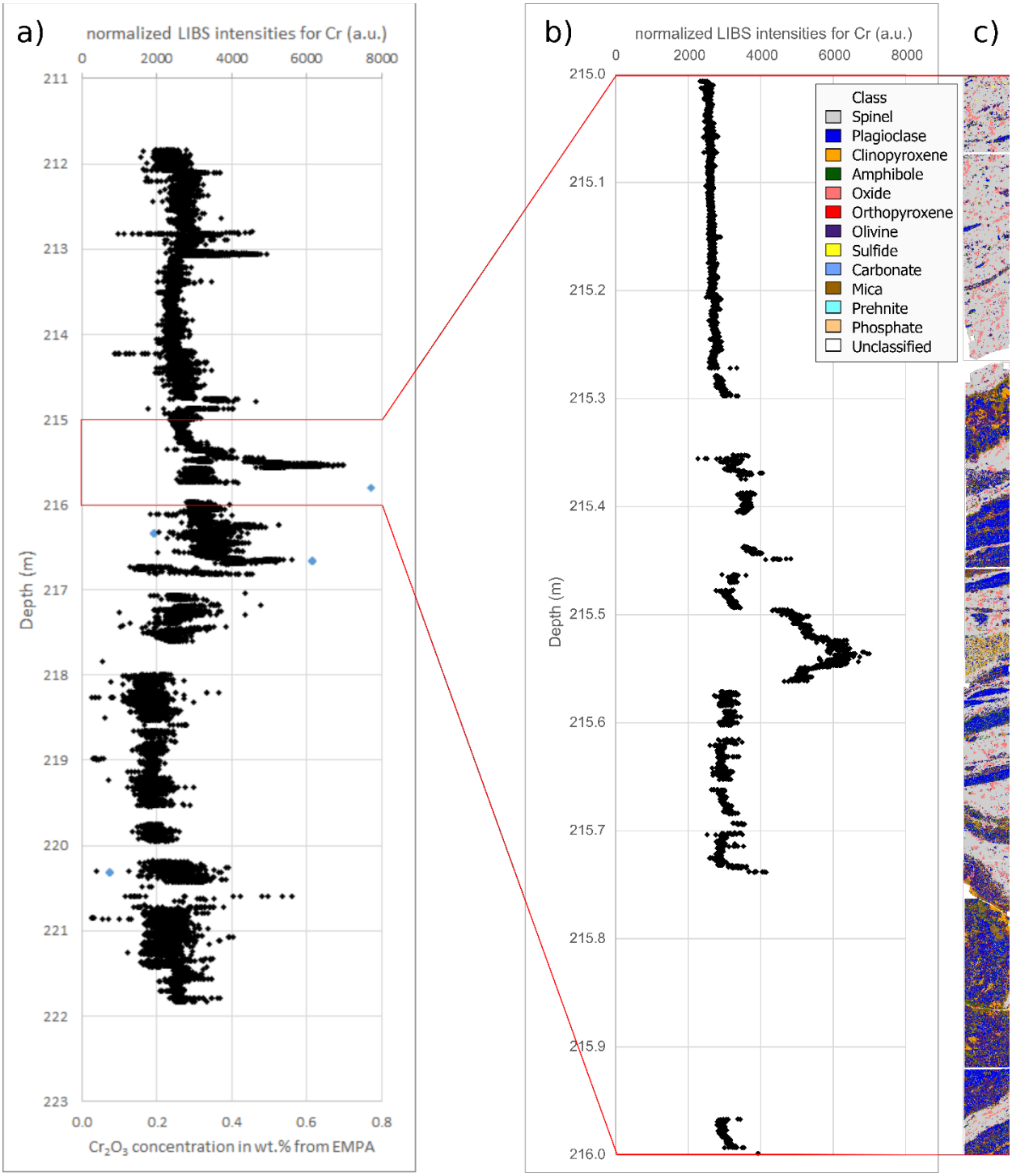

Figure 2. Cr intensities normalized to sum intensities from LIBS (a,b) along the drill core. Each point reflects the median of a 75 µm row. The median Cr_2O_3 concentrations (blue) per thin section from EMPA are plotted on the lower axis. EMPA data at 215.8 m has no corresponding LIBS data, since the grains were too small to receive a pure LIBS pixel. A one meter zoom-in is displayed in the middle (b). The mineral distribution from µEDXRF for sub-section b) is shown in c).

information in 2D opens new possibilities to analyse and understand the mechanisms of magnetitite layer formation and the metasomatic influence triggered by late magma emplacement.

Acknowledgements

The results of this work are part of research that is funded by the German Research Foundation (DFG) within the Project Spectroscopic mineral - chemical analysis of drill cores: Development of fast 2D LIBS, EDXRF and hyperspectral scanning with application to outstanding problems of the Bushveld Complex layered intrusion (457479532). We would like to express our gratitude to Impala Platinum Ltd. for donating the core, Prof. Roelofse from the University of the Free State, Bloemfontein for logging the core and Dr. Veksler from GFZ Potsdam for logistics. We thank Dr. Simon Goldmann, Christian Wöhrl and

Dominic Göricke for assistance with EMPA and M4 Tornado Plus measurements.

References

Barnes SJ, Mole DR, Le Vaillant M, Campbell MJ, Verrall MR, Roberts MP, Evans NJ (2016) Poikilitic textures, heteradcumulates and zoned orthopyroxenes in the Ntaka Ultramafic Complex, Tanzania: implications for crystallization mechanisms of oikocrysts. J Pet 57:1171-1198.

Cawthorn RG, McCarthy TS (1980) Variations in Cr content of magnetite from the upper zone of the Bushveld Complex — evidence for heterogeneity and convection currents in magma chambers. Earth Planet Sci Lett 46:335-343. doi: https://doi.org/10.1016/0012-821X(80)90049-7.

Junge M, Oberthür T, Melcher F (2014) Cryptic variation of chromite chemistry, platinum group element and platinum group mineral distribution in the UG-2 chromitite: an example from the Karee Mine, western Bushveld Complex, South Africa. Econ Geol 109:795-810.

Junge M, Wirth R, Oberthür T, Melcher F, Schreiber A (2015) Mineralogical siting of platinum-group elements in pentlandite from the Bushveld Complex, South Africa. Miner Depos 50:41-54. doi: 10.1007/s00126-014-0561-0.

Kaskes P, Déhais T, de Graaff SJ, Goderis S, Claeys P (2021) Micro–X-ray fluorescence (μXRF) analysis of proximal impactites: High-resolution element mapping, digital image analysis, and quantifications In: Reimold WU, Koeberl C (eds) Large Meteorite Impacts and Planetary Evolution VI. Geological Society of America, pp 0.

Klemm D, Henckel J, Dehm R, Von Gruenewaldt G (1985) The geochemistry of titanomagnetite in magnetite layers and their host rocks of the eastern Bushveld Complex. Econ Geol 80:1075-1088.

Kruger W, Latypov R (2020a) Fossilized solidifications fronts in the Bushveld Complex argues for liquid-dominated magmatic systems. Nat Commun 11:2909. doi: 10.1038/s41467-020-16723-6.

Kruger W, Latypov R (2020b) Fossilized solidification fronts in the Bushveld Complex argue for liquid-dominated magmatic systems. Nat Commun 11:2909. doi: 10.1038/s41467-020-16723-6.

Kuhn K, Meima JA, Rammlmair D, Ohlendorf C (2016) Chemical mapping of mine waste drill cores with laser-induced breakdown spectroscopy (LIBS) and energy dispersive X-ray fluorescence (EDXRF) for mineral resource exploration. J Geochem Explor 161:72-84.

Meima J, Rammlmair D, Junge M, Nikonow W (2022a) Continuous measurement of Mg/Fe and Ca/Na ratios with scanning Laser Induced Breakdown Spectroscopy in 6 meter of drill core through Merensky Reef, Bushveld Complex, South Africa EGU General Assembly 2022. Copernicus Meetings, Vienna, Austria.

Meima JA, Rammlmair D, Junge M (2022b) The use of Laser Induced Breakdown Spectroscopy for the mineral chemistry of chromite, orthopyroxene and plagioclase from Merensky Reef and UG-2 chromitite, Bushveld Complex, South Africa. Chem Geol 589:120686. doi: 10.1016/j.chemgeo.2021.120686.

Molyneux T (1974) A geological investigation of the Bushveld Complex in Sekhukhuneland and part of the Steelpoort valley. South Afr J Geol 77:329-338.

Nikonow W, Rammlmair D (2016) Risk and benefit of diffraction in Energy Dispersive X-ray fluorescence mapping. Spectrochim Acta B: At Spectrosc 125:120-126.

Nikonow W, Rammlmair D (2017) Automated mineralogy based on micro-energy-dispersive X-ray fluorescence microscopy (μ-EDXRF) applied to plutonic rock thin sections in comparison to a mineral liberation analyzer. Geosci Instrum Method Data Syst 6:429-437. doi: 10.5194/gi-6-429-2017.

Nikonow W, Rammlmair D, Meima JA, Schodlok MC (2019) Advanced mineral characterization and petrographic analysis by μ-EDXRF, LIBS, HSI and hyperspectral data merging. Mineral Petrol 113:417-431. doi: 10.1007/s00710-019-00657-z.

Scoon R, Mitchell A (2012) The Upper Zone of the Bushveld Complex at Roossenekal, South Africa: geochemical stratigraphy and evidence of multiple episodes of magma replenishment. South Afr J Geol 115:515-534.

Tegner C, Cawthorn RG, Kruger FJ (2006) Cyclicity in the Main and Upper Zones of the Bushveld Complex, South Africa: crystallization from a zoned magma sheet. J Pet 47:2257-2279.

Veksler IV, Charlier B (2015) Silicate liquid immiscibility in layered intrusions Layered intrusions. Springer, pp 229-258.

Von Gruenewaldt G (1973) The main and upper zones of the Bushveld Complex in the Roossenekal area, eastern Transvaal. Trans Geol Soc SA 76:207-227.

Yao Z, Mungall JE (2022) Magnetite layer formation in the Bushveld complex of South Africa. Nat Commun 13:1-11.

Exploring mineral chemistry variations in tourmaline and chlorite at the Triangle orogenic gold deposit (Val-d'Or, Québec): Implications for mineralisation vectors

Giovanni Pedemonte[1,2], Bertrand Rottier[1,2], Georges Beaudoin[1,2], Jacques Simoneau[3], Pape Mactar-Dieng[3]

[1]*Département de géologie et de génie géologique, Université Laval, Québec, Canada*
[2]*Centre de Recherche sur la Géologie et L'ingénierie de Ressources Minérales (E4m), Université Laval, Québec, Canada*
[3]*Eldorado Gold Corporation, Québec, Canada*

Abstract: Recent efforts in the research of ore deposits focus on the chemical characterisation of key minerals in mineralised systems to define vectors and indicator minerals constituting new and powerful exploration tools. The present study reports systematic tourmaline and chlorite chemical variability from the Triangle orogenic gold deposit (Val-d'Or, Québec). A detailed study of the paragenetic sequence allows defining at least three main mineralisation events. This study focuses on the characterisation of tourmaline and chlorite chemistries contained in the Au-bearing quartz-tourmaline- ankerite-chlorite veins of the second and main mineralising event, in the two main shear zones of the deposit, named C2 and C4. Chemical variability of chlorite and tourmaline have been explored using Principal Component Analysis, which allows to find some elemental ratios that strongly correlate with the elevation and Au grade of the samples along both shears. Further investigation on the physicochemical factors, including the effect of host rocks, controlling tourmaline and chlorite chemistries is in progress to define potential tracers that will allow vectorisation towards the high-grade ore shoots in the Triangle deposit and other shear-hosted orogenic gold deposits.

1 Introduction

1.1 Geology of the Sigma-Lamaque-Triangle district

Triangle is an orogenic gold deposit located in the Val-d'Or mining district. The main rock types of the district are the Val-d'Or Formation, a sequence of andesitic to rhyolitic lavas (Pilote 2000; Scott et al. 2002) and of mafic to intermediate pyroclastic rocks (Robert and Brown 1986a, b; Robert and Kelly 1987). This formation is strongly deformed, and show an E-W trending, sub-vertical schistosity (Latulippe 1976; Pilote et al. 1998; Pilote 2000; Scott et al. 2002) and are crosscut by different intrusive units mainly gabbroic and dioritic in composition (Pilote 2000; Neumayr et al. 2000; Scott et al. 2002). The Triangle deposit is structurally controlled and developed along third-order shears associated to the Larder Lake-Cadillac Break, crosscutting mafic tuffs belonging to the Val-d'Or Formation and dioritic intrusions such as the *Triangle Plug* and the *Dyke North* (Figures. 1 and 2). Gold mineralisation is hosted in several parallel shear zones trending approximately NW-SE, in veins composed of quartz, tourmaline, ankerite and chlorite associated with a strong quartz-sericite-feldspar alteration. The present study focuses on the characterisation of the geochemical variability of tourmaline and chlorite present in the orogenic veins from the two main shear zones of the deposit, named C2 and C4.

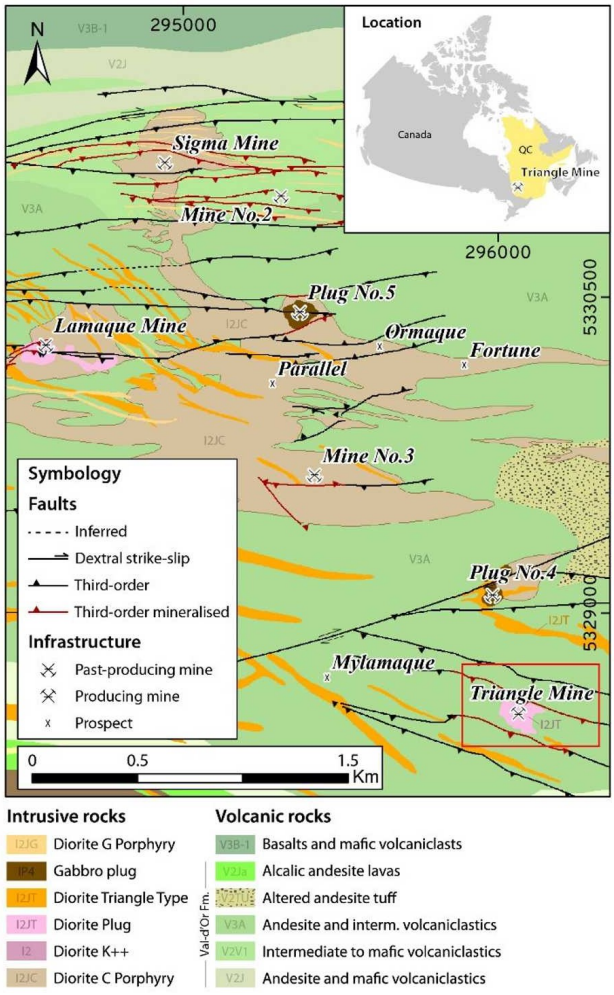

Figure 1. Geological map of the Triangle deposit (prepared with data from Eldorado Gold Corporation).

1.2 Mineralising events and paragenesis

Three main mineralisation events have been recognised at the Triangle deposit. The first event is characterised by early, deformed quartz-chlorite-sericite-carbonate veins with disseminated pyrite and minor gold mostly as inclusions in quartz. This event is accompanied by an intense deformation of the host rock and by an epidote, chlorite, and carbonate alteration associated with deformed pyrite. The second event consists of a proximal alteration zone at the contact of the shear,

characterised by widespread quartz-sericite-feldspar with traces of chlorite and undeformed pyrite. This event includes the main vein-filling stage, formed by massive quartz-tourmaline-ankerite-pyrite-chlorite veins emplaced along the shears. This second event is the most important for Au mineralisation, where Au occurs as inclusions associated with Au-Ag tellurides (krennerite and petzite) in pyrite. Finally, the third event consists of small pyrite-tourmaline-quartz veinlets crosscutting the veins of the second event. Those veinlets are associated to a third generation of gold commonly occurring as fracture filling inclusions (mainly in pyrite) associated with chalcopyrite and Pb-Bi tellurides (altaite and tellurobismuthite).

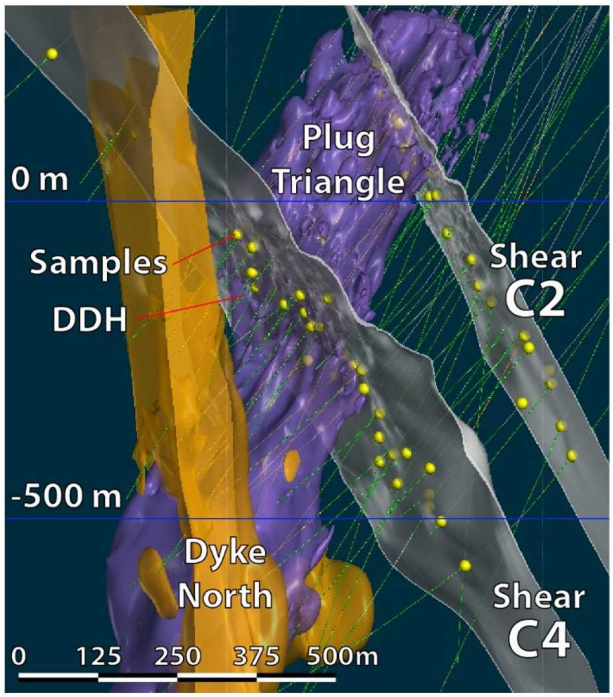

Figure 2. 3D view (facing NW) of the distribution of samples used for the present study (yellow spheres), along the two main shear zones (C2 and C4) in the Triangle deposit, and the influence of the intrusive rocks in the area. Empty areas in the 3D render correspond to the mafic tuffs of the Val-d'Or formation (Leapfrog Geo® model from Eldorado Gold Corporation).

2 Analytical methods and mineral chemistry

Tourmaline and chlorite from the quartz-tourmaline-ankerite-pyrite-chlorite veins of the second event have been analysed for major elements by EPMA and for minor and trace elements by LA-ICP-MS. Selected samples are from the shears C2 and C4, between -355.2 to +130.6m, and between -445.6 to 231.7 m, respectively (Figure 2). The Au grade of the samples varies between <0.01 (under detection limit, <d.l.) to 197.66 ppm and <0.01 to 151.93 ppm for shears C2 and C4 respectively. Grades has been classified in four intervals: barren (<0.01 – 0.5 ppm), low to cut-off grade (0.5 – 3 ppm), high grade (3 – 10 ppm) and above 10 ppm. For shear C2 most of the analysed vein samples crosscut the mafic tuffs whereas for C4 some veins also crosscut the Triangle plug (Figure 2). Tourmaline from shears C2 and C4 show contrasting mean composition of the following elements (Δ is the percentage of variation): Cr (144 vs 266 ppm, Δ=84%), K (1813 vs 3824 ppm, Δ=111%), Ti (1758 vs 2884 ppm, Δ=64%), Cu (3.94 vs 0.96 ppm, Δ=-76%), Ba (37.2 vs 88.6 ppm, Δ=138%), W (3.78 vs 16.5 ppm, Δ=336%), Pb (10.3 vs 155 ppm, Δ=1414%). Some elements remain almost constant between the two shears (Δ<5%), like Fe (4.4 vs 4.5 wt%), and Al (15.5 vs 15.2 wt%).

Conversely, the chlorite from shears C2 and C4 shows contrasting mean composition of B (11.3 vs 57.9 ppm, Δ=412%), Ca (2952 vs 6660 ppm, Δ=126%), Cr (85 vs 43.5 ppm, Δ=-49%), Cu (0.46 vs 1.12 ppm, Δ=144%), Sr (19.4 vs 9.1 ppm, Δ=-53%), La (2.54 vs 0.51 ppm, Δ=-80%) and Pb (1.49 vs 5.39 ppm, Δ=263%). Some elements remain relatively constant between the two shears (Δ<5%), such as Mg (7.9 vs 8.2 wt%), V (227 vs 230 ppm) or Fe (15.7 vs 15.8 wt%).

In shear C4, samples hosted in the dioritic Triangle Plug have been analysed. The preliminary results seem to indicate that tourmaline and chlorite chemistry varies as function of the host rock. In this sense, tourmaline from the veins that crosscuts the intrusive rocks compared to those crosscutting the mafic tuffs shows contrasting content of Sc (28 vs 50.1 ppm, Δ=79%), Cr (276 vs 191 ppm, Δ=-31%), Mn (109 vs 188 ppm, Δ=72%), Fe (3.86 vs 5.1 wt%, Δ=32%), Co (3.45 vs 13.2 ppm, Δ=283%), Cu (1.09 vs 2.75 ppm, Δ=153%) and Zn (499 vs 370 ppm, Δ=-26%). Similarly, chlorite shows contrasting content of Ca (1.6 vs 0.4 wt%, Δ=-73%), Sc (12.9 vs 32.9 ppm, Δ=155%), V (150 vs 241 ppm, Δ=60%), Cr (133 vs 52.9 ppm, Δ=-60%), Co (9.4 vs 16.1 ppm, Δ=71%), Sr (40.7 vs 9.5 ppm, Δ=-77%) and La (3.7 vs 0.5 ppm, Δ=-87%).

2.1 Tourmaline and chlorite geochemistry as a function of Au grade and elevation

Both tourmaline and chlorite show systematic change of composition as function of the Au grade of the samples and of their position along the shear. However different trends are observed for samples from shears C2 and C4. For samples from shear C2, there is a correlation between the Au grades and the sample elevation, where higher grades are recorded in shallower samples. Therefore, as Au grade increases (from <0.01 to >10 ppm) and as elevation increases (from -288.1 to 217.6 m), tourmaline shows a systematic decrease in V (574 to 440 ppm), Fe (5.16 to 3.77 wt%) and an increase in Ni (10.3 to 33.5 ppm), Zn (309 to 378 ppm) and Sr (233 to 475 ppm). Chlorite shows a systematic increase of Li (86.8 to 140 ppm), Sc (8.6 to 39.8 ppm) and Zn (408 to 637 ppm), and a decrease in Mn (1204 to 405 ppm) and Co (25.9 to 3.8 ppm).

In the case of shear C4, following an increase in the Au grade (from <0.01 to >10 ppm), tourmaline shows a systematic increase in Zn (228 to 407 ppm)

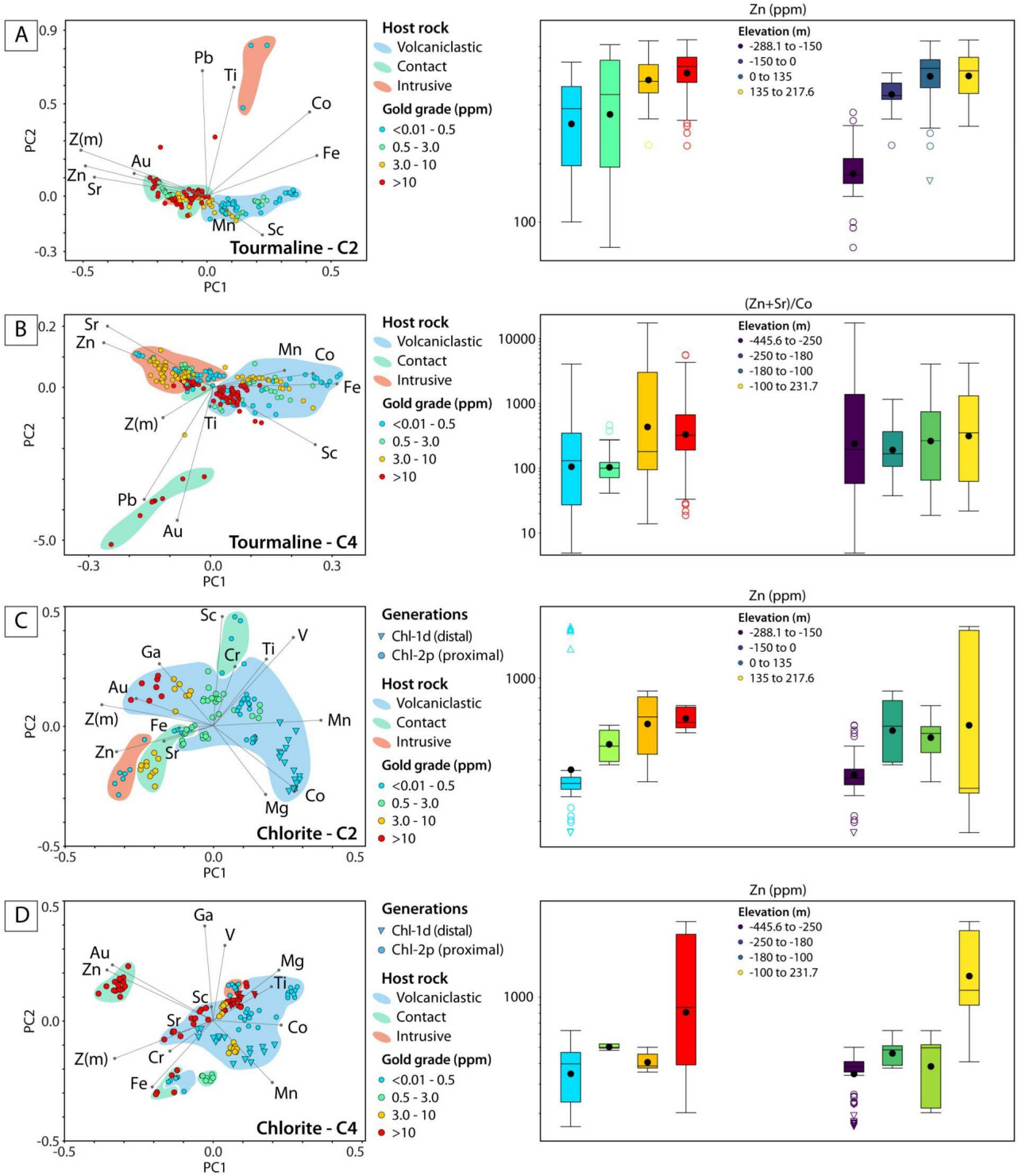

Figure 3. Principal Component Analysis of selected elements in tourmaline and chlorite from the shears C4 and C2, and the elements selected that better control the distribution of Au grades (ppm) and elevation (m) of the samples.

and Cr (34.8 to 216 ppm), and a decrease in Ca (3248 to 2872 ppm). Chlorite shows a systematic increase in Li (78.8 to 148 ppm) and Zn (413 to 2199 ppm) contents. With variations in elevation for C4 (from -445.6 to 231.7 m), tourmaline shows a systematic decrease in Sc (42 to 32 ppm), V (506 to 212 ppm) and an increase in Ni (35 to 70 ppm); chlorite shows a systematic increase in Zn (357 to 498 ppm) and Li (65 to 101 ppm). Therefore, Zn contents in chlorite seems to be sensitive to variations in Au grade and elevation in both shear C2 and C4.

2.2. Principal Component Analysis (PCA) and elemental ratios

Principal Component Analysis (PCA) allows to define the main elements controlling the chemical variabilities and correlating with either the elevation or the Au grade of the samples. Each PC explains

part of the variance of the data, with the first (PC1) capturing the greatest variance, followed by the second (PC2), and so forth. For tourmaline from shear C2, PC1 is mainly controlled by Au grade, elevation, Zn Sr, Co and Fe; and PC2 by Ti, Pb, Mn and Sc (Figure 3A). For tourmaline from shear C4, PC1 is mainly controlled by Zn, Mn and Fe, PC2 is controlled by Au grade, Pb and Ti, and both PC1 and PC2 are controlled by elevation, Sr, Co and Sc (Figure 3B). For shear C2, the PCA confirm the strong correlation between samples elevation, Au grades, and the Zn content (Figure 3A). For shear C4, the (Zn+Sr)/Co ratio increases with the Au grade of the samples and it is also controlled by the elevation (Figure 3B). For chlorite from shear C2, PC1 is controlled by Mn, Zn, Fe, Sr, elevation and Au grades. PC2 is controlled by Sc and Cr. Both PC1 and PC2 are controlled by Mg, Co, V, Ti and Ga. In the case of shear C4, both PC1 and PC2 are controlled by Mn, Zn, Au grades, elevation, Mg and Ti. PC1 is controlled by Co and Sr, and PC2 is controlled by Sc, Ga and V. The Zn content increases with Au grades and elevation for both shear C2 and C4 (Figure 3C and 3D).

3 Discussion

As show by the PCA, the chemical variation of chlorite and tourmaline as a function of sample elevation and Au grade are different between shears C2 and C4, for both chlorite and tourmaline, with the only exception of Zn. The reason of the discrepancy still needs to be evaluated. It can also be noted in the PCA that the vein host rock can have a strong effect on the chemistry of both minerals, which requires further investigation (Figure 3).

Most of the chemical variation of tourmaline and chlorite along both shears C2 and C4 are associated with variation of the Au grade and elevation of the samples. This correlation complicates the interpretation of the observed chemical variation as they can be either due to changes of the physicochemical conditions of the mineralising fluid associated with Au precipitation, or it can reflect the progressive evolution of the ascending mineralising fluid along the shears.

In shear C2, where most of the samples come from the shear that crosscut the mafic tuffs, both tourmaline and chlorite display an enrichment of Zn and Sr with an increase of the sample elevation, along with a depletion of Co. This variation may be linked to an increase content of those elements in the fluid, in response of the alteration of the mafic tuffs along the pathway of the ascending mineralising fluids, as suggested by Sciuba et al. (2021). However, further analyses need to be performed to clearly identify the different factors controlling the chemical variability of tourmaline and chlorite along the two shear zones.

4 Conclusions

Preliminary mineral chemistry results for tourmaline and chlorite in the Triangle deposit show that the chemistry of both minerals vary as a function of the Au grade and/or the elevation of the samples. These results also demonstrate that both minerals have the potential to be used as vector to target high grade zones in orogenic Au mineralised shear zones. However, some discrepancies between the chemical variation of both tourmaline and chlorite along the two investigated shear zones need to be explained before the development of such exploration tools. Further analysis will be performed to investigate the effects of host rock composition on chlorite and tourmaline trace element content along the two shears, and to identify the different factors controlling the chemical variability observed in both minerals.

Acknowledgements

This research is supported by the *Fonds de Recherche du Québec Nature et Technologies* (FRQNT), grant #FT130375. The authors would like to thank Eldorado Gold Corporation for allowing access to the property and for all the support during logging and sampling.

References

Latulippe M (1976) Excursion géologique: la région de Val-d'Or-Malartic.(Ed.) Ministère des richesses naturelles du Québec: Institut canadien des mines et de la métallurgie.

Neumayr P, Hagemann SG, Couture J-F (2000) Structural setting, textures, and timing of hydrothermal vein systems in the Val d'Or camp, Abitibi, Canada: implications for the evolution of transcrustal, second- and third-order fault zones and gold mineralization. Can J Earth Sci 37:95–114. https://doi.org/10.1139/e99-105

Pilote P (2000) Géologie de la région de Val d'Or, Sous-province de l'Abitibi-Volcanologie physique et évolution métallogénique

Pilote P, Moorhead J, Mueller W (1998) Développement d'un arc volcanique, le région de Val d'Or, ceinture de l'Abitibi - volcanologie physique et évolution métallogénique : guide d'excursion A2, 14-17 mai 1998

Robert F, Brown AC (1986a) Archean gold-bearing quartz veins at the Sigma Mine, Abitibi greenstone belt, Quebec; Part II, Vein paragenesis and hydrothermal alteration. Economic Geology 81:593–616. https://doi.org/10.2113/gsecongeo.81.3.593

Robert F, Brown AC (1986b) Archean gold-bearing quartz veins at the Sigma Mine, Abitibi greenstone belt, Quebec; Part I, Geologic relations and formation of the vein system. Economic Geology 81:578–592. https://doi.org/10.2113/gsecongeo.81.3.578

Robert F, Kelly WC (1987) Ore-forming fluids in Archean gold-bearing quartz veins at the Sigma Mine, Abitibi greenstone belt, Quebec, Canada. Economic Geology 82:1464–1482. https://doi.org/10.2113/gsecongeo.82.6.1464

Sciuba M, Beaudoin G, Makvandi S (2021) Chemical composition of tourmaline in orogenic gold deposits. Minerallium Deposita 56:537–560. https://doi.org/10.1007/s00126-020-00981-x

Scott CR, Mueller WU, Pilote P (2002) Physical volcanology, stratigraphy, and lithogeochemistry of an Archean volcanic arc: evolution from plume-related volcanism to arc rifting of SE Abitibi Greenstone Belt, Val d'Or, Canada. Precambrian Research 115:223–260. https://doi.org/10.1016/S0301-9268(02)00011

Exploring semi-supervised generation of mineral list for automated mineralogy systems

L. Pereira[1], R. Tolosana-Delgado[1], S. Thiele [1], R. Japarov[1], M. Frenzel[1], K. Bachmann[1], K.G. van den Boogaart[1], J. Gutzmer[1]

[1] Helmholtz-Zentrum Dresden-Rossendorf, Helmholtz Institute Freiberg for Resource Technology, Germany

Abstract. The quality of results obtained by a scanning electron microscope-based automated mineralogy system strongly depend on the project-specific list of spectra of the minerals being mapped [1]. Mineral lists can be selected manually from existing universal lists that construct theoretical spectra from typical mineral composition, and/or can be constructed based on spectra measured in the samples of a specific project. Regardless of the source, the choice of mineral list is subjective: One can prefer extensive mineral lists to enhance the chances of capturing variations in chemical composition of specific minerals (e.g., splitting chlorite compositions); or else smaller, compact (lumped) mineral lists to reduce misclassification [2]. No general, perfect balance within generality-specificity or extension-compaction exists, so that users end up interactively and iteratively building the spectral library for each project in tedious steps of adding and removing mineral spectral candidates. This process is also project-, ore-and operator-specific. While some automated mineralogy devices provide operating modes for automatically constructing mineral lists throughout a measurement, these commonly offer only limited settings and are not clear about the data processing steps. Additionally, these established strategies do not provide the user with any measure of uncertainty, essential for geometallurgy [3].

The goal of this contribution is to compare the performance of several components of a strategy to automatically and objectively construct automated mineralogy mineral lists, making use of several machine learning algorithms, for the specific case of dataset collected with the Mineral Liberation Analyser (MLA). The strategy, which is illustrated in Figure1, has five steps: (1) preliminary data transformation, (2) dimension reduction, (3) endmember detection, (4) phase detection, and (5) spectral unmixing.

For each of these steps, several options were tested. These included for data transformation peak extraction and Box-Cox transformations [4], which at the same time embraces logarithm/log-ratio transformations, square root transformations and the identity transformation. Regarding dimension reduction, principal component analysis [5]. In step three, we considered QHull convex hull detection, and N-FINDER [6], a conventional linear endmember detection method. In step four, the goal is to find the groups of spectra that can be identified with the members of the mineral list, not all of them being necessarily endmembers. Algorithms tested here correspond to model-free unsupervised classification algorithms, such as k-means [7]. Finally, in step five we tried several sparse and non-negative-constrained linear unmixing algorithms. This unmixing was done within the sample of spectra forming the training data only in order to determine the number of necessary groups (or clusters) to extract from step four, as the actual final phase attribution will be done by the MLA software for the whole project after delivering the mineral list. Some of the results obtained in a Chromite deposit from the Bushveld complex are presented in Fig. 2. The strategy presented here offers not only improvements to the workflow of scanning electron microscope-based automated mineralogy systems but also is a step stone for compiling mineral lists in analytical devices such as µX-Ray Fluorescence automated mineralogy, where spectra mixing is a bigger issue.

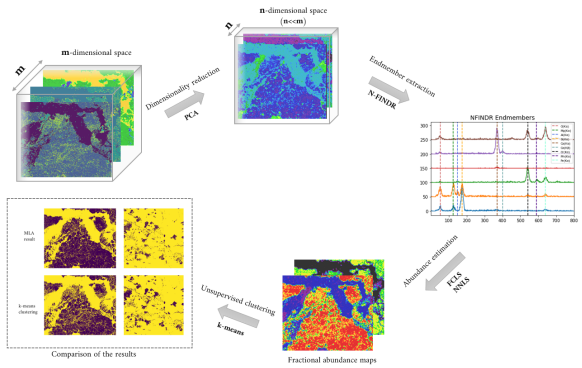

Figure 1. Schematic representation of the methodology applied in here.

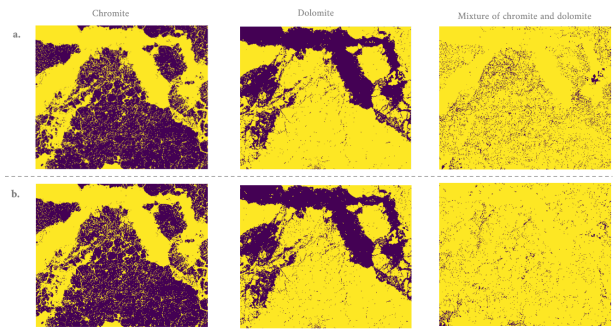

Figure 2. Summary of classification results obtained with the MLA (a) and the proposed method (b), illustrating the issue of mixed spectra.

References

Y. Gu, R. P. Schouwstra, and C. Rule, "The value of automated mineralogy," *Miner. Eng.*, vol. 58, pp. 100–103, Apr. 2014, doi: 10.1016/j.mineng.2014.01.020.

M. Kern, R. Möckel, J. Krause, J. Teichmann, and J. Gutzmer, "Calculating the deportment of a fine-grained and compositionally complex Sn skarn with a modified approach for automated mineralogy," *Miner. Eng.*, vol.

116, pp. 213–225, Jan. 2018, doi: 10.1016/j.mineng.2017.06.006.
K. G. van den Boogaart and R. Tolosana-Delgado, “Predictive Geometallurgy: An Interdisciplinary Key Challenge for Mathematical Geosciences,” in *Handbook of Mathematical Geosciences: Fifty Years of IAMG*, B. S. Daya Sagar, Q. Cheng, and F. Agterberg, Eds., Cham: Springer International Publishing, 2018, pp. 673–686. doi: 10.1007/978-3-319-78999-6_33.
“The Box-Cox Transformation Technique: A Review - Sakia - 1992 - Journal of the Royal Statistical Society: Series D (The Statistician) - Wiley Online Library.” https://rss.onlinelibrary.wiley.com/doi/abs/10.2307/2348250 (accessed May 15, 2023).
N. Kambhatla and T. K. Leen, “Dimension Reduction by Local Principal Component Analysis,” *Neural Comput.*, vol. 9, no. 7, pp. 1493–1516, Jul. 1997, doi: 10.1162/neco.1997.9.7.1493.
M. E. Winter, “N-FINDR: an algorithm for fast autonomous spectral end-member determination in hyperspectral data,” in *Imaging Spectrometry V*, M. R. Descour and S. S. Shen, Eds., SPIE, 1999, pp. 266–275. doi: 10.1117/12.366289.
A. Likas, N. Vlassis, and J. J. Verbeek, “The global k-means clustering algorithm,” *Pattern Recognit.*, vol. 36, no. 2, pp. 451–461, Feb. 2003, doi: 10.1016/S0031-3203(02)00060-2.

Critical Minerals: Germanium and Cobalt in the Bornite Deposit, Southwestern Brooks Range, Alaska

Katharina Pfaff[1] , Garth Graham[2] , Alexander Jones[1] , Karen Kelley[2]
[1]Center to Advance the Science of Exploration to Reclamation in Mining (CASERM), Department of Geology and Geological Engineering, Colorado School of Mines, USA
[2]U.S. Geological Survey, Geology, Geophysics, and Geochemistry Science Center, Denver, USA

Abstract. Increasing demand for Ge and Co has led to a renewed interest and focus on advancing our understanding of the occurrence, distribution, and sequestration of these critical elements in known ore deposits. A workflow using a variety of analytical techniques and co-registered datasets has been developed and was applied to the carbonate hosted Bornite Cu-Co (Zn,-Ge) deposit in Alaska, where a new orebody ("the South Reef") was discovered in 2011. The South Reef is host to substantial amounts of high-grade Cu, Co, and appreciable Zn, but also contains localised elevated concentrations of Ge. We describe the mineralogy and paragenesis of the South Reef based on detailed optical petrography, scanning electron microscopy, scanning electron microscopy-based automated mineralogy, and mapping μ-X-ray fluorescence analysis. Germanium was found to exist in renierite, white mica, illite, galena and feldspars within the South Reef. Cobalt was found to occur in cobaltiferous pyrite, carrollite, and cobaltite.

1 Introduction

Our society has become increasingly dependent on mineral commodities to facilitate our transition to green energy and ever advancing technologies. The United States government recently included Ge and Co as "critical minerals", which are necessary for the manufacture of a product, but where we currently have a dependency on foreign sources. The absence of these commodities can have significant consequences for the U.S. economy or national security (Executive Office of the President 2017, U.S. Geological Survey, 2022). Identification of domestic sources of critical mineral commodities is an important step toward independence from foreign sources which may be unreliable. However, little is known about the occurrence, distribution, and sequestration of many critical minerals in known ore deposits.

The aim of this study was to develop a workflow that efficiently and effectively characterises the ore, gangue, and alteration mineralogy to inform us about the occurrence, distribution, and sequestration of all critical minerals in the South Reef. Improved understanding of the nature of mineralised zones provides fundamental information for development of systems models that unravel ore forming processes that can guide critical mineral exploration and assessment.

The Bornite deposit is located in the Cosmos Hills, on the southern flank of the western Brooks Range, approximately 260 km east of Kotzebue and 460 km north of Fairbanks (Fig. 1).

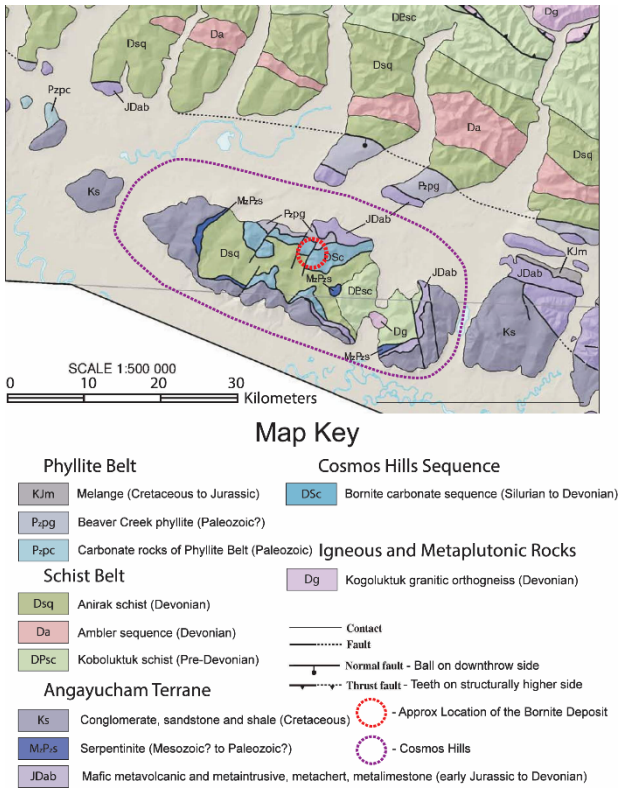

Figure 1. Regional geology and location of the Bornite deposit. Geology modified after Hitzman (1986) and Till et al. (2008).

Mostly Devonian schists and carbonates are exposed in a N-W trending, double plunging anticline (Hitzman 1986). The Bornite Cu-Co (Zn, Ge) deposits are hosted in the Devonian-Silurian Bornite carbonate sequence. Ore forming processes appear to have included brecciation and replacement of carbonates, and influx of copper-rich metalliferous fluids that led to a complex paragenesis, dominated by chalcopyrite (with high grade zones containing bornite, chalcocite and tennantite). The deposit has an indicated Cu resource of 40.5 Mt with an average grade of 1.02% and a total inferred 141.9 Mt at an average grade of 1.74%. The deposit is also host to a significant amount of Co with an inferred 182.4 Mt of Co at an average grade of 0.019% (Davis et al. 2008). Germanium resource values have not been published.

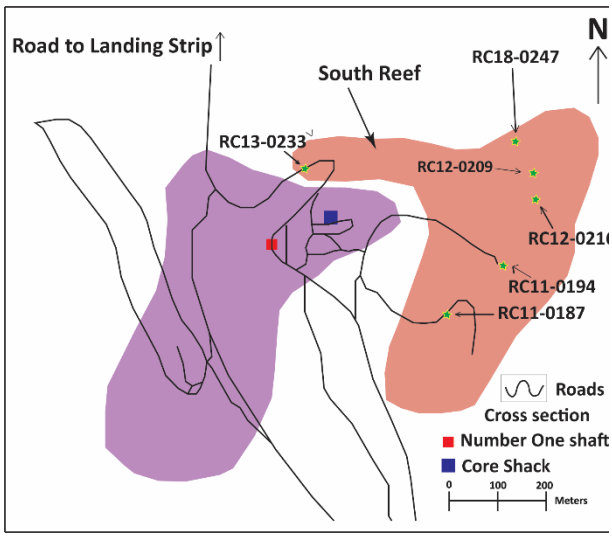

Figure 2. Plan view map of the location of the historical main Number One orebodies (purple) and the South Reef (orange), and drill hole collars from which samples were collected.

Although standard analytical methods are effective at accurately measuring the abundance of numerous elements including Cu, Co, and Zn, Ge concentrations are commonly under-represented because of volitisation during sample digestion. However, limited multi-element data (Grannito et al. 2019, Trilogy Metals, Written Communication, 2018) demonstrate that elevated Ge concentrations occur locally in the Bornite deposit.

Reconnaissance, high-quality data indicate that Ge-rich intervals correlate with bornite-rich copper zones. Cobalt mainly occurs as cobaltiferous pyrite within and around the copper mineralised zones and as carrollite and cobaltite directly associated with copper bearing minerals. Therefore, areas with visibly high chalcocite, bornite and chalcopyrite were chosen for sampling.

The aim of this study was to improve our understanding of the occurrence and sequestration of Ge in the South Reef of the Bornite deposit and to develop a workflow using co-registered datasets to better understand the critical mineral endowment. Optical microscopy, μ-X-ray fluorescence (μ-XRF) mapping, field emission scanning electron microscopy (FE-SEM) backscattered electron (BSE) imaging coupled with energy dispersive spectroscopy (EDS) for semi-quantitative chemical analysis, and SEM-based automated mineralogy were employed on samples taken from the South Reef orebody.

2 Samples and Methods

2.1 Samples

Quarter-core samples were collected from variably mineralised Cu intercepts from 6 drill holes in the South Reef (shown in Fig. 2). Drill hole RC11-0187 was the most extensively sampled (48 of the 98 total samples) because of its extremely thick Cu-mineralised intercept. Samples from the Number One ore body were provided by the U.S. Geological Survey (USGS) prior to sample collection for the purpose of initial reconnaissance. The South Reef samples were chosen based on the availability of modern drill core, modern reconnaissance Ge assay data, and the opportunity to sample different intensities of mineralisation.

2.2 Methods

Forty-one of the 98 drill core samples collected were selected for analysis in the Mineral and Materials Characterization Facility at the Colorado School of Mines because they reflect different intensities of mineralisation. Our workflow was multi-step. First, a mapping μ-XRF (M4 Tornado, Bruker) was used as a reconnaissance tool to determine elemental distributions in these 41 samples so that a sub-sampling strategy could be determined. Next, billets from selected areas on 25 samples were cut for thin section preparation for more detailed study. These billets were mapped using the μ-XRF at a higher resolution prior to thin section preparation. Third, the finished thin sections were inspected under transmitted and reflected light, FE-SEM BSE (MIRA, Tescan) and EDS (XFlash® 6/30 silicon drift detector, Bruker) and SEM-based automated mineralogy (TIMA, Tescan) to understand mineral paragenesis and related occurrence and distribution of cobalt and germanium in the South Reef.

3 Results and Discussion

Mineral paragenesis of the South Reef was determined based on a combination of petrography and co-registered micro-analytical methods such as mapping μ-XRF, SEM-based automated mineralogy, and traditional FE-SEM BSE and EDS analyses. The South Reef consists of localised high grade Cu intercepts, including massive bornite and chalcocite that extend laterally into more abundant chalcopyrite-rich zones.

Micro-XRF mapping (Fig. 3) showed that Co is hosted in cobaltiferous pyrite, carrollite, and cobaltite and revealed a strong correlation between Cu and Fe, and that high Co values almost always correspond to high Ni values. Barium and K as well as Ge and K show a significant spatial correlation. A notable correlation was seen between Co, Bi, As, and Pb in some samples. Within areas showing high Cu (Cu sulphides), bright areas of Ge could be found.

Five paragenetic stages were delineated: (I) dolomitisation, (II) ferroan alteration, (IIIa) veining, (IIIb) brecciation, (IV) main ore forming event (Fig. 4), and (V) a post ore forming event. Stage I predominantly consists of diagenetic low-temperature dolomite and pyrite, followed by ferroan stage II dolomite and pyrite as reported by Hitzman (1986). Stage III includes different carbonates, pyrite, cobaltiferous pyrite, and the Ba-minerals cymrite and alstonite. During the main ore forming stage IV, cobaltiferous pyrite was replaced by mainly chalcocite and subordinately bornite. Trace elements in stage III cobaltiferous pyrite (Co, As, Pb) were liberated and precipitated as cobaltite, carrolite, galena, tennantite (Mahaffey 2021; this study). Petrographic observations reveal a distinct precipitation succession of the different Cu-sulphide minerals in stage IV. Chalcocite, bornite, and chalcopyrite did not precipitate in equilibrium but are staggered in space and time, with chalcocite precipitating first in the centre of the deposit,

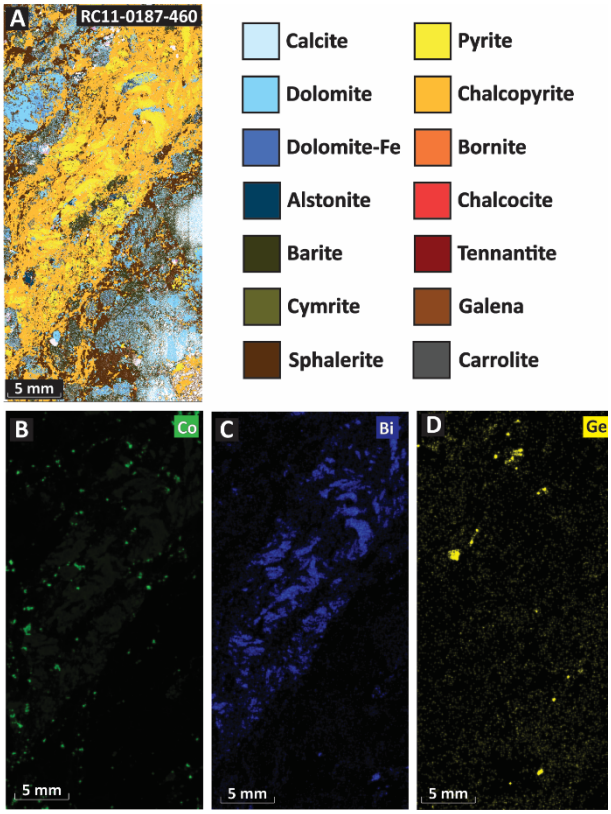

Figure 3. Sample RC11-0187-460. A) SEM-based automated mineralogy images, and μ-XRF element maps of B) Co, C) Bi, and D) Ge.

followed by bornite and then chalcopyrite (Hitzman 1986, Conner 2015, this study). The mineral renierite is the Ge bearing sulphide in the South Reef orebody. Renierite predominantly occurs as inclusions in chalcocite and bornite and is significantly less abundant in chalcopyrite. Renierite grains in chalcopyrite are commonly in contact with residual bornite and are always much smaller than renierite inclusions in chalcocite and bornite. These textures suggest that renierite, like bornite and chalcocite, is no longer in equilibrium in the presence of chalcopyrite. Discrete cobalt minerals occur in high-grade Cu zones and are represented by carrolite and cobaltite.

Hitzman (1986) suggested that the mineralizing fluid was a warm (100 to 215°C) basinal brine, rich in hydrocarbons, suggesting that the fluid responsible for ore formation was highly reduced. A reduced and acidic basinal brine at 200°C is able to transport significant amounts of Cu, Ba, and Zn (Cooke et al. 2000; Pfaff and Graham 2013).

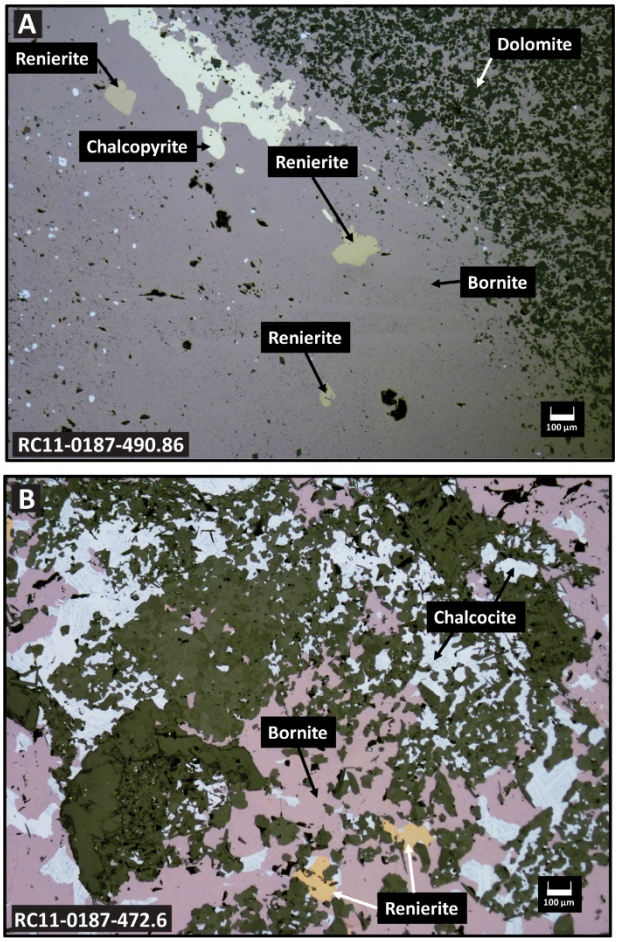

Figure 4. Stage IV ore mineralogy. Renierite hosted in bornite and in association with chalcocite and minor chalcopyrite.

This is consistent with observations from other carbonate hosted Cu-sulphide deposits such as the Black Butte deposit in Montana (Pfaff and Graham 2013) or the lead-zinc clastic sediment hosted Sullivan Deposit (Cooke et al. 2000). It is suggested here that reduced acidic basinal brines ascended along basin faults and interacted with carbonates at the site of ore deposition, causing the fluid to shift in pH towards more alkaline conditions, resulting in the precipitation of ore minerals. The succession of Cu-sulphide minerals is interpreted to reflect the evolving fluid during fluid-rock interaction leading to more alkaline conditions and to a concomitant decrease in sulphide activity in the mineralizing fluid over space and time. When the sulfur activity in the fluid decreases, chalcopyrite is formed at the expense of bornite and pyrite and renierite is destabilised (Einaudi et al. 2005). Similar textural evidence can also be observed at Kipushi where renierite preferentially occurs in chalcocite and bornite (De Vos et al. 1974, Schneider et al. 2007).

5

6 5 Conclusions

The South Reef of the Bornite Cu-Co-(Ge) deposit is host to substantial amounts of high-grade Cu, Co, and Zn, but also hosts elevated concentrations of Ge. With an increasing demand for Co and Ge and the lack of literature on their occurrence and sequestration within primary ore deposits, understanding known Co- and Ge-bearing ore deposits is critical for future exploration efforts. Five

paragenetic stages have been delineated at the South Reef of the Bornite Cu-Co-(Ge) deposit: (I) dolomitisation, (II) ferroan alteration, (IIIa) veining, (IIIb) brecciation, (IV) ore forming event, and (V) post ore forming event. Cobalt occurs in cobaltiferous pyrite, carrollite, and cobaltite. Germanium occurs in renierite as well as enrichments in white mica, illite, galena and feldspars within the South Reef. Highest Ge-mineral (renierite) as well as Co-minerals (carrolite and cobaltite) abundances appear to correlate with highest bornite and chalcocite concentrations.

We propose that reduced acidic basinal brines capable of transporting significant amounts of Cu entered the organic matter rich carbonates and phyllites, leading to fluid-rock interaction at the site of deposition. The ore-forming basinal brine was subsequently buffered to an intermediate oxidation state and a near-neutral pH. Petrographic observations and SEM-based automated mineralogy reveal a distinct spatial and temporal precipitation succession from chalcocite, bornite, followed by chalcopyrite. This succession in Cu-minerals is interpreted to reflect the evolving ore forming fluid at the site of deposition, characterised by a decrease in temperature and a concomitant decrease in sulphide activity of the mineralizing fluid. This shift in pH towards more alkaline conditions, and subordinately a decrease in temperature and concomitant decrease in sulphide activity, are thought to have been the predominant precipitation mechanism leading to the distinct mineral zonation in space and time. Cobalt, which predominantly occurs in pre-main ore stage cobaltiferous pyrite, was replaced and Co was liberated during the ore forming process, leading to the formation of discrete Co-minerals (carrolite and cobaltite). Germanium is interpreted to have precipitated contemporaneously with chalcocite and bornite when the sulphur activity in the fluid was still high, forming discrete renierite minerals.

The Bornite deposit shares many similarities with other Ge-bearing carbonate hosted base metal deposits in Africa such as the Tsumeb, Kipushi, Khusib Springs, Kombat, and Kabwe deposits, however it seems to be of lower germanium grade than these deposits.

7 Acknowledgements

We thank Trilogy Minerals, and specifically Andy West, Bonnie Broman, and Dave Szumigala for access to drill core. Thanks to Heather Lowers and Mitchel Bennett for thorough reviews, which improved this contribution significantly.

Disclaimer

Any use of trade, firm, or product names is for descriptive purposes only and does not imply endorsement by the U.S. Government

8 References

Cooke D, Bull S, Large R, McGoldrick P (2000) The importance of oxidized brines for the formation of Australian Proterozoic stratiform sediment-hosted Pb-Zn (sedex) deposits. Econ Geol 95: 1-18.

Conner DT (2015) Geology of the Bornite copper-zinc-cobalt carbonate-hosted deposit, southwestern Brooks Range, Alaska, Masters Thesis, Colorado School of Mines, 70p.

Davis B, Rim R, Austin J (2008) NI 43-101 Technical Report on the Bornite Project, Northwest Alaska, USA. Prepared for Trilogy Metals Inc.

De Vos W, Viaene W, Moreau J (1974) Minéralogy du gisement de Kipushi, Shaba, Zaïre. Cent de la Soc Géol 165-183.

Einaudi MT, Hedenquist JW, Esra Inan E (2005) Sulfidation state of fluids in active and extinct hydrothermal systems: Transitions from porphyry to epithermal environments. In: Volcanic, Geothermal, and Ore-Forming Fluids: Rulers and Witnesses of Processes with the Earth, Sturart F. Simmons, Ian Graham. https://doi.org/10.5382/SP.10.15

Granitto M, Wang B, Shew NB, Karl SM, Labay KA, Werdon MB, Seitz SS, Hoppe JE (2019) Alaska Geochemical Database Version 3.0 (AGDB3) including best value data compilations for rock, sediment, soil, mineral, and concentrate sample media: U.S. Geological Survey data release, https://doi.org/10.5066/P98NHRAD.

Hitzman M (1986) Geology of the Ruby Creek copper deposit, southwestern Brooks Range, Alaska, Economic Geology 81: 1644-1674 https://doi.org/10.2113/gsecongeo.81.7.1644

Jones A (2021) Germanium occurrence in the Bornite deposit, southwestern Brooks Range, Alaska, Masters Thesis, Colorado School of Mines, 103p. https://hdl.handle.net/11124/176411

Mahaffey ZB (2021) The mineralogical associations, distribution, and mineral zoning of cobalt in the Bornite deposit, southwest Brooks Range, Alaska, University of Alaska Fairbanks, Masters Thesis, 134 p. plus appendices., http://hdl.handle.net/11122/12625

Pfaff K, Graham GE (2013) The Black Butte Cu-(Co-Ag) deposit, Montana: A thermodynamic model. GSA Annual Meeting & Exposition, Denver, Colorado, USA. https://gsa.confex.com/gsa/2013AM/webprogram/Paper229705.html

Schneider J, Melcher F, Brauns M (2007) Concordant ages for the giant Kipushi base metal deposit (DR Congo) from direct Rb-Sr and Re-Os dating of sulfides. Miner Depos 42: 791-797.

Till AB, Dumoulin JA, Harris AG, Moore TE, Bleick H, Siwiec B (2008) Preliminary integrated geologic map databases for the United States: digital data for the geology of the southern Brooks Range, Alaska: U.S. Geological Survey Open-File Report 2008-1149.

U.S. Geological Survey, 2016, 2022 Final List of Critical Minerals: Federal Register/Vol. 87, No.37/Thursday, February 24, 2022/Notices: 10381-10382.

Exploring the preservation potential of mineral deposits in the northern Canadian Cordillera through low temperature thermochronology: preliminary insights

Nicolas Pinet[1], Dawn Kellett[2], Isabelle Coutand[3], Patrick Sack[4]
[1]Geological Survey of Canada, Québec, QC, Canada
[2]Geological Survey of Canada, Dartmouth, NS, Canada
[3]Department of Earth Sciences, Dalhousie University, Halifax, NS, Canada
[4]Yukon Geological Survey, Whitehorse, YK, Canada

Abstract. In northern Canada and eastern Alaska, Late Cretaceous to Eocene mineral deposits formed at upper crustal levels, after the accretion of allochthonous terranes against North America. To analyse their preservation potential, an orogen-scale study of multiple low temperature thermochronometers has been initiated. This study will enable a large-scale investigation into spatio-temporal variations in exhumation, and thus delineate areas favourable for preservation of mineral deposits formed at shallow depths.

1 Introduction

Reflecting its complex geological history, the northern Cordillera, which spans northern British Columbia, Yukon (Canada) and eastern Alaska (USA), is endowed with diverse mineral deposit types of various ages. Some deposits were formed before or during the primarily Jurassic accretion of allochthonous terranes against ancestral North America, whereas others are linked to post-accretionary tectonism and magmatism. Post Jurassic mineral deposits include (Fig. 1A; Allan et al., 2013; Nelson et al., 2013):

1) mid-Cretaceous gold mineralization occurring in an elongated belt extending from eastern Alaska to easternmost Yukon, associated with the emplacement of several mid-Cretaceous (115-98 Ma) intrusive suites. Mineralization includes intrusion breccia complexes, Au- and W-skarns, reduced intrusion-related deposits and epithermal mineralization, and polymetallic veins.
2) Late Cretaceous (79-72 Ma) Cu-Mo-Au porphyries, skarns and epithermal deposits that are significantly enriched in Au. In Alaska and west-central Yukon, some of the mineral deposits are associated with small volume, high-level intrusive bodies that have isotopic signatures and geochemical affinities to mantle-derived magmas with minor crustal inheritance. Carlin-type deposits located in east-central Yukon also formed during this metallogenic event.
3) Latest Cretaceous to Eocene (70-50 Ma) porphyry Cu, Mo systems and polymetallic veins, carbonate replacements, skarn bodies and epithermal systems. Some of the mineralized zones overlap in age with extensive regional emplacement of the volcanic rocks of the 71-68 Ma Carmacks Group that once covered much of central-southwest Yukon (Fig. 1)

Aside from exposed magmatic rocks, and the Tintina and Denali faults, parallel, major right-lateral strike-slip faults with ~ 370 and ~ 430 km of mainly Cenozoic displacement, respectively (Fig. 1A), there are few constraints on the mid-Cretaceous to Eocene geological history of the northern Cordillera. However, this time interval was marked by a change in plate-margin geometry, possible variations in lithospheric thickness and a subtropical climate, that collectively likely have had a profound impact on landscape evolution of the mountain belt. Late Cretaceous to Cenozoic geological history potentially resulted in variations in exhumation distribution and intensity across the orogen that may have impacted the preservation potential of shallow-crustal level hydrothermal deposits. We are undergoing a regional-scale multi-thermochronology study to quantify spatio-temporal variations in crustal exhumation and hereby introduce preliminary insights.

2 Geomorphological setting

Between the Denali and Tintina faults, the Yukon uplands represent a relatively low erosional surface that truncates metamorphic rocks and intrusions. The base of the shallowly dipping (generally < 10°) volcanic rocks of the Carmacks Group preserved in central Yukon represent the paleo-topography at 71-68 Ma. This suggests that the age of the planation of the Yukon uplands is at least Late Cretaceous. This led Ryan et al. (2017) to propose that there has been little net incision since the late Mesozoic. However, the amount of eroded, post 71 Ma rocks is poorly constrained (Dusel-Bacon et al., 2016).

3 Low-temperature thermochronology

Figure 1B shows available published and unpublished low-temperature thermochronology data including (U-Th)/He analyses on zircon (ZHe), apatite fission track analyses (AFT) and (U-Th)/He analyses on apatite (AHe) with closure temperature ranges of ~20–200°C, ~80–120°C and ~30–120°C, respectively (Ault et al., 2019).

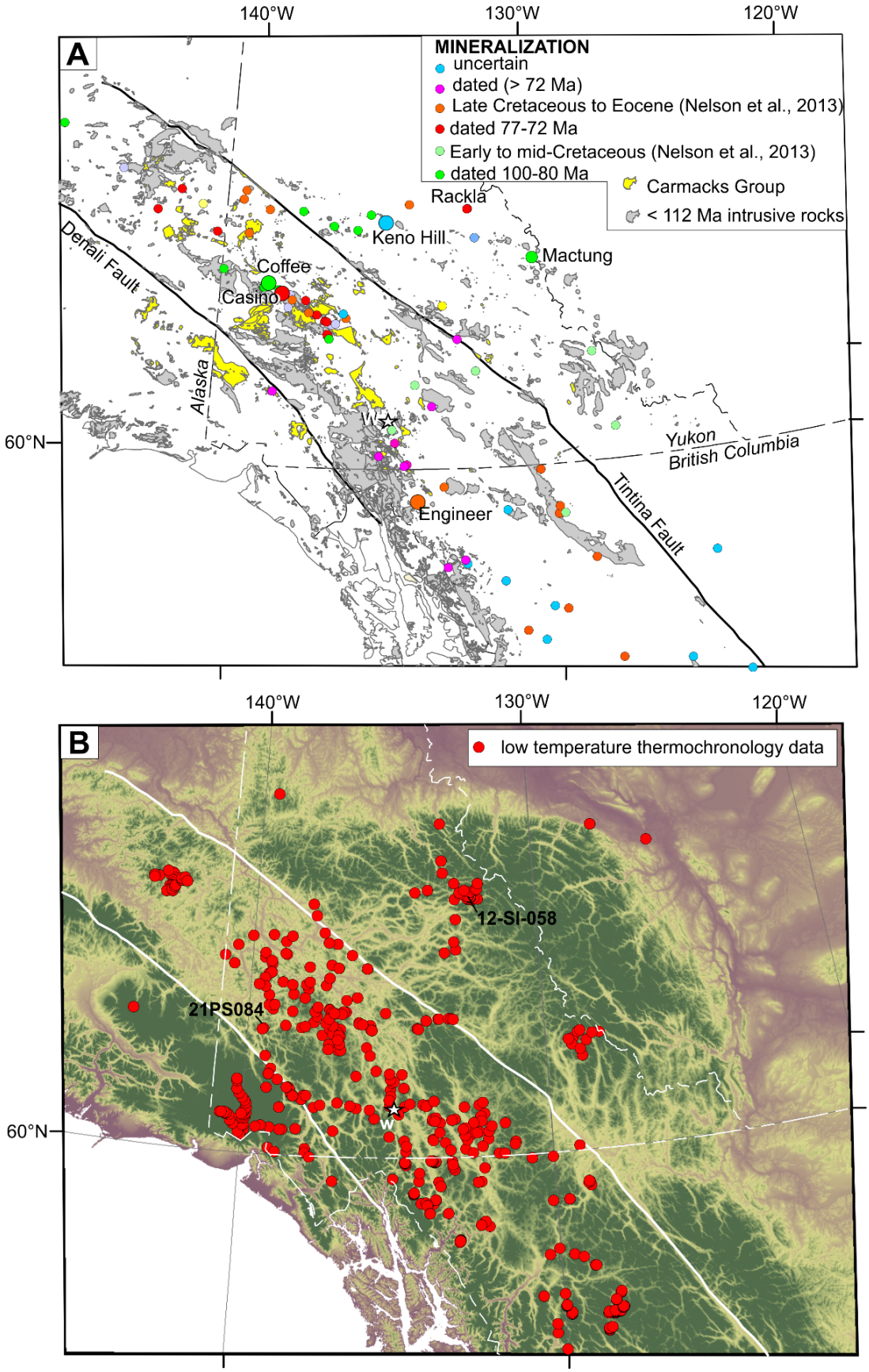

Figure 1. A- Geological setting of the northern Cordillera with location of the mid-Cretaceous to recent mineralized zones; Methods to constrain the age of dated mineralized zones include Re–Os, $^{40}Ar/^{39}Ar$ and U-Pb. Volcanic rocks of the Carmacks Group (71-68 Ma) and intrusive rocks younger than 112 Ma are located. B- Available low-temperature thermochronology data. W, Whitehorse.

Among the > 600 compiled samples, ca. 32% include several thermochronometers, providing independent information on the T-t path in the upper crust.

When several thermochronometers are used on the same sample, dates usually conform to the expected order, with ZHe > AFT > AHe, especially in young orogens (Whipp et al., 2022). The time difference between ZHe, AFT and/or AHe dates on a single sample varies significantly within the dataset, which indicates a difference in exhumation rates (i.e., rapid exhumation is expected to yield minimal difference between dates).

Dated samples represent a wide range of sedimentary, metamorphic and plutonic rocks of various ages, collected at various elevations which add complexity to the interpretation of regional exhumation patterns. However, for each sample, predictable ZHe, AFT and/or AHe dates are expected for various T-t scenarios (Fig. 2). To facilitate T-t modelling, recently collected data target Cretaceous magmatic rocks which record only thermal events postdating crystallization.

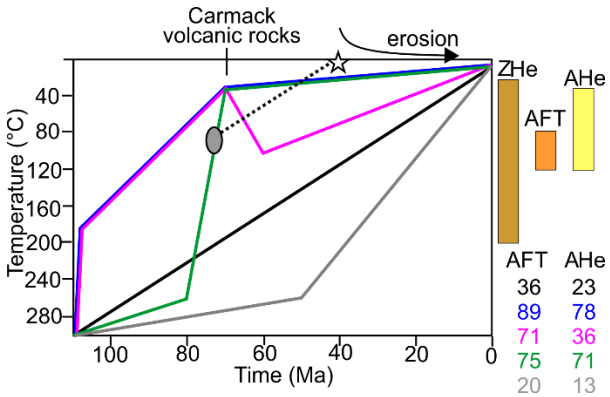

Figure 2. Time-temperature diagram for an intrusive rock emplaced at ca. 110 Ma and showing expected AFT and AHe dates (in Ma) for different potential T-t paths. The closure temperature windows of thermochronometers are indicated. The ellipse, dashed line and star illustrate the T-t path of a hypothetical mineral deposit formed at 2-3 km depth during the Late Cretaceous (ca. 74 Ma) in an area characterized by constant cooling (black T-t path). Such deposit would be eroded at ca. 40 Ma.

4 Preliminary results

Figure 3 shows two examples that illustrate how independent geological constraints may help to define Late Cretaceous to Cenozoic T-t paths.

Sample 12-SI-058 (location in Fig. 1B) yields an AFT age of 49.2 ± 5.3 Ma, with a mean track length of 13.6 µm. It was sampled from Neoproterozoic sedimentary rocks located 2 km from Carlin-type deposits in central Yukon (Pinet et al., 2023). Pyrobitumen reflectance and programed pyrolysis results constrain the maximum temperature during the Late Cretaceous to 230-150 °C (constraint 1, Fig. 3A). Maximum temperature during mineralization at ca. 74 Ma is 91 °C based on fluid inclusion and clumped isotope thermometry on late ore stage minerals (constraint 2, Fig. 3A). Inverse modeling suggests a period of rapid cooling at ca. 35 Ma.

Sample 21PS084 (location in Fig 1B) yields an AFT date of 34.8 Ma ± 2.6 Ma, with a mean track length of 14.5 ± 0.4 µm. It is an intrusive sample collected from the mid-Cretaceous Whitehorse magmatic suite (constraint 1: temperature > 300°C at 112-98 Ma, Fig. 3B). This sample is located 4.2 km from exposed Carmacks Group at an elevation only 125 m lower than the base of the group (constraint 2: temperature < 60 °C during volcanic rocks emplacement at ca. 70 Ma, Fig. 3B). Inverse modelling indicates that only scenarios with one or several heating episode(s) during the Cenozoic may account for the data if geological constraint 2 is considered, even if no rock younger than the Carmacks Group is known in the area.

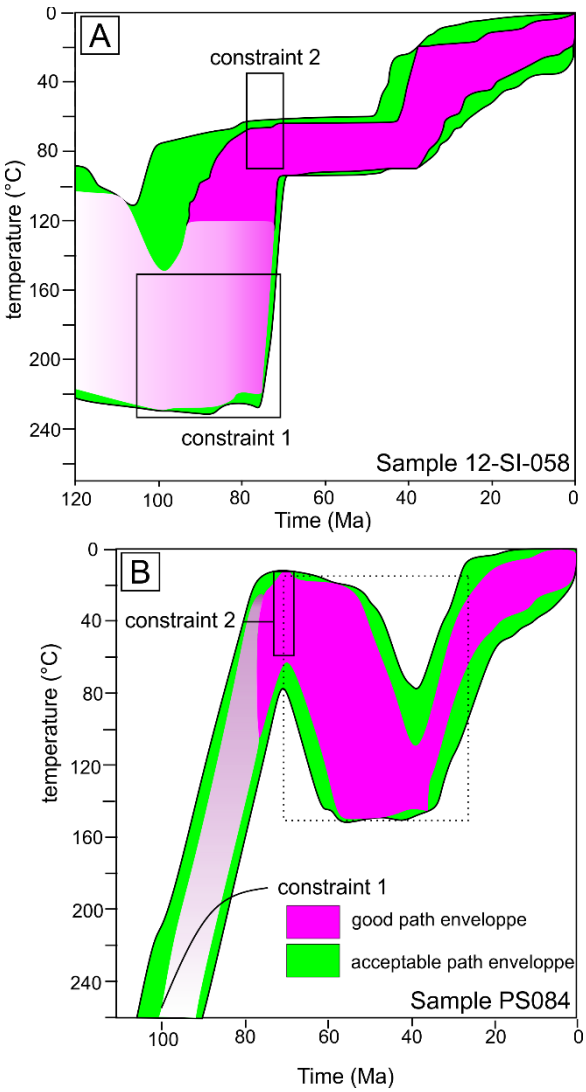

Figure 3. Inverse modelling results using *HeFTy* software (Ketcham, 2013). The black boxes are geological constraints used during modelling. The part of the magenta envelope with a colour gradient is almost unconstrained by modelling.

5 Future work

New low-temperature thermochronology analyses are in the process of being added to this compiled ZHe, AFT and AHe dataset with the aim to apply a large spatial- and temporal- coverage to investigate rates, patterns and drivers of orogen-wide exhumation, within a regionally consistent framework. This approach should help to depict spatial trends of exhumation, possibly linked to plate-boundary processes, tectonic activity, magmatism and post-orogenic surface processes and ultimately provide insight on the preservation of Late Mesozoic to Cenozoic mineral deposits.

Acknowledgements

All the participants of the GEM GeoNorth project 'Faults, fluids and landscape evolution: Cretaceous to Cenozoic in the Northern Cordillera' are warmly acknowledged.

References

Allan M.M., Mortensen J.K., Hart C.J.R., Bailey L.A., Sanchez M.G., Ciolkiewicz W., McKenzie G.G., Creaser R.A. (2013) Magmatic and metallogenic framework of west-central Yukon and eastern Alaska: Society of Economic Geologists, Special Publication 17, p. 111–168.

Ault A.K., Gautheron C, King G.E. (2019) Innovations in (U-Th)/He, fission track, and trapped charge thermochronometry with applications to earthquakes, weathering, surface-mantle connections, and the growth and decay of Mountains. Tectonics, 38:3705-3739.

Dusel-Bacon C., Bacon C., O'Sullivan P.B., Day W.C. (2016) Apatite fission-track evidence for regional exhumation in the subtropical Eocene, block faulting, and localizes fluid flow in east-central Alaska. Can. J. Earth Sci., 53:260-280.

Ketcham RA (2013) HeFTy, version 1.8.2. Manual user dated 2 october 2013.

Nelson J.L., Colpron M., Israel S., 2013. The Cordillera of British Columbia, Yukon and Alaska: tectonics and metallogeny. Soc. Econ. Geol., Special Publication 17, pp. 53-109.

Pinet, N., Haeri-Ardakani O., Jautzy J., Savard M.M., Sack P., Mercier-Langevin P., 2023. Thermal history of Carlin-type gold deposits in Yukon (Canada) as revealed by organic matter geothermometry, clumped isotope data, fluid inclusion microthermometry, and apatite fission-track analyses. Mineralium Deposita, https://doi.org/10.1007/s00126-023-01162-2

Ryan J.J., Hayward N., Jackson Jr., L.E. (2017). Landscape antiquity and Cenozoic drainage development of southern Yukon, through restoration modeling of the Tintina Fault. Can. J. Earth Sci., 54:1085-1100.

Whipp D.M., Kellett D.A., Coutand I. and Ketcham R.A. (2022) Modeling competing effects of cooling rate, grain size, and radiation damage in low-temperature thermochronometers. Geochronology, 4:143-152.

A hyperspectral detailed view on a magnetitite horizon in the Bushveld Complex, SA.

Dieter Rammlmair[1], Wilhelm Nikonow[2]
[1]*Institute of Mineralogy, Leibniz University Hannover*
[2]*Federal Institute of Geosciences and Natural Resources*

Abstract. More than 20 individual magnetitite layers occur within the Upper Zone of the layered Bushveld igneous complex, South Africa. Three individual layers from drill core BH7772, Marula Mine, Eastern Lobe were analyzed, offering a wide range of textural patterns. Investigations by LIBS, µEDXRF and HSI revealed mineralogical, mineral chemical, rock chemical and textural information in a continuous mode. Whilst mineralogical information can be quite easily derived by either method, the access to proper mineral grain information such as area grain size, grain shape and orientation, as well as deformation needs more effort. Both, µEDXRF and LWIR HSI are sensitive for individual grain orientation by changing the chemical signal due to diffraction, or the spectral reflectance or absorbance feature, respectively. By applying ENVI spectral angle mapper (SAM) an evaluation of either method can be performed given that a proper endmember collection is provided. Whilst spatial resolution of µEDXRF provide detailed information for selected parts, LWIR mapping with 400 µm step size can be acquired from large core intervals. The evaluation of signals controlled by orientation within an individual mineral mask allows the extraction of size, shape and orientation of individual grains within a continuous core section, providing a new insight into the genesis of magnetite layers.

1 Introduction

Drill cores provide continuous information of parts of the Bushveld igneous complex, the worldwide largest layered mafic to ultramafic intrusion hosting huge PGE, Cu/Ni sulphides, chromitite, and Ti and V in magnetitite deposits (Scoon and Mitchell 2012; Molyneux 1974). Optical, chemical and physical hyperspectral methods such as VNIR, SWIR, LWIR, LIBS, µEDXRF next to remanent magnetization, radiation, electric resisti-vity, heat capacity, x-ray absorption, CT, spectral CT provide among others information in 1D, 2D and even 3D. These methods provide the basis for detailed mineralogical, chemical and textural investigation (Nikonow et al., 2019) in a more objective way that logging geologists could perform for later interpretation and further sampling for more detailed investigation of exceptional samples by quantitative methods such as EPMA, LA-ICP-ToF-MS among others.

Sample handling and data acquisition and turnover time of results are crucial aspects for the mining industry. Therefore, the focus is based on easy-to-handle fast methods. Unfortunately, a single method will not cover all aspects of interest and combining methods is necessary.

LIBS, despite strong matrix effects, has become an outstanding tool to identify individual phases based on chemical patterns by ENVI spectral angle mapper (SAM) algorithm. It can further be used to monitor Mg# and An# of orthopyroxene, clinopyroxene, olivine, chromite, and plagioclase, respectively, in relation to the pixel neighbourhood, to highlight fractionation and reversal pattern comparable to EPMA derived pattern down to 50 µm spatial resolution (Meima et al. 2022a,b). It further provides detailed information on the changes of trace element chemistry of individual mineral phases in a continuous mode for several meters. With µEDXRF at 20 µm spatial resolution even more details can be extracted in an automated way providing SAM based phase modality, area grainsize distribution and phase orientation as far segmentation of grains works in an acceptable way. But, monomineralic aggregates are a challenge for a correct grainsize attribution on a chemical basis. µEDXRF on coarse materials is governed by diffraction signals based on the crystallographic orientation of individual mineral grains. This aspect can promote the extraction of individual grains within aggregates to obtain better area grainsize and grain shape and orientation (Nikonow and Rammlmair 2016). An additional aspect is, that by selection of areas of interest a direct 2D correlation of modality and chemistry can be achieved.

Hyperspectral imaging (HSI) of visible-near Infrared, short and long wave infrared, VNIR, SWIR and LWIR, respectively, can be used as an alternative method. It is the fastest screening method - despite the aspect of proper core surface cleaning - of full core prior to cutting applied by the mining industry to highlight mineral distribution and lithological changes in drill core boxes at spatial resolution of approx. 1.4 mm. Since most pixels will record mineral mixtures spectral unmixing has to be obtained to highlight the mineral fractions within individual pixels. By scanning a half core at higher resolution, a strong reduction of mixed pixels, always in relation to the grain size of the investigated phases, can be obtained down to 25 µm for VNIR and SWIR and 400 µm for LWIR thus monomineralic spectra are obtained. This brings in a new aspect for data interpretation. Since spectra of individual grains have to be interpreted the orientation of the mineral grain might change a signal pattern dramatically. This needs an enormous development of individual mineral endmembers referring to the changes in orientation, thus being able to identify a mineral distribution pattern with SAM. But as a positive side effect the grain orientation signals within a mineral mask can

be used to extract again individual grains for further textural analyses, namely optimization of area grainsize distribution, grain shape and grain orientation.

The fusion of data sets based on LIBS or µEDXRF derived phase maps used to mask phases of interest with HSI can promote the acquisition of textural details on larger scale at sub-mm level for identification of grain size changes.

2 Materials and methods

Core BH7772 from the Marula Mine was donated to the University of Bloemfontain for the ICDP by Impala Platinum Ltd.. Logging and logistics were done by Prof. Roelofse (Univ. Bloemfontain). Three magnetite layers from the lower central and upper portion were selected each with transitions to foot and hanging wall, anorthosites, lithologies and sampling of continuous slices through three magnetitites, in total 11.33 m was done by Dr. Veksler from GFZ, Potsdam.

Data acquisition by spectral methods followed a scheme of minimum disturbance of primary setting. Hyperspectral imaging was performed as the first step by SisuRock scanner from Specim. An approx. 15 cm field of view was used for long wave infrared, (LWIR) resulting in 400µm pixel resolution, whilst for short wave infrared (SWIR) and visible to near infrared (VNIR) a 5 cm FOV was applied generating 125 and 42 µm pixels, respectively. Measurement started with LWIR followed by SWIR and VNIR to reduce preheating artefacts. Row data were radiometrically and geometrically corrected to obtain reflectance. The noise was minimized by MNF transformation and spike removal was performed to obtain a calibrated and corrected reflectance data set. For individual minerals, the focus was on LWIR, a number of endmembers were extracted reflecting different grain orientation to be used for ENVI hyperspectral software based spectral angle mapper (SAM) classification.

Laser induced breakdown spectroscopy (LIBS) imaging was applied prior to cutting samples into subsample. The GeoLIBS Scanner from Laser Technik Berlin (LTB) with a 1064 nm Nd:YAG laser was applied to map a 1 cm stripe with 75 µm step size. For LIBS results refer to Nikonow et al. 2023 at SGA 2023.

Continuous element mapping of drill core sections was done by a Bruker M4-Tornado Plus micro energy dispersive x-ray fluorescence (µEDXRF) system, too. Samples were cut to a size of 20 cm length to feed the system. Analysis was performed under vacuum with a Rh tube at 50 kV, 30 µA, with a poly-capillary beam guide with 51° incidence angle, without filters, and two opposing detectors with 51° take off angle, 90 ° to the tube. Mapping was performed in 40 µm steps in x and y direction and at 5 msec acquisition time. Data from both detectors were extracted and the minimum per pixel per channel of both detectors was calculated to obtain a minimum dataset (*min) with reduced diffraction signal side effects for 165 region of K/L/M lines of elements of interest as an ENVI database. Additionally a dataset (*D1-D2) of the difference of both detectors was used reflecting the signal deviation for each of the detectors regarding the minimum per channel per pixel thus reflecting the diffraction signals of individual grains (Nikonow and Rammlmair, 2016).

3 Results and discussion

The results from the LIBS and EDXRF data evaluation are presented by Nikonow et al. at SGA 2023. LIBS profiles reflect the chemical changes within an individual mineral distribution. Meima et al. (2022a,b) showed in a section through 6 m Merensky Reef, and a section from UG2 chromitite from Karee Mine, Western Lobe of the Bushveld Complex how detailed and accurate - validated by EPMA analysis - Mg# of pyroxenes, olivine and chromite, as well as anorthite content of plagioclase reflects changes related to fractional crystallization and reversals due to new magma input. Similar effects can be observed in the upper zone magnetitite layers, too (Nikonow et al. at SGA2023). The µEDXRF data evaluation provide very detailed mineral distribution pattern based on supervised ENVI SAM classification using approx. 8000 mineral spectra as a data base, but elemental analysis of individual grains might be disturbed by prominent diffraction signals influencing the intensities of other elements, due to not complete pattern removal in some grains.

These disturbing diffraction signals can provide additional thus quite valuable information. By masking a classified individual phase distribution, all changes in signal within this frame would represent changes in crystal orientation, and therefore form a basis for further segmentation of individual grains in monomineralic compounds in a better way then watershed segmentation could do.

To achieve this, an elevated effort is needed to obtain a reliable grain orientation data base per mineral for millions of possibilities. Focusing on the most prominent signals of a selected mineral like magnetite the number of endmembers to be created could be reduced to a minimum by using a wider threshold. Since grains are often randomly orientated conflicts due to identical orientation are minimized. Figure 1 shows an example of some almost massive magnetite layers with ilmenite and a late clinopyroxene rich aggregate with fine interstitial magnetite. Wang 2023 assumes for Hongge layered Intrusion in China that fractional crystallization-based aggregation of magnetite will range around maximum 60%. He stated that hydrothermal input is needed to get higher magnetite concentrations in a layer. The hydrothermal input is supported by extremely light delta $\delta^{56}Fe$ in secondary magnetite compared to primary magnetite thus 20% to 30% could be hydrothermally mobilized from deeper units. The hydrothermal addition of Fe coinciding

with silicate resorption and therefore increasing compaction would generate a relative loss Cr, Ti, V, Mn etc..

This brings us back to the element variability in the Bushveld magnetitites, documented by both LIBS profiles and µEDXRF mapping (Figure 1a) and to the partial strong magnetite enrichment, where grains are compacted and only diffraction signals (Fig.1b) would record grain size changes within the system prior to applying other time-consuming methods.

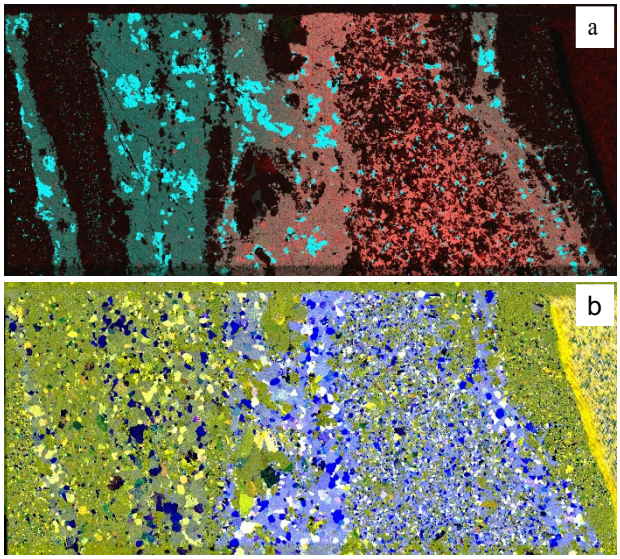

Figure 1. a) Distribution of Cr, V and Ti as RGB image showing strong gradient of Cr from interstitial fine-grained magnetite within a clinopyroxene, plagioclase, apatite aggregate via a massive proximal magnetite layer with coarse ilmenite at intermediate values into a distal massive magnetite with coarse ilmenite at low values.
b) shows the grain size pattern of two strongest lines at RhLa (D1-D2) and RhLb D1-D2) in RGB with D1 (red) and D2 (green) and superimposed Cr min (blue) for magnetite with bluish background and silicates and ilmenite in greenish. Note the rapid grain size changes displayed by diffraction pattern (Length 18cm)

The extremely elevated Cr content within fine grained magnetite in the clinopyroxene aggregate. A number of models exist discussing replenishment, reactive melt infiltration, fractional crystallisation, inversals etc. (Tegner et al. 2006; Junge et al. 2014; Scoon and Mitchell 2012, Yao and Mungall 2022; Kruger and Latypov 2020b). What definitely can be observed is an extreme complexity of textural features which all do influence the chemical pattern of magnetite, and in the case of figure 1 showing a prominent metasomatic Cr halo around a relatively thin clinopyroxene rich feature. Similar pattern occurs at some anorthosite layers, too.

Besides evaluation of EDXRF diffraction pattern, suitable for spinels, LWIR can be helpful to obtain a quick overview of misorientation of silicates. But data extraction on a grain size basis for LWIR is a huge challenge since signals related to remote sensing reflect homogeneous powder samples with sum signals that can easily be compared with available

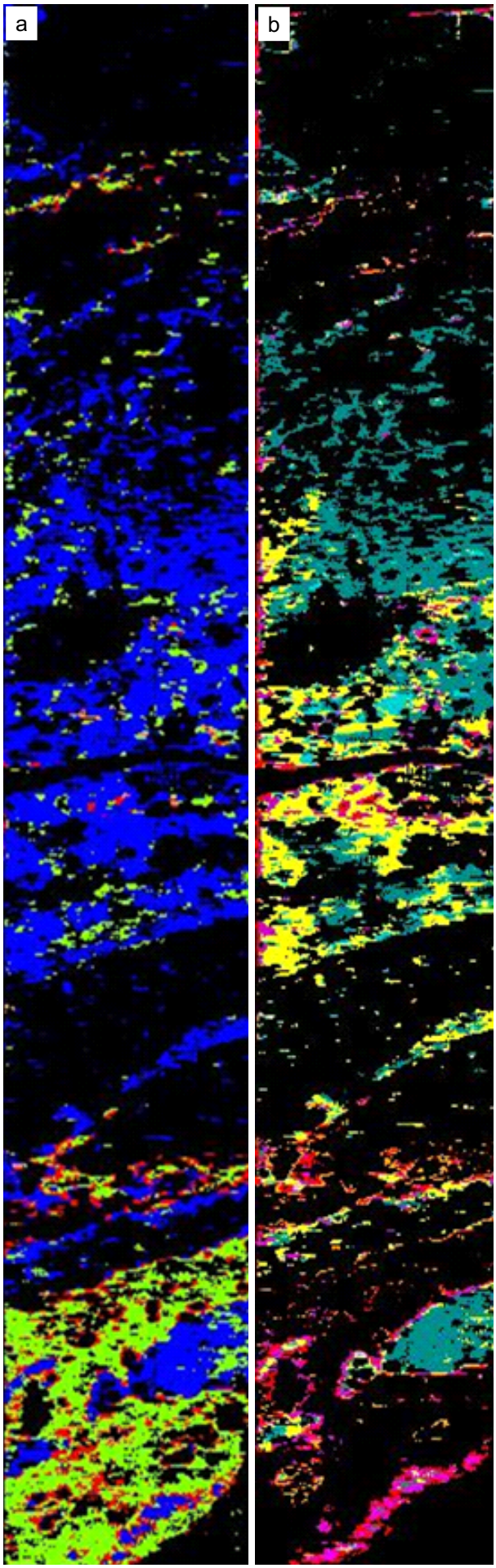

Figure 2. LWIR Endmember based classification showing silicate distribution in magnetite layer (Sample UZ223-15_24 from 217.86m to 218.15m) showing a) plagioclase in blue, clinopyroxene in green and biotite in red, Fayalite in purple and magnetite, ilmenite and sulfide in black, and b) different orientation of plagioclase grains in different color (Length 29 cm).

spectral data sets. At 400µm resolution where single grains at different 3D orientation are measured each signal appears to be individual showing changes in the number and ratio of spectral features. One way to solve this problem is to acquire hundreds of individual spectral patterns of each mineral, and adding spectra of not recognized grains to the database.

Spectral sets for individual minerals can be combined to obtain a mineral distribution (Fig. 2a), but even individual pattern can be used to outline similar orientation or even individual grains (Fig. 2b). By translation of the information into grains, evaluation can be performed for size, shape and orientation of single grains, for neighbourhoods providing additional information to modality, mineral and rock chemistry. If automatized this evaluation scheme will promote detailed view to a drill core to achieve a highly valuable pattern identification and comparison in a continuous mode.

4 Conclusions

The analyses of magnetitite core sections from the Bushveld Complex by HSI, LIBS, and µEDXRF provides huge chemical, mineralogical and textural data sets (Nikonow et al. 2019). Whilst chemical and mineralogical aspects are relatively easy to be achieved by hyperspectral evaluation methods, micro textural information such as proper area grain size characterization require new tools. For both µEDXRF and HIS, disturbing signals based on diffraction and mineral grain orientation dependent distortion of reflectance as well as absorption signals, respectively, can be used to identify individual grain boundaries in monomineralic aggregates. By obtaining a better grain area size, grain shape and grain orientation of individual minerals without elevated analytical effort in a continuous mode detail such as hidden grading, recrystallized shear zones etc. can be extracted which could be used for better interpretation of chemical anomalies in a magnetitite core section.

Acknowledgements

This project is funded in the frame of ICDP by the German Research Foundation (DFG). Project 457479532 “Spectroscopic mineral - chemical analysis of drill cores: Development of fast 2D LIBS, EDXRF and hyperspectral scanning with application to outstanding problems of the Bushveld Complex layered intrusion”. We would like to thank Impala Platinum Ltd. for donating the core, Prof. Roelofse from the University of the Free State, Bloemfontein for logging the core and Dr. Veksler from GFZ Potsdam for logistics. Data acquisition was performed by Dr. Meima, Dr. Goldmann, Christian Woehrl, Dominic Goericke, Christopher Specht at BGR.

References

Junge M, Oberthür T, Melcher F (2014) Cryptic variation of chromite chemistry, platinum group element and platinum group mineral distribution in the UG-2 chromitite: an example from the Karee Mine, western Bushveld Complex, South Africa. Economic Geology 109:795-810.

Kruger W, Latypov R (2020a) Fossilized solidifications fronts in the Bushveld Complex argues for liquid-dominated magmatic systems. Nat Commun 11:2909. doi: 10.1038/s41467-020-16723-6.

Kruger W, Latypov R (2020b) Fossilized solidification fronts in the Bushveld Complex argue for liquid-dominated magmatic systems. Nature Communications 11:2909. doi: 10.1038/s41467-020-16723-6.

Meima J, Rammlmair D, Junge M, Nikonow W (2022a) Continuous measurement of Mg/Fe and Ca/Na ratios with scanning Laser Induced Breakdown Spectroscopy in 6 meter of drill core through Merensky Reef, Bushveld Complex, South Africa EGU General Assembly 2022. Copernicus Meetings, Vienna, Austria.

Meima JA, Rammlmair D, Junge M (2022b) The use of Laser Induced Breakdown Spectroscopy for the mineral chemistry of chromite, orthopyroxene and plagioclase from Merensky Reef and UG-2 chromitite, Bushveld Complex, South Africa. Chem Geol 589:120686. doi: 10.1016/j.chemgeo.2021.120686.

Nikonow W, Rammlmair D (2016) Risk and benefit of diffraction in Energy Dispersive X-ray fluorescence mapping. Spectrochimica Acta Part B: Atomic Spectroscopy 125:120-126.

Nikonow W, Rammlmair D, Meima JA, Schodlok MC (2019) Advanced mineral characterization and petrographic analysis by µ-EDXRF, LIBS, HSI and hyperspectral data merging. Mineralogy and Petrology 113:417-431. doi: 10.1007/s00710-019-00657-z.

Scoon R, Mitchell A (2012) The Upper Zone of the Bushveld Complex at Roossenekal, South Africa: geochemical stratigraphy and evidence of multiple episodes of magma replenishment. South African Journal of Geology 115:515-534.

Tegner C, Cawthorn RG, Kruger FJ (2006) Cyclicity in the Main and Upper Zones of the Bushveld Complex, South Africa: crystallization from a zoned magma sheet. Journal of Petrology 47:2257-2279.

Wang D (2023) The formation of Hongge Fe-Ti-V oxide deposit hosted in layered intrusion, Emeishan Large Igneous Province, Southwest China. PhD Thesis. 210.pp., LUH, Hanover, Germany

Yao Z, Mungall JE (2022) Magnetite layer formation in the Bushveld complex of South Africa. Nature communications 13:1-11.

Petrography and geochemistry of rare earth element occurrences in the Koumbizick Massive (South Region, Cameroon)

Benjamin Ndobe Tarkang[1], Wilson Tasing Ngirnyu[1]
[1]*University of Maroua Faculty of Earth Science, P.O. Box 16, maroua* Cameroon
[2]*National Advance School of Mines and Petroleum Industries* Kaele, P.O. Box 08, kaele Cameroon

Abstract. The Koumbizick Massive (South Region, Cameroon) occurs in the north-western part of the Congo Craton in the Nyong Complex, and is a target for rare earth element (REE) mineralization. The objective of this work is to evaluate the occurrence of rare earth elements of some geological formations such as Gneiss that crop out in the Koumbizick massive. The Nyong unit is characterised by metamorphic rock units of different grades associated with Magnetite-Bearing gneisses and magmatic intrusions that are generally oriented NE-SW. Six representative samples were collected during fieldwork. Geochemical and outlook evaluation approach methods were used to evaluate the REE potential of the samples. The results show that the samples are strongly enriched in REE, especially light REE (La, Ce, Nd, Sm). Petrographic analysis shows that the host rock has a porphyroblastic to granoblastic texture and mineral phases of quartz, plagioclase feldspar, biotite, pyroxenes, and amphibole. According to Pearson's correlation coefficient value, REE show good positive correlation among themselves and fair correlation with other elements such as Cr, Cu, V Zn. These data suggest that the REE concentration outcropping the Koumbizick massive are high.

1 Introduction

Koumbizick is a village located southeast of the Lolodorf subdivision in ocean division of the South Region of Cameroon (Figure 1). The village of Koumbizick has a surface area of 120 km^2 and is located about 30 km north from the town of Lolodorf. It is bound to the east by Abam and west by Mbango.

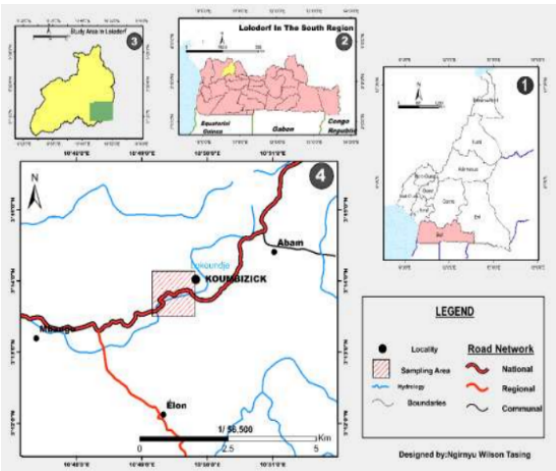

Figure 1. Sketch localization map (1) of Cameroon with South Region of Cameroon highlighted (2) Lolodorf in the South Region of Cameroon (3) position of Koumbizick and study area in the Lolodorf sub-division. (4) Localised map of Koumbizick within the study area.

The Koumbizick massive is located in the western part of the Congo craton. The Koumbizick massive covers a total area of 50km^2 Comprising Archean crust, early to mid- Proterozoic fold belt. This massive consist of Migmatite Gneiss, plutonic rocks of the charkokite suit, Granodiorite. The Koumbizick massive dates the same age as the Congo craton making it favourable for various mineralogical prospection.

2 Methodology

Fieldwork and sampling was conducted in conjunction with satellite imagery. The maps were made at the IRGM Spatial Imaging Research Center. Geological, topographical, hydrographic, location, relief, sampling map and the three-dimensional maps of the study area were also produced. The study of the geological map makes it possible to obtain information on the local geological context and the geological formations present. The topographic map shows the relief units bearing the work area. The mineral resource map shows the mineral indices in the work area and the geology to which these mineral resources are assigned. The sampling map represents the sampling points taken in the field. Petrographic analysis was carried out in order to analyze the occurrence of REE in the rock mass formation using the binocular microscope of the OPTIC IVYMEM SYSTEM brand

X-Ray diffraction (XRD) mineralogical analysis was conducted which uses X ray beams by accelerating the electron into a copper target and directed toward the sample, were the atoms deflect them. Angles of constructive interference will diffract X-rays into the detector which transduces the x-ray intensity and plots them in form of curves (diffractogram) which presents peaks at very specific diffraction angles. The position of these peaks is a true signature of the arrangement of atoms inside a crystal (distance between atoms, and between intracrystalline planes). The empirical relation that connects the angles at which the peaks are observed and the distances between atomic planes is the Bragg's Law. X-ray diffraction makes it possible to distinguish products having the same chemical composition but different atomic arrangements. X-ray fluorescence (XRF) was also use which is a method used to measuring the wavelength and intensity of "light" (X-rays in this case) emitted by energized atoms in the sample. In XRF, irradiation with a primary X-ray beam from an X-ray tube causes the emission of fluorescent X-rays

with discrete energies with characteristics of the elements present in the sample

Figure 2. Graphical illustration of major element variation

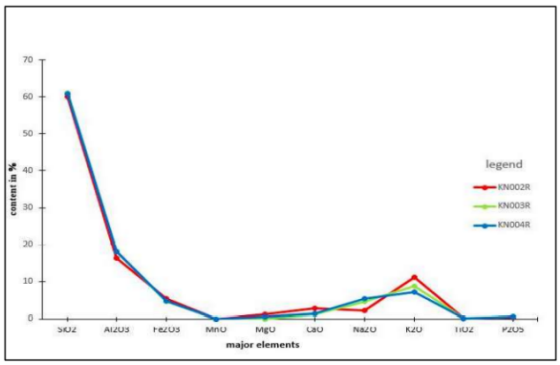

in samples at Koumbizick.

Table 1: Rare earth element concentration of samples from the Koumbizick massive.

Elements	KN001S	KNR005C	KNR006C
	%wt.	%wt.	%wt.
SiO2	60.37	59.12	61.28
Al2O3	16.57	19.03	17.8
Fe2O3	5.09	3.65	4.71
MnO	0.06	0.06	0.06
MgO	1.14	0.71	0.01
CaO	2.54	1.88	1.04
Na2O	3.47	4.65	3.73
K2O	9.19	7.18	9.27
TiO2	0.24	0.4	0.22
P2O5	0.4	0.91	0.5
L.O.I.	0.92	2.02	0.79
TOTAL	99.99	99.61	99.41
Elements	KN002R (ppm)	KN003R (ppm)	KN004R (ppm)
La	825	471	900
Ce	1604	600.5	1716.5
Pr	182.5	100	208.5
Nd	624	296.5	676.5
Sm	87	28	94
Eu	8.5	6.5	9
Gd	68.5	23.5	74
Tb	6.76	2.05	7.1
Dy	34.88	7.01	35.65
Ho	5.94	1.36	5.99
Er	15.21	3.96	15.25
Tm	1.88	0.67	1.83
Yb	9.5	2.71	9.78
Lu	1.45	0.67	1.45
Y	138	59.5	151.5

3 Results and Discussion

The study of rock samples under an optical microscope shows that they have a porphyroblastic to granoblastic texture. The mineral phases identified are quartz, plagioclase feldspar, biotite, pyroxenes, and amphibole. Quartz crystals occupy 50-55% of the rock and are sub-automorphic to xenomorphic. The sub automorphic crystals vary in size between 0.5 and 2 mm and are interstices of potassium feldspar and biotite lamellae or are included in amphibole and potassium feldspar. The xenomorphic crystals appear in the form of stretched bands with dimension up to 1 cm in the long axis and in some places, occurring as clusters of quartz with a triple junction. Rare earth minerals are disseminated in the various sampling profiles, but only a few occurrences have values high enough to be classified as “showings”. Microscope and electron microprobe work has shown that the minerals hosting REEs are allanite($A_2M_3Si_3O_{12}[OH]$), bastnasite($Ce(CO_3)F$), and monazite ($(Ce, La, Th) PO_4$).

Figure 3. (a) Fragmented blocks at site 2 (b) photo of sample KN004R from site 2

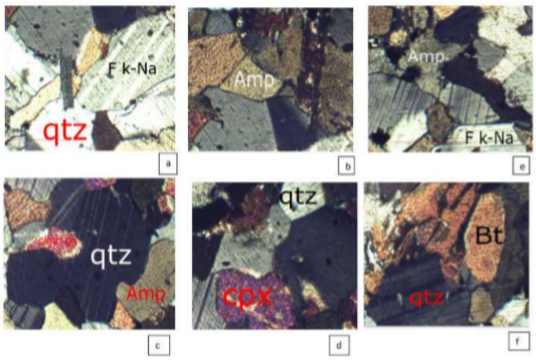

Figure 4. Thin section of gneiss sample showing the different mineral phases present in thin section. (define the minerals)

Cerium is the most enriched LREE in all the samples with a maximum concentration of 2715 ppm recorded in sample KNR006C, and minimum concentration of 1300 ppm in samples KNR001S. Europium has the lowest content for light REE in all samples with maximum concentration of 11.5 ppm in samples KNR005C and minimum concentration of 8.3 ppm in samples KNR001S. After cerium in concentration, Lanthanum, Neodymium, Praseodymium, Samarium, Gadolinium respectively follow in the order for light REE abundant in all the samples Generally, sample KNR006C records the highest concentration in light REE, ranging from 2715 ppm for Cerium to 11.3 ppm for Europium. Meanwhile, sample KNR001 records the lowest light REE concentrations (Fig5.).

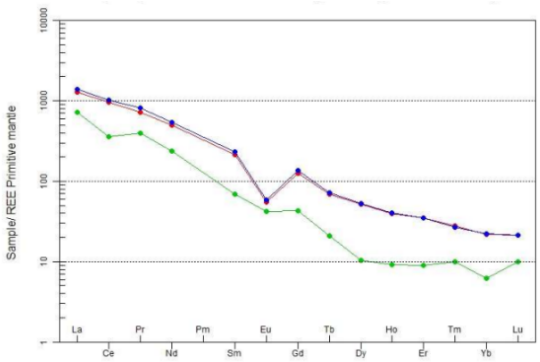

Figure 5. Primitive mantle-normalised (McDonough and Sun 1995) multi-element diagram of samples from the Koumbizick Massive.

4 Conclusions

After analyses, mineralogical result reveals the presents of REEs mineralogy of allanite's as the main mineral in samples which is made up of about 2.01% to 2.22%. Followed by monazite and bastnaesite. Light REEs are concentrated to a greater degree than other REEs (up to 2715 ppm). It appears that the rocks have a syenitic lithological nature rich in REEs, Making koumbizick massive highly favourable for REE prospection.

Acknowledgements

Thanks to the IRGM laboratory in Yaoundé were all the analysis were carried out.

References

Tchouankoue JP 1992. The Bangangte syenite: A Pan-African complex with intermediate characters: petrology and geochemistry. Doctorate of Third Cycle thesis. Cameroon: University of Yaoundé; p.160.

Peng Guo, Dmitri A. Ionov., Mantle and Recycle Oceanic crustal components in mantle Xenolith from north-eastern china and their mantle sources p. 7.

U-Pb dating and trace-element characterisation of potential cassiterite reference materials applicable to Sn-W mineralisation systems

Tonny B. Thomsen*,[1], Benjamin Heredia[1], Jakub Ryznar[2], Wladyslaw Zygo[3], Hugh O'Brien[4], Matthew Goodey[5], Simon Tapster[5], Anouk M. Borst[6], Nynke Keulen[1], Sebastian Malkki[1], Diogo Rosa[1]
[1] Geological Survey of Denmark and Greenland (GEUS), Øster Voldgade 10, 1350 Copenhagen, Denmark, tbt@geus.dk
[2] PROXIS Sp. z o.o. ul. Cieszyńska 23G, 43-170 Łaziska Górne, Poland
[3] AGH University of Science and Technology, Kraków, Poland
[4] Geological Survey of Finland (GTK)
[5] Geochronology and Tracers Facility, British Geological Survey (BGS), UK
[6] KU Leuven & Royal Museum for Central Africa, Belgium

Abstract. To support the traceability of Sn and W minerals to their deposit type (i.e., skarn, greisen or vein), various cassiterite and scheelite materials were investigated for their potential as quality standard reference materials. One cassiterite material in particular, the Kivu-2, revealed encouraging results when measured by laser-ablation inductively coupled plasma mass spectrometry (LA-ICPMS) at GEUS and GTK, which showed that e.g., this cassiterite contains virtually no common-Pb. ID-TIMS analyses of the Kivu-2 cassiterite material are being obtained at the BGS to further constrain the isotopic composition. It is anticipated that the ID-TIMS results will support this cassiterite's potential to be an international standard reference material for matrix matched U-Pb dating. In contrast, the internal variations in trace elements abundance as measured by LA-ICPMS most probably are too large to constitute a robust element quantification standard material. The complete data set of this study will be presented at the meeting together with an assessment of the potential applicability of the studied cassiterite materials to Sn-W ore systems.

1 Introduction

Sn and W occurrences in East Greenland were extensively studied by the Nordmine exploration company during the late 1960s to early 1980s. Their survey was succeeded by 40 years of investigations by GEUS and the Greenlandic Ministry of Mineral Resources (MMR), of which the latest work was during the Summer of 2022. As described in the abstract by Keulen et al. (this conference), Sn and W occur in the minerals cassiterite and scheelite, respectively, and most of the Sn and W occurrences are associated with the East Greenland Caledonian orogeny. These minerals occur in skarn, greisen, and hydrothermal veins, depending on their host rock and the proximity of adjacent granites (Hallenstein & Pedersen, 1982). Literature data shows that skarn, greisen, and vein-type deposits show distinct mineral trace element compositions (e.g., Wang et al. 2022, Sciuba et al. 2020 and many others). Thus, a good understanding of the mineral trace element content and associated element patterns together with the age of the mineralisation would help characterise the deposit type(s) in which cassiterite and/or scheelite occur. However, well characterized standard reference materials for microanalysis of this kind of minerals are required, in particular for U-Pb mineral dating. Unfortunately, for cassiterite and scheelite these are rare to non-existent. The aim of this study is therefore to analyse different cassiterites and scheelites to evaluate their potential as robust standard reference materials.

2 Cassiterite materials studied

Several cassiterite and scheelite mineral samples were investigated, however, focus of this study was put on cassiterite, because none of the scheelite materials studied proved to hold potential as robust standard reference material. The investigated cassiterites included two samples from the western province of the Rubavu District in Rwanda, three samples from the Musha-Ntunga pegmatite quartz veins in Eastern Rwanda (Kivu rift), two from the Manono-Kitotolo pegmatites in DR Congo, two samples from East Greenland, and samples from three different locations in Portugal (Montesinho, Panasqueira, Vale das Gatas). Separated mineral grains or small chunks of rock with a high proportion of cassiterite were encapsulated in epoxy pucks and polished prior to analysis. In addition, 5 samples of standard or potential standard cassiterite material (Jian-1, CH1, SPG4, ELS, and RZMEGA) provided by the BGS along with the Yankee cassiterite standard provided by courtesy of Patrick Carr from Université de Lorraine, CNRS, CREGU, France, were included in the study for testing the reproducibility and repeatability of the LA-ICPMS measurements.

3 Laboratory investigations

3.1 SEM

The epoxy mounts with cassiterite were studied by Scanning Electron Microscopy (SEM) to identify textural and compositional variations. Cathodo-luminescence (CL) and back-scattered electron (BSE) images were obtained to identify features such as internal zoning and inclusions in the cassiterite mineral grains. Automated quantitative mineralogy (AQM) software on the SEM was used for some samples to locate smaller cassiterite mineral grains and to establish compositional and spatial homogeneity within individual grains. AQM is a scanning electron microscope technique that combines BSE imaging with chemical analyses by energy dispersive spectroscopy in a mosaic with a small step-size (Keulen et al. 2020).

3.2 LA-ICPMS and ID-TIMS

Laser-ablation inductively coupled plasma mass spectrometry (LA-ICPMS) was performed at GEUS and GTK using both non-matrix matched and matrix matched analysis protocols. Analyses at GEUS were performed using a NWR213 solid state Ng:YAG laser ablation system from ESL coupled to a Thermo Scientific Element2 SF-ICPMS. At GTK a Teledyne ArF excimer 193 nm laser system coupled to a Nu Instruments TM AttoM high resolution ICP-MS was used. The U-Pb Geochronology and Trace Element data reduction schemes of iolite 4 were used to obtain U-Pb dates and trace elements abundances of the cassiterite grains analysed.

It is well-known that cassiterite is challenging to decompose by regular acid dissolutions protocols. For ID-TIMS analyses, protocols were implemented and performed at BGS following Tapster and Bright (2020), this to assess the potential of the non-matrix matched results obtained by LA-ICPMS analyses, and the evaluation of a correction factor. It is anticipated that the ID-TIMS measurements confirm the LA-ICPMS data, and further improve the accuracy and precision of the U-Pb dating for the Kivu-2 cassiterite sample material.

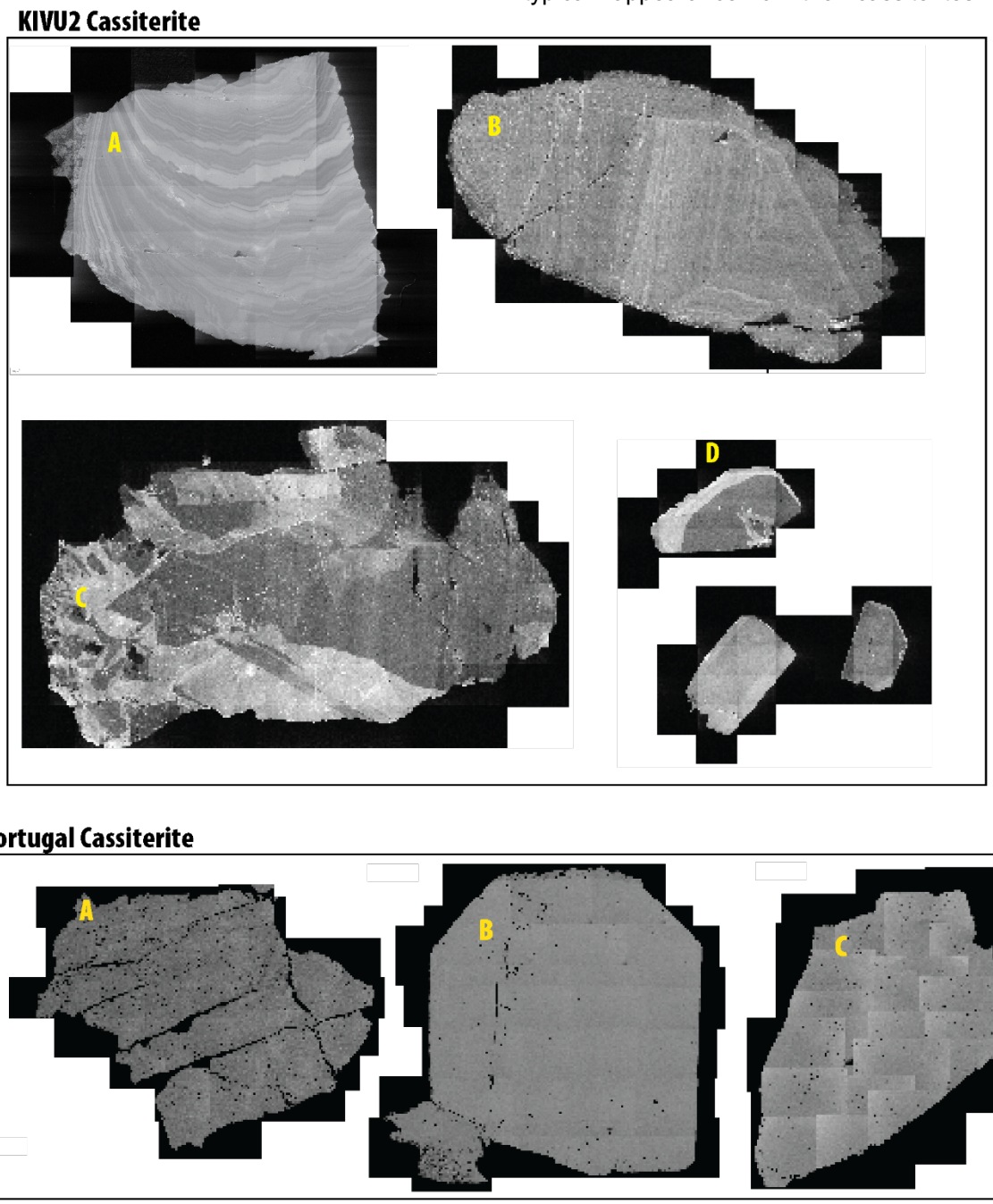

Figure 1. SEM CL images showing distinct section zoning in Kivu-2 (A to D mineral grains in top image), and cassiterites from Portugal (lower image; A: Montesinho; B: Panasqueira; C: Vale das Gatas.

4 Textural and compositional variations

CL images are presented in figure 1 to show the typical appearance of the cassiterites Kivu-2, Montesinho, Panasqueira, and Vale das Gatas. For Kivu-2 in particular, four different samples were collected from the same rock at the very same sample site (A to D), of which three samples (B, C and D) showed a low U content at around 1 ppm on

average, whereas the sample A contains much more U (~several hundred ppm U on average). Despite this large difference in the U and Pb abundances and clear zoning of the grains, all Kivu-2 samples yield comparable dates within error or each other. The clear zonation that can be observed in these grains does not seem to significantly influence the U/Pb dates. The trace element abundances, however, show significant variations that, based on the current analyses, do not appear to constitute a robust reference for determination of elemental contents. Comparable variations are observed in the analysed cassiterite grains from Portugal that show a less pronounced zoning and have low common-Pb content. The cassiterites from Greenland contain a high proportion of common-Pb and are less suitable as reference material for both dating and trace element determination, but nevertheless show reasonably comparable dates within single occurrences.

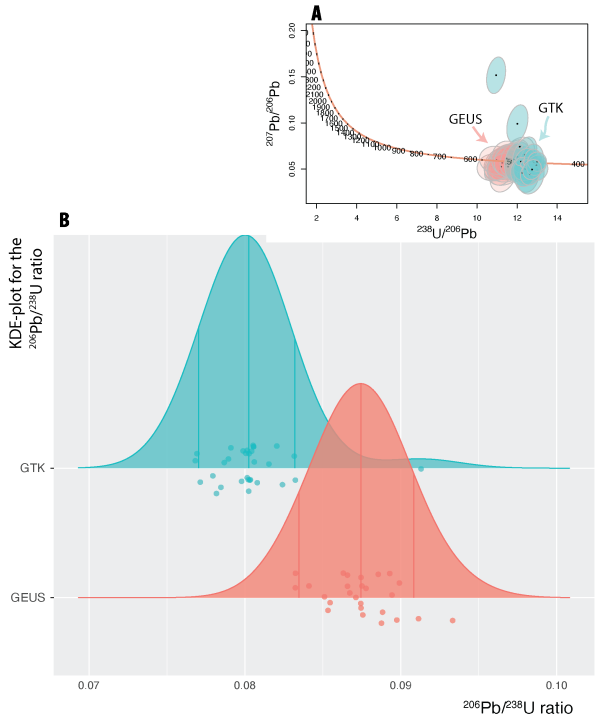

Figure 2. LA-ICPMS analyses of the Kivu-2 cassiterite obtained at GEUS (red) and GTK (blue), respectively, shown in $^{206}Pb/^{238}U$ ratio plot and Tera-Wasserburg diagram (A). The smaller discrepancy observed in the raw 206Pb/238U ratios (B) most probably result from the different analytical setup and the non-matrix matched analysis approach employed in the two laboratories. A more complete data set and data also from other cassiterite materials will be presented at the meeting.

5 Kivu-2 – a new cassiterite standard?

The results of two independent laser ablation sessions from the two laboratories show that the non-matrix matched U/Pb dating analyses plot near concordia (Fig. 2A) indicative of a very low initial-Pb contribution. The apparent variation can thus be represented by the $^{206}Pb/^{238}U$ ratios on a KDE graph as in Figure 2B. The mean dates of 516±11 Ma (GEUS) and 509±9 Ma (GTK) correspond to a <2-5 % difference. This deviation is most probably related mainly to the differences between the analytical protocol and to different matrix-related elemental fractionation instrumental setup rather than representing true variations in the isotope systematics of both U and Pb. The ID-TIMS U-Pb analyses will constrain the isotopic ratios and assess the LA-ICPMS results. Further absolute LA-ICPMS geochronometry and trace elements measurements will constrain the data towards a very robust data set for U/Pb dating with minimal requirements for common Pb correction, and a constrained trace elemental characterisation of the Kivu-2 material. The dating of cassiterite offers a potential platform for linking time relations between magmatism and hydrothermal processes, and our contribution is thus beneficial for the development of well characterised materials to use for calibration and verification of U/Pb dates and elemental databases generated by microbeam analysis methods.

6 Acknowledgements

The study is financed by GEUS and EIT-RM project MinExTarget #109674 and the Greenlandic Ministry of Mineral Resources, Government of Greenland. M. Alaei and H. Vesturklett are thanked for laboratory assistance.

7 References

Hallenstein, C. & Pedersen, J. 1982: Study of Scheelite Mineralization in Central East Greenland. Nordisk Mineselskab A/S, 152 pp. GEUS Dodex file report 20688.

Keulen N, Malkki SN, Graham S (2020) Automated Quantitative Mineralogy Applied to Meta-morphic Rocks. Minerals 10, 47, 29pp. DOI: 10.3390/min10010047.

Sciuba, M., Beaudoin, G., Grzela, D. & Makvandi, S. (2020) Trace element composition of scheelite in orogenic gold deposits. Mineral Dep 55:1149-1172.

Tapster, S., Bright, JWG. 2020: High-precision ID-TIMS cassiterite U–Pb systematics using a low-contamination hydrothermal decomposition: implications for LA-ICP-MS and ore deposit geochronology. GChron 2, 425-441. doi: 10.5194/gchron-2-425-2020.

Wang, C, Zhao, K, Chen, J & Ma, X (2022) Examing fingerprint trace elements in cassiterite: Implications for primary tin deposit exploration. Ore Geol Rev 149:105082, 13 pp.

Nation-wide low-density geochemical mapping using composite sample, Korea

Seung-Jun Youm [1], Joo Sung Ahn [2], Yong-Chan Cho[2], Gil-Jae Yim [2], Sang-Woo Ji [2], Jung-Hwa Lee[2], Jung-Ho Lee[1]

[1]Critical Minerals Research Centre, Korea Institute of Geoscience and Mineral Resources, Korea
[2]Geo-Environment Research Centre, Korea Institute of Geoscience and Mineral Resources, Korea

Abstract. Nation-wide low-density geochemical maps are being constructed using composite samples of stream sediments for 10 elements (As, Be, Bi, Cd, Mo, Sb, Sn, Tl, U, W) that have not been previously mapped at the national level. To obtain high-quality geochemical data, rigorous quality control (QC) procedures were implemented, which included (1) the randomization of project samples, (2) the introduction of project standards, and (3) the insertion and analysis of analytical replicates. Threshold values were calculated and geochemical maps were created for five elements (Be, Bi, Sn, Tl, U). The remaining five elements that did not pass the QC are currently undergoing re-analysis. Low-density geochemical mapping can result in a loss of detailed geochemical information, but it is useful for identifying regional geochemical patterns and establishing threshold values.

1 Introduction

An efficient way to obatin the geochemical information of crustal constituents is to create a geochemical map that shows the spatial distribution of element concentration within terrestrial materials (Zhizhong et al. 2014). The geochemical map is useful not only for mineral resource exploration but also for various fields, such as agricultural and livestock productivity, forest management, human health, environmental standard setting, water quality, and land use planning. Therefore, many countries have created multi-element and multi-media geochemical maps at different scales to better understand the geochemical distribution in various environment. In the fast-changing global metal market, the demand for metal minerals continues to rise due to the development of high-tech industries. Meanwhile, industrial development and urbanization have led to artificial pollution in the surface environment. Recently, the natural concentration of harmful elements of geological origin has been reported across the country, possibly due to the effects of rapid climate change. Therefore, preparing a national-scale geochemical map is essential for effectively addressing these issues. However, in Korea, the number of elements covered in national-scale geochemical maps is currently limited to only 18 elements (Ba, CaO, Co, Cr, Cu, Fe_2O_3, K_2O, Li, MgO, MnO, Ni, Pb, Rb, Sr, TiO_2, V, Zn, Zr) (KIGAM 2007).

The number of samples collected in geochemical exploration is determined by the purpose and area of the survey. The more the number of samples (i.e., the higher the sample density), the more detailed geochemical information can be obtained. However, if the investigation area is large, sampling and chemical analysis can become costly and time-consuming. Therefore, conducting geochemical mapping over a national-scale or larger area may not even be feasible. To address this, it is necessary to create a low-density geochemical map that can reduce the number of required samples, thereby reducing the cost and time required for sample collection and analysis (Negrel et al. 2019). Composite sampling is a technique for mixing and homogenizing several spatially spaced samples and treating them as one individual. Lately, low-density geochemical maps have been prepared in this way (Birke et al. 2015).

The purpose of this study is to create nation-wide low-density geochemical maps using composite sample of stream sediments for 10 elements (As, Be, Bi, Cd, Mo, Sb, Sn, Tl, U, W) that have not been previously mapped on a national-scale.

2 Geology

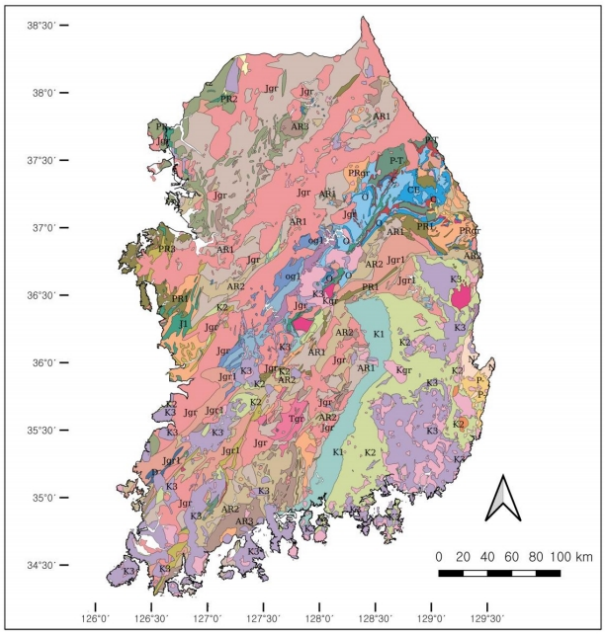

Figure 1. Geological map of Korea (1:1,000,000 scale; KIGAM 1995)

The geology of Korea is composed of complex rocks that have been formed over a long geological period, from the Precambrian to the Cenozoic era (Figure 1).

The late Archean-late Proterozoic gneisses and schists (AR, PR) form the base of geologic setting in Korea and are widely exposed on the surface due to uplift and erosion. The Ogcheon group (Og), which is distributed in the NE-SW direction from central region, is composed of metasedimentary rocks from the Cambrian-Ordovician period. The Chosun Supergroup (O) is composed mainly of carbonate rocks from the early Paleozoic era, while the

Pyongan Group (C, P, T) is composed of various sedimentary rocks from the late Paleozoic era. Both groups are distributed in the NE region. During the Jurassic period, igneous activity occurred extensively throughout the country, and granitic rocks (Jgr) were distributed widely in a NE-SW direction. In the SE region, the Gyeongsang Supergroup (K), composed of Cretaceous sedimentary rocks and volcanic-clastic rocks, was intruded by late Cretaceous granitic rocks (Kgr) and early Tertiary acidic rocks (P). In the Quaternary period, small-scale basic volcanic rocks were formed.

3 Methodology

It is both time consuming and costly to collect geochemical samples. Therefore, we decided to utilize about 23,500 stream sediments (particle size <0.015 mm; sampling density, 1 sample per 3.6 km^2), that had been collected and stored in the previous project (KIGAM 2007). To prepare the composite sample, we divided a 1:50,000 scale topographical map (approximately 600 km^2) into six cells by splitting it into three horizontally and two vertically. All of stream sediment samples (2 gr. each) within each cell were combined into a single composite sample (Figure 2). To maintain sampling consistency, the entire procedure was performed by the same person.

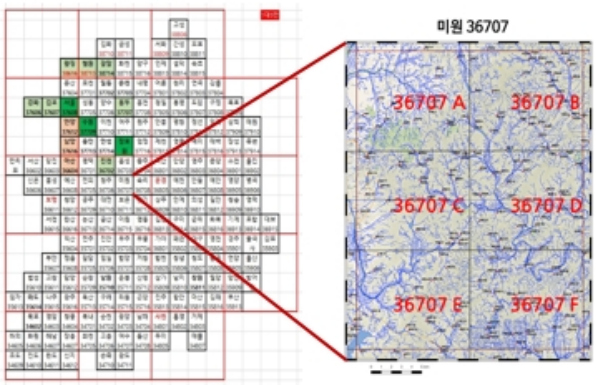

Figure 2. Cells for preparation of composite sample

Overall, 953 project samples were prepared across the country covering an area of ca. 100,000 km2 (sample density, 1 sample per 100 km2). Prior to analysis, all samples underwent a 4-acid decomposition (hydrofluoric acid, nitric acid, perchloric acid, hydrochloric acid) and were analysed using HR-ICP-MS (High Resolution Inductively Coupled Plasma Mass Spectrometer) in KIGAM laboratory. Rigorous quality control measures were carried out, including the randomization of project samples, the insertion and analysis of project standard, which was prepared from standards the project samples, and the insertion and analysis of analytical replicate (Eggen et al. 2019). All project samples were divided into 25 batches, and each batch contained two project and two analytical replicates. Certified reference standards (NCSDC73308 and NCSDC73301) were also inserted and analysed three times for each batch by the lab.

The colour surface maps were produced by IDW method with a circular window of radius of 30 km in QGIS. The locations of the composite samples were determined as the centre point of the cell, and if the centre point was located in the sea, it was moved to the centre point of the inland (Figure 3). Class boundaries for the maps were based on percentiles (5, 10, 15, 25, 50, 75, 90, 95, 99%).

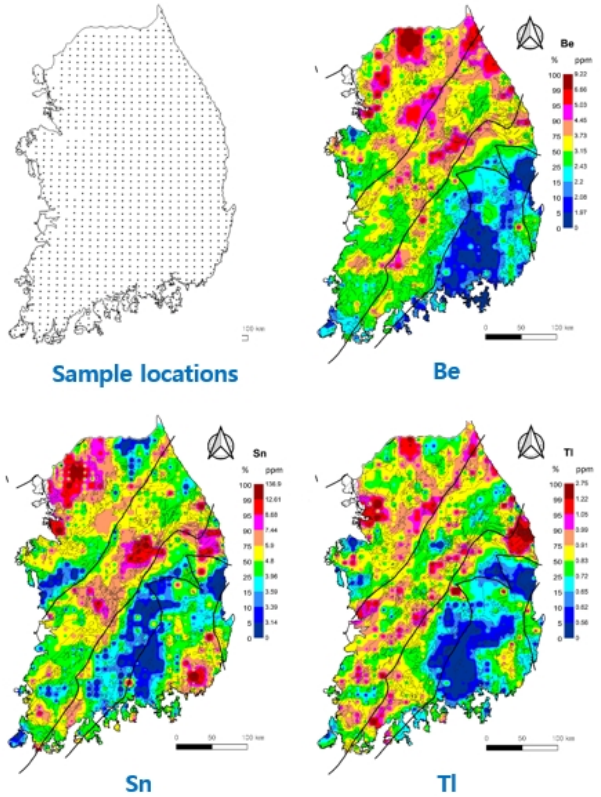

Figure 3. Composite sample locations and geochemical maps for Be, Sn and Tl. Bold line indicates geotectonic boundaries

4 Results and Discussion

After all data were received from the laboratory, simple graphics for the quality control data were drawn. In the random plots for the project samples, most elements (Be, Bi, Cd, Sb, Sn, Tl, U, W) displayed random variation over all samples. However, in the case of As, the weakly increasing trend in observed variation was found, and Mo showed breaks in concentration range during late-stage.

To determine repeatability, X-Charts for the project standard was drawn. Black line was plotted for the median and then stippled line either for 20% (green) and 30% (red) precision around the median. In the X-Chart, five elements (Be, Bi, Sn, Tl, U) did not deviate from the agreed precision (20%), but rest of the elements, especially As, showed deviations in lots of batches. In some last batch, Mo represented

poor precision, which is consistent with the result of the random plot (Figure 4).

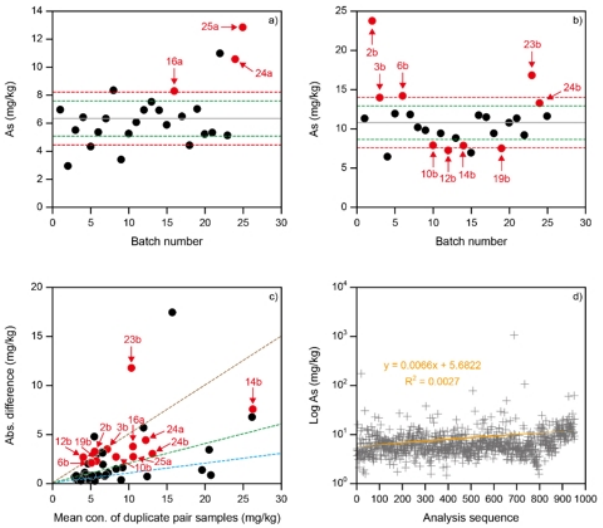

Figure 4. Quality control results for As (a & b, X-Chart; c, Thompson and Howarth plot; d, random plot). Red circle indicates re-analyses batch

To assess the overall analytical precision, the mean of each replicate pair was plotted against the absolute difference between the two analyses. On these plots, stippled lines were drawn for predefined precision level (10%, blue; 20%, green; 50% brown). Similar to QC result for the project samples, many replicate pairs deviated from the predefined level (20%) for As and less for Mo, Cd, Sb, Sn and W. All samples in the batches that deviated from the predefined precision (20%) of project standards, and at the same time, from the predefined level (20%) of analytical replicates, were selected and currently, 339 project samples are being reanalysed (Figure 4).

Table 1. Statistics for Be, Bi, Sn, Tl, U (ppm)

	Be	Bi	Sn	Tl	U
Minimum	1.3	0.1	1.4	0.3	1.7
25%	2.3	0.3	3.6	0.7	3.3
Median	2.9	0.4	4.4	0.8	4.6
90%	4.6	0.8	7.5	1.1	9.7
95%	5.6	1.2	9.0	1.2	11.5
98%	7.1	1.9	12.7	1.3	14.4
Maximum	9.2	9.5	137.1	2.8	38.3
Mean	3.2	0.5	5.2	0.8	6.0
Stdev.	1.3	0.6	5.1	0.2	3.4

Statistics was calculated for the 5 elements (Be, Bi, Sn, Tl, U) that passed the quality control test (Table 1). Threshold value was calculated using two robust methods, which are not significantly affected by statistical assumptions: (1) Tukey Inner Fence (TIF) = Q75 (75 percentile) + 1.5 x IQR (interquartile range), and (2) MAD = Median + 2 x median absolute deviation (Table 2).

Low-density geochemistry can lead to loss of detailed geochemical information compared to high density. Therefore, in order to confirm whether the low-density geochemical mapping method applied in this project was valid, the concentration of main elements (e.g. CaO) was analysed in the same way as the target elements, and compared with the result of high-density geochemical data in the previous project (KIGAM 2007).

Table 2. Threshold values for Be, Bi, Sn, Tl, U (ppm)

	Be	Bi	Sn	Tl	U
Threshold values					
MAD	4.8	0.7	7.1	1.1	9.1
TIF	7.7	1.5	12.3	1.5	20.9
Number of samples above threshold					
MAD	90	117	121	76	122
TIF	11	28	24	6	6

When comparing the distributions of CaO content between the high-density and the low-density geochemical maps, it becomes apparent that the detailed geochemical information in the latter was lost, specifically, the decreasing of highest value and the increasing of lowest value. However, the mean/median values and content ranges of 10-90% were similar, and the regional distribution pattern of the two geochemical maps was also similar, which confirm that low-density geochemical mapping can be used to identify regional distribution pattern and establish threshold value (Figure 5).

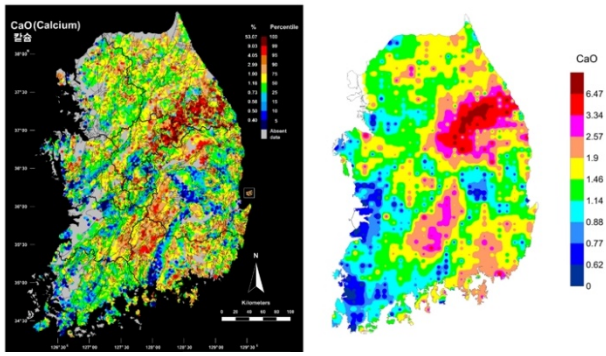

Figure 5. Comparison of high-density (KIGAM 2007) and low-density (in this study) geochemical maps for CaO

Regional geochemical distribution patterns of the geochemical maps generally reflects the underlying geology, but the effects of mineralization related to metal deposits have also been identified. For example, the regional distribution pattern of uranium is consistent with the geological distribution (Figure 6). Areas with high U concentration are associated with gneiss and granite, and low content is found in sedimentary rock.

In the case of bismuth, high concentrations are found in the gneiss and limestone, whereas low concentrations are found in Jurassic granite. Limestone is generally known to have a low Bi content, but it is thought to have a high content due to the formation of the Skarn deposits such as W, Mo, Pb, and Zn in this type of rock (Figure 7).

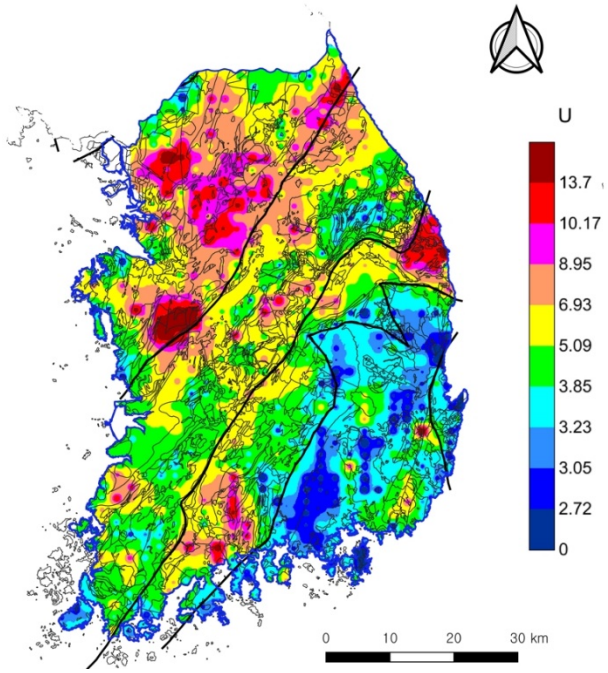

Figure 6. Low-density geochemical map for U. Bold line indicates geotectonic boundaries

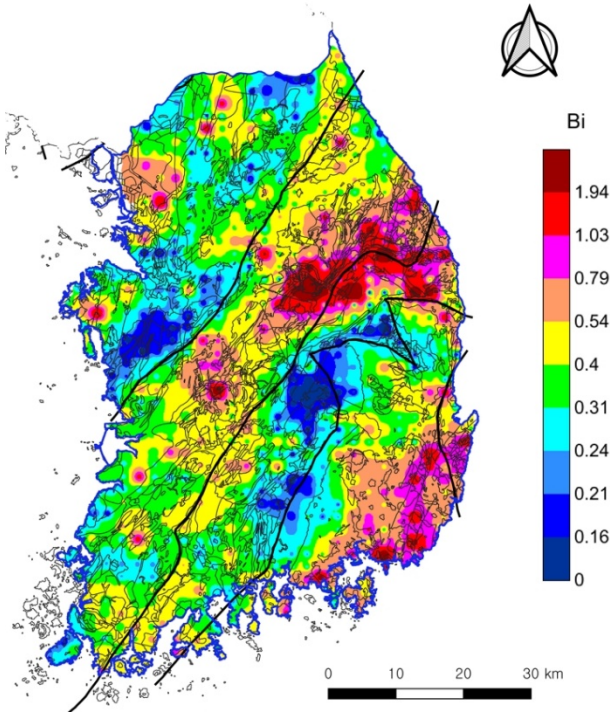

Figure 7. Low density geochemical map for Bi. Bold line indicates geotectonic boundaries

5 Conclusions

To create regional geochemical maps efficiently, we have chosen the composite sampling method that can save costs and time in sampling and analysis. A total of 953 composite samples were divided into 25 batches and analyzed for 10 elements (As, Be, Bi, C d, Mo, Sb, Sn, Tl, U, W) using ICP-MS. To obtain accurate analytical results, we conducted rigorous quality control. All project samples in batches that did not pass the QC procedure are currently undergoing re-analysis. Meanwhile, for the five elements that passed the QC, we calculated statistics and threshold values, and created national-scale geochemical maps. The regional distribution patterns of the elements largely reflect the underlying geology, but some can also show the influence of mineralization. Compared to the high-density geochemical map, it has been confirmed that low-density geochemical mapping using composite samples can be applied to identify regional geochemical distribution patterns and establish threshold values. However, low-density geochemical mapping can result in the loss of detailed geochemical information. To address this drawback, it would be necessary to carry out high-density geochemical surveys for anomalous areas.

8 Acknowledgements

This research was supported by the Basic Research Project of the Korea Institute of Geoscience and Mineral Resources (KIGAM) funded by the Ministry of Science and ICT of Korea (Code: 22-3412-2).

9 References

Birke, M., Rauch, U. and Stummeyer, J. (2015) How robust are geochemical patterns? A comparison of low and high sample density geochemical mapping in Germany, Journal of Geochemical Exploration, 154, p. 105-128

Eggen, O.A., Reimann, C. and Flem, B. (2019) Reliability of geochemical analyses: Déjà vu all over again, Science of the Total Environment, 670, p. 138-1148

KIGAM (1995) Geological Map of Korea 1:1,000,000. Korea Institute of Geoscience $ Mineral Resources.

KIGAM (2007) Geochemical Atlas of Korea (1:1,800,000), Series 9. Korea Institute of Geoscience & Mineral Resources, 68p [in Korean]

Negrel, P. Ladenberger, A., Reimann, C., Birke, M., Demetriades, A., Sadeghi, M., and The GEMAS Project Team (2019) Geochemical background and mineral potential of emerging tech-critical elements in Europe revealsed from low-sampling density geochemical mapping, Applied Geochemistry, 111, p. 104424

Zhizhong, C., Xuejing, X., Wensheng, Y., Jizhou, F., Qin, Z. and Jindong, F. (2014) Multi-element geochemical mapping in Southern China, Journal of Geochemical Exploration, 139, p. 183-192